UNIVERSITAT POLITÈCNICA DE VALÈNCIA

UNIVERSITAT
POLITÈCNICA
DE VALÈNCIA

Study of the thermal field of turbulent channel flows via Direct Numerical Simulations

PhD Thesis

Author: Francisco Alcántara Ávila

Thesis director: Dr. Sergio Hoyas Calvo

October 2021

Contents

Acknowledgments

En primer lugar, me gustaría dar las gracias a mi director de tesis, Sergio Hoyas. Su apoyo y guiado durante todos estos años son los máximos responsables de que mi trabajo sea lo que es hoy en día.

También, dar las gracias al profesor Luís García por su apoyo incondicional, el trabajo conjunto y las muchas facilidades y consejos que nos ha dado durante estos años.

Por supuesto, también agradezco la oportunidad ofrecida por el profesor Martin Oberlack y su buen recibimiento en Darmstadt. Parte de esta tesis tiene su marca.

Y de ese viaje a Alemania, como no agradecer la compañía de Alpa y Tim, los cuales hicieron mi estancia durante la pandemia mucho más entretenida.

Por último, no me olvido de mis compañeros y amigos con los que he compartido despacho, en particular Joja, Mara, Orlando, Nacho, Kiko y Chili.

Fuera del mundo académico, como no, el principal apoyo que he recibido ha sido de mis padres. Sin vosotros, esta tesis hubiera sido más complicada.

Y por supuesto, dar las gracias a mis hermanos, familiares y amigos por estar siempre a mi lado.

Finalmente, agradecer la ayuda de MINECO/FEDER. Este proyecto a sido apoyado por el proyecto ENE2015-71333-R.

Nomenclature

List of symbols

a_{ij}	Anisotropic stress tensor
B	Logarithmic profile constant
B_{ij}	Balance equation for $\overline{u_i u_j}$
c_p	Specific heat capacity at constant pressure
D	Mass diffusion
e	Identity element of a group
g	Gravitational acceleration
G	Group of elements
h	Channel half height
H	Correlation function for instantaneous variables
$\mathfrak{h}$	Convective heat transfer coefficient
$h_g,\ h_v$	Nonlinear terms of the evolution equations
I	Correlation functions for instantaneous variables involving pressure
k	Turbulent kinetic energy/thermal conductivity/wavenumber
$L_x,\ L_y,\ L_Z$	Computational box dimensions
n	Order of the velocity moment
$N_x,\ N_y,\ N_Z$	Number of collocation points
Nu	Nusselt number
m	Order of the temperature moment
p	Fluctuating pressure
P	Instantaneous pressure
$P_\bullet$	Production term
Pe_τ	Friction Péclet number
Pr	Prandtl number
Pr_t	Turbulent Prandtl number
$\dot{q}$	Heat flux
R	Correlation function for fluctuating variables
Re	Reynolds number
Re_D	Reynolds number based on the diameter of a pipe
Re_τ	Friction Reynolds number
Ri_τ	Friction Richardson number
S_{ij}	Deformation tensor
Sc	Schmidt number
t	Time
$\mathcal{T}$	Period of time
T	Temperature/Lie group of transformation

CONTENTS

$T_\bullet$	Turbulent diffusion term
$\boldsymbol{u}$	Fluctuating velocity components $(u, v, w) = (u_1, u_2, u_3)$
$\boldsymbol{U}$	Instantaneous velocity components $(U, V, W) = (U_1, U_2, U_3)$
U_b	Bulk velocity
u_τ	Friction velocity
$V_\bullet$	Viscous diffusion term
$\boldsymbol{x}$	Spatial coordinate $(x, y, z) = (x_1, x_2, x_3)$
X	Infinitesimal operator

Greek

α	Thermal diffusion/scaling parameter
β	Scaling parameter
γ	Exponent of the scaling of the conductive sublayer thickness
δ_{ij}	Kronecker delta
$\Delta_x, \Delta_y, \Delta_z$	Mesh resolution
Δ_θ	Conductive sublayer thickness
ε	Dissipation/group parameter
$\varepsilon_\bullet$	Dissipation budget term
η	Kolmogorov length scale
η_θ	Batchelor length scale
θ	Transformed temperature fluctuation
Θ	Instantaneous transformed temperature
θ_τ	Friction temperature
κ	Von Kármán constant
κ_t	Thermal von Kármám constant
λ	Wavelength
μ	Dynamic viscosity
ν	Kinematic viscosity
ν_{eff}	Effective viscosity
ν_τ	Turbulent viscosity
ξ	Infinitesimal
Ξ	Diagnostic function of the velocity
Ξ_T	Diagnostic function of the temperature
$\Pi_\bullet$	Pressure budget term
ρ	Constant density/density fluctuation
ρ_t	Instantaneous density
$\sigma_1, \sigma_2, \sigma_\Theta$	Scaling parameters
τ	Shear stress
τ_{ij}	Reynolds stress tensor
ϕ	Law of composition
ω	Scaling parameter
$\boldsymbol{\omega}$	Fluctuating vorticity component $(\omega_1, \omega_2, \omega_3)$
$\boldsymbol{\Omega}$	Instantaneous vorticity component $(\Omega_1, \Omega_2, \Omega_3)$

Superscripts

$\bullet'$	Root mean square
$\bar{\bullet}$	Statistically averaged/filtered variable
$\bullet^*$	Normalized by h, U_b and ν
$\bullet^+$	Normalized by u_τ, θ_τ and ν

Subscripts

$\langle \bullet \rangle_{x_i}$ Averaged in time and x_i directions
$\bullet_c$ Related to the center of the channel
$\bullet_C$ Related to Couette flows
$\bullet_l$ Related to the smallest scaled of the flow
$\bullet_L$ Related to the largest scales of the flow
$\bullet_P$ Related to Poiseuille flows
$\bullet_w$ Related to the wall
$\bullet_\eta$ Related to Kolmogorov scales
$\bullet_\theta$ Related to the thermal field

Abstract

The main goal of this thesis is the study of heat transfer in turbulent channels to obtain a better knowledge about the phenomenon of turbulence. For this, a study has been carried out from the point of view of computational fluid mechanics, specifically, the technique of direct numerical simulations (DNS) has been used. This type of simulation is very computationally expensive, but the results they provide are highly accurate and faithful to reality, as long as the discretization schemes are correct. The main idea of the simulations conducted has been to expand the current state of the art, regarding the two main parameters that characterize the flow: the friction Reynolds number, Re_τ and the Prandtl number, Pr . Two flow configurations have been used: Poiseuille flow and Couette flow, the former being the main focus of the study. Regarding the temperature field, a mixed boundary condition has been used and it has been considered as a passive scalar.

Thus, the simulated friction Reynolds numbers for a Poisuille flow have been $Re_\tau = 500$, 1000 and 2000, for Prandtl numbers ranging from 0.007 (molten metals) up to 10 (water) , passing through 0.71 which is the most used value since this is the Prandtl number of the air. Also, a simulation has been performed with $Re_\tau = 5000$ and $Pr = 0.71$, which is the thermal DNS with the highest friction Reynolds number up to date. A first distinction of heat flux can be made for Prandtl numbers less or greater than $Pr = 0.3$. When the Prandtl number is less than 0.3, the conductive region extends above the logarithmic layer, and even penetrates to the central region of the channel, forming a practically laminar thermal field, for the lowest Prandtl numbers. For thermal fields where the logarithmic layer begins to emerge, the value of the von Kármán thermal constant, κ_t tends to a constant value of approximately $\kappa_t = 0.44$ as the Reynolds number tends to infinity, and that value is independent of the Prandtl number. Regarding the variance of the temperature, θ'^+ and the turbulent heat flow in the direction of the current, $\overline{u^+\theta^+}$, the collapse in the outer region is determined by the friction Péclet number, $Pe_\tau = Re_\tau Pr$, instead of the Reynolds or Prandtl number. Furthermore, it has been observed that for the highest Prandtl numbers, the maximum value of the variance of the temperature is constant. This has a significant impact on the scaling of the θ'^+ budget terms. Specifically, the dissipation and viscous diffusion, which scale with much greater precision near the wall for high Prandtl numbers. This is an important result, since many models of the energy equation are based on these budget equations, so obtaining good scaling for different parameters means greater reliability of the models. Finally, it should be noted that new correlations have been presented for the Nusselt number, Nu, valid for the ranges of Re_τ and Pr studied.

Finally, with regard to Poiseuille flow simulations, the isothermal case has been studied with $Re_\tau = 10000$, which is also the largest DNS of a turbulent channel. It should be noted that, for the first time in a DNS, a perfectly developed logarithmic layer has been observed in the velocity field, with a value of the von Kármán constant of $\kappa = 0.394$.

A theoretical study has been carried out in parallel to the simulations. The objective of this study, based on Lie symmetries, was the generation of scaling laws of velocity and temperature field and high order moments of both. Although this theory had been applied to the velocity field, it is the first time that it has been applied to the temperature field and to high order moments of velocity and temperature. The result is that for sufficiently high Reynolds numbers, and moderate Prandtl numbers, the velocity,

temperature, and high order moment of both scale as defect laws of power functions of the distance from the wall in the center of the channel. The main advantages of these scaling laws are that they have been obtained from first principles, that is, they have been directly derived from the Navier-Stokes and energy equations, and that it is enough to calculate the scaling of the first two velocity and temperature moments to know the exponent of the scaling of any higher order moment. In the same way, a scaling of the velocity in the logarithmic layer has been obtained for the case of $Re_\tau = 10000$, obtaining the classical logarithmic function for the average velocity and a potential function for the moments of higher orders. The validation of these scaling laws has been carried out using the data obtained in the simulation. The result is an excellent precision by scaling laws to represent DNS values.

Finally, a Couette flow simulations have been performed with the Prandtl number of air, $Pr = 0.71$, and friction Reynolds numbers of values $Re_\tau = 180, 250$ and 500. The main objective was the study of the coherent structures that are formed in these Couette flows, which extend along the streamwise direction. These structures had already been studied for the velocity field and the first detailed study of temperature structures has been presented in this work. Specifically, it has been seen that structures affect turbulent intensities and that is why the width of the computational domain is key in Couette flow simulations. A minimum width of $6\pi h$ is required for the statistics to be independent of the computational domain.

A last series of simulations has been performed considering stratified flow, that is, the thermal field is an active scalar. The objective is to study whether Couette structures persist in this type of flow. For this, the Couette flow and a constant temperature difference between both walls have been taken as the boundary conditions. Thus, for a $Re_\tau = 500$ and the Prandtl number of air, $Pr = 0.71$, the values of the friction Richardson number have been varied according to, $Ri_\tau = 0.5, 1.65$ and 2.90, for each simulation. For the two cases with the highest friction Richardson number, the Couette flow structures have been observed to weaken to the point of being almost non-existent.

The principal statistics of the simulations are available in the database of the research group, which is open to the scientific community in the following link

http://personales.upv.es/serhocal/

Resumen

El principal objetivo de esta tesis es el estudio de flujos térmicos turbulentos en canales para obtener un mayor conocimiento sobre el fenómeno de la turbulencia. Para ello, se ha realizado un estudio desde el punto de vista de la mecánica de fluidos computacional, en concreto, se ha utilizado la técnica de las simulaciones numéricas directas (DNS de sus siglas en inglés). Este tipo de simulaciones tienen un alto coste computacional, pero los resultados que proporcionan son de una gran exactitud y fieles a la realidad, siempre y cuando los esquemas de discretización sean correctos. La idea principal de las simulaciones realizadas ha sido ampliar el estado del arte actual, en lo referente a los dos parámetros principales que caracterizan el flujo: el número de Reynolds de fricción, Re_τ, y el número de Prandtl, Pr. Dos configuraciones del flujo han sido utilizadas: flujo de Poiseuille y flujo de Couette, siendo la primera el principal foco del estudio. En cuanto al campo de temperaturas, se ha utilizado una condición de contorno mixta y se ha considerado como un escalar pasivo.

Así pues, los números de Reynolds de fricción simulados para un flujo de Poisuille han sido $Re_\tau = 500$, 1000 y 2000, para números de Prandtl que varían desde 0.007 (metales fundidos) hasta 10 (agua), pasando por 0.71 que es el valor más utilizado por ser éste el número de Prandtl del aire. Además, se ha realizado una simulación con $Re_\tau = 5000$ y $Pr = 0.71$, la cual es la DNS térmica con el número de Reynolds de fricción más alto hasta la fecha. Una primera distinción del flujo térmico puede hacerse para números de Prandtl menores o mayores a $Pr = 0.3$. Cuando el número de Prandtl es menor que 0.3, la región conductiva se extiende por encima de la capa logarítmica, e incluso penetra hasta la zona central del canal, formando un campo térmico prácticamente laminar, para los números de Prandtl más bajos. Para los campos térmicos donde la capa logarítmica empieza a emerger, el valor de la constante térmica de von Kármán, κ_t tiende a un valor constante de aproximadamente $\kappa_t = 0.44$ conforme el número de Reynolds tiende a infinito, y ese valor es independiente del número de Prandtl. Respecto a la varianza de la temperatura, θ'^+ y el flujo térmico turbulento en la dirección de la corriente, $\overline{u^+\theta^+}$, el colapso en la zona exterior está determinado por el número de Péclet de fricción, $Pe_\tau = Re_\tau Pr$, en vez del número de Reynolds o de Prandtl. Además, se ha observado que para los números de Prandtl más altos, el valor máximo de la varianza de la temperatura es constante. Esto tiene una importante repercusión en el escalado de los términos del balance de energía de θ'^+. En concreto la disipación y la difusión viscosa, los cuales escalan con mucha más precisión cerca de la pared para los casos de un número de Prandtl altos. Este es un importante resultado, pues muchos modelos de la ecuación de la energía se basan en estas ecuaciones de balances, por lo que obtener un buen escalado para diferentes parámetros significa una mayor precisión de los modelos. Finalmente, destacar que se han presentado nuevas correlaciones para el número de Nusselt, Nu, válidas para los rangos de Re_τ y Pr estudiados.

Por último en lo referente a simulaciones de flujos de Poiseuille, se ha estudiado el caso isotérmico con $Re_\tau = 10000$, la cual es también la mayor DNS de un canal turbulento. Cabe destacar que, por primera vez en una DNS, se ha observado una capa logarítmica perfectamente desarrollada en el campo de velocidades, con un valor de la constante de von Kármán de $\kappa = 0.394$.

Un estudio teórico ha sido llevado a cabo en paralelo a las simulaciones. Este estudio, basado en las simetrías de Lie, ha tenido como objetivo la generación de leyes de escaldo del campo de velocidades,

temperatura y momentos de altos órdenes de ambos campos. Si bien esta teoría había sido aplicada al campo de velocidades, es la primera vez que se aplica al campo de temperaturas y a los momentos de velocidad-temperatura de altos órdenes. El resultado es que para números de Reynolds suficientemente altos, y números de Prandtl moderados, los campos de velocidad, temperatura y momentos de altos órdenes de ambos, escalan como leyes de defecto de funciones de potencia de la distancia de la pared en el centro del canal. Las principales ventajas de estas leyes de escalado son que han sido obtenidas de primeros principios, es decir, han sido directamente derivadas de las ecuaciones de Navier-Stokes y de la energía, y que basta con conocer el escalado de los dos primeros momentos de velocidad y temperatura para conocer el exponente del escalado de cualquier momento superior. De la misma forma, se ha obtenido un escalado de la velocidad en la capa logarítmica para el caso de $Re_\tau = 10000$, obteniendo la clásica función logarítmica para la velocidad media y una función potencial para los momentos de órdenes superiores. La validación de estas leyes de escalado ha sido llevada a cabo utilizando los datos obtenidos en la simulación. El resultado es de una precisión excelente por parte de las leyes de escalado para representar los valores de las DNS.

Por último, se han realizado una simulaciones de flujo de Couette con el número de Prandtl de aire, $Pr = 0.71$, y números de Reynolds de fricción de valores $Re_\tau = 180$, 250 y 500. El principal objetivo era el estudio de las estructuras coherentes que se forman en estos flujos de Couette, que se prolongan a lo largo de la dirección del flujo. Estas estructuras, se habían estudiado ya para el campo de velocidades y se ha presentado en este trabajo el primer estudio detallado de las estructuras de temperatura. En concreto, se ha visto que las estructuras afectan a las intensidades turbulentas y es por ello que la anchura del dominio computacional es clave en las simulaciones de flujos de Couette. Se necesita como mínimo una anchura de $6\pi h$ para que las estadísticas sean independientes del dominio computacional.

Una última serie de simulaciones ha sido llevada a cabo considerando flujo estratificado, es decir, el campo térmico es un escalar activo. El objetivo es estudiar si las estructuras de Couette persisten en este tipo de flujos. Para ello, se han tomado las condiciones de contorno de flujo de Couette y de una diferencia de temperatura constante entre ambas paredes. Así pues, para un $Re_\tau = 500$ y el número de Prandtl de aire, $Pr = 0.71$, se han tomado valores del número de Richardson de fricción, $Ri_\tau = 0.5$, 1.65 y 2.90. Para los dos casos con el número de Richardson de fricción más alto, se ha observado que las estructuras del flujo de Couette se debilitan hasta el punto de ser casi inexistentes.

Las principales estadísticas de las simulaciones se encuentran disponibles en la base de datos del grupo de investigación, la cual está abierta a la comunidad científica y se puede acceder desde el siguiente enlace

http://personales.upv.es/serhocal/

Resum

El principal objectiu d'aquesta tesi és l'estudi de fluxos tèrmics turbulents en canals per obtenir un major coneixement sobre el fenomen de la turbulència. Per a això, s'ha realitzat un estudi des del punt de vista de la mecànica de fluids computacional, en concret, s'ha utilitzat la tècnica de les simulacions numèriques directes (DNS de les seues sigles en anglès). Aquest tipus de simulacions tenen un alt cost computacional, però els resultats que proporcionen són d'una gran exactitud i fidels a la realitat, sempre que els esquemes de discretització siguen correctes. La idea principal de les simulacions realitzades ha sigut la de ampliar l'estat de l'art actual, en el referent als dos paràmetres principals que caracteritzen el flux: el número de Reynolds de fricció, Re_τ i el número de Prandtl, Pr. Dos configuracions del flux han sigut utilizades: flux de Poiseuille i flux de Couette, sent la primera el principal focus de l'estudi. Pel que fa a el camp de temperatures, s'ha utilitzat una condició de contorn mixta i s'ha considerat com un escalar passiu.

Així doncs, els números de Reynolds de fricció simulats per a un flux de Poisuille han sigut $Re_\tau = 500$, 1000 i 2000, per a números de Prandtl que varien des de 0.007 (metalls fosos) fins 10 (aigua), passant per 0.71 que és el valor més utilitzat per ser aquest el número de Prandtl de l'aire. A més, s'ha realitzat una simulació amb $Re_\tau = 5000$ i $Pr = 0.71$, la qual és la DNS tèrmica amb el número de Reynolds de fricció més alt fins a la data. Una primera distinció del flux tèrmic pot fer-se per a números de Prandtl menors o majors a $Pr = 0.3$. Quan en número de Prandtl és menor que 0.3, la regió conductiva s'estén sobre de la capa logarítmica, i arriba a penetrar fins a la zona central del canal, formant un camp tèrmic pràcticament laminar, per als números de Prandtl més baixos. Per als camps tèrmics on la capa logarítmica comença a emergir, el valor de la constant tèrmica de von Kármán, κ_θ tendeix a un valor constant d'aproximadament $\kappa_\theta = 0.44$ per a números de Reynolds que tendeixen a infinit, i aquest valor és independent del número de Prandtl. Pel que fa a la variància de la temperatura, θ'^+ i el flux tèrmic turbulent en la direcció del corrent, $\overline{u^+\theta^+}$, el col·lapse a la zona exterior està determinat per el número de Péclet de fricció, $Pe_\tau = Re_\tau Pr$, en comptes del número de Reynolds o de Prandtl. A més, s'ha observat que per als números de Prandtl més alts, el valor màxim de la variància de la temperatura és constant. Això té una important repercussió en l'escalat dels termes del balanç d'energia de θ'^+. En concret la dissipació i la difusió viscosa, els quals escalen amb molta més precisió a prop de la paret per als casos d'un número de Prandtl alts. Aquest és un important resultat, ja que molts models de l'equació de l'energia es basen en aquestes equacions de balanços, de manera que obtenir un bon escalat per a diferents paràmetres significa una major precisió dels models. Finalment, destacar que s'han presentat noves correlacions per al número de Nusselt, Nu, vàlides per als rangs de Re_τ i Pr estudiats.

Finalment pel que fa a simulacions de fluxos de Poiseuille, s'ha estudiat el cas isotèrmic amb $Re_\tau = 10000$, la qual és també la major DNS d'un canal turbulent. Cal destacar que, per primera vegada en una DNS, s'ha observat una capa logarítmica perfectament desenvolupada en el camp de velocitats, amb un valor de la constant de von Kármán de $\kappa = 0394$.

Un estudi teòric ha sigut dut a terme en paral·lel a les simulacions. Aquest estudi, basat en les simetries de Lie, ha tingut com a objectiu la generació de lleis de escalat del camp de velocitats, temperatura i moments d'alts ordres de tots dos camps. Si bé aquesta teoria havia estat aplicada a el camp de velocitats, és la primera vegada que s'aplica a el camp de temperatures i als moments de velocitat-temperatura d'alts

ordres. El resultat és que per a números de Reynolds suficientment alts, i números de Prandtl moderats, els camps de velocitat, temperatura i moments d'alts ordres de tots dos, escalen com a lleis de defecte de funcions de potència de la distància de la paret al centre del canal. Els principals avantatges d'aquestes lleis d'escalat són que han sigut obtingudes de primers principis, és a dir, han estat directament derivades de les equacions de Navier-Stokes i de l'energia, i que n'hi ha prou amb conèixer l'escalat dels dos primers moments de velocitat i temperatura per conèixer l'exponent de l'escalat de qualsevol moment superior. De la mateixa manera, s'ha obtingut un escalat de la velocitat a la capa logarítmica per al cas de $Re_\tau = 10000$, obtenint la clàssica funció logarítmica per la velocitat mitjana i una funció potencial per als moments d'ordres superiors. La validació d'aquestes lleis d'escalat ha estat portada a terme utilitzant les dades obtingudes en la simulació. El resultat és d'una precisió excel·lent per part de les lleis d'escalat per representar els valors de les DNS.

Finalment, s'han realitzat unes simulacions de flux de Couette amb el número de Prandtl de l'aire, $Pr = 0.71$, i números de Reynolds de fricció de valors $Re_\tau = 180$, 250 i 500. El principal objectiu era l'estudi de les estructures coherents que es formen en aquests fluxos de Couette, que es perllonguen al llarg de la direcció del flux. Aquestes estructures, s'havien estudiat ja per al camp de velocitats i s'ha presentat en aquest treball el primer estudi detallat de les estructures de temperatura. En concret, s'ha vist que les estructures afecten les intensitats turbulentes i és per això que l'amplada del domini computacional és clau en les simulacions de fluxos de Couette. Es necessita com a mínim una amplada de $6\pi h$ perquè les estadístiques siguin independents del domini computacional.

Una última sèrie de simulacions ha estat portada a terme considerant flux estratificat, és a dir, el camp tèrmic és un escalar actiu. L'objectiu és estudiar si les estructures de Couette persisteixen en aquest tipus de fluxos. Per a això, s'han pres les condicions de contorn de flux de Couette i d'una diferència de temperatura constant entre les dues parets. Així doncs, per a un $Re_\tau = 500$ i el número de Prandtl d'aire, $Pr = 0.71$, s'han pres valors del número de Richardson de fricció, $Ri_\tau = 0.5$, 1.65 i 2.90. Per als dos casos amb el número de Richardson de fricció més alt, s'ha observat que les estructures del flux de Couette es debiliten fins al punt de ser pràcticament inexistents.

Les principals estadístiques de les simulacions es troben disponibles en la base de dades del grup d'investigació, la qual està oberta a la comunitat científica i es pot accedir des del següent enllaç

http://personales.upv.es/serhocal/

Chapter 1

Introduction

This work presents an analysis of wall turbulence, with a special focus on thermal flows. Although an exact definition of turbulence does not exist, it is quite intuitive to detect when a flow is turbulent. A turbulent flow is characterized by a chaotic and random movement of its particles.

Turbulent flows are the most usual type of flow in nature and our everyday life. From examples at very small scales, like the mixing of fuel with air in the combustion chamber of an engine, up to examples at big scales, as the oceanic or air currents (figure 1.1), all are cases of turbulent flows. Almost any flow one can think of in an engineering problem, except for lubrication problems, is a turbulent flow, which makes it extremely important to understand their behavior. For this reason, turbulent flows have been extensively studied in the past, with still a considerable amount of open questions to be solved.

Two main approaches are used to study the dynamics of turbulent flows: experimental analysis and numerical simulations. The focus of this study will be on the last one, also known as Computational Fluid Dynamics (CFD). Inside the field of CFD, there are several ways of treating the equations that describe the flow motion to numerically solve them. Direct Numerical Simulation (DNS) is a technique characterized by its high precision and fidelity to the reality of the results obtained. It is the ideal tool to obtain answers about the behavior of turbulence.

Despite DNS are a powerful method from the theoretical point of view, for practical purposes, their computational cost is extremely expensive. Even today the simulation of the flow around a plane would cost hundreds of thousands of years using the most powerful supercomputer on Earth. The trend has been to create models that considerably simplify the physics of the flow. In many cases, only mean quantities are considered. However, these models must be based on reliable data, and therefore, the role of DNS is crucial. Regarding the models used, the most common method at the industry level is the Reynolds-averaged Navier–Stokes (RANS) equations (explained in more detail in section §2.1). After averaging the governing equations of turbulence, an extra term appear and the system of equations has more unknowns than equations. This extra term, known as the Reynolds stress tensor is approximated by models such as $k - \varepsilon$, $k - \omega$, Spalart–Allmaras,... each one being more or less accurate in different types of flows.

Regarding the search for better turbulence models, a relatively new mathematical theory in the sense of when it started to be applied to turbulence, is the Lie symmetry theory. Symmetry analysis is a powerful mathematical method to obtain an invariant solutions of a partial derivative system of equations. The use of Lie symmetries has proven to be very useful in the field of turbulence, where these invariant solutions are known as scaling laws. Therefore, using Lie symmetries one can obtain, from first principles, scaling laws that describe universal behaviors of turbulent flows.

In this study, we try to answer some of these questions, or at least to advance towards a possible theory for a better understanding of the turbulence phenomena, using DNS as the main tool of work. The focus of the analysis will be the thermal field. After that, Lie symmetries will be used to obtain
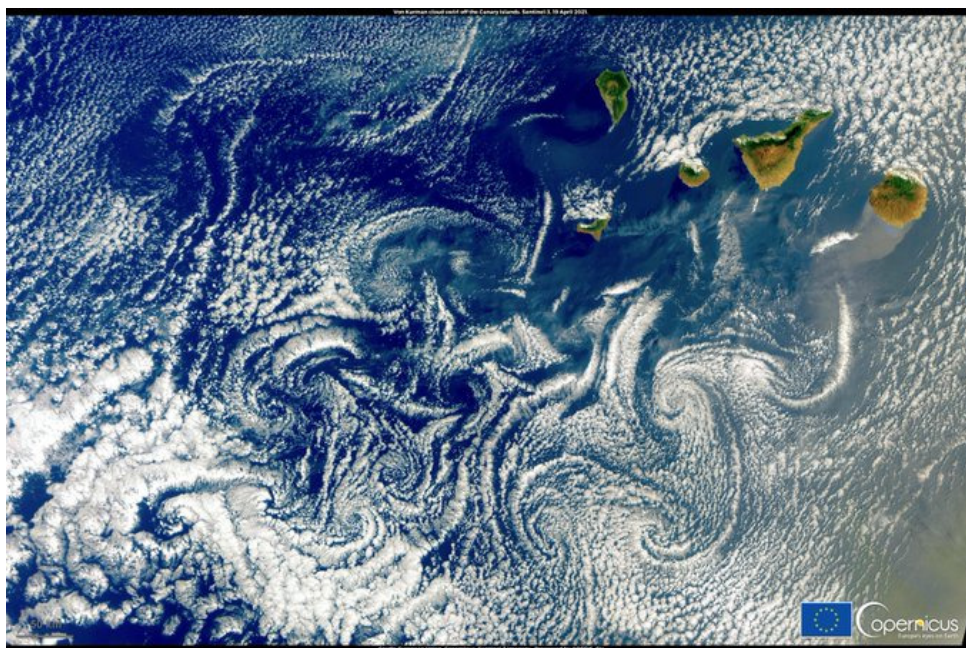
Figure 1.1: Air currents from the north-east on its way through the Canary Islands. The emerging islands induce turbulent structures downstream, known as the Kármán vortex street. Image courtesy of ESA.

scaling laws of the moments of the velocity and temperature field.

1.1 Introduction to turbulence

The etymological origin of the word turbulence is, from Latin, *turbulentia*, referring to the quality of being turbid and agitated. Its lexical components are turbo (rapid circular movement) and the suffixes -ulentus (indicates that it has the nature of) and -ia (quality). Although the knowledge of the quality of turbulence is very old, it was not until the XIX century, when the turbulent flows started to be studied as a concept.

The first important work about turbulence was done by Osborne Reynolds in 1883 [1], where differentiation between laminar and turbulent flows was made. In his experiment, Reynolds observed the flow of water through a tube. At the beginning of this tube, some ink drops were injected to observe the path of the drop particles. At low velocities, the drop formed a perfectly straight line through the tube. This is the main characteristic of laminar flows, the opposite of turbulent flows. In laminar flows, the particles move in an orderly fashion and changes occur smoothly. In laminar flows, one can perfectly follow the path that a particle travels through the flow, which is called a pathline. When the velocity of the water was increased up to a certain speed, at some point in the tube, the ink started to disperse and mix with the surrounding water, filling the rest of the downstream tube with a mass of the ink. The faster the velocity was, the sooner the dispersion of the ink drops started. When this feature occurs in the flow, it is said to be a turbulent flow. In contrast to laminar flows, in a turbulent flow, one could not predict the pathlines of the particles. The fast mixing of the ink with the water is also a very important property of turbulent flows, which is its capacity to break gradients. Turbulent flows are very good at mixing. For example, the fuel and the air in a combustion chamber or the hot air coming from a stove with the cold air in a room. If the flow were laminar, no combustion would be possible in a reasonable
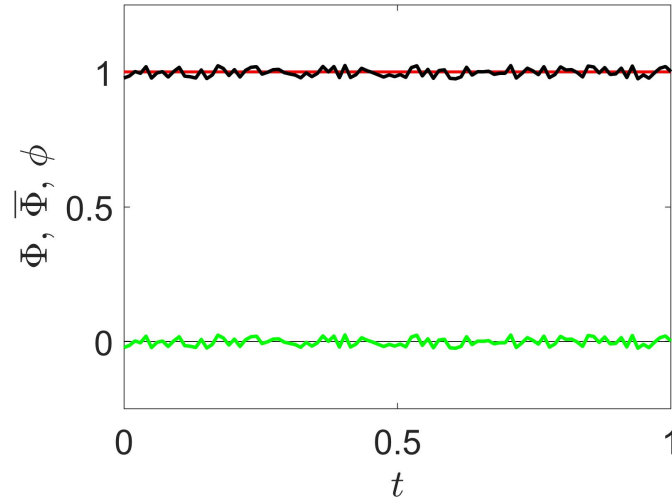
Figure 1.2: Exemplification of the Reynolds decomposition. Black line is the instantaneous value, $\Phi(t, \boldsymbol{x})$; red line is the average part, $\overline{\Phi}(\boldsymbol{x})$; and green line is the fluctuating part, $\phi(t, \boldsymbol{x})$.

time, and it would take hours, or days, for the stove to warm up a room. Reynolds could approximately determine when a flow went from being laminar to turbulent with the famous dimensionless Reynolds number, defined as

$$Re = \frac{hU}{\nu}, \tag{1.1}$$

where h is a characteristic length of the problem, in the case of the experiment carried out in [1], the diameter of the tube; U is the mean velocity of the flow, and ν is the kinematic viscosity of the fluid. The Reynolds number can be seen as the ratio between the inertial and the viscous forces on the flow.

The critical value of Re that divided laminar and turbulent flows was of the order of 10^3. However, the transition from the laminar to the turbulent regime was not obtained at a specific Re value, but a gradual progression was observed. Actually, there is not a specific value to determine when a flow is laminar or turbulent and a transitory regime exists. Furthermore, it also depends on the geometry of the problem and the surface roughness. Nevertheless, in almost all flows of interest in engineering, except in lubrication problems, the Reynolds numbers of these problems are orders of magnitude above the critical value. Hence, the importance of studying turbulent flows. Another important characteristic of turbulent flows is that they are not stationary, and they forget, in small scales of time, about the previous conditions of the flow. This generates big differences in the final state of the flow under very small changes of the initial conditions.

In the next decade, Osborne Reynolds proposed what is known as the Reynolds decomposition [2]. For statistically steady flows, he stated that any instantaneous variable of the flow, such as velocity, density, pressure, temperature,..., can be divided into a mean part, independent of time, and the temporal fluctuating part

$$\Phi(t, \boldsymbol{x}) = \overline{\Phi}(\boldsymbol{x}) + \phi(t, \boldsymbol{x}), \tag{1.2}$$

where Φ is the instantaneous value of any variable of the flow (velocity, density, pressure, temperature,...); the overline, $\overline{\bullet}$, represents average in time of the variable; and lower case states for the temporal fluctuating

3

part. The averaged variable is defined as

$$\overline{\Phi}(\boldsymbol{x}) = \lim_{\mathcal{T} \to \infty} \frac{1}{\mathcal{T}} \int_0^{\mathcal{T}} \Phi(t, \boldsymbol{x}) dt, \tag{1.3}$$

where t is the time and $\mathcal{T}$ is a period of time, which should be large enough, compared with the characteristic time of the fluctuations, so that $\overline{\Phi}$ is independent of t. Figure 1.2 shows an example of the Reynolds decomposition for a variable Φ. Two important properties are obtained from (1.2) and (1.3), and can be easily observed in figure 1.2. The average in time of an average is the average itself, and the average in time of a fluctuation is 0. These and some additional properties can be written as

$$\overline{\overline{\Phi}} = \overline{\Phi}, \quad \overline{\phi} = 0$$
$$\overline{\overline{\Phi}\,\overline{\Phi}} = \overline{\Phi}\,\overline{\Phi}, \quad \overline{\overline{\Phi}\phi} = 0, \quad \overline{\phi(t, \boldsymbol{x})\phi(t, \boldsymbol{x})} = \overline{\phi\phi}(\boldsymbol{x}). \tag{1.4}$$

In the last relation, note that the average of the product of two fluctuating parts is not 0 and the time and space dependencies have been explicitly written to remark the fact that the resulting of the average is treated as a single variable that does not depend on time. The Reynolds decomposition has been the basis of one of the principal techniques to numerically solve the governing equations that describe the motion of fluids. These equations are the famous Navier-Stokes equations, which are composed of the continuity and momentum equations. For constant properties Newtonian fluids, they are written as

$$\mathcal{C}(\boldsymbol{x}) \equiv \frac{\partial U_i(t, \boldsymbol{x})}{\partial x_i} = 0, \tag{1.5}$$

$$\mathcal{M}_i(\boldsymbol{x}) \equiv \frac{\partial U_i(t, \boldsymbol{x})}{\partial t} + U_j(t, \boldsymbol{x}) \frac{\partial U_i(t, \boldsymbol{x})}{\partial x_j} = -\frac{1}{\rho} \frac{\partial P(t, \boldsymbol{x})}{\partial x_i} + \nu \frac{\partial^2 U_i(t, \boldsymbol{x})}{\partial x_j \partial x_j}. \tag{1.6}$$

In these equations, $\boldsymbol{x}$ are the spatial coordinates, and ρ and ν are the density and kinematic viscosity, respectively, which are considered constants, and P is the pressure. It is also of special interest due to engineering applications, the governing equation of the temperature field, known as the energy equation

$$\mathcal{E}(\boldsymbol{x}) \equiv \frac{\partial T(t, \boldsymbol{x})}{\partial t} + U_j(t, \boldsymbol{x}) \frac{\partial T(t, \boldsymbol{x})}{\partial x_j} = \alpha \frac{\partial^2 T(t, \boldsymbol{x})}{\partial x_j \partial x_j}, \tag{1.7}$$

where T is the temperature and α is the thermal diffusion coefficient, which is considered constant. Here, we only present the energy equation and further analysis will be done in section §1.1.2.

Introducing the Reynolds decomposition (1.2) into the the continuity equation (1.5), taking the average, and considering relations from (1.4), results in

$$\frac{\partial \overline{U}_i(\boldsymbol{x})}{\partial x_i} = 0, \tag{1.8}$$

which indicates that the mean variables also fulfill the continuity condition. If the same procedure is done for the momentum equations (1.6), it is obtained

$$\overbrace{\left(\frac{\partial \overline{U}_i(\boldsymbol{x})}{\partial t}\right)}^{=0} + \overline{U}_j(\boldsymbol{x}) \frac{\partial \overline{U}_i(\boldsymbol{x})}{\partial x_j} = -\frac{1}{\rho} \frac{\partial \overline{P}(\boldsymbol{x})}{\partial x_i} + \frac{\partial}{\partial x_j} \left(\nu \frac{\partial \overline{U}_i(\boldsymbol{x})}{\partial x_j} - \overline{u_i u_j}(\boldsymbol{x}) \right). \tag{1.9}$$

Equations (1.8) and (1.9) are the denominated Reynolds Averaged Navier-Stokes (RANS) equations. The last term on the right-hand side of the averaged momentum equation (1.9) comes from the nonlinearity of the Navier-Stokes equations. This extra term is known as the Reynolds stress tensor, also written

as $\tau_{ij} = -\overline{u_i u_j}$, and each component of the tensor is treated as an extra unknown. RANS equations are composed of four equations: one continuity and three momentum equations; with ten unknowns: pressure, three velocities and six components of the Reynolds stress tensor (note that this tensor is symmetric). If one looks for extra equations for the components of the Reynolds stress tensor, more unknowns of the type $\overline{u_i u_j u_k}$ will appear, making it impossible to achieve a determinate system of equations. This is known as the closure problem of the Navier-Stokes equations. Although analytical solutions of the Navier-Stokes equations have been obtained for very concrete cases, a general analytical solution is still unknown, and the proof of existence, uniqueness, and smoothness of this solution is one of the seven mathematical problems of the millennium.

During the first decades of the 20th century, different authors presented models of the Reynolds stress tensor to solve the closure problem [3, 4, 5]. These models are equations that estimate τ_{ij} from the analogy between eddies in a turbulent flow and the molecules in a gas, as proposed by Boussinesq in 1877 [6].

A new theory arose in 1920 developed by Richardson [7]. He introduced the concept of the energy cascade to explain how energy is transferred in the flow. First, the biggest eddies of the flow receive the energy from external forces and due to the dynamics of the flow, these eddies break into smaller eddies. This process is repeated until the eddies are small enough and can be dissipated by viscosity.

In the 40s, Kolmogorov quantified the energy transferred and the length scales of the eddies that formed the energy cascade [8, 9]. The energy injected in the flow from the external forces to the largest structures is u_L^3/L_L. Here, L_L is the length scale of the biggest structures on the flow, which is of the same order of magnitude as the domain of the problem; and u_L are the velocity variations of these structures. Their associated Reynolds number, Re_L is big enough so the viscosity has no effect. Therefore, no energy is dissipated and all the energy from the external forces must be transferred to smaller structures. This procedure reaches a point where the small structures have forgotten the origin of the external forces and, thus, turbulence is homogeneous and isotropic for these and smaller scales. In the equilibrium, the energy transferred should be constant and equal to the dissipation, ε, since viscosity is not effective in dissipating energy at this level. Therefore, the velocity variations, u_l, and length scales, l of these eddies should scale as

$$u_l \sim \left(\frac{u_L^3 l}{L_L}\right)^{1/3} \sim (\varepsilon l)^{1/3}, \tag{1.10}$$

with an associated Reynolds number that scales as

$$Re_l \sim \frac{u_l l}{\nu} \sim \left(\frac{\varepsilon l^4}{\nu^3}\right)^{1/3}. \tag{1.11}$$

After several jumps in the energy cascade, the Reynolds number of the eddies reaches the order of the unity, and viscosity is then important and dissipates the energy. Doing a dimensional analysis, it is obtained that the length and velocity scales of the eddies for this to occur must be

$$\eta = \left(\frac{\nu^3}{\varepsilon}\right)^{1/4}, \quad u_\eta = (\nu\varepsilon)^{1/4}. \tag{1.12}$$

The length scale, η, and velocity scale u_η are known as the Kolmogorov scales. The range where the scale of the eddies is of the order of the Kolmogorov scales, i.e., $l \sim \eta$, is called dissipative range since it is where the energy is dissipated. On the other hand, in the range where the eddies are smaller than the integral scales but bigger than the Kolmogorov scales, i.e., $\eta \ll l \ll L_L$, relation (1.10) holds and it called inertial range because the inertial terms of the momentum equations are dominant in the dynamics of the flow.
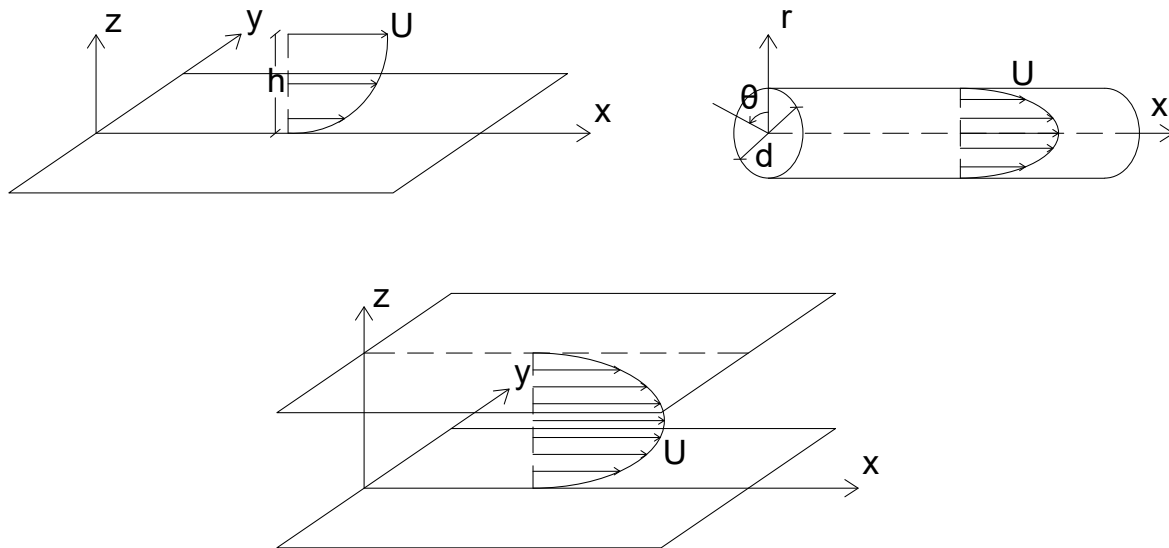
Figure 1.3: Sketch of the three main domains of wall bounded turbulence. Boundary layer (top left), pipe flows (top right) and channels with parallel walls (bottom).

1.1.1 Wall turbulence

The model described in the previous section is for homogeneous turbulence. However, in almost every practical case, there is a boundary that delimits the domain and breaks the homogeneity. This boundary is usually a wall and hence, these types of problems are known as wall bounded turbulence. Because of its importance in engineering problems, wall bounded turbulence has been extensively studied since the 19th century. However, a great number of questions are still open.

The most studied cases of wall turbulence are the canonical geometries of boundary layers, pipe flows, and channels with parallel walls, this last one being the focus of this work. A sketch of each one can be seen in figure 1.3. A classical theory of wall turbulence has been developed during the last 150 years and it is collected in classic textbooks such as Tennekes and Lumley 1972 [10], Townsend 1976 [11] and Pope 2000 [12], among others.

For channels with parallel walls, also known as turbulent channel flows, the x axis goes in the direction of the movement of the flow, the streamwise direction. Then, the y coordinate is normal to the walls of the channel and the z coordinate is transversal to the direction of the flow, the spanwise direction, forming an orthogonal system of reference. The domain has infinite dimensions in the homogeneous directions x and z and dimensions of $2h$ in the y direction, being h the channel half height and the origin of the reference system being in the lower wall of the channel, i.e., the walls are at $y = 0$ and $2h$. The instantaneous velocities of the flow are U, V, and W in each direction x, y, and z, respectively. This notation is completely equivalent to $x_1 \equiv x$, $x_2 \equiv y$, $x_3 \equiv z$, $U_1 \equiv U$, $U_2 \equiv V$ and $U_3 \equiv W$, which will also be used when working with index notation. The velocities can be decomposed using the Reynolds decomposition (1.2) as $U_i = \overline{U}_i + u_i$. At this point, turbulent channel flows can be divided into two main categories: flows that are driven by a pressure difference, known as Poiseuille flows; and flows that are moved due to the difference in movement between both walls, known as Couette flows. The former will be used to explain the classical theory of wall turbulence since it is the main type of flow studied in this work (nevertheless, a specific section §5.2.1 is dedicated to present results of Couette flows). A

statistically steady flow fully developed is considered, so that the derivatives of the mean variables in the wall parallel directions x and z are equal to 0, i.e., $\partial_x \overline{\Phi} = \partial_z \overline{\Phi} = 0$, where $\overline{\Phi}$ is any mean variable and the subscript indicates the direction of the derivative. The only exception in the case of a Poiseuille flow is $\partial_x \overline{P} \neq 0$ since this pressure difference is what moves the flow. Besides, the mean velocity in the spanwise direction is $\overline{W} = 0$ by definition. Considering this, the continuity equation (1.8) results in

$$\frac{d\overline{V}}{dy} = 0. \tag{1.13}$$

Integrating, it is obtained that $\overline{V}$ must be a constant. Since the value at the wall is $\overline{V}_w = 0$, the value of the constant should be 0, and in all the domain $\overline{V} = 0$. Therefore, the nonlinear term in (1.9), $\overline{U}_j(\boldsymbol{x})\partial\overline{U}_i(\boldsymbol{x})/\partial x_j$, should be zero for each $i = 1$, 2 and 3 and $j = 1$, 2 and 3. Then, the momentum equations (1.9) can be written as

$$\mathrm{x - moment:} \qquad \frac{d\overline{uv}(y)}{dy} = -\frac{1}{\rho}\frac{\partial\overline{P}(x,y)}{\partial x} + \nu\frac{d^2\overline{U}(y)}{dy^2}, \tag{1.14a}$$

$$\mathrm{y - moment:} \qquad \frac{d\overline{v^2}(y)}{dy} = -\frac{1}{\rho}\frac{\partial\overline{P}(x,y)}{\partial y}, \tag{1.14b}$$

$$\mathrm{z - moment:} \qquad \frac{d\overline{vw}(y)}{dy} = 0. \tag{1.14c}$$

Integrating (1.14c), it is obtained that $\overline{vw}(y)$ should be equal to 0 because that is its value at the wall. Integrating now (1.14b), results in

$$\overline{P}(x,y) = -\rho\overline{v^2}(y) + P_0(x), \tag{1.15}$$

where P_0 is the integrating constant with respect to y. Introducing (1.15) into (1.14a), the pressure term is only a function of x and then, it can be directly integrated, obtaining

$$\overline{uv}(y) = -\frac{y}{\rho}\frac{dP_0(x)}{dx} + \nu\frac{d\overline{U}(y)}{dy} + C. \tag{1.16}$$

Evaluating the last result at the wall

$$0 = \nu\frac{d\overline{U}(y)}{dy}\bigg|_{y=0} + C. \tag{1.17}$$

The first term can be identified as the shear stress at the wall, τ_w. It has units of velocity square and it is also written as u_τ^2, which is known as the friction velocity square. Therefore, $C = -u_\tau^2$. The value of $P_0(x)$ can be obtained evaluating (1.16) at the center of the channel, $y = h$, where the first and third term must be 0 due to statistical symmetry in the channel. Therefore

$$\frac{dP_0(x)}{dx} = \frac{\rho}{h}u_\tau^2. \tag{1.18}$$

Now, the final equation of the total shear stress at the channel can be written as

$$\tau = \nu\frac{d\overline{U}(y)}{dy} - \overline{uv}(y) = u_\tau^2(1 - y/h). \tag{1.19}$$

Dimensionless variables are introduced at this point: $\tau/u_\tau^2 = \tau/\tau_w = \tau^+$, $\overline{u^+v^+} = \overline{uv}/u_\tau^2$, $\overline{U}^+ = \overline{U}/u_\tau$ and $y^* = y/h$. The coordinate y^* is also known as the outer coordinate, because it is used for

non-dimensionalization magnitudes in the center of the channel and far from the wall. The relation $Re_\tau = u_\tau h/\nu$ is known as the friction Reynolds number. Thus, the dimensionless form of (1.19) in outer coordinates is

$$\tau^+ = \frac{1}{Re_\tau}\frac{d\overline{U}^+(y^*)}{dy^*} - \overline{u^+v^+}(y^*) = (1 - y^*). \tag{1.20}$$

The total shear stress, τ^+, decreases linearly from value 1 at the wall to 0 at the center of the channel. For $Re_\tau \to \infty$, the viscous term is negligible and the total shear stress corresponds to the turbulent shear, $-\overline{uv}$. However, $-\overline{uv}$ at the wall is 0 and the total shear stress, which is equal to 1, must be dominated by the viscous term. A second non-dimensionalization is used to analyze the near-wall region, where the dimensionless coordinate $y^+ = u_\tau y/\nu$ is introduced. The coordinate y^+ receives the name of inner coordinates. Therefore, the dimensionless shear stress equation can be written as

$$\tau^+ = \frac{d\overline{U}^+(y^+)}{dy^+} - \overline{u^+v^+}(y^+) = 1 - \frac{y^+}{Re_\tau}. \tag{1.21}$$

The total shear stress near the wall is constant and equal to 1 when $Re_\tau \to \infty$. This is true in what is called the viscous sublayer, where the viscous effects are dominant and the turbulent shear stress is negligible. The viscous sublayer reaches approximately $y^+ \approx 5$. In this near-wall region, considering $Re_\tau \to \infty$, the total shear stress equation (1.21) can be easily integrated, obtaining that

$$\frac{d\overline{U}^+(y^+)}{dy^+} = 1 \to \overline{U}^+(y^+) = y^+. \tag{1.22}$$

This relation is known as the law of the wall and it indicates that the velocity increases linearly in the viscous sublayer. The importance of this law is that it is universal for every wall-bounded flow, and not only for Poiseuille flows.

For the value of $\overline{U}(y)$ at the central region of the channel, relation (1.20) gives no information about it, since the mean velocity appears in the viscous term, which is neglected for $Re_\tau \to \infty$. Nevertheless, in 1930, von Kármán [5] proposed the following relation which is valid on the center of the channel and it is based on h and u_τ, the characteristic length and velocity scales, respectively

$$\overline{U}^+(y^*) - \overline{U}_c^+ = f(y^*), \tag{1.23}$$

where the subscript c denotes the value at the center of the channel and $f(y)$ is a function with value 0 in the center of the channel. This relation is known as the defect law. Despite the function $f(y)$ is not universal for every flow geometry and for different boundary conditions, relation (1.23) holds.

In between these two regions, there is a transition with special characteristics. We consider that the mean velocity has the following form

$$\overline{U}^+(y^*) = f_1(y^*), \quad \overline{U}^+(y^+) = f_2(y^+). \tag{1.24}$$

Therefore, using the chain rule and the definitions of y^* and y^+, it is obtained that

$$\frac{d\overline{U}^+(y^*)}{dy} = \frac{dy^*}{dy}\frac{df_1(y^*)}{dy^*} = \frac{1}{h}\frac{df_1(y^*)}{dy^*}, \tag{1.25a}$$

$$\frac{d\overline{U}^+(y^+)}{dy} = \frac{dy^+}{dy}\frac{df_2(y^+)}{dy^+} = \frac{u_\tau}{\nu}\frac{df_2(y^+)}{dy^+}. \tag{1.25b}$$

In the limit of $y^* \to 0$ and $y^+ \to \infty$, both (1.25a) and (1.25b) should be equal. Multiplying by y, it is obtained

$$y^*\frac{df_1(y^*)}{dy^*} = y^+\frac{df_2(y^+)}{dy^+} \tag{1.26}$$

Integrating, the solutions obtained are

$$f_1(y^*) = A\ln(y^*) + B_1, \quad f_2(y^+) = A\ln(y^+) + B_2. \tag{1.27}$$

Obtaining the final result

$$\overline{U}(y^+) = \frac{1}{\kappa}\ln(y^+) + B, \tag{1.28}$$

where $1/\kappa = A$ is the classical nomenclature and κ is the von Kármán constant. This region of the flow, where the mean profile has a logarithmic behavior, is called the logarithmic region. It was first deduced by von Kármán in 1930 [5] using dimensional analysis.

Regarding the tangential stress, $\overline{u^+v^+}$, according to dimensionless shear equation in outer coordinates (1.20), $\overline{u^+v^+} \to -1$ when $y^* \to 0$ and $Re_\tau \to \infty$. On the other hand, taking the dimensionless shear equation in inner coordinates (1.21), and introducing the value of $\overline{U}^+$ in the logarithmic region (1.28), it is obtained that $\overline{u^+v^+} = 1/(\kappa y^+) - 1$. Therefore, $\overline{u^+v^+} \to -1$ when $y^+ \to \infty$, and, in the logarithmic region, a constant tangential shear stress is obtained, with $\overline{u^+v^+} = -1$, which agrees with Townsend's hypothesis [11].

1.1.2 The thermal field

In the previous section, a theoretical description of the flow field of a Poiseuille flow has been developed. However, in many practical applications, the temperature in the domain of study is different from the surrounding temperature, and heat is transported creating gradients of temperature. For this reason, the study of the temperature field is crucial for real live applications. This was also stated in a recent study of NASA, where Slotnick et al. [13] remarked the importance of thermal flows in aeronautical applications. For example, the performance of the high-pressure turbines of engines is limited by the maximum temperature that a blade can support without deforming. Therefore, a good treatment of the temperature field will improve its performance, with a direct reduction in the emissions of the engine. The numbers of examples are countless and it is one of the main focuses of this work to get a better understanding of heat transfer in turbulent flows.

The equation that describes the temperature field is the energy equation (1.7), previously presented. That is the most general way of describing the temperature field in homogeneous turbulence. However, as mentioned before, in practical applications the flow is often bounded by walls and different sources of heat can be treated with. It is important to mention that the temperature will be considered as a passive scalar (although a specific section §5.2.2 is dedicated to present results of active scalar fields), which means that it has no influence in the velocity field and does not appear in the momentum equations. As for the flow field, the analysis of the energy equation will be done for channel flows. In the same way that the momentum can be introduced in the flow through a pressure difference or a difference in movement between the walls, heat can be introduced from an internal heat source, from a difference in temperature between both walls, or from the application of uniform heat flux at the wall, among others. The last one is the case that will be used in this work. This thermal boundary condition is known as the Mixed Boundary Condition (MBC).

In the MBC, both walls of the channel are heated with an averaged constant uniform heat flux. Therefore, the average temperature at the walls is independent of time and, due to the global heat balance obtained for constant heat flux, it increases linearly in the streamwise direction. Due to reasons related to the numerical resolution of the equations, which will be explained in chapter §2, the averaged temperature field should be constant in the computational domain. For this reason, it is introduced the so-called transformed temperature

$$T(t, \boldsymbol{x}) = \langle T_w \rangle_z(x) - \Theta(t, \boldsymbol{x}), \tag{1.29}$$

where $\langle T_w \rangle_z$ is the temperature at the walls averaged in time and in the z direction. In such a way, $\langle T_w \rangle_z$ is carrying the linear increase of T along the streamwise direction and the wall-normal dependence is carried by Θ. Introducing transformation (1.29) into the energy equation (1.7) (and multiplying by -1), it is obtained that

$$\frac{\partial \Theta(t, \boldsymbol{x})}{\partial t} + U_j(t, \boldsymbol{x}) \frac{\partial \Theta(t, \boldsymbol{x})}{\partial x_j} - U(t, \boldsymbol{x}) \frac{\partial \langle T_w \rangle_z(x)}{\partial x} = \alpha \frac{\partial^2 \Theta(t, \boldsymbol{x})}{\partial x_j \partial x_j} - \alpha \frac{\partial^2 \langle T_w \rangle_z(x)}{\partial x^2}. \tag{1.30}$$

If the Reynolds decomposition is used and the average is taken, using relations (1.4), results in

$$\overline{U}_j(\boldsymbol{x}) \frac{\partial \overline{\Theta}(\boldsymbol{x})}{\partial x_j} + \frac{\partial \overline{u_j \theta}(\boldsymbol{x})}{\partial x_j} - \overline{U}(\boldsymbol{x}) \frac{d \langle T_w \rangle_z(x)}{dx} = \alpha \frac{\partial^2 \overline{\Theta}(\boldsymbol{x})}{\partial x_j \partial x_j} - \alpha \frac{\partial^2 \langle T_w \rangle_z(x)}{\partial x_j \partial x_j}, \tag{1.31}$$

As mentioned before, due to the global heat balance, when a constant heat flux is imposed at the walls, the value of $\langle T_w \rangle_z$ increases linearly with x. Therefore, the diffusive term (the last term of the equation), where a second derivative appears, should be 0. Furthermore, the value of $d \langle T_w \rangle_z / dx$ can be determined as

$$\frac{d \langle T_w \rangle_z(x)}{dx} = \mathcal{K} \frac{1}{U_b}, \tag{1.32}$$

where $\mathcal{K}$ is a constant with units K/s and U_b is the bulk velocity, which is the average of the velocity in the entire domain, i.e., the integral of $U(t, x, y, z)$ in time and the three directions of the space. For fully developed and statistically steady flows, U_b is directly obtained as

$$U_b = \frac{1}{2h} \int_0^{2h} \overline{U}(y) dy. \tag{1.33}$$

If the conditions of fully developed flow and the definition (1.32) are introduced in equation (1.31), the following equation results

$$\alpha \frac{d^2 \overline{\Theta}(y)}{dy^2} - \frac{d \overline{v\theta}(y)}{dy} = -\frac{\mathcal{K}}{U_b} \overline{U}(y). \tag{1.34}$$

This equation can be integrated with respect to y, obtaining

$$\alpha \frac{d \overline{\Theta}(y)}{dy} - \overline{v\theta}(y) = C - \frac{\mathcal{K}}{U_b} \int_0^y \overline{U}(\hat{y}) d\hat{y}, \tag{1.35}$$

where C is the constant of integration and $\hat{y}$ is the integration variable. Applying this result at the wall it is obtained that

$$\alpha \frac{d \overline{\Theta}(y)}{dy} \bigg|_{y=0} = C = u_\tau \theta_\tau. \tag{1.36}$$

The integral term is 0 because the value of $\overline{U}$ at the wall is linear in y, as obtained in previous section in equation (1.22). In analogy with the velocity field, and because the first term has units of velocity times temperature, $C = u_\tau \theta_\tau$, where θ_τ is the friction temperature. To define θ_τ, the last equation can be multiplied by a reference density, ρ_0, and the heat capacity at constant pressure, c_p, to obtain the wall heat flux in the first term

$$\dot{q}_w = \rho c_p \alpha \frac{d \overline{\Theta}(y)}{dy} \bigg|_{y=0} = \rho c_p C = \rho c_p u_\tau \theta_\tau. \tag{1.37}$$

Then, the definition of θ_τ is

$$\theta_\tau = \frac{\dot{q}_w}{\rho c_p u_\tau} = \frac{\alpha}{u_\tau} \frac{d \overline{\Theta}(y)}{dy} \bigg|_{y=0}. \tag{1.38}$$

The final result of the integration of the energy equation (1.35) is

$$\alpha \frac{d\overline{\Theta}(y)}{dy} - \overline{v\theta}(y) = u_\tau \theta_\tau - \frac{\mathcal{K}}{U_b} \int_0^y \overline{U}(\hat{y}) d\hat{y}. \tag{1.39}$$

The dimensionless equation can now be written in outer coordinates, where $\Theta^+ = \Theta/\theta_\tau$ and $\mathcal{K} = u_\tau \theta_\tau / h$, obtaining as a result

$$\dot{q}^+ = \frac{1}{PrRe_\tau} \frac{d\overline{\Theta}^+(y^*)}{dy^*} - \overline{u^+\theta^+}(y^*) = 1 - \frac{1}{U_b^+} \int_0^{y^*} \overline{U}^+(\hat{y}^*) d\hat{y}^*, \tag{1.40}$$

where Pr is the Prandtl number, defined as ν/α. The Prandtl number represents the ratio between the momentum diffusivity and the thermal diffusivity. The product of the Prandtl and friction Reynolds numbers is defined as the friction Péclet number: $Pe_\tau = Re_\tau Pr$. This equation represents the balance of the heat transfer, and it is analogous to equation (1.20), which represented the balance of shear stresses. In the same way that τ^+ decreases from 1 at the wall to 0 at the center of the channel, $\dot{q}^+$ follows the same tendency, although not in a linear manner. Also, for $Re_\tau \to \infty$ the wall-normal heat flux, $\overline{v\theta}$, is dominant over the diffusive heat flux.

Again, as for the shear stress equation, to analyze the heat fluxes near the wall, dimensionless form with inner coordinates should be adopted obtaining as a result

$$\dot{q}^+ = \frac{1}{Pr} \frac{d\overline{\Theta}^+(y^+)}{dy^+} - \overline{u^+\theta^+}(y^+) = 1 - \frac{1}{Re_\tau U_b^+} \int_0^{y^+} \overline{U}^+(\hat{y}^+) d\hat{y}^+. \tag{1.41}$$

An analogous result to the shear stress is obtained here. Near the wall $\overline{u^+\theta^+}$ is negligible, and when $Re_\tau \to \infty$, the integral term tends to 0 and the total heat flux tends to be constant with value 1. This is only true in a very small sublayer equivalent to the viscous sublayer, but for the temperature field, named diffusive sublayer. When the Prandtl number is of order 1, the diffusive sublayer is of the same order as the viscous sublayer. Under these conditions, equation (1.41) can be easily integrated, obtaining

$$\overline{\Theta}^+ = Pr \, y^+. \tag{1.42}$$

This result is completely equivalent to the law of the wall (1.22) of the velocity field, and it is a universal law valid for any boundary condition and any geometry.

Based on the length and temperature scales in the center of the channel, h and θ_τ, respectively, the same defect law as for the mean velocity (1.23), can be proposed for the mean temperature, so that

$$\overline{\Theta}^+(y^*) - \overline{\Theta}_c^+ = g(y^*), \tag{1.43}$$

Regarding the logarithmic region that was obtained for the mean velocity, the same procedure can be done for the mean temperature, obtaining that when $y^+ \to \infty$ and $y^* \to 0$ a logarithmic behavior of the mean temperature is obtained

$$\overline{\Theta}^+ = \frac{1}{\kappa_t} \ln(y^+) + C, \tag{1.44}$$

where κ_t is the von Kármán constant for the mean temperature and C is a constant that varies with the Prandtl number.

Analogous to the tangential shear stress, is the wall-normal heat flux. According to the heat balance equation in outer coordinates (1.40), when $y^* \to 0$ and $Re_\tau \to \infty$, $\overline{u^+\theta^+} \to -1$. Regarding the heat balance equation in inner coordinates (1.41), if the logarithmic profile of the mean temperature (1.44) is introduced, for $Re_\tau \to \infty$, it is obtained that $1/(Pr \, \kappa_t y^+) - \overline{u^+\theta^+} = 1$. Therefore, in the limit of $y \to \infty$, it is also obtained that $\overline{u^+\theta^+} \to -1$. This result means that the wall-normal heat transfer is constant and equal to -1 in the logarithmic region for $Re_\tau \to \infty$, which is an analogous result to the Townsend's hypothesis for the velocity field [11].

1.2 Lie symmetries

Lie symmetries are a powerful mathematical theory to develop scaling laws of turbulent flows. The origin of the Lie symmetries method dates back to the end of the 19th century when the mathematician Sophus Lie proposed it for obtaining solutions of ordinary differential equations (ODE). Obviously, the method can also be used to obtain solutions of partial differential equations (PDE) and, most important, is also applicable to systems of PDE, such as the Navier-Stokes equations. The basis of the method consists in finding the symmetries of the system of PDE. A symmetry refers to a variable transformation that leads to an identical system of PDE, i.e. the transformed system of PDE has the same solution as the original one. With these symmetries, one can formulate a characteristic system. Details about how to obtain the characteristic system and its properties will be given in chapter §3. Solving the characteristic system leads to what is known as invariant solutions, which in turbulence are also known as scaling laws.

For a concrete application, Lie symmetries possess a number of advantageous properties. First, symmetries can be obtained using computer algebra methods such as Maple. Second, symmetries give fundamental insight into the physics of the problem. And third, the scaling laws obtained are solutions to the moment equations and, hence, are based on first principles, and not just pure curve fits. For these reasons, Lie symmetries could be one of the most powerful tools to obtain scaling laws of turbulent flows.

The method has been widely studied by Oberlack and co-workers in several papers. Starting with [14], scaling laws for the three regions of wall-parallel shear flows (viscous sub-layer, logarithmic law, and deficit law in the center of the channel) were obtained. Classical mechanical symmetries of the Navier-Stokes equations were used, but the key to the analysis was to employ the Multi-Point Correlation (MPC) equations. Two additional symmetries, not visible in the Navier-Stokes equations and called statistical symmetries, were used to derive the scaling laws that describe the flow statistics even for high moments. More details about the MPC equations will be given in chapter §3. After this successful application of Lie symmetries to turbulent flows several more works have been done with different geometries or boundary conditions [15, 16, 17, 18, 19, 20].

In this work, the Lie symmetries theory will be used to derive new scaling laws of the temperature, velocity, and high order moments of both. In order to achieve this, symmetries of the energy equation and the MPC equations of the energy and heat fluxes equations are obtained, from which the new scaling laws are formulated. This new scaling laws will be validated in subsection §5.1.5 using the DNS data presented in previous subsections of section §5.1.

Chapter 2

Computational methods

In the previous sections, a theoretical approach to turbulence was revised. However, only partial solutions, in specific regions of the channel and under specific conditions, were obtained. Other methods to study turbulence are needed. Two main approaches have been historically considered: experimental and computational.

Experimental results are always the most representative of the actual behaviour of the flow since direct information of the statistics of the flow is obtained. However, it requires specific installations to properly carry out the experiment, which can be very expensive. For example, in the design of an aircraft, it is extremely expensive to experiment in a wind tunnel with a full-size model. For this reason, from the industrial point of view, experimental analysis is the best tool in the late stages of a design process. From the theoretical point of view, experiments have been historically used as the main approach to understand the dynamics of turbulent flows, especially until the end of the 20th century, when computational power was not as advanced as nowadays. In a basic installation, like a pipe or a channel, it is easy to recover the actual statistics of the flow. An obvious advantage is that the only errors that are obtained are those introduced by the measuring devices, which should be small.

On the other hand, computational methods, consist of solving numerically the governing equations of the flow, i.e. the Navier-Stokes (1.5)-(1.6) and energy (1.7) equations. This branch of fluid dynamics is known as Computational Fluid Dynamics (CFD) and with the increase of computational power, they have been gaining importance in the study of turbulence. The main issue of CFD compared with experiments is that numerical errors are introduced due to the discretization of the domain or due to the introduction of models that describe turbulence in an approximated manner. However, they are much cheaper than experiments. Following the example of aircraft design, creating a virtual model of a plane and analysing it with CFD software is much cheaper than the experimental analysis. Also, fast modifications and parametric analyses can be performed easily. For this reason, CFD is the main tool for the early stages of a design.

Regarding theoretical turbulence, a big advantage arises with the computational methods. In wall turbulence, it is very important to understand how turbulence behaves in the boundary layer of the flow, where the flow goes from zero to velocities of the order of the free-stream velocity. Another important factor of the boundary layer is that almost the entire losses by drag are produced in this region. The boundary layer is composed of the viscous, logarithmic, and buffer sublayers, being this last one the transition sublayer between the viscous and the logarithmic sublayers (previously described in subsection §1.1.1). Although this very important phenomena, named before, occur in the boundary layer, it is very thin. Thus, in an experiment, the number of measuring points that can be placed in the boundary layer is extremely limited due to physical constraints. However, in CFD, one can put as many points as are needed to properly discretize the domain in these regions and to obtain valuable data. Information about the mechanism of energy transfer in the boundary layer is crucial to understand turbulence, and

numerical methods play a key role in this point.

Different approaches are also considered inside the branch of CFD. Following the usual classification of lower to higher approximation to the actual behaviour of the flow, there are three main techniques: Reynolds averaged Navier-Stokes equations (RANS), Large Eddy Simulation (LES), and Direct Numerical Simulation (DNS).

2.1 Reynolds averaged Navier-Stokes equations

The Reynolds averaged Navier-Stokes equations (RANS) were briefly introduced in section §1.1. They are derived by introducing the Reynolds decomposition (1.2) to the instantaneous equations (1.5)-(1.7), and taking the average of the resulting equations, obtaining the RANS equations (1.8), (1.9) and (1.31). As mentioned before, an extra term is obtained due to the nonlinearity of the equations. For the case of the momentum equation, this extra term is known as the Reynolds stress tensor, $\tau_{ij} = -\overline{u_i u_j}$. This term plays a similar role in the equation as the viscous term does, although its nature is completely different. To solve the closure problem that arises from the viscous stress tensor, modeling of this term is needed. To do so, typically the isotropic and anisotropic parts of this tensor are split. The turbulent kinetic energy, i.e. the isotropic component, is defined as

$$k = \overline{u_i u_i} = \frac{1}{2}\overline{u^2 + v^2 + w^2}. \tag{2.1}$$

Now, the anisotropic stress tensor can be defined as

$$a_{ij} = \overline{u_i u_j} - \frac{2}{3}k\delta_{ij}, \tag{2.2}$$

where δ_{ij} is the Kronecker delta with value 1 when $i = j$ and value 0 otherwise. The viscous turbulent hypothesis was introduced in 1877 by Boussinesq,

$$\rho a_{ij} = \rho\nu_T\left(\frac{\partial \overline{U}_i}{\partial x_j} + \frac{\partial \overline{U}_j}{\partial x_i}\right), \tag{2.3}$$

relating a_{ij} to the deformation tensor, defined as

$$\overline{S}_{ij} = \frac{1}{2}\left(\frac{\partial \overline{U}_i}{\partial x_j} + \frac{\partial \overline{U}_j}{\partial x_j}\right). \tag{2.4}$$

In these equations, Boussinesq introduced a new constant, ν_T, as the turbulent viscosity. However, ν_T is actually not a viscosity and it is not constant. It receives that name due to unit consistency.

Introducing these definitions into the RANS equations (1.9), the following relation is obtained after rearranging the terms

$$\overbrace{\left(\frac{\partial \overline{U}_i(\boldsymbol{x})}{\partial t}\right)}^{=0} + \overline{U}_j(\boldsymbol{x})\frac{\partial \overline{U}_i(\boldsymbol{x})}{\partial x_j} = \frac{1}{\rho}\frac{\partial}{\partial x_i}\left(\overline{P}(\boldsymbol{x}) + \frac{2}{3}k(\boldsymbol{x})\right) + \frac{\partial}{\partial x_j}\left(\overbrace{(\nu + \nu_T)}^{\nu_{eff}}\frac{\partial \overline{U}_i(\boldsymbol{x})}{\partial x_j}\right). \tag{2.5}$$

The new viscosity is defined as $\nu_{eff} = \nu + \nu_T$. One of the main sources of errors of the RANS methods is that ν_T strongly depends on the space coordinate and also on time and type of problem. The value of ν_T is modelled in different manners depending on the RANS model that is being used. The choice of the correct RANS model for a specific problem is crucial to obtain reliable results. The basis of the

RANS models states that this turbulent viscosity must be modelled with a characteristic velocity and a characteristic length, i.e.

$$\nu_T = u^* \ell^*. \tag{2.6}$$

These parameters must be determined for each problem. However, when using a two-equation model, in the sense that two turbulent parameters are modelled, one can form a length scale, a time scale, etc, derived from the two turbulent quantities modelled. Therefore, no characteristic velocity and length must be specified for this type of model. The most common RANS method, named the $k - \varepsilon$ model, will be explained as an example. It happens that the $k - \varepsilon$ model is a two-equation model. The turbulent magnitudes k and ε are modelled and the turbulent viscosity can be calculated directly as

$$\nu_T = C_\mu \frac{k^2}{\varepsilon}, \tag{2.7}$$

where C_μ is a constant with a usual value of 0.09. The first turbulent quantity, k is modelled with the transport equation which has the form of (dependencies of the functions have been omitted for the sake of brevity)

$$\frac{Dk}{Dt} = \frac{\partial k}{\partial t} + \overline{U}_j \frac{\partial k}{\partial x_j} = P + T - \varepsilon = 0, \tag{2.8}$$

where $D/DT = \partial/\partial t + \overline{U}_j \partial/\partial x_j$ is the total derivative, which should be 0. The right-hand side of the equation is composed of the three terms that can modify the kinematic viscosity, i.e. a production term, P, a transport term, T, and a dissipative term, ε. While the production term is defined by gradients of mean velocities, i.e. it does not introduces new unknowns, the transport and dissipation terms must be modelled, since terms of the form $\overline{u_i u_j u_j}$ appear, which introduced new unknowns. The transport term is modelled as

$$T = \frac{\partial}{\partial x_j} \left(\frac{\nu_T}{\sigma_k} \frac{\partial k}{\partial x_j} \right), \tag{2.9}$$

where σ_k is a constant of the model with typical value of 1. Finally, the dissipation term is modelled with the second transport equation of the $k - \varepsilon$ model, which has a very similar form to the one of the k (2.8):

$$\frac{D\varepsilon}{Dt} = \frac{\partial \varepsilon}{\partial t} + \overline{U}_j \frac{\partial \varepsilon}{\partial x_j} = C_{\varepsilon 1} \frac{\mathcal{P}\varepsilon}{k} + \frac{\partial}{\partial x_j} \left(\frac{\nu_T}{\sigma_\varepsilon} \frac{\partial \varepsilon}{\partial x_j} \right) - C_{\varepsilon 2} \frac{\varepsilon^2}{k} = 0, \tag{2.10}$$

where the three terms on the right-hand side of the equation are the transport, production, and dissipation terms, respectively. They are modelled with the constants $C_{\varepsilon 1}$, σ_ε and $C_{\varepsilon 2}$, whose values are typically 1.44, 1.3 and 1.92, respectively. The values of the five constants of the $k - \varepsilon$ model are taken from a fitting to the results of a vast number of experiments for different turbulent flows. Nevertheless, this is a simplification of the resolution of the Navier-Stokes equations, which introduces an error. The $k - \varepsilon$ model is the most accurate RANS method to calculate turbulent flows in channels and pipe flows. Numerous methods have been developed with more precision for different types of flows, such as Spalart-Allmaras, which is often used for open flows; or $k - \omega$, which is a variation of the $k - \varepsilon$ model, where the vorticity ω is modelled instead of the dissipation.

In general, RANS methods are much faster than LES and DNS methods but they present the worst accuracy among the three of them. Due to their fastness, they are widely used, especially in the early stages of a design process, where a large number of parametric studies can be carried out and more realistic precision can be left out for the latest stages of the design with experimental analysis. In these practical applications, a point in favor of the RANS methods is that the turbulent fluctuations are not simulated but modelled, so that the mesh used to discretize the domain only depends on the geometry of the problem. It has a weak dependence with the Reynolds number. Although a slightly more precise mesh is required for higher Reynolds numbers, specially near the walls, the increase of the computational cost is usually negligible compared with the requirements of the mesh to adapt to complex geometries of

the flow. Therefore, any practical Reynolds number can be studied with RANS methods. LES and DNS present a problem here, and it is that the computational power required to simulate Reynolds numbers of the order of the ones appearing in most practical applications is no achievable nowadays.

In conclusion, the RANS methods can be considered as interpolation schemes obtained from a wide number of experiments. They are very powerful in industrial applications since different methods can provide an accurate solution for specific problems. However, the constants used to model the flow are set from the fitting of numerous experiments, which introduces an error in the results obtained. Regarding theoretical turbulence, which is the aim of this work, there is no space for RANS methods, since they do no simulate the turbulence of the flow. And here is where LES and DNS play a role.

2.2 Large Eddy Simulation

The Large Eddy Simulations (LES) is the intermediate method between RANS and DNS regarding precision and computational cost. As the name indicates, this method is based on the simulation of the large eddies of the flow, which are dependent on the flow geometry, and the modelling of the smaller scales of the flow, which, according to Kolmogorov's theory, are universal for every flow.

To achieve this, the variables of the flow are filtered by a low-pass filter. To do so, the convolution product must be applied

$$\overline{f}(t, \boldsymbol{x}) = \int \int K(t - \tau, \boldsymbol{x} - \boldsymbol{s}) f(t, \boldsymbol{x}) d\boldsymbol{s} d\tau, \tag{2.11}$$

where K is the filter kernel, f is any variable and $\overline{\bullet}$ here represents the filtered variable. Note that the filter can be understood as a time and space averaging, but both t and $\boldsymbol{x}$ dependencies are kept in the filtered variable. Since a low-pass filter is used, the high frequencies in the Fourier space are ignored, removing from the simulation all the small scales of time and space. These small scales, of course, have their influence in the governing equations, but that influence is modelled. After introducing the filtered variables into the governing equations, it is obtained

$$\frac{\partial \overline{U}_i}{\partial t} + \frac{\partial \overline{u_i u_j}}{\partial x_j} = -\frac{1}{\rho}\frac{\partial \overline{P}}{\partial x_i} + \nu \frac{\partial}{\partial x_j} \overbrace{\left(\frac{\partial \overline{U}_i}{x_j} + \frac{\partial \overline{U}_j}{x_i} \right)}^{2\overline{S}_{ij}}. \tag{2.12}$$

According to [21], the filtered Reynolds shear stress term can be separated as $\overline{u_i u_j} = \overline{\tau}_{ij} + \overline{u}_i \overline{u}_j$. Finally obtaining

$$\frac{\partial \overline{U}_i}{\partial t} + \frac{\partial \overline{u_i u_j}}{\partial x_j} = -\frac{1}{\rho}\frac{\partial \overline{P}}{\partial x_i} + \frac{\partial}{\partial x_j}\left(2\nu \overline{S}_{ij} - \overline{\tau}_{ij} \right). \tag{2.13}$$

At this point, the filtered shear stress term, $\overline{\tau}_{ij}$, introduces new unknowns, and the closure problem arises again. Therefore, models should be implemented to estimate the value of $\overline{\tau}_{ij}$. A typical trend is to decompose this term as

$$\overline{\tau}_{ij} = \overline{T}_{ij} + \frac{1}{3}\delta_{ij}\overline{\tau}_{kk}. \tag{2.14}$$

Here, $\overline{\tau}_{kk}$ is the isotropic component, which can be introduced in the pressure term, obtaining an effective pressure, $\overline{P}_{eff}$, which does not need further models, unless the pressure term, $\overline{P}$, need to be explicitly known. Only the shear component, $\overline{T}_{ij}$, needs to be modelled now. We cite here one of the most iconic models of LES methods because it was the first used in an LES simulation in [22]; it is the model proposed by Smagorinsky [23]

$$\overline{T}_{ij} = -2\nu_t \overline{S}_{ij}. \tag{2.15}$$

Reaching a very similar equation to that obtained in the RANS model (2.5). Extensive research has been done in LES models, reaching very accurate results, especially for isotropic and homogeneous

16

turbulence. LES have proven to be very precise in spray flows, for example. A good point on the LES methods is that filters are applied so that scales below $L/10$ are ignored, where L is the characteristic length of the problem. This value is independent of the Reynolds number, so LES are valid to study practical engineering problems, where $Re > 10^6$.

However, for heterogeneous or anisotropic flows, like wall turbulence, still some inaccuracies in the results are obtained. Furthermore, the closer to the wall, the more anisotropic a flow is, obtaining bigger errors in this region. A more precise technique is needed to properly study the turbulence behaviour of wall-bounded turbulence, which is the last method presented here, DNS.

2.3 Direct Numerical Simulations

Direct Numerical Simulations (DNS), are the most precise computational method to study turbulence. In contrast to RANS and LES methods, DNS does not model any scale of the flow, and all of them must be resolved. To achieve this, the mesh used to discretize the problem must capture the smallest spatial scales of the flow, as defined by the Kolmogorov scales (1.12), when $Pr < 1$. If the Prandtl number is higher than 1, then the smallest thermal structures are smaller than those of the velocity. Thermal structures are defined by the Batchelor length scale as $\eta_\theta = \eta Pr^{-1/2}$. Furthermore, no symmetry property can be applied like in RANS methods, where the averaged variables are used and only half of the domain is calculated. In DNS, as in LES, the entire domain must be used, since the instantaneous variables are not symmetric in turbulent problems. Regarding the time step of the simulation, it must be smaller than the time that a particle takes to cross a cell of the mesh. In addition, a DNS must be run for several cycles, once the flow is in a statistically steady-state, to recover a big amount of valid statistics.

With all this, the number of mesh points and the number of time steps are huge compared with RANS and LES, which makes DNS extremely expensive computationally speaking. Only simple geometries can be simulated. Furthermore, in contrast to RANS and LES, the mesh resolution in a DNS depends on the Reynolds number. The number of mesh points grows very fast with Re, and it can be estimated as $Re^{9/4}$. Therefore, Reynolds numbers of practical applications are far from being possible to simulate. For these reasons, DNS must be run in the biggest supercomputers, with very efficient and optimized codes that use parallelization techniques.

Despite these disadvantages, DNS present several points in their favour. The most important one is that the results obtained are indistinguishable from those of the experiments, with the advantage that the amount of information obtained is much bigger and easier to work with. For example, in a simulation of a turbulent channel with $Re = 5 \cdot 10^4$ approximately 10^9 points are needed in the mesh and each point can be understood as a pitot tube, able to register heat too. Also, since no model of the flow is used, crucial information about the mechanisms of energy transfer can be directly obtained to understanding how turbulence behaves at every scale, which is the principal aim of this study.

Finally, an important point on DNS is the boundary and initial conditions. While in turbulent boundary layers this can be problematic, see [24], in channel flows periodic conditions can be imposed in the homogeneous directions, i.e. the boundaries in the streamwise and spanwise directions; while no-slip conditions are imposed in the boundaries of the wall-normal direction. Regarding the initial conditions, a file with a similar field to that of the solution should be used. This file is called the initial file. It should be taken from another DNS with similar geometry, boundary conditions, and dimensionless number. For example, if a DNS of a Poiseuille channel flow is going to be run for $Re_\tau = 2000$ and $Pr = 2$ it would be ideal to use a file from a simulation of a Poiseuille channel for $Re_\tau = 2000$ and $Pr = 1$ or $Re_\tau = 1000$ and $Pr = 2$ (if it is possible). If the initial file is not chosen correctly, the transition from the conditions of the initial file until the simulation has reached a statistically steady state in the final conditions can be as long as the simulation itself.

In conclusion, despite its impossible application in practical problems due to computational limits, DNS should be the base to create new and more accurate models for both, RANS and LES. Regarding

the theoretical part, DNS is the only valid method in CFD to recover reliable statistics and to investigate the physical properties of flows which are little understood. Since the aim of this work is to gain a better understanding of turbulence, DNS is thus the perfect tool to work with. For this reason, DNS has been chosen as the main work tool of this project. Deeper information about DNS are given in Appendix §7.1, where the code used for this work, named LISO, is described. In such a way, specific details of DNS will be addressed with a specific example, getting a clearer explanation.

2.3.1 State of the art of DNS

As it was explained in the previous section, the main problem of DNS is the computational cost of the simulations. This makes DNS go hand in hand with state-of-the-art supercomputers. Then, the increase of the computational power allows more complex DNS. For such a reason, it was not until the late 80s, when the first DNS was performed for a Poiseuille isothermal flow by Kim et al. in 1987 [25]. In this first work, statistics of the velocity field were obtained and compared with experimental data from different works [26, 27, 28, 29]. The main result of this work was the validation of DNS to obtain accurate data flow. The law of the wall (1.22), as well as the deficit law in the center of the channel (1.23), were perfectly fulfilled. The logarithmic region, though, was not observed due to the small Reynolds number and the high viscous effects. Several correlations of the statistics were compared finding great accuracy of the DNS. In addition, new statistical correlations were reported for the first time. Also in this work, it was given a brief explanation of the code used and how they solved the equations. This method, which consists of solving two evolution equations of the Navier-Stokes equations, is the one adopted in the present work, and it is extensively explained in the appendix §7.1.

Later in the same year, Kim and Moin [30] conducted the first DNS of a turbulent thermal flow, which is the main interest of this work. They treated the thermal field as a passive scalar and the velocity field was the same as in [25]. The friction Reynolds number used was $Re_\tau = 180$, while three Prandtl numbers were considered, $Pr = 0.1$, 0.71 and 2. It is important to note that $Pr = 0.71$ corresponds to the Prandtl number of air. This is one of the reasons why this value of the Prandtl number is the most used historically. The boundary condition for the thermal field consisted of an internal heat generation, and this heat was removed from both isothermal walls. This work also served as a validation of the DNS for the thermal field. Experimental results obtained in [31, 32, 33] were compared with the ones of that work, obtaining a very good agreement between the main statistics of the thermal field, such as the mean temperature, temperature fluctuations, and heat fluxes. Also, the law of the wall for the thermal field (1.42), and the deficit law for the temperature profile in the center of the channel (1.43) were perfectly fulfilled. The thermal logarithmic region was not observed due to the small Reynolds number used and the high conductive effects. The turbulent Prandtl number, Pr_t, which represents the ratio between the momentum eddy diffusivity and the heat transfer eddy diffusivity, was calculated. Values of $Pr_t \approx 1$ at the wall were obtained, as was expected from experimental data. The most important result was the high correlation between the temperature fluctuations and the streamwise velocity fluctuations in the near-wall region when the Prandtl number is close to 1. A value of the velocity-temperature correlation, $R_{u\theta} \approx 0.95$, was obtained near the wall. Also, several images of the structures of these statistics at $y^+ = 5$, i.e. the viscous and diffusive sublayer, showed that regions of negative or positive streamwise velocity fluctuations coincided with a region of negative or positive temperature fluctuation, respectively. This important result was further validated with the joint probability distribution and the two-point correlation function. This high correlation near the wall indicates that both fields, streamwise velocity, and temperature, are linked, suggesting that it is possible to model the scalar fluxes in the same way as the momentum fluxes. Finally, some instantaneous visualizations were shown, demonstrating that in the near-wall region, the same streaky structure of the velocity field was obtained for the thermal field.

In an extension of the work [30], Antonia and Kim performed a deep analysis of the turbulent Prandtl

number in [34]. The exact definition of Pr_t is

$$Pr_t = \frac{\overline{u^+v^+}}{\overline{v^+\theta^+}} \frac{\frac{d\overline{\Theta}^+}{dy^+}}{\frac{d\overline{U}^+}{dy^+}}. \tag{2.16}$$

In [34], a Taylor expansion of the different velocity and temperature statistics was done near the wall, so that

$$\overline{U}^+ = y^+ + O(y^{+2}), \tag{2.17a}$$

$$\overline{\Theta}^+ = Pr y^+ + O(y^{+2}), \tag{2.17b}$$

$$u'^+ = b_1 y^+ + c_1 y^{+2} + O(y^{+3}), \tag{2.17c}$$

$$v'^+ = c_2 y^{+2} + d_2 y^{+3} + O(y^{+4}), \tag{2.17d}$$

$$w'^+ = b_3 y^+ + c_3 y^{+2} + O(y^{+3}), \tag{2.17e}$$

$$\theta'^+ = Pr\left(b_\theta y^+ + c_\theta y^{+2} + O(y^{+3})\right), \tag{2.17f}$$

$$\overline{u^+v^+} = d_{12} y^{+3} + e_{12} y^{+4} + O(y^{+5}), \tag{2.17g}$$

$$\overline{u^+\theta^+} = Pr\left(c_{1\theta} y^{+2} + d_{1\theta} y^{+3} + O(y^{+4})\right), \tag{2.17h}$$

$$-\overline{v^+\theta^+} = Pr\left(d_{2\theta} y^{+3} + e_{2\theta} y^{+4} + O(y^{+5})\right), \tag{2.17i}$$

where the apostrophe, ϕ', indicates the root-mean-square of a variable ϕ, i.e. $\phi' = \sqrt{\overline{\phi\phi}}$. Therefore, the value of Pr_t near the wall can be calculated as

$$Pr_t|_{y^+ \to 0} = \frac{d_{12}}{d_{2\theta}}. \tag{2.18}$$

For the values of Pr used in [34], which were the same than in [30] ($Pr = 0.1$, 1 and 2), the values of the first coefficients of the Taylor expansion were approximately constant, and the ratio $d_{12}/d_{2\theta}$ gave approximately $Pr_t = 1.1$ at the wall independently of the molecular Prandtl number, in great accordance with the experimental results obtained. Nevertheless, for much lower and much higher values of Pr, Antonia and Kim [34] speculated higher values of Pr_t, since the temperature is not that well organized in positive and negative streaks as for $Pr \approx 1$. This result will be confirmed in future DNS.

In 1991, Lyons, Hanratty, and McLaughlin performed a DNS whose results were published in [35] for the velocity field and [36] for the thermal field. In this last work, a Poiseuille flow at $Re_\tau = 150$ was simulated for $Pr = 1$. The boundary condition for the temperature field consisted of a heated lower wall and a cooling upper wall with the same heat flux rate so the temperature difference between the walls was fixed constant. Obviously, this boundary condition created an antisymmetric temperature field analogous to that of the velocity field when a Couette flow is imposed. Therefore, several differences between the velocity and temperature field arose in the center of the channel. Nevertheless, a high correlation of both fields was obtained in the near-wall region. Correlations between the velocity and temperature field and Pr_t were calculated, obtaining similar results to those from [30]. In addition, the dimensionless Nusselt number, Nu, which represents the ratio between the convective and conductive heat transfer, was computed, with similar results to those of experiments and classical correlations. Finally, the energy transfer equations or budget equations for the mean temperature and temperature fluctuations were obtained. These energy equations were compared with the ones of the mean velocity, and fluctuating velocity, obtaining remarkable similarities in the near-wall region. The difference in the center of the channel was due to the different boundary conditions for each field.

A third important DNS of a thermal channel flow was performed by Kasagi et al. in 1992 [37]. As in [36], the friction Reynolds number simulated was $Re_\tau = 150$, while the Prandtl number of air,

$Pr = 0.71$, was used. Regarding the boundary condition, a more realistic one than that of [30] was used, the MBC, which was already introduced in section §1.1.2. Remember that the MBC is the thermal boundary condition used in this work. Similar to the two previous studies, the main thermal statistics were analysed and compared with experimental data and with the result from Kim and Moin [30]. The result was a high accuracy from the DNS when comparing the mean and fluctuating temperature, the Nusselt and turbulent Prandtl number, and several correlation coefficients. A study of the logarithmic layer was carried out. However, a perfect logarithmic behaviour was not observed due to the strong viscous and conductive effects for such a low Reynolds number. Nevertheless, the tendency of the main temperature may indicate a possible logarithmic region for higher Reynolds numbers. With this in mind, Kasagi et al. [37] computed the value of the theoretical von Kármán constant for the thermal field, defined in section §1.1.2, obtaining a value of $\kappa_t = 0.36$. As noted by the authors of the paper, that value was considerably smaller than the generally accepted value of 0.47, obtained in experiments for higher Reynolds numbers. Finally, a deep analysis of the turbulent budgets was performed. Balance equations of the temperature variance, k_θ, its dissipation rate, ε_θ, and both heat fluxes, streamwise, $\overline{u\theta}$, and wall-normal, $\overline{v\theta}$, were presented together with the values of each budget term. These budget equations are now presented to facilitate the understanding of the discussion. The transport equation of k_θ is obtained after multiplying the equation (1.7) by θ and taking the average. In dimensionless inner coordinates, it is given by

$$\frac{Dk_\theta^+}{Dt^+} = P_\theta^+ + T_\theta^+ + V_\theta^+ + \varepsilon_\theta^+. \tag{2.19}$$

The different terms on the right hand side are referred to as production, turbulent diffusion, viscous or molecular diffusion and dissipation. They are respectively defined according to

$$P_\theta^+ = -\overline{u_j^+ \theta^+} \frac{\partial \overline{\Theta}^+}{\partial x_j^+}, \tag{2.20a}$$

$$T_\theta^+ = -\frac{1}{2} \frac{\overline{u_j^+ \theta^+ \theta^+}}{\partial x_j^+}, \tag{2.20b}$$

$$V_\theta^+ = \frac{1}{2Pr} \frac{\overline{\theta^+ \theta^+}}{\partial x_j^+ \partial x_j^+}, \tag{2.20c}$$

$$\varepsilon_\theta^+ = -\frac{1}{Pr} \overline{\frac{\partial \theta^+}{\partial x_j^+} \frac{\partial \theta^+}{\partial x_j^+}}, \tag{2.20d}$$

and for the specific case of a statistically steady thermal channel flows:

$$P_\theta^+ = -\overline{v^+ \theta^+} \frac{\partial \overline{\Theta}^+}{\partial y^+}, \tag{2.21a}$$

$$T_\theta^+ = -\frac{1}{2} \frac{\overline{v^+ \theta^+ \theta^+}}{\partial y^+}, \tag{2.21b}$$

$$V_\theta^+ = \frac{1}{2Pr} \frac{\overline{\theta^+ \theta^+}}{\partial y^+ \partial y^+}, \tag{2.21c}$$

$$\varepsilon_\theta^+ = -\frac{1}{Pr} \overline{\frac{\partial \theta^+}{\partial y^+} \frac{\partial \theta^+}{\partial y^+}}. \tag{2.21d}$$

The transport equation for ε_θ is obtained after deriving equation (1.7) with respect to x_l, multiplying the result by $(2/Pr)\partial\theta/\partial x_l$ and taking the average. In dimensionless inner coordinates, it is given by

$$\frac{D\varepsilon_\theta^+}{Dt} = P_{\varepsilon_\theta,m}^+ + P_{\varepsilon_\theta,mg}^+ + P_{\varepsilon_\theta,g}^+ + P_{\varepsilon_\theta,t}^+ + T_{\varepsilon_\theta}^+ + V_{\varepsilon_\theta}^+ + \varepsilon_{\varepsilon_\theta}^+. \tag{2.22}$$

In this case, the terms are named mixed production, mean gradient production, gradient production, turbulent production, turbulent transport, molecular diffusion and dissipation. They are defined as follows:

$$P^+_{\varepsilon_\theta,m} = -\frac{2}{Pr}\overline{\frac{\partial u^+_j}{\partial x^+_l}\frac{\partial \theta^+}{\partial x^+_l}}\frac{\partial \overline{\Theta}^+}{\partial x^+_j}, \tag{2.23a}$$

$$P^+_{\varepsilon_\theta,mg} = -\frac{2}{Pr}\overline{\frac{\partial \theta^+}{\partial x^+_j}\frac{\partial \theta^+}{\partial x^+_l}}\frac{\partial \overline{U_j}^+}{\partial x^+_l}, \tag{2.23b}$$

$$P^+_{\varepsilon_\theta,g} = -\frac{2}{Pr}\overline{u^+_j\frac{\partial \theta^+}{\partial x^+_l}}\frac{\partial^2 \overline{\Theta}^+}{\partial x^+_j\partial x^+_l}, \tag{2.23c}$$

$$P^+_{\varepsilon_\theta,t} = -\frac{2}{Pr}\overline{\frac{\partial \theta^+}{\partial x^+_j}\frac{\partial \theta^+}{\partial x^+_l}\frac{\partial u^+_j}{\partial x^+_l}}, \tag{2.23d}$$

$$T^+_{\varepsilon_\theta} = -\frac{1}{Pr}\frac{\partial}{\partial x^+_j}\left(\overline{u^+_j\frac{\partial \theta^+}{\partial x^+_l}\frac{\partial \theta^+}{\partial x^+_l}}\right), \tag{2.23e}$$

$$V^+_{\varepsilon_\theta} = \frac{1}{Pr^2}\frac{\partial^2}{\partial x^+_j\partial x^+_l}\left(\overline{\frac{\partial \theta^+}{\partial x^+_l}\frac{\partial \theta^+}{\partial x^+_l}}\right), \tag{2.23f}$$

$$\varepsilon^+_{\varepsilon_\theta} = -\frac{2}{Pr^2}\overline{\frac{\partial^2 \theta^+}{\partial x^+_j\partial x^+_l}\frac{\partial^2 \theta^+}{\partial x^+_j\partial x^+_l}}, \tag{2.23g}$$

which for the case of statistically averaged thermal channel flows reduce to

$$P^+_{\varepsilon_\theta,m} = -\frac{2}{Pr}\overline{\frac{\partial v^+}{\partial x^+_l}\frac{\partial \theta^+}{\partial x^+_l}}\frac{\partial \overline{\Theta}^+}{\partial y^+}, \tag{2.24a}$$

$$P^+_{\varepsilon_\theta,mg} = -\frac{2}{Pr}\overline{\frac{\partial \theta^+}{\partial x^+}\frac{\partial \theta^+}{\partial y^+}}\frac{\partial \overline{U}^+}{\partial y^+}, \tag{2.24b}$$

$$P^+_{\varepsilon_\theta,g} = -\frac{2}{Pr}\overline{v^+\frac{\partial \theta^+}{\partial y^+}}\frac{\partial^2 \overline{\Theta}^+}{\partial y^+\partial y^+}, \tag{2.24c}$$

$$P^+_{\varepsilon_\theta,t} = -\frac{2}{Pr}\overline{\frac{\partial \theta^+}{\partial x^+_j}\frac{\partial \theta^+}{\partial x^+_l}\frac{\partial u^+_j}{\partial x^+_l}}, \tag{2.24d}$$

$$T^+_{\varepsilon_\theta} = -\frac{1}{Pr}\frac{\partial}{\partial y^+}\left(\overline{v^+\frac{\partial \theta^+}{\partial x^+_l}\frac{\partial \theta^+}{\partial x^+_l}}\right), \tag{2.24e}$$

$$V^+_{\varepsilon_\theta} = \frac{1}{Pr^2}\frac{\partial^2}{\partial y^+\partial y^+}\left(\overline{\frac{\partial \theta^+}{\partial y^+}\frac{\partial \theta^+}{\partial y^+}}\right), \tag{2.24f}$$

$$\varepsilon^+_{\varepsilon_\theta} = -\frac{2}{Pr^2}\overline{\frac{\partial^2 \theta^+}{\partial x^+_j\partial x^+_l}\frac{\partial^2 \theta^+}{\partial x^+_j\partial x^+_l}}. \tag{2.24g}$$

Finally, the budget equation for the turbulent heat fluxes, $\overline{u_i\theta}$, is derived after taking the average of the following expression: $(1.5)\theta^+ + (1.7)u_i$. After simplifications, it is obtained, for dimensionless inner coordinates:

$$\frac{D\overline{u^+_i\theta^+}}{Dt} = P^+_{i\theta} + T^+_{i\theta} + V^+_{i\theta} + \Pi^{s+}_{i\theta} + \Pi^{d+}_{i\theta} + \varepsilon^+_{i\theta}, \tag{2.25}$$

The different terms on the right hand side are referred to as production, turbulent diffusion, viscous or molecular diffusion, pressure-temperature gradient correlation, pressure diffusion and dissipation. Each term is defined as

$$P_{i\theta}^+ = -\overline{u_j^+ \theta^+}\frac{\partial \overline{U_i}^+}{\partial x_j^+} - \overline{u_i^+ u_j^+}\frac{\partial \overline{\Theta}^+}{\partial x_j^+}, \tag{2.26a}$$

$$T_{i\theta}^+ = -\frac{\partial \overline{u_i^+ u_j^+ \theta^+}}{\partial x_j^+}, \tag{2.26b}$$

$$V_{i\theta}^+ = \frac{\partial}{\partial x_j^+}\left(\overline{\theta^+ \frac{\partial u_i^+}{\partial x_j^+}} + \frac{1}{Pr}\overline{u_i^+ \frac{\partial \theta^+}{\partial x_j^+}}\right), \tag{2.26c}$$

$$\Pi_{i\theta}^{s+} = \overline{p^+ \frac{\partial \theta^+}{\partial x_i^+}}, \tag{2.26d}$$

$$\Pi_{i\theta}^{d+} = -\frac{\partial \overline{p^+ \theta^+}}{\partial x_i^+}, \tag{2.26e}$$

$$\varepsilon_{i\theta}^+ = -\left(1 + \frac{1}{Pr}\right)\overline{\frac{\partial u_i^+}{\partial x_j^+}\frac{\partial \theta^+}{\partial x_j^+}}. \tag{2.26f}$$

The specific terms of the streamwise heat flux for statistically steady thermal channel flows are

$$P_{u\theta}^+ = -\overline{v^+ \theta^+}\frac{\partial \overline{U}^+}{\partial y^+} - \overline{u^+ v^+}\frac{\partial \overline{\Theta}^+}{\partial y^+}, \tag{2.27a}$$

$$T_{u\theta}^+ = -\frac{\partial \overline{u^+ v^+ \theta^+}}{\partial y^+}, \tag{2.27b}$$

$$V_{u\theta}^+ = \frac{\partial}{\partial y^+}\left(\overline{\theta^+ \frac{\partial u^+}{\partial y^+}} + \frac{1}{Pr}\overline{u^+ \frac{\partial \theta^+}{\partial y^+}}\right), \tag{2.27c}$$

$$\Pi_{u\theta}^{s+} = \overline{p^+ \frac{\partial \theta^+}{\partial x^+}}, \tag{2.27d}$$

$$\Pi_{u\theta}^{d+} = 0, \tag{2.27e}$$

$$\varepsilon_{u\theta}^+ = -\left(1 + \frac{1}{Pr}\right)\overline{\frac{\partial u^+}{\partial x_j^+}\frac{\partial \theta^+}{\partial x_j^+}}, \tag{2.27f}$$

and for the wall-normal heat flux

$$P_{v\theta}^+ = -\overline{v^+ v^+}\frac{\partial \overline{\Theta}^+}{\partial y^+}, \tag{2.28a}$$

$$T_{v\theta}^+ = -\frac{\partial \overline{v^+ v^+ \theta^+}}{\partial y^+}, \tag{2.28b}$$

$$V_{v\theta}^+ = \frac{\partial}{\partial y^+}\left(\overline{\theta^+ \frac{\partial v^+}{\partial y^+}} + \frac{1}{Pr}\overline{v^+ \frac{\partial \theta^+}{\partial y^+}}\right), \tag{2.28c}$$

$$\Pi_{v\theta}^{s+} = \overline{p^+ \frac{\partial \theta^+}{\partial y^+}}, \tag{2.28d}$$

$$\Pi_{v\theta}^{d+} = -\frac{\partial \overline{p^+ \theta^+}}{\partial y^+}, \tag{2.28e}$$

$$\varepsilon_{v\theta}^+ = -\left(1 + \frac{1}{Pr}\right)\overline{\frac{\partial v^+}{\partial x_j^+}\frac{\partial \theta^+}{\partial x_j^+}}. \tag{2.28f}$$

The splitting of the pressure in two different terms, $\Pi_{i\theta}^{s^+}$ and $\Pi_{i\theta}^{d^+}$ is not unique, but this one offers more information [38]. However, in the work of Kasagi et al. [37], the summation of both terms, named temperature pressure-gradient correlation, is considered in their analysis. Coming back to the results of the turbulent budgets obtained in [37], as in the previous works, big similarities were found between the budget terms of k_θ^+ and the ones of the streamwise velocity, due to the high correlation between both fields. For the case of k_θ^+ and ε_θ^+, a balance of the production term with the dissipation was obtained in the entire channel. Regarding $\overline{u^+\theta^+}$, the dissipation and the temperature pressure-gradient correlation acted as sink terms to compensate for production. Except in the balance equation, this temperature pressure-gradient correlation is predominantly effective and compensated by the production term. It was also noted that the molecular and turbulent diffusion was only appreciable in the near-wall region.

These three works constitute the basis for the rest of the DNS of thermal channel flows performed in the sense that these are the most used boundary conditions for the thermal field. After them, one of the main ideas has been to perform simulations at higher Reynolds numbers, with the problem of a higher computational cost. For this reason, the maximum Reynolds number simulated has been growing slowly over the years, as the supercomputers have been improving. The other tendency has been to simulate a broader range of Prandtl numbers, reaching low Prandtl numbers like 0.025, which is the Prandtl number of the liquid mercury, or high Prandtl numbers like 10, which is approximately the Prandtl number of water. As it was explained in previous section (§2.3), simulating Prandtl numbers higher than the unity requires the use of a finer mesh to capture the smallest thermal structures, determined by the Batchelor length scale, η_θ. For this reason, it is more often to see works with lower Prandtl numbers than higher ones.

In 1993, Kasagi and Ohtsubo [39] published a complementary study to the one published the previous year [37], but for a low Prandtl number of 0.025. The objective was to examine the differences in the thermal field between both cases, i.e. $Pr = 0.71$ from [37] and $Pr = 0.025$ from [39]. The same friction Reynolds number of value 150 and the MBC were used. The first important difference was that, for such a small Prandtl number, the conductive sublayer gets thicker and the logarithmic region completely disappears. Regarding the turbulent fluctuations, θ'^+, $\overline{u^+\theta^+}$ and $\overline{v^+\theta^+}$, their values decrease for smaller Prandtl numbers and their peak value moves away from the wall. The turbulent Prandtl number was observed to increase its value at the wall, up to $Pr_t \approx 3$, far from the typical value 1 obtained for molecular Prandtl numbers close to 1, confirming the speculations of Antonia and Kim [34]. A significant decrease of the velocity-temperature correlation coefficient was obtained down to values of $R_{u_\theta} \approx 0.6$. Also, the one-dimensional energy spectra were examined. Again, big similarities were observed between the velocity, and temperature spectra when $Pr = 0.71$, but a lower spectra was obtained for $Pr = 0.025$, indicating a less energetic thermal field. The same turbulent budgets as in [37] were calculated. The main difference was that for low Prandtl numbers the production term was always balanced by the dissipation term, except in the wall, where the molecular diffusion is compensated by dissipation. An important difference is that the turbulent diffusion and the temperature pressure-gradient correlation terms in $\overline{u^+\theta^+}$ and $\overline{v^+\theta^+}$ were negligible in the entire channel. Finally, several instantaneous images of velocity and temperature structures were presented. First, it was obtained that the streaky structures in the near-wall region were thicker and less elongated than those of $Pr = 0.71$. And second, it was noticed that in the low-pressure regions of the flow, streamwise vortical structures appear. In addition, the production and destruction mechanisms of turbulent stresses and heat fluxes always appeared associated with those vortical structures. This occurs for both Prandtl numbers, although for $Pr = 0.025$, the molecular diffusion was the sink term near the wall, instead of the temperature pressure-gradient correlation.

The next important DNS of a thermal channel flow was done by Kawamura et al. in 1998 [40]. Here, a wide range of Prandtl numbers, from 0.025 up to 5, were simulated for $Re_\tau = 180$ using the MBC. In this work, the same Taylor expansion decomposition as in [34] (equations (2.17a)-(2.17i)) was used to analyse Pr_t. It was observed that (see coefficients from equation (2.18)), while the coefficient d_{12} was constant for every Pr (which is trivial since a passive scalar is considered), the coefficient $d_{2\theta}$ drastically

decreases for $Pr \leq 0.1$. This supposes an increase in the value of Pr_t, confirming again the speculation of [34]. On the other hand, for the case of $Pr = 5$, no change in the limiting value of Pr_t was observed. However, in future DNS, it will be obtained an increase of Pr_t for such high Prandtl numbers. The reason why it was not obtained in the work of Kawamura et al. [40] may be associated with a low mesh resolution near the wall. All this supported the fact that, in modelling of heat transfer, a constant value of Pr_t is used for Pr close to 1. Finally, budgets of the turbulent heat flux and the temperature variance were obtained. An important result was that the production term in the temperature variance reaches thermal equilibrium at a certain wall distance location, being its maximum determined by $P_{\theta,\max}^+ = Pr/4$ and the wall coordinate scaling with $Pr^{1/3}$. This equilibrium was reached for $Pr > 0.1$.

One year later, in 1999, Kawamura et al. [41], extended the study of the previous year, simulating, for the first time a flow at $Re_\tau = 395$. The MBC condition was imposed and the Prandtl numbers used were $Pr = 0.025$, 0.2 and 0.71. In that sense, only the effects of Re_τ were analyzed for medium and low Prandtl numbers. For the mean temperature, a region closer to a properly developed logarithmic behaviour was obtained. In fact, a value of $\kappa_t = 0.43$ was obtained for $Re_\tau = 395$. With respect to the value obtained in [30], $\kappa_t = 0.39$ for $Re_\tau = 180$, the new value was much closer to the experimental one of $\kappa_t = 0.47$ obtained for higher Reynolds numbers by Kader [31]. Regarding the turbulent fluctuations, θ'^+, $\overline{u^+\theta^+}$ and $\overline{v^+\theta^+}$, weaker dependencies on Re_τ were observed for higher Pr. Another important conclusion was that the higher the Reynolds is, the wider the range of Prandtl where a collapsing of the statistics occurs. For example, the coefficient of the Taylor expansions of the statistics (2.17a)-(2.17i) perfectly collapse for $Pr = 0.71$ and $Pr = 0.2$ with $Re_\tau = 395$. However, small variations were obtained for $Re_\tau = 180$. Similarly, the peak in the production budget of the temperature variance reached the theoretical maximum of $Pr/4$ obtained in [40] for lower Prandtl numbers as the Reynolds number increases. As another example, Pr_t, whose value increases at the wall for low Pr, tends towards a value of 1 for higher Re_τ. An analysis of the budget terms of the wall-normal heat flux was done. The dominant budget terms were found to relatively increase with the Reynolds number more than the non-dominant terms. Also, for $Pr = 0.2$, where the dissipation and the temperature pressure-gradient correlation are competitive in the destruction of thermal energy, an increase of Re_τ contributes to an increase of the temperature pressure-gradient correlation, but no increase of the dissipation is obtained. Finally, flow visualizations were presented. A special focus was given to the near-wall streaks of the velocity and temperature field. While both fields are very similar for $Pr = 0.71$, longer and slender structures are obtained for $Re_\tau = 395$ than those obtained at $Re_\tau = 180$.

Using the data from [41], Kawamura et al. [42] compared the velocity and thermal flow under four combinations of boundary conditions: a Poiseuille flow with the MBC, i.e. the flow from [41]; and with a temperature wall difference; and a Couette flow with the MBC and a temperature wall difference. The main difference between Poiseuille and Couette velocity fields is that higher intensities are obtained for Couette flows in the center of the channel. These higher velocity fluctuations come from the higher production of turbulent energy due to the non-zero gradient of the velocity in the center of the channel. When the MBC is applied, the Couette flow produces a more flattened temperature profile in the center of the channel because a large thermal diffusion is caused by the much larger turbulent intensities. Therefore, lower temperature fluctuations appear in the central region of the channel and all budget terms are lower due to the decrease of the temperature gradient. In conclusion, similar thermal fields are obtained near the wall for different boundary conditions. However, differences appear in the central region of the channel, which comes from the zero or non-zero gradient of the mean velocity and temperature.

Regarding high Prandtl numbers, Na and coworkers published in two different articles [43, 44] the results of a simulation at $Re_\tau = 150$ and $Pr = 1$, 3 and 10, aiming to study the effects of high Prandtl numbers on the thermal field. The same thermal boundary condition used in Lyons et al. [36] was employed, i.e. a temperature difference between the lower and upper walls of the channel. An important result obtained was that the conductive sublayer thickness, Δ_θ scales as $\Delta_\theta \sim Pr^{-1/2}$, so it gets thinner with increasing Prandtl number. Also, the correlations of the temperature and velocity fields, $R_{u\theta}$ and

$R_{v\theta}$, decrease for high Prandtl numbers. To understand the decrease of $R_{v\theta}$, the cumulative co-spectral density function of $\overline{v^+\theta^+}$ and $\overline{\theta'^{+2}}$ were calculated at $y^+ = 25$, i.e. in the near-wall region. It was observed that the high wavenumbers of the co-spectra contribute more significantly to $\overline{\theta'^{+2}}$ than to $\overline{v'^{+2}}$ at large Pr. Therefore, the correlation $R_{v\theta} = \overline{v^+\theta^+}/\left(\sqrt{\overline{\theta'^{+2}}}\sqrt{\overline{v'^{+2}}}\right)$ decrease with Pr. A direct consequence of this high contribution of high wavenumbers to $\overline{\theta'^{+2}}$ is that the analogy between the velocity and thermal field is no longer accurate to model the thermal diffusivity for high Prandtl numbers. This fact is studied in the works of Na and coworkers, finding a decrease of the thermal diffusivity k_t with increasing Prandtl number. As a result, the turbulent Prandtl number, Pr_t increases its value, as it was speculated in [34].

It was not until 2004 when the maximum friction Reynolds number simulated in a DNS of heat transfer reached $Re_\tau = 1000$. Abe et al. [45] performed several DNSs for $Re_\tau = 180$, 395, 640 and 1020, with Prandtl numbers of air $Pr = 0.71$ and liquid mercury $Pr = 0.025$. Effects of the Reynolds and Prandtl numbers on the surface heat flux, $\dot{q}_w$, were examined. First, it was obtained that the root-mean-square (rms) of $\dot{q}_w$ increased with Re_τ, with higher values for the case of $Pr = 0.71$. However, the rate of increase with Re_τ was higher for the lower Prandtl number of 0.025, due to the increasing conductive effect, expecting larger values of the rms of $\dot{q}_w$ for $Pr = 0.025$ with $Re_\tau \gg 1000$. Also, instantaneous visualizations of the surface heat flux were provided. Inspection of the interaction of the outer and inner layers showed that the large-scale motions of positive and negative temperature fluctuations in the outer region have an influence in the inner scale, where corresponding positive and negative rms of $\dot{q}_w$ appear. This, confirms the results of [30] for Re_τ up to 1000 and low Prandtl numbers of value $Pr = 0.025$.

Chronologically, two important works regarding high Prandtl numbers were published in the following years. First, Schwertfirm and Manhart in 2007 [46], conducted several simulations for $Re_\tau = 180$ and $Pr = 3$, 10, 25 and 49, which is the highest Prandtl number ever simulated in a DNS. The thermal boundary condition was a temperature difference between both walls. Several temperature statistics, such as mean and fluctuating temperature, heat fluxes, and budgets of the temperature variances were calculated, obtaining an extrapolation of the results presented in [40, 43, 44]. Schwertfirm and Manhart [46] also calculated the turbulent Prandtl number, with the same trend as previously mentioned, increasing Pr_t for high Pr. Specifically, a value of $Pr_t = 2.15$ was obtained for $Pr = 49$. Finally, the conductive sublayer was calculated, obtaining that it scales as $\Delta_\theta \sim Pr^{-0.29}$. This absolute value of the exponent was lower than all precedent predictions, which may be due to the different boundary conditions or to the different definition of the conductive sublayer depth.

Later, Kozuka et al. in 2009 [47], performed a huge parametric study of high Prandtl numbers for $Re_\tau = 180$ and 395 and $Pr = 0.71$, 1, 2, 5, 7 and 10. A decrease of the mean temperature was obtained at the center channel with increasing Re_τ if $Pr > 1$. This indicates that turbulence can mix heat in a more efficient way when Pr is higher. Thus, the thermal field becomes more homogeneous due to a higher convective effect. Mean temperature profiles of different heat transfer models [31, 48, 49] were compared, concluding that better precision is needed from the models for high Pr. Regarding the turbulent Prandtl number, a lower Re_τ dependence in the near-wall region was observed for high Pr, since heat conduction is more dominant than convection, and thus the effect of Re_τ is small. A constant value of $Pr_t = 0.8$ independent of Pr was obtained in the outer region. A comparison of the budget terms of ε_θ^+ and ε^+ was done, obtaining a lot of similarities for $Pr = 1$. This indicates that models for ε_θ^+ can be constructed in a similar way to that of ε^+. Small differences were obtained only in the dissipation term near the wall, which was explained using the Taylor decomposition (2.17a)-(2.17i). A comparison of existing models of ε_θ^+ with the DNS data was performed. The conclusions were that some models give reasonable results near the wall with $Pr \approx 1$. However, with increasing Pr, none of the existing models can predict the correct near-wall behavior of the budget terms of ε_θ^+. Finally, an analysis of the $\overline{u_i^+\theta^+}$ budget was presented, with a special focus on the $\varepsilon_{i\theta}^+$ term. For the $\overline{u^+\theta^+}$ budgets, with increasing Pr, $\varepsilon_{1\theta}^+$ and the viscous diffusion term, become more effective in the viscous sublayer. For the $\overline{u^+\theta^+}$ budgets, with increasing Pr, the effect of $\varepsilon_{2\theta}^+$ becomes noticeable in the near-wall region.

The last remarkable work of a thermal Poiseuille flow was performed in 2016 by Pirozzoli et al. [50]. In this work, Reynolds numbers of values $Re_\tau = 550$, 1000, 2000 and 4000 were simulated for $Pr = 0.2$, 0.71 and 1. The thermal boundary condition applied was a uniform heat generation as in [30]. Mean temperature profiles were presented, showing a good agreement with Kader's correlation [31]. A deep analysis of the logarithmic layer is carried out, obtaining a von kármán constant of value $\kappa_t = 0.46$, very close to the value of $\kappa_t = 0.47$ from experiments. However, a plateau is still not perfectly observed for $Re_\tau = 4000$, and a linear dependence with Re_τ is obtained. This matches the analogous suppositions for the velocity field of Jiménez and Moser [51], where a linear dependence of the logarithmic layer with Re_τ was also supposed. This linear dependence tends to 0 for increasing Re_τ. The correlation coefficient of the streamwise velocity and temperature is reduced in the center of the channel due to the reduced effectiveness of ejection events. Finally, Nu and Pr_t are calculated, obtaining good agreement with proposed correlations and following the same trend as lower Reynolds number studies.

As mentioned, the work of Pirozzoli et al. [50] simulated the higher Re_τ in a DNS of a thermal channel flow. On the other hand, the highest Re_τ simulated using the MBC condition was performed by Lluesma-Rodríguez et al. [52], where a value of $Re_\tau = 2000$ was used. In this work, a validation of a computational box of dimensions $2\pi h \times 2h \times \pi h$ in the streamwise, wall-normal, and spanwise directions, respectively, is demonstrated for first- and second-order statistics.

The second type of flow analyzed in this work is the Couette flow, where the flow is moved by a difference in the velocity of the walls. Until very recently, Couette flows have been simulated at a relatively small Reynolds number [53, 54, 55, 56, 57]. This is due to the existence of very large-scale roll-like motions extending along with the domain, which were found experimentally [58, 59, 60]. In the latter, Kitoh and Umeki used an experimental apparatus with a size of $5120 \times 27 \times 880 \ mm$ with a lower wall moving belt. They performed several experiments at $Re = U_w h/\nu = 3750$, where U_w was half of the velocity of the moving belt, using a hot-wire probe to measure flow statistics. To reduce the randomness of the appearance of the structures in the experiment, they used a vortex generator in the core region of the channel. The streamwise rolls that appeared downstream this vortex generator became quasistationary without a noticeable decay. To properly capture these rolls in numerical simulations, long and wide computational boxes are needed. In isothermal flows, these rolls are defined as coherent regions of either positive or negative streamwise velocity fluctuations. They appear in pairs, creating a *structure* in the velocity field composed of a couple of counter-rotating vortices aligned with the streamwise direction [54, 61]. There is not a clear criterion to identify these structures. They are mostly identified through visualization employing some filtering [54, 55]. As it is shown later, there is a clear organization of the velocity and thermal rolls in larger structures, with two clear symmetries. As these rolls and structures have not received a name, the generic term CTFS (Couette Thermal Flow Superstructure) will be used to identify not only one particular velocity or thermal roll, but the set composed of several of them.

There exists a rich bibliography about the problem of heat transfer in Poiseuille flows, as previously presented. However, only a few works address the problem of heat transfer for Couette flows [42, 64, 65]. These works were a challenge in their times, but unfortunately in most of them, either the computational box used is too narrow and short to properly describe the CTFS or the Reynolds number used is low. In fact, in the work of Debusschere and Rutland [64] it is explicitly stated that they are using a narrow box to remove the effects of the velocity rolls. These authors affirm that these rolls are not probably present in real-life devices. However, as it is said before, the rolls have been found experimentally [58, 59, 60]. They are very long and could be even infinite in length [55]. The rolls are also stable even to transversal flows [63] and they affect the flow as secondary flows in ducts do [66]. Moreover, as it is stated in this work, CTFS do affect both the statistics of the flow and the thermal field, as it is composed of rolls of both fields. This appears to be an effect of Couette boundary conditions. Gandía-Barberá et al. [56] linked the existence of the rolls to only negative values on the one-point statistics of Reynolds stress in transitional Couette-Poiseuille flows. Table 2.1 shows the parameters of the previous Couette flows simulations, such as Re_τ, computational box size, and mesh resolution. In the case of Poiseuille flow, a

Work	Re_τ	L_x/π	L_z/π
Tsukahara et al. [53]	52	14	4
	126		
	126	20	2
Avsarkisov et al. [54]	$125 - 550$	20	6
Pirozzoli et al. [62]	$171 - 986$	18	8
Lee and Moser [55]	$93 - 501$	100	5
	547	60	6
Kraheberger et al. [63]	$250 - 1000$	8	3
Gandía-Barberá et al. [56]	132	128	6
Komminaho et al. [57]	52	28	8
Kawamura et al. [42]	180, 395	2	1
Debusschere and Rutland [64]	160	3.8	0.6
Tsukahara et al. [65]	52, 126	28.5	4
Present work	$180 - 500$	16	6

Table 2.1: Parameters of previous Couette flow simulations. Works in bold denotes that the thermal field has also been simulated. Third and fourth column show the maximum computational domain used in each work in x and z, respectively. Second column shows the ranges of Re_τ simulated at the corresponding computational boxes.

relatively small computational box of a stream- and span-wise sizes of only $2\pi h \times \pi h$ can satisfactorily recover the one- and two-point statistics of the flow, as previously mentioned from [52]. However, the proper box dimensions in Couette flow are not that clear, as can be seen from table 2.1. The existence and characterization of the CTFS and its influence in the one-point statistics are addressed for the first time in this work.

Finally, the last type of flow analysed in this work is the stratified flow. The main idea of using stratified flows is to destabilize the counter-rotating rolls from Couette flows, introducing an active thermal field, which causes a density stratification in the flow. The effect of stratification on rolls in the plane Couette flow is relatively less studied. There are some indications that even in the weakly stratified plane Couette flow at high Re_τ, coherent structures, and the near-wall turbulence regeneration cycle may be affected by the vertical stratification [67, 68]. Perhaps, one candidate for this phenomenon could be a rare cloud formation called the Morning Glory cloud, [69]. However, due to certain limitations in the atmospheric measurements techniques and spatial coverage, this comparison requires more observational and numerical efforts. Anyway, the results of the present analysis are relevant to the stratified turbulence in the atmosphere, as it is found at a large variety of stratification rates and Reynolds numbers [70].

Chapter 3

Lie symmetries

3.1 Governing equations

As mentioned in chapter §1, Lie symmetries are a powerful method to obtain invariant solutions of systems of PDEs, which in turbulence are also known as scaling laws. In the case of turbulence, the Lie symmetries method is used to obtain symmetries of the equations that describe the behaviour of turbulent flows, i.e. the continuity (1.5), momentum (1.6) and energy (1.7) equations. These equations can also be written in the average form, obtaining (1.8), (1.9) and (1.31), respectively. If the averaged equations are subtracted from the instantaneous equations, it is obtained the fluctuating equations. For the case of the continuity equation, subtracting (1.5)-(1.8) the following is obtained (for the sake of readability, the temporal and spatial dependencies will be omitted if uniqueness allows to do so):

$$\frac{\partial u_i}{\partial x_i} = 0, \tag{3.1}$$

which indicates that the fluctuating variables also fulfill the continuity condition. Equivalently, for the momentum equation, it is obtained that

$$\frac{\partial u_i}{\partial t} + \overline{U}_k \frac{\partial u_i}{\partial x_k} + u_k \frac{\partial \overline{U}_i}{\partial x_k} + \frac{\partial u_i u_k}{\partial x_k} - \frac{\partial \overline{u_i u_k}}{\partial x_k} = -\frac{\partial p}{\partial x_i} + \nu \frac{\partial^2 u_i}{\partial x_k^2}. \tag{3.2}$$

For the generic case of the energy equation (no boundary condition is included), if Θ represents the temperature, the fluctuating energy equation is written as

$$\frac{\partial \theta}{\partial t} + \overline{U}_k \frac{\partial \theta}{\partial x_k} + u_k \frac{\partial \overline{\Theta}}{\partial x_k} + \frac{\partial \theta u_k}{\partial x_k} - \frac{\partial \overline{\theta u_k}}{\partial x_k} = \alpha \frac{\partial^2 \theta}{\partial x_k^2}. \tag{3.3}$$

In the latter equations, one-point quantities have been used. In addition, it can be defined the two-point correlation functions, or two-point moments, which based on the fluctuating velocity can be written as

$$R_{ij}(\boldsymbol{x}, \boldsymbol{r}) = \overline{u_i(\boldsymbol{x})u_j(\boldsymbol{x}+\boldsymbol{r})}, \quad R_{ij}^0(\boldsymbol{x}) = \lim_{\boldsymbol{r}\to 0} R_{ij}(\boldsymbol{x}, \boldsymbol{r}) = \overline{u_i(\boldsymbol{x})u_j(\boldsymbol{x})}. \tag{3.4}$$

Employing an equivalent definition based on the instantaneous variables, reads

$$H_{ij}(\boldsymbol{x}, \boldsymbol{r}) = \overline{U_i(\boldsymbol{x})U_j(\boldsymbol{x}+\boldsymbol{r})}, \quad H_{ij}^0(\boldsymbol{x}) = \lim_{\boldsymbol{r}\to 0} H_{ij}(\boldsymbol{x}, \boldsymbol{r}) = \overline{U_i(\boldsymbol{x})U_j(\boldsymbol{x})}, \tag{3.5}$$

and a relation between the two correlation functions R_{ij} and H_{ij} reads as follows

$$R_{ij}(\boldsymbol{x}, \boldsymbol{r}) = H_{ij}(\boldsymbol{x}, \boldsymbol{r}) - \overline{U}_i(\boldsymbol{x})\overline{U}_j(\boldsymbol{x}+\boldsymbol{r}). \tag{3.6}$$

29

This two-point concept can be extended for any number of points and ultimately forms the basis of the following analysis as well as the resulting scaling laws. Hence, it is introduced the Multi-Point Correlation (MPC) equations (see e.g. [17, 18, 19, 20]). For high-order moments of velocity and temperature, they give additional information that is not provided in the one-point statistic equations, such as length scales. Also, when deriving higher order moment equations, only one unclosed function arises. As observed in equation (3.4), from the two-point statistics one can obtain every one-point statistic. Finally, regarding Lie symmetries, two extra symmetries are obtained from the MPC equations, which are the key for determining the new scaling laws of the high-order moments.

Equations (3.4) and (3.5) are the basis of the two different approaches that can be used to obtain the MPC equations: the fluctuating approach or the instantaneous approach, where the MPC equations are derived from the fluctuating equations (3.1), (3.2) and (3.3). On one hand, the fluctuating approach has some advantages such as a straightforward relation to the Reynolds stress tensor or the turbulent heat fluxes. However, as noted in [71], a non-linear system of equations is obtained. Furthermore, all moment equations are coupled to the mean velocity or temperature, and equations of the third moment or higher, are coupled to the second moment. All this complicates the symmetry analysis that will be done below and, therefore, the derivation of the MPC equations from the fluctuating approach will not be contemplated here. On the other hand, the instantaneous approach results in a linear system of MPC equations with an equivalent but much simpler symmetry analysis. For this reason, the instantaneous approach is the one used in this work. Before presenting the MPC equations, some notation must be clarified. The correlation functions for the velocity are defined as

$$H_{i_{\{n\}}} = H_{i_{(1)}i_{(2)}...i_{(n)}} = \overline{U_{i_{(1)}}(\boldsymbol{x}_{(1)})U_{i_{(2)}}(\boldsymbol{x}_{(2)})...U_{i_{(n)}}(\boldsymbol{x}_{(n)})} = \overline{\prod_{a=1}^{n} U_{i_{(a)}}(\boldsymbol{x}_{(a)})}, \qquad (3.7)$$

which for $n = 2$, $\boldsymbol{x}_{(1)} = \boldsymbol{x}$ and $\boldsymbol{x}_{(2)} = \boldsymbol{x}+\boldsymbol{r}$ yields to (3.5), while for $n = 1$ the mean velocity, $H_{i_{(1)}} = \overline{U}_i(\boldsymbol{x})$ is obtained. The definition for the temperature correlation is

$$H_{\Theta_{\{m\}}} = H_{\Theta_{(1)}\Theta_{(2)}...\Theta_{(m)}} = \overline{\Theta(\boldsymbol{x}_{(1)})\Theta(\boldsymbol{x}_{(2)})...\Theta(\boldsymbol{x}_{(m)})} = \overline{\prod_{b=1}^{m} \Theta(\boldsymbol{x}_{(b)})}. \qquad (3.8)$$

In the same way, $H_{\Theta_{(1)}}$ represents the mean temperature $\Theta(\boldsymbol{x})$. Mixed moments of velocity and temperature, which in the limit of only one temperature and one velocity reduces to the turbulent heat fluxes, reads

$$H_{i_{\{n\}}\Theta_{\{m\}}} = H_{i_{(1)}i_{(2)}...i_{(n)}\Theta_{(n+1)}\Theta_{(n+2)}...\Theta_{(n+m)}} =$$
$$\overline{U_{i_{(1)}}(\boldsymbol{x}_{(1)})U_{i_{(2)}}(\boldsymbol{x}_{(2)})...U_{i_{(n)}}(\boldsymbol{x}_{(n)})\Theta(\boldsymbol{x}_{(n+1)})\Theta(\boldsymbol{x}_{(n+2)})...\Theta(\boldsymbol{x}_{(n+m)})} =$$
$$\overline{\prod_{a=1}^{n} U_{i_{(a)}}(\boldsymbol{x}_{(a)}) \prod_{b=n+1}^{n+m} \Theta(\boldsymbol{x}_{(b)})}. \qquad (3.9)$$

Note that (3.7) and (3.8) are just particular cases of (3.9) for m and n equal to 0, respectively, but for the sake of readability they are presented separately. When pressure is involved in the correlation, the notation, in the general form, is

$$I_{i_{\{n-1\}}[l]_P\Theta_{\{m\}}} = H_{i_{(1)}...i_{(l-1)}Pi_{(l+1)}...i_{(n)}\Theta_{(n+1)}\Theta_{(n+2)}...\Theta_{(n+m)}} =$$
$$\overline{U_{i_{(1)}}(\boldsymbol{x}_{(1)})...P(\boldsymbol{x}_{(l)})...U_{i_{(n)}}(\boldsymbol{x}_{(n)})\Theta(\boldsymbol{x}_{(n+1)})...\Theta(\boldsymbol{x}_{(n+m)})} =$$
$$\overline{P(\boldsymbol{x}_{(l)}) \prod_{a=1,a\neq l}^{n} U_{i_{(a)}}(\boldsymbol{x}_{(a)}) \prod_{b=n+1}^{n+m} \Theta(\boldsymbol{x}_{(b)})}, \qquad (3.10)$$

where the subindex $[l]_P$ indicates that the l-th term is replaced by pressure, with $1 \leq l \leq n$. Finally, the following notation

$$
\begin{aligned}
&H_{i_{\{n\}}\Theta_{\{m\}}[i_{(l)}\to k]}(\boldsymbol{x}_{(l)} \to \boldsymbol{x}_{(p)}) = \\
&\overline{U_{i_{(1)}}(\boldsymbol{x}_{(1)})...U_{i_{(l-1)}}(\boldsymbol{x}_{(l-1)})U_k(\boldsymbol{x}_{(p)})U_{i_{(l+1)}}(\boldsymbol{x}_{(l+1)})...U_{i_{(n)}}(\boldsymbol{x}_{(n)})\Theta(\boldsymbol{x}_{(n+1)})...\Theta(\boldsymbol{x}_{(n+m)})}
\end{aligned}
$$

(3.11)

is used to indicate a change in the correlation function of velocity direction, $i_{(l)}$, to k and/or the coordinate where the variable is applied, $\boldsymbol{x}_{(l)}$, to $\boldsymbol{x}_{(p)}$. With these definitions, the MPC equations of velocity and temperature mixed moments of order $n + m$ can be derived, which is the more general case. The derivation of the MPC equations of the momentum and energy are just two specific cases of the velocity and temperature mixed moments MPC equation.

The simplest case of the MPC are the Two-Point Correlation (TPC) equations. Three equations can be derived, one for the velocity, one for the velocity and temperature mixed moments and one for the temperature. The following operations, using equations (1.6) and (1.7), must be applied in order to derive them

$$
\overline{\mathcal{M}_{i_{(1)}}(\boldsymbol{x}_{(1)})U_{i_{(2)}}(\boldsymbol{x}_{(2)})} + \overline{U_{i_{(1)}}(\boldsymbol{x}_{(1)})\mathcal{M}_{i_{(2)}}(\boldsymbol{x}_{(2)})} = 0, \tag{3.12a}
$$

$$
\overline{\mathcal{M}_{i_{(1)}}(\boldsymbol{x}_{(1)})\Theta(\boldsymbol{x}_{(2)})} + \overline{U_{i_{(1)}}(\boldsymbol{x}_{(1)})\mathcal{E}(\boldsymbol{x}_{(2)})} = 0, \tag{3.12b}
$$

$$
\overline{\mathcal{E}(\boldsymbol{x}_{(1)})\Theta(\boldsymbol{x}_{(2)})} + \overline{\Theta(\boldsymbol{x}_{(1)})\mathcal{E}(\boldsymbol{x}_{(2)})} = 0, \tag{3.12c}
$$

respectively. The general case, the MPC equations, are an extension of the TPC equations. The derivation of the MPC equations of order $n + m$ starts from the following equation:

$$
\begin{aligned}
&\overline{\mathcal{M}_{i_{(1)}}(\boldsymbol{x}_{(1)})U_{i_{(2)}}(\boldsymbol{x}_{(2)})...U_{i_{(n)}}(\boldsymbol{x}_{(n)})\Theta(\boldsymbol{x}_{(n+1)})...\Theta(\boldsymbol{x}_{(n+m)})} \\
&+\overline{U_{i_{(1)}}(\boldsymbol{x}_{(1)})\mathcal{M}_{i_{(2)}}(\boldsymbol{x}_{(2)})U_{i_{(3)}}(\boldsymbol{x}_{(3)})...U_{i_{(n)}}(\boldsymbol{x}_{(n)})\Theta(\boldsymbol{x}_{(n+1)})...\Theta(\boldsymbol{x}_{(n+m)})} \\
&+ \quad ... \\
&+\overline{U_{i_{(1)}}(\boldsymbol{x}_{(1)})...U_{i_{(n-1)}}(\boldsymbol{x}_{(n-1)})\mathcal{M}_{i_{(n)}}(\boldsymbol{x}_{(n)})\Theta(\boldsymbol{x}_{(n+1)})...\Theta(\boldsymbol{x}_{(n+m)})} \\
&+\overline{U_{i_{(1)}}(\boldsymbol{x}_{(1)})...U_{i_{(n)}}(\boldsymbol{x}_{(n)})\mathcal{E}(\boldsymbol{x}_{(n+1)})\Theta(\boldsymbol{x}_{(n+2)})...\Theta(\boldsymbol{x}_{(n+m)})} \\
&+\overline{U_{i_{(1)}}(\boldsymbol{x}_{(1)})...U_{i_{(n)}}(\boldsymbol{x}_{(n)})\Theta(\boldsymbol{x}_{(n+1)})\mathcal{E}(\boldsymbol{x}_{(n+2)})\Theta(\boldsymbol{x}_{(n+3)})...\Theta(\boldsymbol{x}_{(n+m)})} \\
&+ \quad ... \\
&+\overline{U_{i_{(1)}}(\boldsymbol{x}_{(1)})...U_{i_{(n)}}(\boldsymbol{x}_{(n)})\Theta(\boldsymbol{x}_{(n+1)})...\Theta(\boldsymbol{x}_{(n+m-1)})\mathcal{E}(\boldsymbol{x}_{(n+m)})} = \\
&= \quad \sum_{a=1}^{n}\overline{\mathcal{M}_{i_{(a)}}(\boldsymbol{x}_{(a)}) \prod_{c=1,c\neq a}^{n} U_{i_{(c)}}(\boldsymbol{x}_{(c)}) \prod_{d=n+1}^{n+m} \Theta(\boldsymbol{x}_{(d)})} \\
&\quad + \sum_{b=n+1}^{n+m}\overline{\mathcal{E}(\boldsymbol{x}_{(b)}) \prod_{c=1}^{n} U_{i_{(c)}}(\boldsymbol{x}_{(c)}) \prod_{d=n+1,d\neq c}^{n+m} \Theta(\boldsymbol{x}_{(d)})} = 0,
\end{aligned}
$$

(3.13)

where $U_{i_{(l)}}$ and $\boldsymbol{x}_{(l)}$ are the velocity directions and the different points where the equations and the variables are applied, for $i_{(l)} = 1, 2, 3$; and $l = 1, 2,...,n+m$ (l can be a or b). Note that for $n = 2$, 1 and 0, and for $m = 0$, 1 and 2, respectively, the TPC equations (3.12a), (3.12b) and (3.12c), respectively, are

obtained. Introducing the momentum (1.6) and energy (1.7) equations, into (3.13), it is obtained that

$$
\begin{aligned}
&\sum_{a=1}^{n} \overline{\frac{\partial U_{i_{(a)}}(\boldsymbol{x}_{(a)})}{\partial t} \prod_{c=1,c\neq a}^{n} U_{i_{(c)}}(\boldsymbol{x}_{(c)}) \prod_{d=n+1}^{n+m} \Theta(\boldsymbol{x}_{(d)})} \\
&+\sum_{a=1}^{n} \overline{U_k(\boldsymbol{x}_{(a)})\frac{\partial U_{i_{(a)}}(\boldsymbol{x}_{(a)})}{\partial x_{k_{(a)}}} \prod_{c=1,c\neq a}^{n} U_{i_{(c)}}(\boldsymbol{x}_{(c)}) \prod_{d=n+1}^{n+m} \Theta(\boldsymbol{x}_{(d)})} \\
&+\sum_{a=1}^{n} \overline{\frac{\partial P(\boldsymbol{x}_{(a)})}{\partial x_{i_{(a)}}} \prod_{c=1,c\neq a}^{n} U_{i_{(c)}}(\boldsymbol{x}_{(c)}) \prod_{d=n+1}^{n+m} \Theta(\boldsymbol{x}_{(d)})} \\
&-\frac{1}{Re_\tau}\sum_{a=1}^{n} \overline{\frac{\partial^2 U_{i_{(a)}}(\boldsymbol{x}_{(a)})}{\partial x_{k_{(a)}}\partial x_{k_{(a)}}} \prod_{c=1,c\neq a}^{n} U_{i_{(c)}}(\boldsymbol{x}_{(c)}) \prod_{d=n+1}^{n+m} \Theta(\boldsymbol{x}_{(d)})} \\
&+\sum_{b=n+1}^{n+m} \overline{\frac{\partial \Theta(\boldsymbol{x}_{(b)})}{\partial t} \prod_{c=1}^{n} U_{i_{(c)}}(\boldsymbol{x}_{(c)}) \prod_{d=n+1,d\neq c}^{n+m} \Theta(\boldsymbol{x}_{(d)})}, \\
&+\sum_{b=n+1}^{n+m} \overline{U_k(\boldsymbol{x}_{(b)})\frac{\partial \Theta(\boldsymbol{x}_{(b)})}{\partial x_{k_{(b)}}} \prod_{c=1}^{n} U_{i_{(c)}}(\boldsymbol{x}_{(c)}) \prod_{d=n+1,d\neq c}^{n+m} \Theta(\boldsymbol{x}_{(d)})}, \\
&-\frac{1}{Pe_\tau}\sum_{b=n+1}^{n+m} \overline{\frac{\partial^2 \Theta(\boldsymbol{x}_{(b)})}{\partial x_{k_{(b)}}\partial x_{k_{(b)}}} \prod_{c=1}^{n} U_{i_{(c)}}(\boldsymbol{x}_{(c)}) \prod_{d=n+1,d\neq c}^{n+m} \Theta(\boldsymbol{x}_{(d)})} = 0.
\end{aligned}
\tag{3.14}
$$

At this point, the continuity equation (1.5) should be applied to introduce the terms $U_k(\boldsymbol{x}_l)$ inside the derivatives with respect to $x_{k_{(l)}}$ in the second and sixth lines of equation (3.14). Also, the product terms can be introduced in the derivatives with respect to the spacial coordinates, since the points $\boldsymbol{x}_{(a)}$ and $\boldsymbol{x}_{(b)}$ are excluded from the product series. Regarding the terms with temporal derivatives in the first and fifth lines of (3.14), the chain rule is applied to reduce it to a single term. Finally, using definitions (3.9), (3.10) and (3.11) one can obtain the MPC equation of the velocity and temperature mixed moments of order $n + m$:

$$
\begin{aligned}
&\frac{\partial H_{i_{\{n\}}\Theta_{\{m\}}}}{\partial t} + \\
&\sum_{a=1}^{n}\left(\frac{\partial H_{i_{\{n+1\}}\Theta_{\{m\}}[i_{(n+m+1)}\to k]}\big(\boldsymbol{x}_{(n+m+1)}\to\boldsymbol{x}_{(a)}\big)}{\partial x_{k_{(a)}}} + \frac{\partial I_{i_{\{n-1\}}\Theta_{\{m\}}[a]_P}}{\partial x_{i_{(a)}}} - \nu\frac{\partial^2 H_{i_{\{n\}}\Theta_{\{m\}}}}{\partial x_{k_{(a)}}\partial x_{k_{(a)}}}\right) \\
&+\sum_{b=n+1}^{n+m}\left(\frac{\partial H_{i_{\{n+1\}}\Theta_{\{m\}}[i_{(n+m+1)}\to k]}\big(\boldsymbol{x}_{(n+m+1)}\to\boldsymbol{x}_{(b)}\big)}{\partial x_{k_{(b)}}} - \alpha\frac{\partial^2 H_{i_{\{n\}}\Theta_{\{m\}}}}{\partial x_{k_{(b)}}\partial x_{k_{(b)}}}\right) = 0.
\end{aligned}
\tag{3.15}
$$

As mentioned before, the MPC equations of the velocity arises if $m = 0$ in (3.15). Similarly, one can obtain the MPC equations of the temperature by setting $n = 0$ in (3.15). Additionally, the continuity equations read

$$
\frac{\partial H_{i_{\{n\}}\Theta_{\{m\}}[i_{(l)}\to k]}}{\partial x_{k_{(l)}}} = 0 \quad \text{for} \quad l = 1, 2, ..., n,
\tag{3.16a}
$$

$$
\frac{\partial I_{i_{\{n-1\}}\Theta_{\{m\}}[a]_P[i_{(l)}\to k]}}{\partial x_{k_{(l)}}} = 0 \quad \text{for} \quad a, l = 1, 2, ..., n, \quad a \neq l, \quad \text{and} \quad n \geq 2.
\tag{3.16b}
$$

Note that pure temperature correlations and mixed moments of velocity and temperature correlations with $l > n$ do not admit continuity equations, since they would have been originated from $\partial \overline{\Theta}(\boldsymbol{x})/\partial x_k$, which is not a continuity equation.

For the case of a statistically steady turbulent channel flow, the MPC equations (3.15) can be reduced to

$$
\sum_{a=1}^{n} \left(\frac{\partial H_{i_{\{n+1\}}\Theta_{\{m\}}[i_{(n+m+1)}\to 2]}\big(\boldsymbol{x}_{(n+m+1)} \to \boldsymbol{x}_{(a)}\big)}{\partial x_{2_{(a)}}} + \frac{\partial I_{i_{\{n-1\}}\Theta_{\{m\}}[a]_P}}{\partial x_{i_{(a)}}} - \nu \frac{\partial^2 H_{i_{\{n\}}\Theta_{\{m\}}}}{\partial x_{2_{(a)}}\partial x_{2_{(a)}}} \right)
$$
$$
+ \sum_{b=n+1}^{n+m} \left(\frac{\partial H_{i_{\{n+1\}}\Theta_{\{m\}}[i_{(n+m+1)}\to 2]}\big(\boldsymbol{x}_{(n+m+1)} \to \boldsymbol{x}_{(b)}\big)}{\partial x_{2_{(b)}}} - \alpha \frac{\partial^2 H_{i_{\{n\}}\Theta_{\{m\}}}}{\partial x_{2_{(b)}}\partial x_{2_{(b)}}} \right) = 0. \tag{3.17}
$$

As was previously noted, the system of the MPC equations (3.15), or (3.17) for turbulent channel flows is linear. Moreover, the dependent variables H and I appear inside spatial or temporal derivatives. As will be seen in the following section, this is the key to obtain two important statistical Lie symmetries necessary to derive the scaling laws.

As an example, and to make the notation easier to understand, the TPC equations for the velocity, heat fluxes, and temperature are presented, which can be obtained by setting in equation (3.15) $n = 2$, 1, 0 and $m = 0$, 1, 2, respectively.

$$
\frac{\partial H_{i_{(1)}i_{(2)}}\big(\boldsymbol{x}_{(1)}, \boldsymbol{x}_{(2)}\big)}{\partial t} + \frac{\partial H_{i_{(1)}i_{(2)}k}\big(\boldsymbol{x}_{(1)}, \boldsymbol{x}_{(2)}, \boldsymbol{x}_{(1)}\big)}{\partial x_{k_{(1)}}} + \frac{\partial H_{i_{(1)}i_{(2)}k}\big(\boldsymbol{x}_{(1)}, \boldsymbol{x}_{(2)}, \boldsymbol{x}_{(2)}\big)}{\partial x_{k_{(2)}}}
$$
$$
+ \frac{\partial I_{Pi_{(2)}}\big(\boldsymbol{x}_{(1)}, \boldsymbol{x}_{(2)}\big)}{\partial x_{i_{(1)}}} + \frac{\partial I_{i_{(1)}P}\big(\boldsymbol{x}_{(1)}, \boldsymbol{x}_{(2)}\big)}{\partial x_{i_{(2)}}}
$$
$$
- \nu \frac{\partial^2 H_{i_{(1)}i_{(2)}}\big(\boldsymbol{x}_{(1)}, \boldsymbol{x}_{(2)}\big)}{\partial x_{k_{(1)}}\partial x_{k_{(1)}}} - \nu \frac{\partial^2 H_{i_{(1)}i_{(2)}}\big(\boldsymbol{x}_{(1)}, \boldsymbol{x}_{(2)}\big)}{\partial x_{k_{(2)}}\partial x_{k_{(2)}}} = 0, \tag{3.18a}
$$
$$
\frac{\partial H_{i_{(1)}\Theta}\big(\boldsymbol{x}_{(1)}, \boldsymbol{x}_{(2)}\big)}{\partial t} + \frac{\partial H_{i_{(1)}\Theta k}\big(\boldsymbol{x}_{(1)}, \boldsymbol{x}_{(2)}, \boldsymbol{x}_{(1)}\big)}{\partial x_{k_{(1)}}} + \frac{\partial H_{i_{(1)}\Theta k}\big(\boldsymbol{x}_{(1)}, \boldsymbol{x}_{(2)}, \boldsymbol{x}_{(2)}\big)}{\partial x_{k_{(2)}}}
$$
$$
+ \frac{\partial I_{P\Theta}\big(\boldsymbol{x}_{(1)}, \boldsymbol{x}_{(2)}\big)}{\partial x_{i_{(1)}}}
$$
$$
- \nu \frac{\partial^2 H_{i_{(1)}\Theta}\big(\boldsymbol{x}_{(1)}, \boldsymbol{x}_{(2)}\big)}{\partial x_{k_{(1)}}\partial x_{k_{(1)}}} - \alpha \frac{\partial^2 H_{i_{(1)}\Theta}\big(\boldsymbol{x}_{(1)}, \boldsymbol{x}_{(2)}\big)}{\partial x_{k_{(2)}}\partial x_{k_{(2)}}} = 0, \tag{3.18b}
$$
$$
\frac{\partial H_{\Theta\Theta}\big(\boldsymbol{x}_{(1)}, \boldsymbol{x}_{(2)}\big)}{\partial t} + \frac{\partial H_{\Theta\Theta k}\big(\boldsymbol{x}_{(1)}, \boldsymbol{x}_{(2)}, \boldsymbol{x}_{(1)}\big)}{\partial x_{k_{(1)}}} + \frac{\partial H_{\Theta\Theta k}\big(\boldsymbol{x}_{(1)}, \boldsymbol{x}_{(2)}, \boldsymbol{x}_{(2)}\big)}{\partial x_{k_{(2)}}}
$$
$$
- \alpha \frac{\partial^2 H_{\Theta\Theta}\big(\boldsymbol{x}_{(1)}, \boldsymbol{x}_{(2)}\big)}{\partial x_{k_{(1)}}\partial x_{k_{(1)}}} - \alpha \frac{\partial^2 H_{\Theta\Theta}\big(\boldsymbol{x}_{(1)}, \boldsymbol{x}_{(2)}\big)}{\partial x_{k_{(2)}}\partial x_{k_{(2)}}} = 0. \tag{3.18c}
$$

Note that developing equations (3.12a), (3.12b) and (3.12c), with the momentum (1.6) and energy (1.7) equations, would lead to the same TPC equations.

To conclude the presentation of the governing equations of turbulence, first the Lie symmetries theory will be applied to the continuity (1.5), momentum (1.6) and energy (1.7) equations, which provide the classical mechanical symmetries. Then, it will be applied to the MPC equations (3.15), which provide two extra Lie symmetries that are the key to derive the scaling laws. All this will be discussed in section §5.1.5.

3.2 Lie Symmetries theory

In this section, the mathematical theory of Lie symmetries will be developed. Definitions and theorems presented in this section are taken from the book Bluman and Anco 2002 [72].

3.2.1 Lie group of transformations

A Lie symmetry or Lie transformation is a group of transformations with certain properties. Therefore, it is convenient to start by defining a group from a mathematical point of view

Definition 3.2.1-1

*A **group** G is a set of elements with a law of composition ϕ between elements satisfying the following conditions:*

- ***Closure property.** For any elements a and b of G, $\phi(a, b)$ is an element of G. For example: G can be all integer numbers, then, a and b will be integers and ϕ can represent summation of a and b. Then, $a + b$ will be an integer, i.e. $a + b$ will belong to G.*

- ***Associative property.** For any elements a, b, c of G: $\phi(a, \phi(b, c)) = \phi(\phi(a, b), c)$. For example: if ϕ represents summation, then, $a + (b + c) = (a + b) + c$.*

- ***Identity element.** There exists a unique identity element e of G such that for any element a of G: $\phi(a, e) = \phi(e, a) = a$. For example: if ϕ represents summation, then, $e = 0$ is the identity element: $a + 0 = a$.*

- ***Inverse element.** For any element a of G there exists a unique inverse element a^{-1} in G such that $\phi(a, a^{-1}) = \phi(a^{-1}, a) = e$. For example: if ϕ represents summation, then $e = 0$, and the inverse element would be $-a$, since $a + (-a) = 0 = e$.*

Once the definition of a group is clear, the next step is to define the transformation group of one coordinate system into another one. For this transformation to be a group, the following conditions must be satisfied

Definition 3.2.1-2

Let $\boldsymbol{x}(x_1, x_2, ..., x_n)$ lie in region $D \subset \mathbb{R}^n$. The set of transformations

$$\boldsymbol{x}^* = \boldsymbol{X}(\boldsymbol{x}; \varepsilon), \tag{3.19}$$

*defined for each $\boldsymbol{x}$ in D and parameter ε in set $S \subset \mathbb{R}$, with $\phi(\varepsilon, \delta)$ defining a law of composition of parameters ε and δ in S, forms a **one-parameter group of transformations** on D if the following hold:*

- *For each ε in S the transformations are one-to-one onto D. Hence, $\boldsymbol{x}^*$ lies in D.*

- *S, with the law of composition ϕ, forms a group G.*

- *For each $\boldsymbol{x}$ in D, $\boldsymbol{x}^* = \boldsymbol{x}$ when $\varepsilon = \varepsilon_0$ corresponds to the identity e, i.e., $\boldsymbol{X}(\boldsymbol{x}; \varepsilon_0) = \boldsymbol{x}$.*

- *If $\boldsymbol{x}^* = \boldsymbol{X}(\boldsymbol{x}; \varepsilon)$, $\boldsymbol{x}^{**} = \boldsymbol{X}(\boldsymbol{x}^*; \delta)$, then*

$$\boldsymbol{x}^{**} = \boldsymbol{X}(\boldsymbol{x}; \phi(\varepsilon, \delta)).$$

Finally, a group of transformations must fulfill the following conditions for it to be a Lie group of transformations.

Definition 3.2.1-3

A one-parameter group of transformations defines a **one-parameter Lie group of transformations** *if, in addition to satisfying axioms in definition 3.2.1-2, the following hold:*

- ε *is a continuous parameter, i.e., S is an interval in $\mathbb{R}$. Without loss of generality, $\varepsilon = 0$ corresponds to the identity element e.*

- $\boldsymbol{X}$ *is infinitely differentiable with respect to $\boldsymbol{x}$ in D and an analytic function of ε in S.*

- $\phi(\varepsilon, \delta)$ *is an analytic function of ε and δ, $\varepsilon \in S$, $\delta \in S$.*

Examples of one-parameter Lie group of transformations

The followings are the most basic one-parameter Lie group of transformations

1. Group of translations:

$$
\begin{aligned}
x^* &= x + \varepsilon, \\
y^* &= y, \quad \varepsilon \in \mathbb{R},
\end{aligned}
\tag{3.20}
$$

   with law of composition $\phi(\varepsilon, \delta) = \varepsilon + \delta$ and identity element: $\varepsilon = 0$.

   This group represents a translation parallel to the x axis.

2. Group of scalings:

$$
\begin{aligned}
x^* &= \alpha x, \\
y^* &= \alpha^2 y, \quad 0 < \alpha < \infty,
\end{aligned}
\tag{3.21}
$$

   with law of composition $\phi(\alpha, \beta) = \alpha\beta$ and identity element: $\alpha = 1$. Since the identity element is not 0 it is not a one-parameter Lie group of transformation. In order to make it a one-parameter Lie group of transformation the following reparametrization must be used, $\varepsilon = \alpha - 1$:

$$
\begin{aligned}
x^* &= (1 + \varepsilon)x, \\
y^* &= (1 + \varepsilon)^2 y, -1 < \varepsilon < \infty,
\end{aligned}
$$

   with law of composition $\phi(\varepsilon, \delta) = \varepsilon + \delta + \varepsilon\delta$, and, identity element: $\varepsilon = 0$.

   This group represents a scaling of the variables in the x and y axes.

3.2.2 Infinitesimal transformations

Consider a one-parameter Lie group of transformations

$$
\boldsymbol{x}^* = \boldsymbol{X}(\boldsymbol{x}; \varepsilon),
\tag{3.22}
$$

with the identity $\varepsilon = 0$ and law of composition ϕ. Using Taylor series of (3.22) about $\varepsilon = 0$, one can write

$$
\begin{aligned}
\boldsymbol{x}^* &= \boldsymbol{x} + \varepsilon \left(\left. \frac{\partial \boldsymbol{X}(\boldsymbol{x}; \varepsilon)}{\partial \varepsilon} \right|_{\varepsilon=0} \right) + \frac{1}{2}\varepsilon^2 \left(\left. \frac{\partial^2 \boldsymbol{X}(\boldsymbol{x}; \varepsilon)}{\partial \varepsilon^2} \right|_{\varepsilon=0} \right) + \dots \\
&= \boldsymbol{x} + \varepsilon \left(\left. \frac{\partial \boldsymbol{X}(\boldsymbol{x}; \varepsilon)}{\partial \varepsilon} \right|_{\varepsilon=0} \right) + O(\varepsilon^2).
\end{aligned}
\tag{3.23}
$$

From this expansion, the following definition can be presented

Definition 3.2.2-1

*The **infinitesimal** of the one-parameter Lie group of transformation (3.22) is denoted by $\boldsymbol{\xi}(\boldsymbol{x})$ and defined as*

$$\boldsymbol{\xi}(\boldsymbol{x}) = \left.\frac{\partial \boldsymbol{X}(\boldsymbol{x};\varepsilon)}{\partial \varepsilon}\right|_{\varepsilon=0}. \tag{3.24}$$

Also, the transformation

$$\boldsymbol{x}^* = \boldsymbol{x} + \varepsilon\boldsymbol{\xi}(\boldsymbol{x}), \tag{3.25}$$

*is called **infinitesimal transformation** of the one-parameter Lie group of transformation (3.22).*

With these definitions, the First Fundamental Theorem of Lie can be presented

Theorem 3.2.2-1: First Fundamental Theorem of Lie

If a one-parameter Lie group of transformation can be parameterized so that its law of composition is $\phi(a,b) = a + b$, and its identity element is $\tau^{-1} = -\tau$, then the Lie group of transformations (3.22) is equivalent to the solution of an initial value problem for a system of first-order ODEs given by

$$\frac{d\boldsymbol{x}^*}{d\tau} = \boldsymbol{\xi}(\boldsymbol{x}^*), \tag{3.26}$$

with

$$\boldsymbol{x}^* = \mathbf{x}, \quad \text{when} \quad \tau = 0. \tag{3.27}$$

The new group parameter τ is defined as

$$\tau(\varepsilon) = \int_0^\varepsilon \Gamma(\varepsilon')d\varepsilon', \tag{3.28}$$

where Γ is a function of the law of composition

$$\Gamma(\varepsilon) = \left.\frac{\partial \phi(a,b)}{\partial b}\right|_{(a,b)=(\varepsilon^{-1},\varepsilon)}, \tag{3.29}$$

and

$$\Gamma(0) = 1. \tag{3.30}$$

The proof of the theorem can be seen in the book from Bluman and Anco [72].

From the First Fundamental Theorem of Lie, it is deduced that the essential information determining a one-parameter Lie group of transformation (3.22) is contained on its infinitesimal (3.24).

Examples of the First Fundamental Theorem of Lie

The following examples will illustrate the First Fundamental Theorem of Lie. The same groups of transformations, (3.20) and (3.21), will be used

1. Group of translations:

   The group of translations is given by

$$\begin{aligned} x^* &= x + \varepsilon, \\ y^* &= y, \end{aligned} \tag{3.31}$$

   with law of composition $\phi(a,b) = a + b$, and $\varepsilon^{-1} = -\varepsilon$. Then, $\partial\phi(a,b)/\partial b = 1$, and $\Gamma(\varepsilon) = 1$. Notice that no further parametrization is needed, since (3.28) will directly give $\tau = \varepsilon$.

Let $\boldsymbol{x} = (x, y)$. Then, the group (3.31) becomes $\boldsymbol{X}(\boldsymbol{x}; \varepsilon) = (x + \varepsilon, y)$ and the infinitesimal (3.24) is

$$\boldsymbol{\xi}(\boldsymbol{x}) = \left. \frac{\partial \boldsymbol{X}(\boldsymbol{x}; \varepsilon)}{\partial \varepsilon} \right|_{\varepsilon = 0} = (1, 0). \tag{3.32}$$

Given the following initial value problem (3.26):

$$\frac{dx^*}{d\varepsilon} = 1, \quad \frac{dy^*}{d\varepsilon} = 0, \\ \text{with} \quad x^* = x, \quad y^* = y, \quad \text{at} \quad \varepsilon = 0. \tag{3.33}$$

By the First Fundamental Theorem of Lie, the group of transformations (3.31) is the solution of the initial value problem (3.33).

2. Group of scalings:

The group of scalings is given by

$$x^* = (1 + \varepsilon)x, \\ y^* = (1 + \varepsilon)^2 y, \quad -1 < \varepsilon < \infty, \tag{3.34}$$

with law of composition: $\phi(a, b) = a + b + ab$, and, $\varepsilon^{-1} = -\varepsilon/(1 + \varepsilon)$. Then, $\partial\phi(a, b)/\partial b = 1 + a$. Hence,

$$\Gamma(\varepsilon) = \left. \frac{\partial \phi(a, b)}{\partial b} \right|_{(a,b) = (\varepsilon^{-1}, \varepsilon)} = 1 + \varepsilon^{-1} = \frac{1}{1 + \varepsilon}.$$

A new parametrization is needed so the law of composition is given by $\phi(a, b) = a + b$, and the identity element is $\tau = \tau^{-1}$. Using (3.28), it is obtained that

$$\tau = \int_0^\varepsilon \Gamma(\varepsilon') d\varepsilon' = \int_0^\varepsilon \frac{1}{1 + \varepsilon'} d\varepsilon' = \log(1 + \varepsilon) \rightarrow \varepsilon + 1 = e^\tau. \tag{3.35}$$

Then, the group of scalings (3.34) becomes

$$x^* = e^\tau x, \\ y^* = e^{2\tau} y, \quad -\infty < \tau < \infty, \tag{3.36}$$

with law of composition $\phi(a, b) = a + b$, and identity element $\tau = \tau^{-1}$.

Let $\boldsymbol{x} = (x, y)$. Then, the new group of scalings (3.36) becomes $\boldsymbol{X}(\boldsymbol{x}; \tau) = (e^\tau x, e^{2\tau} y)$, and the infinitesimal (3.24) is given by

$$\boldsymbol{\xi}(\boldsymbol{x}) = \left. \frac{\partial \boldsymbol{X}(\boldsymbol{x}; \tau)}{\partial \tau} \right|_{\tau = 0} = (x, 2y). \tag{3.37}$$

Then, by the First Fundamental Theorem of Lie (3.26), the group of scalings (3.36) is the solution of the following initial value problem

$$\frac{dx^*}{d\tau} = x^*, \quad \frac{dy^*}{d\tau} = 2y^*, \\ \text{with} \quad x^* = x, \quad y^* = y \quad \text{at} \quad \tau = 0. \tag{3.38}$$

One final definition is needed in the theory of the Lie groups of transformations.

Definition 3.2.2-2

The operator

$$X = X(\boldsymbol{x}) = \boldsymbol{\xi}(\boldsymbol{x}) \cdot \nabla = \sum_{i=1}^{n} \xi_i(\boldsymbol{x}) \frac{\partial}{\partial x_i}, \tag{3.39}$$

*is defined as the **infinitesimal generator** of the one-parameter Lie group of transformation (3.22).* ∇ *is the gradient operator.*

$$\nabla = \left(\frac{\partial}{\partial x_1}, \frac{\partial}{\partial x_2}, ..., \frac{\partial}{\partial x_n} \right). \tag{3.40}$$

The application of the infinitesimal generator for any differentiable function $F(\boldsymbol{x}) = F(x_1, x_2, ..., x_n)$ is

$$XF(\boldsymbol{x}) = \boldsymbol{\xi}(\boldsymbol{x}) \cdot \nabla F(\boldsymbol{x}) = \sum_{i=1}^{n} \xi_i(\boldsymbol{x}) \frac{\partial F(\boldsymbol{x})}{\partial x_i}. \tag{3.41}$$

Note that the application of the infinitesimal generator to $\boldsymbol{x}$ leads to $X\boldsymbol{x} = \boldsymbol{\xi}(\boldsymbol{x})$.

A one-parameter Lie group of transformation (3.22) can be written equivalently by using the infinitesimal generator (3.39). This is shown in the following theorem, which determines how to obtain the infinitesimal generator (3.39) from a given transformation group of the form (3.22).

Theorem 3.2.2-2

The one-parameter Lie group of transformations (3.22) is equivalent to

$$\boldsymbol{x}^* = e^{\varepsilon X}\boldsymbol{x} = \boldsymbol{x} + \varepsilon X\boldsymbol{x} + \frac{1}{2}\varepsilon^2 X^2 \boldsymbol{x} + ... = \left[1 + \varepsilon X + \frac{1}{2}\varepsilon^2 X^2 + ... \right] \boldsymbol{x} = \overbrace{\sum_{k=0}^{\infty} \frac{\varepsilon^k}{k!} X^k}^{e^{\varepsilon X}} \boldsymbol{x}, \tag{3.42}$$

where the operator $X = X(\boldsymbol{x})$ *is defined by (3.39) and the operator* $X^k = X^k(\boldsymbol{x})$ *is given by* $X^k = XX^{k-1}$, $k = 1, 2, ...$

A formal proof of the theorem can be found in the book Bluman and Anco [72]. Here, an example will be used to illustrate the previous theorem.

The scaling group (3.36) will be taken with $\tau \to \varepsilon$.

$$\begin{aligned} x^* &= e^{\varepsilon}x, \\ y^* &= e^{2\varepsilon}y, \quad -\infty < \varepsilon < \infty, \end{aligned} \tag{3.43}$$

with infinitesimal (3.24) given by $\boldsymbol{\xi}(\boldsymbol{x}) = (x, 2y)$. Therefore, the infinitesimal generator is given by equation (3.39) as

$$X = x\frac{\partial}{\partial x} + 2y\frac{\partial}{\partial y}. \tag{3.44}$$

One can easily calculate the terms X^2, X^3,..., X^n as

$$\begin{aligned} X^2 &= \left(x\frac{\partial}{\partial x} + x^2\frac{\partial^2}{\partial x^2} \right) + 4\left(y\frac{\partial}{\partial y} + y^2\frac{\partial^2}{\partial y^2} \right), \\ X^3 &= \left(x\frac{\partial}{\partial x} + 3x^2\frac{\partial^2}{\partial x^2} + x^3\frac{\partial^3}{\partial x^3} \right) + 8\left(y\frac{\partial}{\partial y} + 3y^2\frac{\partial^2}{\partial y^2} + y^3\frac{\partial^3}{\partial y^3} \right), \\ &\vdots \\ X^n &= \left(x\frac{\partial}{\partial x} + O\left(\frac{\partial^2}{\partial x^2}\right) \right) + 2^n\left(y\frac{\partial}{\partial y} + O\left(\frac{\partial^2}{\partial y^2}\right) \right). \end{aligned} \tag{3.45}$$

Using equation (3.42) from theorem 3.2.2-2, the one parameter Lie group of transformations (3.43) can be recovered from its infinitesimal generator (3.44):

$$x^* = e^{\varepsilon X} x = x + \varepsilon X x + \frac{1}{2}\varepsilon^2 X^2 x + ... + \frac{\varepsilon^n}{n!}X^n x + ...,$$
$$y^* = e^{\varepsilon X} y = y + \varepsilon X y + \frac{1}{2}\varepsilon^2 X^2 y + ... + \frac{\varepsilon^n}{n!}X^n y + ...$$

(3.46)

Introducing the values of the infinitesimal generators (3.44) and (3.45), it is obtained

$$x^* = x + \varepsilon x + \frac{1}{2}\varepsilon^2 x + ... + \frac{\varepsilon^n}{n!}x + ... = e^{\varepsilon}x$$
$$y^* = y + \varepsilon y + \frac{1}{2}\varepsilon^2 2y + ... + \frac{\varepsilon^n}{n!}2^n y + ... = e^{2\varepsilon}y,$$

(3.47)

which corresponds to the scaling transformation (3.43).

Therefore, only the infinitesimal (3.24) determines the coefficient of the $O(\varepsilon)$ term of the Taylor series expansion about $\varepsilon = 0$ of a Lie group of transformations (3.22).

3.2.3   Invariant functions and PDEs

Once all the definitions that will be used from the Lie symmetries theory have been presented, the next step is to understand how the method is used to obtain the Lie symmetries of a system of PDEs. These Lie symmetries will then be used to obtain invariants of the system of PDEs of the problem, i.e. the Navier-Stokes and the energy equation. Before defining an invariant system of PDEs, some basic concepts about invariant functions are needed.

Definition 3.2.3-1

*An infinitely differentiable function $F(\boldsymbol{x})$ is an **invariant function** of a Lie group of transformations (3.22), if and only if, for any group transformation (3.22),*

$$F(\boldsymbol{x}^*) = F(\boldsymbol{x}).$$

(3.48)

If $F(\boldsymbol{x})$ is an invariant function of (3.22), then $F(\boldsymbol{x})$ is called an invariant of (3.22) and $F(\boldsymbol{x})$ is said to be invariant under (3.22).

In theorem 3.2.2-2, it is presented an equivalent form of defining a Lie group of transformation (3.22) employing its infinitesimal generator (3.39). In the same manner, the definition of an invariant function (3.48) can be equivalently represented through the infinitesimal generator (3.39)

Theorem 3.2.3-1

$F(\boldsymbol{x})$ is invariant under a Lie group of transformations (3.22) if and only if,

$$XF(\boldsymbol{x}) = 0.$$

(3.49)

The proof of the theorem can be found in Bluman and Anco [72]. A simple example with the scaling group is given to illustrate the theorem:

The function

$$F(x, y) = \frac{x^2}{y},$$

(3.50)

is invariant under the scaling group of transformations (3.43). It can be proved using equation (3.48):

$$F(x^*, y^*) = F(x, y) \rightarrow \frac{x^{*2}}{y^*} = \frac{e^{-2\varepsilon}x^2}{e^{-2\varepsilon}y} = \frac{x^2}{y}. \tag{3.51}$$

Equivalently, equation (3.49) can be used to proof that (3.50) is invariant under (3.43):

$$XF(\boldsymbol{x}) = \left(x\frac{\partial}{\partial x} + 2y\frac{\partial}{\partial y} \right) \frac{x^2}{y} = 2\frac{x^2}{y} - 2\frac{x^2}{y} = 0. \tag{3.52}$$

Therefore (3.50) is an invariant of (3.43).

The concept of invariant function can be extended to a system of PDEs. Let $\boldsymbol{x} = (x_1, x_2, ..., x_n)$ be the n independent variables and $\boldsymbol{u} = (u^1, u^2, ..., u^m)$ the m dependent variables of the system of PDEs, which depend on the independent variables. Note that the superscript does not indicate a power function but the component of the set of $\boldsymbol{u}$. Then, the N equations of the system of PDEs can be represented as

$$F^\sigma = (\boldsymbol{x}, \boldsymbol{u}, \partial\boldsymbol{u}, \partial^2\boldsymbol{u}, ..., \partial^k\boldsymbol{u}), \quad \sigma = 1, 2, ..., N, \tag{3.53}$$

where k indicates the highest derivative that appears in the PDE and $\partial^l\boldsymbol{u}$ represent all possible derivatives of any u^i with respect to any combination of x_j. For example, for the first derivatives:

$$\partial\boldsymbol{u} = \left(\frac{\partial u^1}{\partial x_1}, \frac{\partial u^1}{\partial x_2}, ..., \frac{\partial u^1}{\partial x_n}, \frac{\partial u^2}{\partial x_1}, \frac{\partial u^2}{\partial x_2}, ..., \frac{\partial u^2}{\partial x_n}, ..., \frac{\partial u^m}{\partial x_1}, \frac{\partial u^m}{\partial x_2}, ..., \frac{\partial u^m}{\partial x_n} \right). \tag{3.54}$$

Also, the notation $u^\mu_{i_1 i_2 ... i_k}$ represents the k-th derivative of u^μ with respect to x_{i_1}, x_{i_2}, ..., and x_{i_k},

$$u^\mu_{i_1 i_2 ... i_k} = \frac{\partial^k u^\mu}{\partial x_{i_1} \partial x_{i_2} ... \partial x_{i_k}}, \tag{3.55}$$

$$\text{for} \quad \mu = 1, 2, ..., m, \quad i_j = 1, 2, ..., n, \quad j = 1, 2, ..., k.$$

If, the infinitesimal notation (3.25) is used to define a Lie group of transformations acting on the variable of the system of PDEs, it is obtained:

$$\boldsymbol{x}^* = X(\boldsymbol{x}, \boldsymbol{u}; \varepsilon) = \boldsymbol{x} + \varepsilon\boldsymbol{\xi}(\boldsymbol{x}, \boldsymbol{u}) + O(\varepsilon^2),$$
$$\boldsymbol{u}^* = U(\boldsymbol{x}, \boldsymbol{u}; \varepsilon) = \boldsymbol{u} + \varepsilon\boldsymbol{\eta}(\boldsymbol{x}, \boldsymbol{u}) + O(\varepsilon^2), \tag{3.56}$$

where $\boldsymbol{\xi}(\boldsymbol{x}, \boldsymbol{u})$ and $\boldsymbol{\eta}(\boldsymbol{x}, \boldsymbol{u})$ are the infinitesimals of the independent and dependent variables, respectively, and they are defined as in (3.24). The infinitesimal generator is

$$X = \xi_i(\boldsymbol{x}, \boldsymbol{u})\frac{\partial}{\partial x_i} + \eta_j(\boldsymbol{x}, \boldsymbol{u})\frac{\partial}{\partial u_j}. \tag{3.57}$$

In the search of Lie symmetries, the derivatives of the dependent variables that appear in the differential equation are considered as extra dependent variables. Therefore, their transformation has to be taken into account, and they can be calculated by applying the chain rule

$$(u^\mu_i)^* = U^\mu_i(\boldsymbol{x}, \boldsymbol{u}, \partial\boldsymbol{u}; \varepsilon) =$$
$$u^\mu_i + \varepsilon\eta^{(1)\mu}_i(\boldsymbol{x}, \boldsymbol{u}, \partial\boldsymbol{u}) + O(\varepsilon^2),$$
$$\vdots \tag{3.58}$$
$$(u^\mu_{i_1 i_2 ... i_k})^* = U^\mu_{i_1 i_2 ... i_k}(\boldsymbol{x}, \boldsymbol{u}, \partial\boldsymbol{u}, ..., \partial^k\boldsymbol{u}; \varepsilon) =$$
$$u^\mu_{i_1 i_2 ... i_k} + \varepsilon\eta^{(k)\mu}_{i_1 i_2 ... i_k}(\boldsymbol{x}, \boldsymbol{u}, \partial\boldsymbol{u}, ..., \partial^k\boldsymbol{u}) + O(\varepsilon^2).$$

These transformations of the derivatives of the dependent variables are called extended transformations. The functions $\eta_i^{(1)\mu}$, ..., $\eta_{i_1 i_2 ... i_k}^{(k)\mu}$ are called the k-th extended infinitesimals, where the number in the parenthesis of the superscript indicates the order of the derivative. The extended infinitesimals can be calculated as

$$\begin{aligned}
\eta_i^{(1)\mu} &= D_i \eta^\mu - (D_i \xi_j) u_j^\mu, \\
\eta_{i_1 i_2 ... i_k}^{(k)\mu} &= D_{i_k} \eta_{i_1 i_2 ... i_{k-1}}^{(k-1)\mu} - (D_{i_k} \xi_j) u_{i_1 i_2 ... i_{k-1} j}^\mu,
\end{aligned} \tag{3.59}$$

for $i_j = 1, 2,..., n$, and $j = 1, 2,..., k$, with $k \geq 2$. The definition of the extended infinitesimals is developed in the book of Bluman and Anco [72] in several theorems. The operator D_i, in (3.59), is the total derivative operator, defined as

$$D_i = \frac{\partial}{\partial x_i} + u_i^\mu \frac{\partial}{\partial u^\mu} + u_{ij}^\mu \frac{\partial}{\partial u_j^\mu} + ... + u_{i i_1 i_2 ... i_k}^\mu \frac{\partial}{\partial u_{i_1 i_2 ... i_k}^\mu} + ... \tag{3.60}$$

Then, definition 3.2.3-1 can be extended to a system of PDEs as

Definition 3.2.3-2

The one-parameter Lie group of point transformations

$$\begin{aligned}
\boldsymbol{x}^* &= X(\boldsymbol{x}, \boldsymbol{u}; \varepsilon), \\
\boldsymbol{u}^* &= U(\boldsymbol{x}, \boldsymbol{u}; \varepsilon),
\end{aligned} \tag{3.61}$$

leaves invariant the system of PDEs (3.53), i.e. is a point symmetry admitted by (3.53), if and only if its $k-$th extension, defined by (3.58), leaves invariant the N surfaces in $(\boldsymbol{x}, \boldsymbol{u}, \partial \boldsymbol{u}, \partial^2 \boldsymbol{u}, ..., \partial^k \boldsymbol{u})$-space, defined by (3.53).

The corresponding k-th extended infinitesimal generator of the Lie group of transformations, composed by (3.56) and (3.58), is defined as

$$\begin{aligned}
X^{(k)} =& \xi_i(\boldsymbol{x}, \boldsymbol{u}) \frac{\partial}{\partial x_i} + \eta^\mu(\boldsymbol{x}, \boldsymbol{u}) \frac{\partial}{\partial u^\mu} + \eta_i^{(1)\mu}(\boldsymbol{x}, \boldsymbol{u}, \partial \boldsymbol{u}) \frac{\partial}{\partial u_i^\mu} + ... \\
&+ \eta_{i_1 i_2 ... i_k}^{(k)\mu}(\boldsymbol{x}, \boldsymbol{u}, \partial \boldsymbol{u}, ..., \partial^k \boldsymbol{u}) \frac{\partial}{\partial u_{i_1 i_2 ... i_k}^\mu}
\end{aligned} \tag{3.62}$$

Again, the development of the definition of equation (3.62) comes in more detail in the book of Bluman and Anco [72]. While theorem 3.2.3-1 was formulated for a function, an equivalent theorem can be now formulated for a system of PDEs

Theorem 3.2.3-2

The one-parameter Lie group of point transformations (3.61), with infinitesimal generator (3.57) and extended infinitesimal generator (3.62), is admitted by the system of PDEs (3.53) if and only if

$$X^{(k)} F^\sigma(\boldsymbol{x}, \boldsymbol{u}, \partial \boldsymbol{u}, \partial^2 \boldsymbol{u}, ..., \partial^k \boldsymbol{u}) = 0, \tag{3.63}$$

when $\boldsymbol{u}$ satisfies (3.53), for each $\sigma = 1, 2,...,N$.

The proof of the theorem is given in Bluman and Anco [72]. In other words, the last theorem states that a system of PDEs (3.53) is invariant under a Lie group of transformation (3.61) if $X^{(k)} F^\sigma = 0$.

3.2.4 Lie algorithm

The advantage of using infinitesimal transformations is that Lie symmetries can be obtained by following a few steps that conform what is known as the Lie algorithm. To explain the algorithm, an illustrative example will be used. Instead of a system of PDEs, a single PDE ($N = 1$) will be used: the heat equation, which reads

$$F(t, x, u, u_t, u_x, u_{tt}, u_{tx}, u_{xx}) = u_t - u_{xx} = 0. \tag{3.64}$$

For the heat equation (3.64), the number of independent variable is $n = 2$: t and x; and the number of dependent variables $m = 1$: u. Since the second derivative is the higher order of a derivative that appears in the PDE, $k = 2$. Now, the first step of the Lie algorithm can be applied

Step 1

Apply the extended infinitesimal generator (3.62) to the PDE (3.64) as stated in theorem 3.2.3-2 (3.63).

For this, the extended infinitesimal generator, $X^{(2)}$, needs to be calculated. Using equation (3.62), it is obtained that

$$
\begin{aligned}
X^{(2)} =& \xi^t(t, x, u)\frac{\partial}{\partial t} + \xi^x(t, x, u)\frac{\partial}{\partial x} + \eta^u(t, x, u)\frac{\partial}{\partial u} + \\
&+ \eta_t^{(1)u}(t, x, u, u_t, u_x)\frac{\partial}{\partial u_t} + \eta_x^{(1)u}(t, x, u, u_t, u_x)\frac{\partial}{\partial u_x} + \\
&+ \eta_{tt}^{(2)u}(t, x, u, u_t, u_x, u_{tt}, u_{tx}, u_{tt})\frac{\partial}{\partial u_{tt}} + \\
&+ \eta_{tx}^{(2)u}(t, x, u, u_t, u_x, u_{tt}, u_{tx}, u_{tt})\frac{\partial}{\partial u_{tx}} + \\
&+ \eta_{xx}^{(2)u}(t, x, u, u_t, u_x, u_{tt}, u_{tx}, u_{tt})\frac{\partial}{\partial u_{xx}}
\end{aligned}
\tag{3.65}
$$

Now, equation (3.63) from theorem 3.2.3-2 can be applied, obtaining:

$$
\begin{aligned}
&X^{(2)}\, F(t, x, u, u_t, u_x, u_{tt}, u_{tx}, u_{xx})|_{F=0} = 0 \\
&X^{(2)}\, [u_t - u_{xx}]|_{u_t = u_{xx}} = 0 \\
&\eta_t^{(1)u}(t, x, u, u_t, u_x) - \eta_{xx}^{(2)u}(t, x, u, u_t, u_x, u_{tt}, u_{tx}, u_{tt})\Big|_{u_t = u_{xx}} = 0
\end{aligned}
\tag{3.66}
$$

Note that the condition $F = 0 \rightarrow u_t = u_{xx}$ comes from the fact that $\boldsymbol{u}$ must satisfy the PDE (3.64).

Step 2

Derive the necessary extended infinitesimals, given by equations (3.59), using the total derivative, D_i, defined in (3.60).

From equation (3.66), the extended infinitesimals that need to be calculated are $\eta_t^{(1)u}(t, x, u, u_t, u_x)$ and $\eta_{xx}^{(2)u}(t, x, u, u_t, u_x, u_{tt}, u_{tx}, u_{tt})$. For the last, the infinitesimal, $\eta_t^{(1)u}(t, x, u, u_t, u_x)$ must be calculated previously. For the sake of readability, the dependencies of the infinitesimals will be omitted. Using equations (3.59) and (3.60), it is obtained

$$
\begin{aligned}
\eta_t^{(1)u} =& D_t\eta^u - (D_t\xi^t)\, u_t - (D_t\xi^x)\, u_x = \\
=& \frac{\partial \eta^u}{\partial t} + u_t\frac{\partial \eta^u}{\partial u} - u_t\frac{\partial \xi^t}{\partial t} - u_t u_t\frac{\partial \xi^t}{\partial u} - u_x\frac{\partial \xi^x}{\partial t} - u_t u_x\frac{\partial \xi^x}{\partial u} = \\
=& \eta_t^u + u_t\eta_u^u - u_t\xi_t^t - u_t u_t\xi_u^t - u_x\xi_t^x - u_t u_x\xi_u^x,
\end{aligned}
\tag{3.67a}
$$

$$\eta_x^{(1)u} = D_x \eta^u - \left(D_x \xi^t\right) u_t - \left(D_x \xi^x\right) u_x =$$
$$= \frac{\partial \eta^u}{\partial x} + u_x \frac{\partial \eta^u}{\partial u} - u_t \frac{\partial \xi^t}{\partial x} - u_t u_x \frac{\partial \xi^t}{\partial u} - u_x \frac{\partial \xi^x}{\partial x} - u_x u_x \frac{\partial \xi^x}{\partial u} = \qquad (3.67\text{b})$$
$$= \eta_x^u + u_x \eta_u^u - u_t \xi_x^t - u_t u_x \xi_u^t - u_x \xi_x^x - u_x u_x \xi_u^x,$$

$$\eta_{xx}^{(2)u} = \overbrace{D_x \eta_x^{(1)u}}^{(a)} - \overbrace{\left(D_x \xi^t\right) u_{tx}}^{(b)} - \overbrace{\left(D_x \xi^x\right) u_{xx}}^{(c)} =$$

$$= \overbrace{\frac{\partial \eta_x^{(1)u}}{\partial x} + u_x \frac{\partial \eta_x^{(1)u}}{\partial u} + u_{tx} \frac{\partial \eta_x^{(1)u}}{\partial u_t} + u_{xx} \frac{\partial \eta_x^{(1)u}}{\partial u_x}}^{(a)}$$

$$- \overbrace{u_{tx} \frac{\partial \xi^t}{\partial x} - u_{tx} u_x \frac{\partial \xi^t}{\partial u}}^{(b)} - \overbrace{u_{xx} \frac{\partial \xi^x}{\partial x} - u_{xx} u_x \frac{\partial \xi^x}{\partial u}}^{(c)} = \qquad (3.67\text{c})$$

$$= \overbrace{\underbrace{\frac{\partial \eta_x^{(1)u}}{\partial x}}_{(a1)} + \underbrace{u_x \frac{\partial \eta_x^{(1)u}}{\partial u}}_{(a2)} + \underbrace{u_{tx} \frac{\partial \eta_x^{(1)u}}{\partial u_t}}_{(a3)} + \underbrace{u_{xx} \frac{\partial \eta_x^{(1)u}}{\partial u_x}}_{(a4)}}^{(a)}$$

$$- \overbrace{u_{tx} \frac{\partial \xi^t}{\partial x} - u_{tx} u_x \frac{\partial \xi^t}{\partial u}}^{(b)} - \overbrace{u_{xx} \frac{\partial \xi^x}{\partial x} - u_{xx} u_x \frac{\partial \xi^x}{\partial u}}^{(c)} =$$
$$= a1 + a2 + a3 + a4 - u_{tx} \xi_x^t - u_{tx} u_x \xi_u^t - u_{xx} \xi_x^x - u_{xx} u_x \xi_u^x,$$

where:

$$a1 = \quad \eta_{xx}^u + u_{xx} \eta_u^u + u_x \eta_{xu}^u - u_{tx} \xi_x^t - u_t \xi_{xx}^t - u_{tx} u_x \xi_u^t - u_t u_{xx} \xi_u^t - u_t u_x \xi_{xu}^t$$
$$- u_{xx} \xi_x^x - u_x \xi_{xx}^x - 2 u_{xx} u_x \xi_u^x - u_x^2 \xi_{xu}^x, \qquad (3.68\text{a})$$
$$a2 = \quad u_x \eta_{xu}^u + u_x u_{xu} \eta_u^u + u_x^2 \eta_{uu}^u - u_x u_{tu} \xi_x^t - u_x u_t \xi_{xu}^t - u_{tu} u_x^2 \xi_u^t - u_x u_t u_{xu} \xi_u^t$$
$$- u_t u_x^2 \xi_{uu}^t - u_x u_{xu} \xi_x^x - u_x^2 \xi_{xu}^x - 2 u_{xu} u_x^2 \xi_u^x - u_x^3 \xi_{uu}^x, \qquad (3.68\text{b})$$
$$a3 = \quad -u_{tx} \xi_x^t - u_{tx} u_x \xi_u^t, \qquad (3.68\text{c})$$
$$a4 = \quad u_{xx} \eta_u^u - u_{xx} u_t \xi_u^t - u_{xx} \xi_x^x - 2 u_{xx} u_x \xi_u^x. \qquad (3.68\text{d})$$

Step 3

Insert the extended infinitesimals in the result obtained on step 1 (3.66) and group the infinitesimals by the dependent variables and their derivatives. The condition $F = 0$ should be introduced in this step.

This results in:

$$\eta_t^u + u_t \eta_u^u - u_t \xi_t^t - u_t u_t \xi_u^t - u_x \xi_t^x - u_t u_x \xi_u^x -$$
$$(a1 + a2 + a3 + a4 - u_{tx} \xi_x^t - u_{tx} u_x \xi_u^t - u_{xx} \xi_x^x - u_{xx} u_x \xi_u^x)|_{u_t = u_{xx}} = 0. \qquad (3.69)$$

Grouping the infinitesimals that are multiplied by the same dependent variable and/or their deriva-

tives:

$$(\eta_t^u - \eta_{xx}^u) + (\xi_{xx}^x - 2\eta_{xu}^u - \xi_t^x)u_x + (\eta_u^u - \xi_t^t + \xi_{xx}^t)u_t + (2\xi_{xu}^x - \eta_{uu}^u)u_x^2 + (2\xi_{xu}^t - \xi_u^x)u_t u_x +$$
$$+ (\xi_{uu}^x)u_x^3 + (\xi_{uu}^t)u_t u_x^2 + (-\xi_u^t)u_t^2 + (2\xi_x^x - \eta_u^u)\underbrace{u_{xx}}_{=u_t} + (2\xi_x^t)u_{tx} + (3\xi_u^x)\underbrace{u_{xx}}_{=u_t}u_x + (2\xi_u^t)u_{tx}u_x +$$

$$+ (2\xi_u^t)u_t \left.\underbrace{u_{xx}}_{=u_t}\right|_{u_t = u_{xx}} = 0. \tag{3.70}$$

Finally, the condition $F = 0 \rightarrow u_t = u_{xx}$ is introduced:

$$(\eta_t^u - \eta_{xx}^u) + (\xi_{xx}^x - 2\eta_{xu}^u - \xi_t^x)u_x + (2\xi_x^x - \xi_t^t + \xi_{xx}^t)u_t + (2\xi_{xu}^x - \eta_{uu}^u)u_x^2 +$$
$$+ (2\xi_u^x + 2\xi_{xu}^t)u_t u_x + (\xi_{uu}^x)u_x^3 + (\xi_{uu}^t)u_t u_x^2 + (\xi_u^t)u_t^2 + (2\xi_x^t)u_{tx} +$$
$$+ (2\xi_u^t)u_{tx}u_x = 0. \tag{3.71}$$

The resulting equations are composed of infinitesimals, that depend on t, x, and u, multiplied by derivatives of u. Since each derivative of u is independent and arbitrary, each of the bracket terms must be 0 to satisfy the equation. This leads to the next step.

Step 4

Solve the system of differential equations obtained from matching each bracket to 0.

The resulting system of differential equations is

$$0 = \eta_t^u - \eta_{xx}^u, \tag{3.72a}$$
$$0 = \xi_{xx}^x - 2\eta_{xu}^u - \xi_t^x, \tag{3.72b}$$
$$0 = 2\xi_x^x - \xi_t^t + \xi_{xx}^t, \tag{3.72c}$$
$$0 = 2\xi_{xu}^x - \eta_{uu}^u, \tag{3.72d}$$
$$0 = \xi_u^x + \xi_{xu}^t, \tag{3.72e}$$
$$0 = \xi_u^t, \tag{3.72f}$$
$$0 = \xi_{uu}^x, \tag{3.72g}$$
$$0 = \xi_{uu}^t, \tag{3.72h}$$
$$0 = \xi_x^t, \tag{3.72i}$$
$$0 = \xi_u^t. \tag{3.72j}$$

It should be noted that some equations are a direct result of others, for example, equation (3.72h) ($\xi_{uu}^t = 0$) is a direct result of equation (3.72j) ($\xi_u^t = 0$). Also, some terms are 0 as a result of other equations, for example, from equations (3.72i) ($\xi_x^t = 0$) and (3.72j) ($\xi_u^t = 0$), one can neglect the last term in equation (3.72e), $\xi_{xu}^t = 0$ and, therefore, (3.72e) results in $\xi_u^x = 0$. After applying all simplifications the system of differential equations is reduced to:

$$0 = \eta_t^u - \eta_{xx}^u, \tag{3.73a}$$
$$0 = \xi_{xx}^x - 2\eta_{xu}^u - \xi_t^x, \tag{3.73b}$$
$$0 = 2\xi_x^x - \xi_t^t, \tag{3.73c}$$
$$0 = \eta_{uu}^u, \tag{3.73d}$$
$$0 = \xi_u^x, \tag{3.73e}$$
$$0 = \xi_x^t, \tag{3.73f}$$
$$0 = \xi_u^t. \tag{3.73g}$$

Using equations (3.73d)-(3.73g), the functions have the following form:

$$\xi^t = \xi^t(t), \tag{3.74a}$$

$$\xi^x = \xi^x(t, x), \tag{3.74b}$$

$$\eta^u = u\tilde{g}(t, x) + \hat{g}(t, x). \tag{3.74c}$$

Since ξ^t does not depend on the space, equation (3.73c) can be integrated with respect to x:

$$0 = \int 2\xi^x_x dx - \int \xi^t_t dx,$$

$$\xi^x(t, x) = \frac{1}{2}\xi^t_t(t)x + g(t). \tag{3.75}$$

Equations (3.74c) and (3.75) can now be introduced into equation (3.73b)

$$0 = \frac{\partial}{\partial x}\left(\frac{\partial}{\partial x}\left(\frac{1}{2}\xi^t_t(t)x + g(t)\right)\right) - 2\frac{\partial}{\partial x}\left(\frac{\partial}{\partial u}\left(u\tilde{g}(t, x) + \hat{g}(t, x)\right)\right)$$
$$- \frac{\partial}{\partial t}\left(\frac{1}{2}\xi^t_t(t)x + g(t)\right). \tag{3.76}$$

The first term can be neglected, since it is linear in x. Operating and integrating now with respect to x:

$$0 = \int\left(-2\frac{\partial}{\partial x}\left(\tilde{g}(t, x)\right) - \frac{1}{2}\xi^t_{tt}(t)x - g_t(t)\right)dx,$$

$$0 = -2\tilde{g}(t, x) - \frac{1}{4}\xi^t_{tt}(t)x^2 - g_t(t)x + \check{g}(t),$$

$$\tilde{g}(t, x) = -\frac{1}{8}\xi^t_{tt}(t)x^2 - \frac{1}{2}g_t(t)x + \frac{1}{2}\check{g}(t). \tag{3.77}$$

Finally, equation (3.74c) can be introduced into equation (3.73a):

$$0 = \eta^u_t(t, x, u) - \eta^u_{xx}(t, x, u),$$

$$0 = \underbrace{(\tilde{g}_t(t, x) - \tilde{g}_{xx}(t, x))}_{(a)} u + \underbrace{(\hat{g}_t(t, x) - \hat{g}_{xx}(t, x))}_{(b)}. \tag{3.78}$$

Each bracket must be 0 for any value of u. Therefore, introducing (3.77) into the bracket (a) results in:

$$0 = \underbrace{\left(-\frac{1}{8}\xi^t_{ttt}(t)\right)}_{(a1)} x^2 + \underbrace{\left(-\frac{1}{2}g_{tt}(t)\right)}_{(a2)} x + \underbrace{\left(\frac{1}{2}\check{g}_t(t) + \frac{1}{4}\xi^t_{tt}(t)\right)}_{(a3)}. \tag{3.79}$$

The functions inside the brackets only depend on t. Therefore, all brackets must be 0 for any arbitrary value of x. Integrating:

$$a1 \rightarrow \xi^t(t) = \frac{1}{2}t^2\tilde{a}_6 + t\tilde{a}_3 + \tilde{a}_2, \tag{3.80a}$$

$$a2 \rightarrow g(t) = t\tilde{a}_5 + \tilde{a}_1, \tag{3.80b}$$

$$a3 \rightarrow \check{g}(t) = -\frac{1}{2}t\tilde{a}_6 + \tilde{a}_4. \tag{3.80c}$$

Finally, using (3.75), (3.77) and (3.80a)-(3.80c), the infinitesimals have the following form:

$$\xi^t(t) = \frac{1}{2}t^2\tilde{a}_6 + t\tilde{a}_3 + \tilde{a}_2, \tag{3.81a}$$

$$\xi^x(t, x) = \frac{1}{2}xt\tilde{a}_6 + \frac{1}{2}x\tilde{a}_3 + t\tilde{a}_5 + \tilde{a}_1, \tag{3.81b}$$

$$\eta^u(t, x, u) = -\frac{1}{8}x^2u\tilde{a}_6 - \frac{1}{4}tu\tilde{a}_6 - \frac{1}{2}xu\tilde{a}_5 + \frac{1}{2}u\tilde{a}_4 + \hat{g}(t, x). \tag{3.81c}$$

The six parameters and the unknown function $\hat{g}(t,x)$ will form seven symmetries. It is worth mentioning now that the unknown function $\hat{g}(t,x)$ appears due to the linearity of the differential equation. Its meaning in the Lie symmetries will be explained in the next step.

Step 5

Formulate the multi-parametric infinitesimal generator of all symmetries and divide them into one-parametric Lie-point symmetries.

The infinitesimal generator (3.57) can be expressed as:

$$X = \left(t^2 a_6 + 2ta_3 + a_2\right)\frac{\partial}{\partial t} + \left(txa_6 + xa_3 + ta_5 + a_1\right)\frac{\partial}{\partial x}$$
$$+ \left(-\frac{1}{4}x^2 u a_6 - \frac{1}{2}tua_6 - \frac{1}{2}xua_5 + ua_4 + f(t,x)\right)\frac{\partial}{\partial u}, \tag{3.82}$$

with $f_t - f_{xx} = 0$ and the new coefficients are defined as: $a_1 = \tilde{a}_1$, $a_2 = \tilde{a}_2$, $a_3 = \frac{1}{2}\tilde{a}_3$, $a_4 = \frac{1}{2}\tilde{a}_4$, $a_5 = \tilde{a}_5$, $a_6 = \frac{1}{2}\tilde{a}_6$ and $f(t,x) = \hat{g}(t,x)$.

Now the seven one-parametric Lie-point symmetries can be obtained by setting one parameter equal to 1 and the rest equal to 0, obtaining:

$$X_1 = \frac{\partial}{\partial t}, \tag{3.83a}$$

$$X_2 = \frac{\partial}{\partial x}, \tag{3.83b}$$

$$X_3 = 2t\frac{\partial}{\partial t} + x\frac{\partial}{\partial x}, \tag{3.83c}$$

$$X_4 = u\frac{\partial}{\partial u}, \tag{3.83d}$$

$$X_5 = t\frac{\partial}{\partial x} - \frac{1}{2}xu\frac{\partial}{\partial u}, \tag{3.83e}$$

$$X_6 = t^2\frac{\partial}{\partial t} + tx\frac{\partial}{\partial x} + \left(-\frac{1}{4}x^2 u - \frac{1}{2}tu\right)\frac{\partial}{\partial u}, \tag{3.83f}$$

$$X_7 = f(t,x)\frac{\partial}{\partial u}, \quad \text{with} \quad f_t - f_{xx} = 0. \tag{3.83g}$$

The two basic symmetries that have been used in several examples so far appear in the heat equation, i.e. translation in time, X_1 (3.83a), and space, X_2 (3.83b), and scaling of time and space, X_3 (3.83c), and of the dependent variable, X_4 (3.83d). A complex physical meaning states for symmetries X_5 (3.83e) and X_6 (3.83f). Finally, symmetry X_7 (3.83g) has its roots in the linearity of the heat equation. This type of symmetry always occurs in linear differential equations. Its meaning is that, if the dependent variable is transformed by a function $f(t,x)$, which is a solution of the heat equation, the transformed heat equation will be equivalent to the original one. This, of course, is true for linear equations, since the summation of two solutions, will also be a solution, due to the linearity.

3.2.5 Invariant Solutions

Once the one-parameter Lie symmetries have been obtained, the last step is to obtain invariant solutions of the system of PDEs, using the symmetries obtained. In the field of fluid dynamics, these invariant solutions are the so-called scaling laws.

A definition of invariant solutions should be introduced

Definition 3.2.5-1

The function $\boldsymbol{u} = \boldsymbol{\Theta}(\boldsymbol{x})$, with components $u^\mu = \Theta^\mu(\boldsymbol{x})$, $\mu = 1, 2,...,m$, is an invariant of the system of PDEs (3.53) *resulting from an admitted point symmetry with infinitesimal generator* (3.57) *if and only if*

1. $u^\mu = \Theta^\mu(\boldsymbol{x})$ *is an invariant surface of* (3.57) *for each $\mu = 1, 2,..., m$.*

2. $\Theta^\mu(\boldsymbol{x})$ *solves* (3.53).

Now, the following theorem can be applied.

Theorem 3.2.5-1

The function $\boldsymbol{u} = \boldsymbol{\Theta}(\boldsymbol{x})$ is an invariant solution of (3.53) *if and only if $\boldsymbol{u} = \boldsymbol{\Theta}(\boldsymbol{x})$ satisfies*

1. $X(u^\mu - \Theta^\mu(\boldsymbol{x})) = 0$*, when $\boldsymbol{u} = \boldsymbol{\Theta}(\boldsymbol{x})$, $\mu = 1, 2,...,m$. Developing the infinitesimal generator:*

$$\xi_i(\boldsymbol{x}, \boldsymbol{\Theta}(\boldsymbol{x}))\frac{\partial\Theta^\mu(\boldsymbol{x})}{\partial\xi_i} = \eta^\mu(\boldsymbol{x}, \boldsymbol{\Theta}(\boldsymbol{x})), \quad \mu = 1, 2, ..., m. \tag{3.84}$$

2. $F^\sigma(\boldsymbol{x}, \boldsymbol{u}, \partial\boldsymbol{u}, \partial^2\boldsymbol{u}, ..., \partial^k\boldsymbol{u}) = 0$*, when $\boldsymbol{u} = \boldsymbol{\Theta}(\boldsymbol{x})$, $\sigma = 1, 2,...,N$, namely*

$$F^\sigma(\boldsymbol{x}, \boldsymbol{\Theta}(\boldsymbol{x}), \partial\boldsymbol{\Theta}(\boldsymbol{x}), \partial^2\boldsymbol{\Theta}(\boldsymbol{x}), ..., \partial^k\boldsymbol{\Theta}(\boldsymbol{x})) = 0, \quad \sigma = 1, 2, ..., N. \tag{3.85}$$

Equations (3.84) are the invariant surface conditions for the invariant solutions of the system of PDEs (3.53) that is invariant under the point symmetries (3.57). Equation (3.85) means that the invariant solution must be a solution of the system of PDEs (3.53).

Different methods can be used to determine the invariant solutions. Here the **invariant form method** will be explained and used. This method consists of solving the invariant surface condition (3.84) by explicitly solving the characteristic equation given by

$$\frac{\partial x_1}{\xi_1(\mathbf{x}, \mathbf{u})} = \frac{\partial x_2}{\xi_2(\mathbf{x}, \mathbf{u})} = ... = \frac{\partial x_n}{\xi_n(\mathbf{x}, \mathbf{u})} = \frac{\partial u^1}{\eta^1(\mathbf{x}, \mathbf{u})} = \frac{\partial u^2}{\eta^2(\mathbf{x}, \mathbf{u})} = ... = \frac{\partial u^m}{\eta^m(\mathbf{x}, \mathbf{u})}. \tag{3.86}$$

When solving the characteristic system, one can obtain $n-1$ invariants resulting from the relation of the independent variables and m invariants resulting from the dependent variables. These invariants are called $y_1, y_2, ..., y_{n-1}$ for the independent variables and $\nu_1, \nu_2, ..., \nu_m$ for the dependent variables. Then, the general solution $\boldsymbol{u} = \boldsymbol{\Theta}(\boldsymbol{x})$ of the system of PDEs (3.53) can be obtained from the invariant form

$$\nu_\mu(\boldsymbol{x}, \boldsymbol{u}) = \Phi^\mu(y_1(\boldsymbol{x}, \boldsymbol{u}), y_2(\boldsymbol{x}, \boldsymbol{u}), ..., y_{n-1}(\boldsymbol{x}, \boldsymbol{u})) \tag{3.87}$$

Finally, the invariants $\nu_\mu(\boldsymbol{x}, \boldsymbol{u})$ should be introduced in the system of PDEs (3.53) to check if the second condition of theorem 3.2.5-1 (3.85) is fulfilled.

To illustrate how invariant solutions are obtained through the invariant form method, the continuation of the example of the heat equation will be used.

The first four symmetries, X_1 to X_4 (3.83a)-(3.83d), provide rather trivial solutions of the heat equation, such that u can be constant in time and space, or linear in space. The sixth symmetry, X_6 (3.83f), will be used, since it leads to a more interesting result that illustrates better the way in which invariant solutions are obtained. Using X_6 (3.83f), the invariant surface condition (3.84) has the following form:

$$t^2 u_t + txu_x = -\left(\frac{1}{4}x^2 + \frac{1}{2}t\right)u. \tag{3.88}$$

The corresponding characteristic equations (3.86) are given by

$$\frac{dt}{t^2} = \frac{dx}{tx} = \frac{du}{-\left(\frac{1}{4}x^2 + \frac{1}{2}t\right)u}. \tag{3.89}$$

Now, $n-1$ invariants can be obtained from the relations of the independent variables. For the heat equation, one invariant, y_1 is obtained:

$$y_1(t, x, u) = \frac{x}{t}. \tag{3.90}$$

One invariant is also obtained from the relation of the dependent variable and one independent var

$$\nu_1(t, x, u) = \sqrt{t}e^{\frac{x^2}{4t}}u. \tag{3.91}$$

Therefore, using equation (3.87), it is obtained the invariant form of the solution of the invariant surface condition (3.84):

$$\nu_1(t, x, u) = \Phi(y_1(t, x, u)) = \sqrt{t}e^{\frac{x^2}{4t}}u. \tag{3.92}$$

Then, u can be solved from the previous equation, obtaining

$$u = \Theta(t, x) = \frac{1}{\sqrt{t}}e^{\frac{-x^2}{4t}}\Phi(y_1(t, x, u)). \tag{3.93}$$

This result can now be introduce into the heat equation. After simplifications, the following ODE is obtained:

$$\Phi''(y_1(t, x, u)) = 0. \tag{3.94}$$

The solution of the ODE is trivial. Substituting the value of the function $\Phi(y_1(t, x, u))$, it is obtained a final solution of the heat equation

$$u = \Theta(t, x) = \frac{1}{\sqrt{t}}\left(C_1 + C_2\frac{x}{t}\right)e^{\frac{-x^2}{4t}}. \tag{3.95}$$

Introducing this result into the heat equation, where C_1 and C_2 are constants of integration that depend on the boundary conditions, one can corroborate that (3.95) is effectively a solution of the heat equation.

3.3 Conclusions

In the first section of this chapter, the governing equations that describe turbulent flows are presented, including the MPC equations. In the second section, the theory relevant to the Lie symmetries method has been introduced. Lie symmetries are a powerful method for calculating invariant solutions of a system of PDEs, i.e. scaling laws that define universal behaviours of the variables. In section §5.1.5 the theory is applied to the governing equations of turbulence, i.e. the Navier-Stokes, energy, and MPC equations. The key to obtaining scaling laws of the velocity and thermal field comes from the Lie symmetries that result from the MPC equations, which describe turbulent statistics of second order.

Chapter 4

Methodology

In the present work, several DNS of a turbulent channel are presented. As has been already stated, the main focus of the study is to analyze heat transfer in these turbulent channels. Specifically, heat transfer of a passive scalar. The boundary condition for the flow is a pressure gradient (Poiseuille flow), while for the temperature, the MBC is applied. Configuration of the DNS under these conditions are presented in section §4.1. Also, a specific subsection, §4.1.2, is dedicated to present the configuration used in a DNS of an isothermal Poiseuille flow for the highest friction Reynolds number ever simulated in a DNS, $Re_\tau = 10000$. In addition, in section §4.2, the case of heat transfer under the MBC in a Couette flow is presented. Finally, the configuration of the simulations of stratified flows is shown in section §4.3, where a scalar difference is imposed between both walls of the channel as the thermal boundary condition. For all cases, the flow is considered incompressible.

The Navier-Stokes, (1.5) and (1.6), and the energy, (1.7), equations are used to simulate the flow. The code employed to run the simulations is the LISO code, already validated in several different turbulent flows, [38, 52, 54, 56, 73, 74]. A detailed description of the code can be found in Appendix §7.1.

4.1 Configuration of the Poiseuille flow simulations

4.1.1 Configuration of heat transfer simulations

For Poiseuille flows with heat transfer, a schematic representation of the lower half of the computational box can be seen in figure 4.1, where contours of the velocity are shown for the case of $Re_\tau = 5000$ and $Pr = 0.71$, and the flow moves from left to right. Periodic conditions are imposed in the streamwise and spanwise boundaries. Four different Reynolds numbers are used, namely $Re_\tau = 500$, 1000, 2000 and 5000. In simulations performed at $Re_\tau = 500$, 1000 and 2000, the computational box dimensions are $L_x = 2\pi h$, $L_y = 2h$ and $L_z = \pi h$ in the streamwise, wall-normal and spanwise directions, respectively. It was stated in [75] for the flow field, and in [52] for thermal flows, that a computational box with such dimensions is big enough to accurately represent the first-order statistics of the velocity and temperature fields. In order to keep the same resolution for the different Reynolds numbers, the number of collocation points is just multiplied by a factor of 2, as the Reynolds number is. However, the friction Reynolds number $Re_\tau = 5000$ is 2.5 times bigger than the closest case at $Re_\tau = 2000$. Increasing the number of collocation points only by a factor of 2 will lead to a poor quality mesh and the results will not be accurate. In order to obtain the same mesh resolution as in the lower Re_τ simulations, the number of collocation points in the x and z directions is set to be 4 times higher than the ones in the simulation of $Re_\tau = 2000$. In order to adjust the mesh resolution, the streamwise and spanwise dimensions of the computational box are multiplied by a factor of 1.6. Therefore, on one hand, the computational cost increases due to the
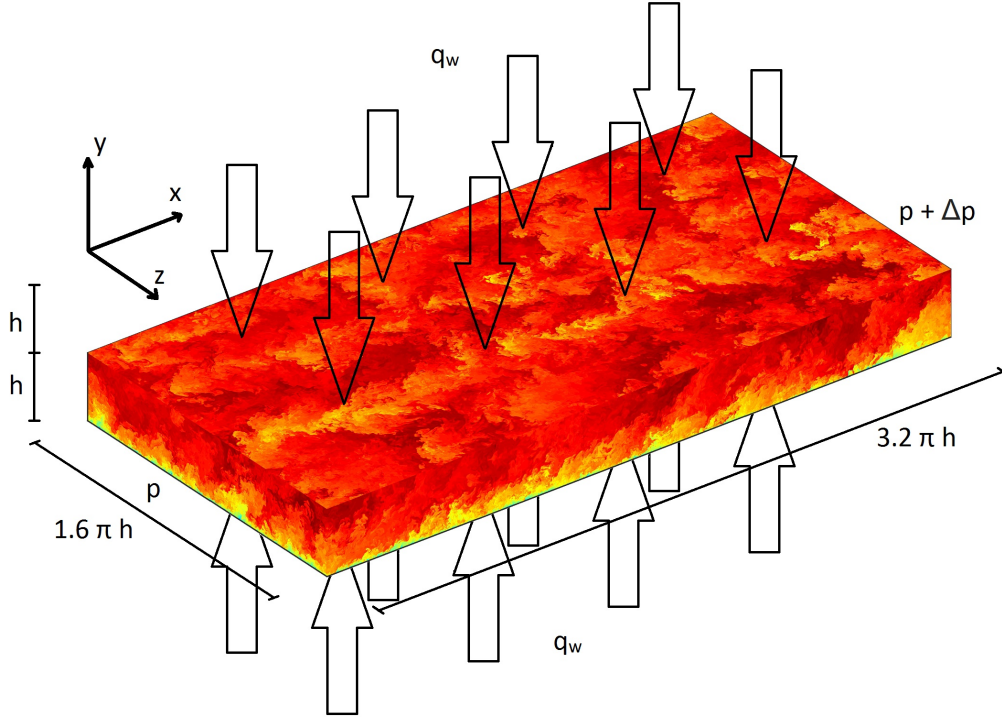
Figure 4.1: Schematic representation of the lower half of the computational box. The flow is driven by a pressure gradient, ΔP, from left to right. A constant heat flux, $\dot{q}_w$, is heating both isothermal walls. Contours represent a snapshot of the streamwise velocity field for the case of $Re_\tau = 5000$ and $Pr = 0.71$.

high increase in collocation points. But, on the other hand, since the domain is increased in the periodic directions, the number of statistics obtained every time step also increases. Then, the dimensions of the computational box for the case of $Re_\tau = 5000$ are set to be $3.2\pi h$, $2h$ and $1.6\pi h$ in the streamwise, wall-normal, and spanwise directions, respectively.

Table 4.1 presents the most important parameters of the simulations. Information about the dimensionless numbers (first to third column), the number of collocation points of the mesh (fourth to sixth column) and its resolution in every direction (seventh to tenth column), and the time of the simulation in wash-outs (eleventh column column) are shown. A wash-out is defined as the time needed for an eddy to cross the channel, L_x/U_b. Δy_w^+ and Δy_{cl}^+ are the wall-normal mesh resolution in the wall and in the center-line of the channel, respectively. For this resolution of the mesh in the wall-normal direction, the spacing between points has been set to be proportional to the local isotropic Kolmogorov scale $\eta = \left(\nu^3/\varepsilon\right)^{1/4}$, for the cases of $Pr \leq 1$. The increment in y is set to be $\Delta y = 1.5\eta$. For the cases where $Pr \geq 1$, the thermal scales are smaller than the velocity scales. Therefore, the mesh resolution in the wall-normal direction is adapted to satisfy Batchelor length scale, $\eta_\theta = \eta Pr^{-1/2}$, when $Pr \geq 1$. On the other hand, the resolution of the mesh in the streamwise and spanwise direction is $\Delta x^+ \sim 8.18$ and $\Delta z^+ \sim 4.09$, respectively, for simulations with $Pr \leq 1$. These values are similar to many other trusted simulations [40, 45, 52, 54, 73]. The mesh resolution in x and z directions has also been adapted for higher Prandtl numbers. In addition, for medium-high Prandtl numbers a mesh with higher resolution in x and z and/or y was simulated for a mesh validation. There were no significant differences in the

Re_τ	Pr	Re	N_x	N_y	N_z	Δx^+	Δy_w^+	Δy_{cl}^+	Δz^+	yu_b/L_x
	0.007									421
	0.01									30
	0.02									332
	0.05									295
	0.1									174
	0.3			251				0.72	5.3		346
500	0.5	10200	384		384	8.18			4.09	210
	0.71									528
	1									143
	2									191
	4									288
	7			351				0.27	3.9		94
	10		768	383	768	4.09		0.22	3.6	2.05	120
	0.007									79
	0.01									114
	0.02									176
	0.05									79
	0.1			383				0.44	7.4		65
1000	0.3	22300	768		768	8.18			4.09	73
	0.5									70
	0.71									130
	1									191
	2									119
	4			583				0.19	4.9		185
	7		1536	633	1536	4.09		0.16	4.5	2.05	86
	0.007									21
	0.01									28
	0.02									29
	0.05									36
	0.1			633				0.32	8.8		36
2000	0.3	48500	1536		1536	8.18			4.09	36
	0.5									35
	0.71									47
	1									97
	2									96
	4			1285				0.12	4.3		56
	7		3072	1285	3072	4.09		0.12	4.3	2.05	29
5000	0.71	135860	6144	1685	6144	8.18		0.2	8.1	4.09	12

Table 4.1: Parameters of the Poiseuille simulations.

51
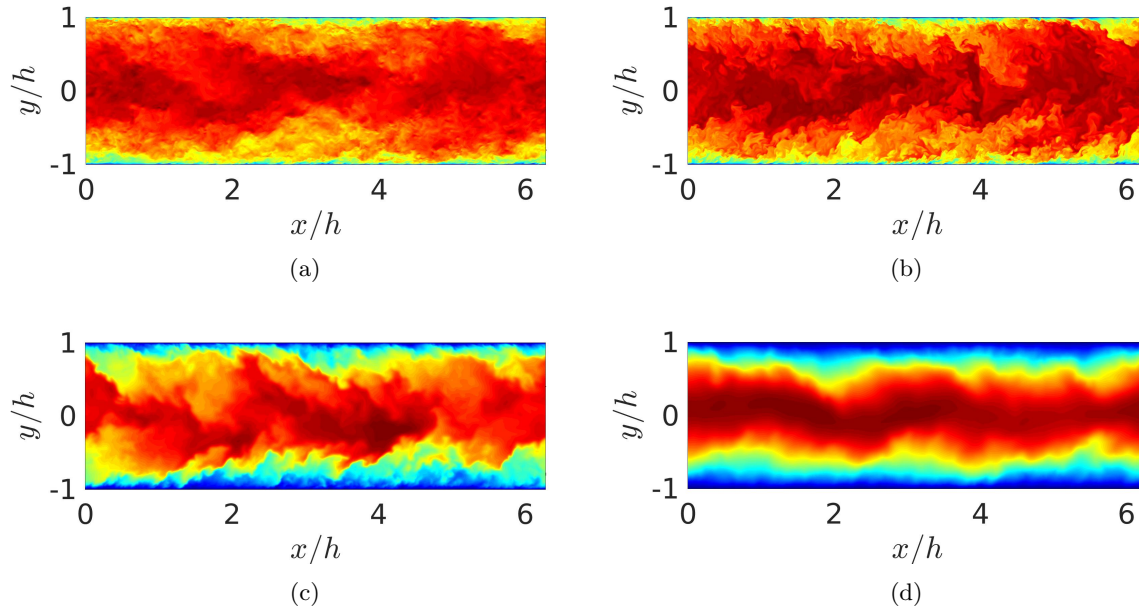
Figure 4.2: Instantaneous visualizations for $Re_\tau = 2000$ and (a) velocity field for $Pr = 0.71$, (b) thermal field for $Pr = 0.71$, (c) thermal field for $Pr = 0.05$ and (d) thermal field for $Pr = 0.007$. All magnitudes are normalized in wall units.

first-order statistics between the different meshes simulated.

A good way to observe the size of the turbulent scales is by plotting isocontours of velocity and temperature fields. They can be seen in figures 4.2 and 4.3, where different instantaneous values of the velocity and temperature field are presented. In figure 4.2a, the velocity field for $Pr = 0.71$ is shown. These turbulent scales are comparable to the ones presented in the thermal field for the same Prandtl number, figure 4.2b. This result was expected since $Pr \sim 1$ and, therefore, $Pe_\tau \sim Re_\tau$. However, the instantaneous temperature fields shown in figures 4.2c ($Pr = 0.05$) and 4.2d ($Pr = 0.007$) are different. For low Prandtl numbers, the thermal flow becomes less turbulent and, for the smallest Prandtl number studied, the thermal flow is almost laminar. This confirms once again that by reducing the Prandtl number, the thermal field is less turbulent, reducing the turbulent heat flux and the heat transferred by convection.

Regarding high Prandtl numbers, in figures 4.3a and 4.3b, a comparison between both fields, velocity and temperature for $Re_\tau = 2000$ and $Pr = 7$, is done in a $x - y$ plane. Unlike temperature fields for $Pr = 1$, the temperature scales for $Pr = 7$ are smaller than the velocity ones. This implies that the temperature field is more turbulent than the velocity one, and, effectively, a finer mesh is needed to properly capture the smaller scales of the thermal field. In addition, one can easily see how the boundary layer of the temperature is thinner than the one of the velocity, which implies higher gradients of temperature in the near-wall region. Remark the fact that both, velocity and temperature structures detach from the wall with an angle of approximately $25°$.

The middle figures, 4.3c and 4.3d, present the temperature field in a $x - z$ plane located in the center of the channel for the cases of $Pr = 1$ and 7, respectively, with $Re_\tau = 2000$. Following the same idea as before, smaller turbulent scales appear for $Pr = 7$. Finally, a comparison of the temperature scales has been done, depending on the distance to the wall. Figures 4.3e and 4.3f are instantaneous images of the temperature field for $Pr = 7$ and $Re_\tau = 2000$ at $y^+ = 240$ and 9, respectively, i.e. the logarithmic
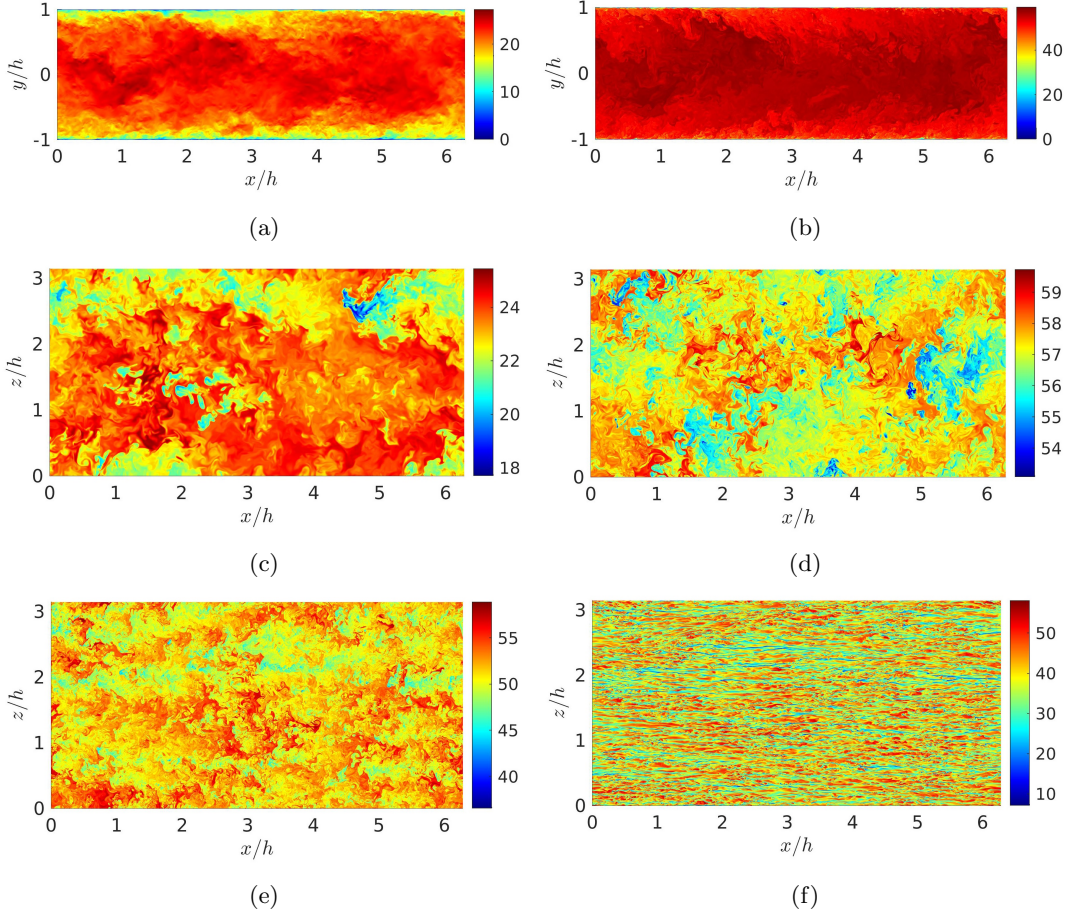
Figure 4.3: Instantaneous visualizations for $Re_\tau = 2000$. (a) Velocity and (b) temperature fields for the $Pr = 7$ case in the $x - y$ plane. Temperature field for (c) $Pr = 1$ and (d) $Pr = 7$ in the $x - z$ central plane of the channel. Temperature field for $Pr = 7$ in a $x - z$ plane located in (e) the logarithmic region, $y^+ = 240$, and (f) in the near-wall region, $y^+ = 9$. All magnitudes are normalized in wall units.

and the conductive region, respectively. In the logarithmic region, intermediate scales are obtained, not as big as in the outer region, but either as small as in the near-wall region. The classical streaks in the near-wall region are perfectly observed in figure 4.3f. Corresponding streaks for the velocity field are also obtained (not shown here for brevity), which reflect the strong correlations between the streamwise velocity and temperature field in the near-wall region. However, it should be noted that this correlation gets weaker as the Prandtl number increases, as it will be presented in chapter §5.

The procedure to run the simulation starts with an initial file from other simulation with similar Reynolds and Prandtl numbers. The process when the flow converges towards a statistically stationary state can be almost as long as the simulation itself. This simulation time is not contemplated in the rightmost column of table 4.1. After that, the simulation is run and the flow statistics are collected. As a first rule of thumb, 10 wash-outs are needed for the highest Reynolds numbers simulations to be statistically converged. After this point, in order to check if the simulation is actually statistically converged, the balance equations of the momentum (1.21) and energy (1.41) equations are computed,
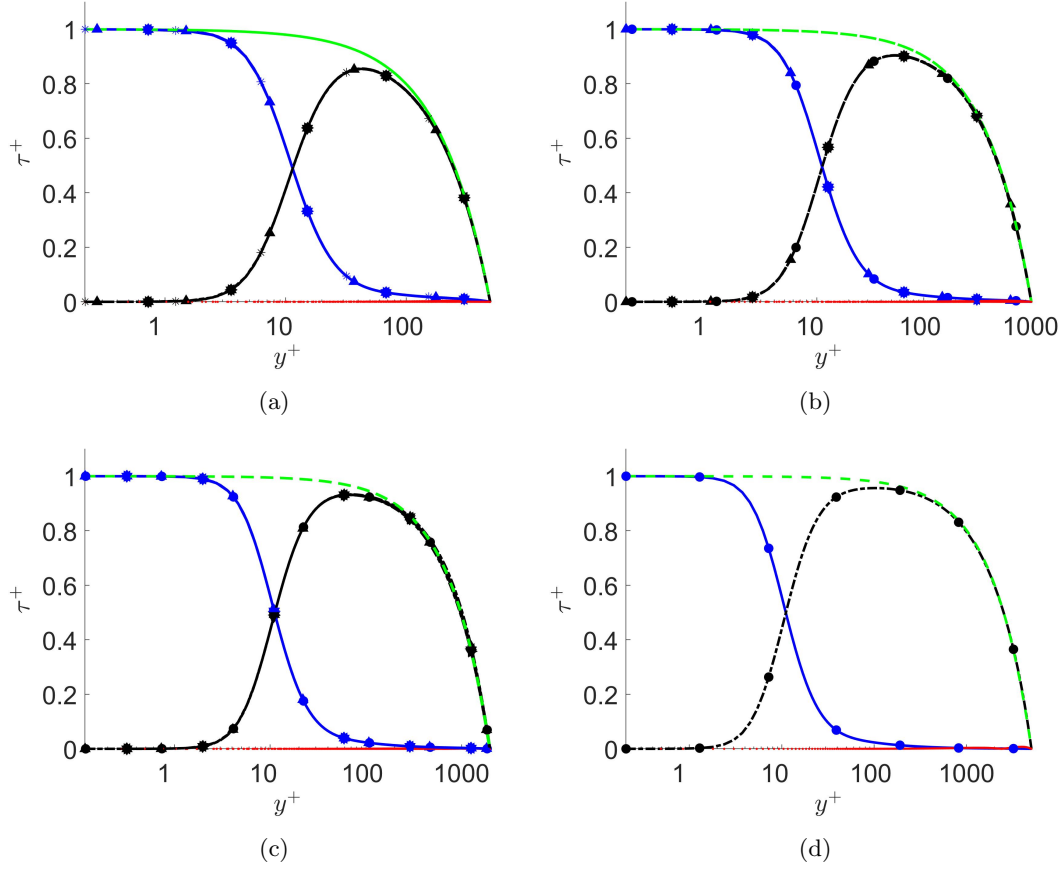
Figure 4.4: Balance of the moment equation (4.1) for (a) $Re_\tau = 500$, (b) $Re_\tau = 1000$, (c) $Re_\tau = 2000$ and (d) $Re_\tau = 5000$. Green dashed lines represents the total shear stress, blue solid lines are the molecular shear stress, black dashed-dotted lines are the turbulent shear stress. Red dotted lines are the differences between the LHS and the RHS of equation (4.1). Different symbols indicate different Prandtl number, which collapse due to the condition of a passive scalar.

which are presented here again to indicate the nature of each term of the equations:

$$\tau^+ = \overbrace{\frac{d\overline{U}^+(y^+)}{dy^+}}^{\text{Molecular}} \overbrace{-\overline{u^+v^+}(y^+)}^{\text{Turbulent}} = \overbrace{1 - \frac{y^+}{Re_\tau}}^{\text{Total}}, \tag{4.1}$$

$$\dot{q}^+ = \underbrace{\frac{1}{Pr}\frac{d\overline{\Theta}^+(y^+)}{dy^+}}_{\text{Molecular}} \underbrace{-\overline{v^+\theta^+}(y^+)}_{\text{Turbulent}} = \underbrace{1 - \frac{1}{Re_\tau U_b^+}\int_0^{y^+} \overline{U}^+(\hat{y}^+)d\hat{y}^+}_{\text{Total}}. \tag{4.2}$$

When the balances in shear stresses and heat fluxes are below 10^{-3} the simulation is considered converged. Figure 4.4 shows the balance terms of equation (4.1). The red dotted line is the residual of the LHS and RHS, which indicates that the simulations are converged. Furthermore, the collapsing of the curves for different Reynolds numbers indicates that the velocity field is statistically converged. On the other hand, figure 4.5 shows the balance terms of equation (4.2). In the same way, the red dotted lines

54
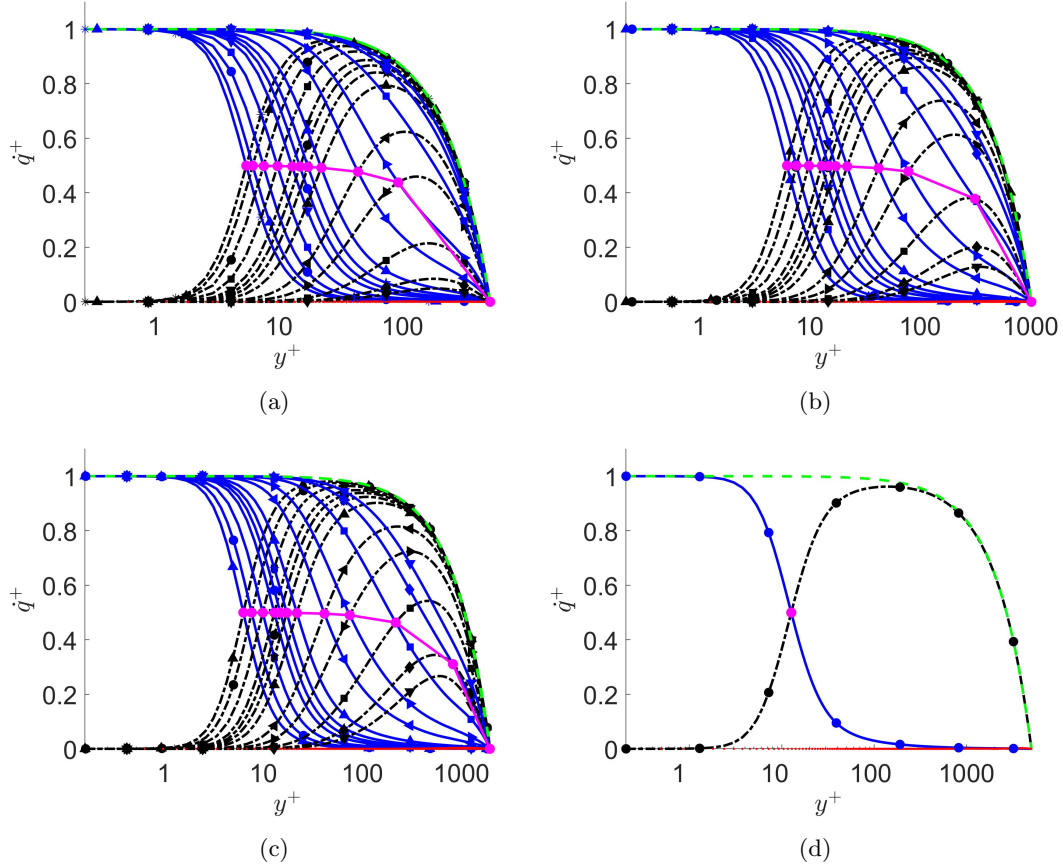
Figure 4.5: Balance of the energy equation (4.2) for (a) $Re_\tau = 500$, (b) $Re_\tau = 1000$, (c) $Re_\tau = 2000$ and (d) $Re_\tau = 5000$. Green dashed lines represents the total heat flux, blue solid lines are the molecular heat fluxes (lower lines indicate a higher Prandtl number), black dashed-dotted lines are the turbulent heat fluxes (upper lines indicate a higher Prandtl number). Red dotted lines are the differences between the LHS and the RHS of equation (4.2). Magenta solid line is formed by the cross points between molecular and turbulent heat fluxes. Symbols represent the different Prandtl number.

at a value of almost 0 indicate that the simulations are converged. An important result is that turbulent heat flux decreases for lower Prandtl numbers. This entails a thermal flow that is less turbulent. The magenta line is formed by the cross points between the molecular and turbulent heat fluxes. For a certain value of Prandtl, turbulent heat flux is lower than molecular heat flux in the whole channel. This value of the Prandtl number increases with the Reynolds number since a higher Re entails a more turbulent flow. Finally, for cases with medium and high Prandtl numbers the y^+ coordinate where the molecular and turbulent heat fluxes cross is independent of Re_τ. In terms of the y coordinate, this means that the viscous layer is smaller when the Reynolds number is increased, as it should. In the central region of the channel, the turbulent heat flux increases its maximum value when the Reynolds number is increased and the area below the turbulent heat flux line also increases. All this implies that the thermal flow is more turbulent for higher Re_τ, as was expected.

Finally, in order to validate the code for low Prandtl numbers, a simulation for $Re_\tau = 400$ and $Pr = 0.025$ has been performed. This Prandtl number is, up to date, the lowest Prandtl number
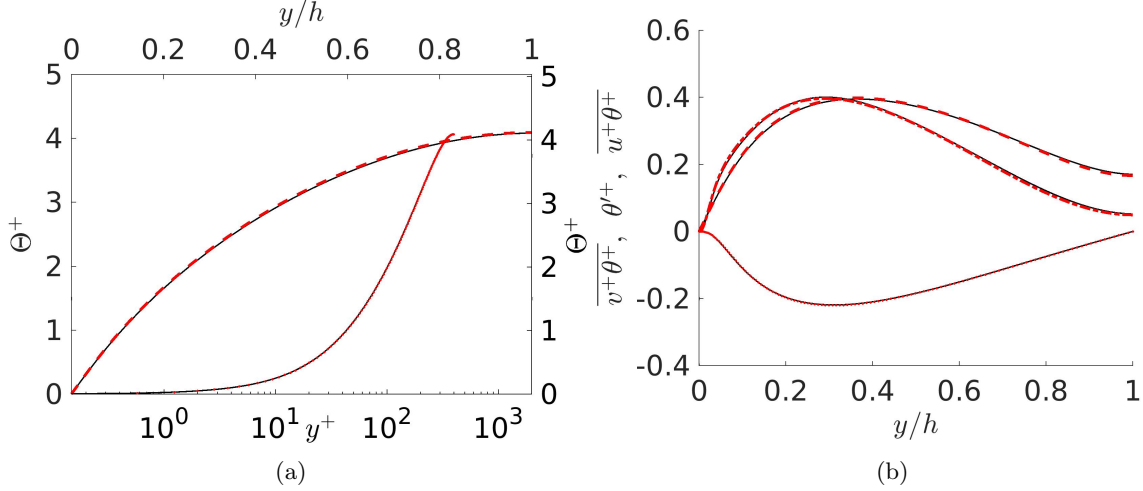
Figure 4.6: (a) Mean temperature profile in inner (bottom, dashed line) and outer (top, pointed line) scales for $Re_\tau = 400$ and $Pr = 0.025$. (b) Temperature RMS (dashed) and streamwise (dash-pointed) and wall-normal (pointed) heat fluxes. Black solid lines from Kawamura's database [45].

Re_τ	Re_b	L_x	L_z	Δx^+	Δz^+	tu_τ/h
10000	261000	$2\pi h$	πh	15.3	7.6	19.8

Table 4.2: Parameters of the Poiseuille isothermal simulation. Δ_x^+ and Δ_z^+ are in terms of dealiased Fourier modes. The last column is the total simulation time without transition in terms of eddy turnovers.

simulated in turbulent channel flows and was done first by Abe et al [45]. The results of the simulation here presented are compared with the data provided in Kawamura's database [45]. This comparison is shown in figure 4.6. Figure 4.6a shows a perfect agreement for the mean temperature in both inner and outer scales. Also, in figure 4.6b all curves collapse almost perfectly for the temperature variance and both streamwise and wall-normal heat fluxes. The very small differences can be due to small statistical uncertainties during the simulation, a slightly different Reynolds number, or a different numerical scheme employed.

4.1.2 Configuration of Poiseuille isothermal flow simulation

Figure 4.7 is a schematic representation of the computational box of the simulation at a nominal $Re_\tau = 10000$, where instantaneous streamwise velocity perturbations are plotted. This simulation has been performed in a computational box of sizes $L_x = 2\pi h$, $L_y = 2h$ and $L_z = \pi h$, as the simulations for $Re_\tau = 500$, 1000 and 2000 of heat transfer in Poiseuille flows. A variation of the LISO code, described in Appendix §7.1, is used. where the energy equation is removed and only the Navier-Stokes equations, (1.5) and (1.6), are simulated. The wall-normal grid spacing is adjusted to keep the resolution at $\Delta y = 1.5\eta$, i.e., approximately constant in terms of the local isotropic Kolmogorov scale. In wall units, Δy^+ varies from 0.3 at the wall, up to $\Delta y^+ \simeq 12$ at the centerline. The resolution in x and z is similar to the largest simulations of turbulence [73, 75, 76].

The initial file of this simulation was taken from a smaller Reynolds number simulation. To accelerate the compilation of statistics, three initial files were prepared and thus three simulations were run at the same time. In every case, the code was run until some transition phase had passed and the flow had
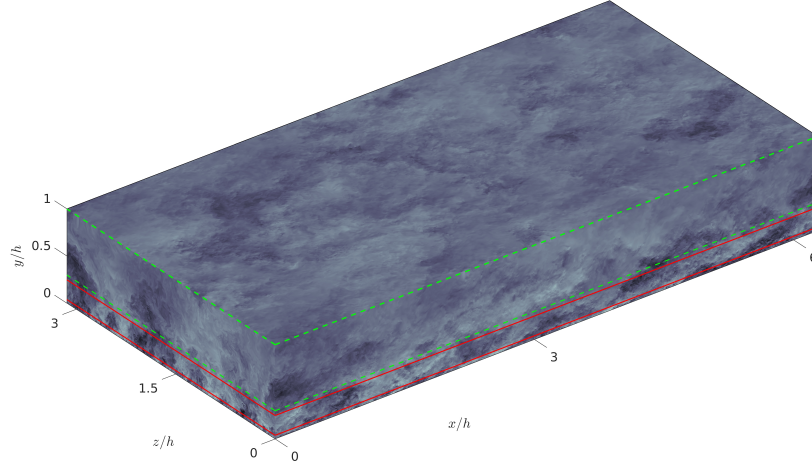
Figure 4.7: Instantaneous streamwise velocity perturbation, arbitrary units. The flow goes from the left to the right. Only the bottom part of the channel is shown. Red lines: log layer. Green lines, outer region.

adjusted to the new set of parameters. Once the flow was in a statistically steady-state, statistics were compiled. The running times to compile statistics are shown in terms of eddy-turnovers in the rightmost column of table 4.2. The transitions until the simulations reached a statistically steady-state, which were very time-consuming, are not contemplated in this table.

To further validate the statistics of the simulation, figure 4.8 shows the error in the balance of the momentum equation (4.1). The difference between both sides of this equation is below 2×10^{-3}, similar to the other tree simulations utilized here. Thus, it has been considered that enough statistical information was obtained. To further post-process the simulation, a total of 300 temporal images of the velocity field have been stored, with a size of roughly 90TB.

4.2 Configuration of the Couette flow simulations

For the study of thermal Couette flows, two DNS of a passive thermal flow in a turbulent channel at $Re_\tau = 250$ and 500, and $Pr = 0.71$ have been conducted within a computational box of $L_x = 16\pi h$, $L_y = 2h$ and $L_z = 6\pi h$, with periodicity in the streamwise and spanwise directions. These are the cases V and VI in table 4.3. In addition, four Couette flow simulations with different size of boxes in x and z dimensions ($4\pi h \times 0.5\pi h$, $2\pi h \times \pi h$, $4\pi h \times 2\pi h$ and $16\pi h \times 6\pi h$) were also conducted at $Re_\tau = 180$ and the Prandtl number of air (cases I-IV in table 4.3). In all cases the MBC is applied to the thermal field. These simulations were performed to check whether or not the size of the box has an influence in the rolls described in subsection §2.3.1 and, consequently, in the mean and one-point statistics. The upper
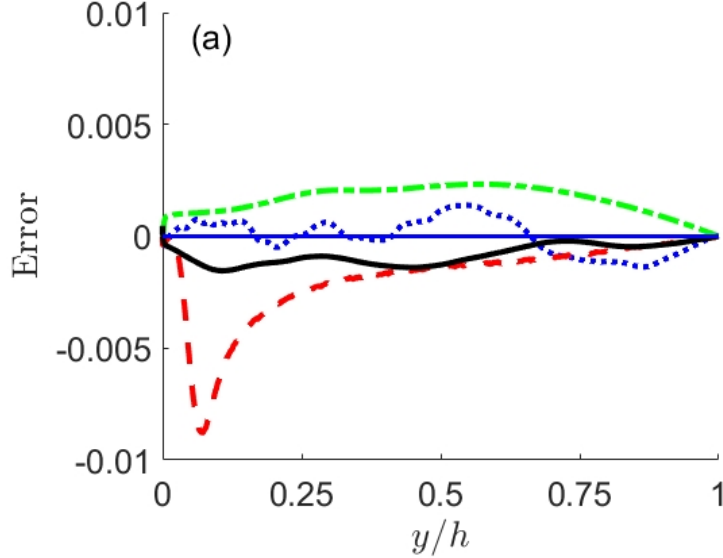
Figure 4.8: Error in the computation of momentum equation (1.6). Black solid line is the result of the simulation of this work at $Re_\tau = 10000$. Green dotted-dashed line is from Lee and Moser [76] for $Re_\tau = 5200$. Red dashed line is from Lozano-Durán and Jiménez [75] for $Re_\tau = 4000$. Blue dotted line is from Hoyas and Jiménez [73] for $Re_\tau = 2000$.

wall is the moving wall, while the lower one is stationary. The average operator $\langle \cdot \rangle_{x_i}$ is defined as

$$\langle \phi \rangle_{x_i} = \frac{1}{L_{x_i}(t_1 - t_0)} \int_{t_0}^{t_1} \int_0^{L_{x_i}} \phi \, dx_i \, dt, \qquad (4.3)$$

where the value of $\langle \phi \rangle_x$ can be thought as the mean in x of the time-averaged field ϕ.

A variation of the LISO code, described in appendix §7.1 is used to solve the equations that describe the flow (1.5), (1.6) and (1.7). This variation introduces a coefficient that imposes a percentage of pressure difference and a percentage of motion of the wall. Setting the coefficient to 1, the motion of the flow comes entirely from the motion of the wall, describing a Couette flow. As usual, the wall-normal grid spacing is adjusted to keep the resolution at $\Delta y = 1.5\eta$. In wall units, Δy^+ varies from 0.83 at the

Cases	Re_τ	Re	Box	N_x	N_y	N_z	tu_τ/h
I	166	3500	$4\pi h \times 0.5\pi h$	384	201	144	57.3
II	177	3500	$2\pi h \times \pi h$	192	201	192	79.9
III	176	3500	$4\pi h \times 2\pi h$	384	201	384	39.2
IV	178	3500	$16\pi h \times 6\pi h$	1536	251	1152	59.1
V	262	5400	$16\pi h \times 6\pi h$	1536	251	1152	88.9
VI	476	10500	$16\pi h \times 6\pi h$	3072	251	2304	58.1

Table 4.3: Parameters of the simulations. Friction and bulk Reynolds numbers are shown in columns two and three, respectively. The fourth column shows the box size of each case. N_x, N_y and N_z are the number of collocation points in each direction. The last column contains the time spent to compile statistics in terms of eddy-turnovers.
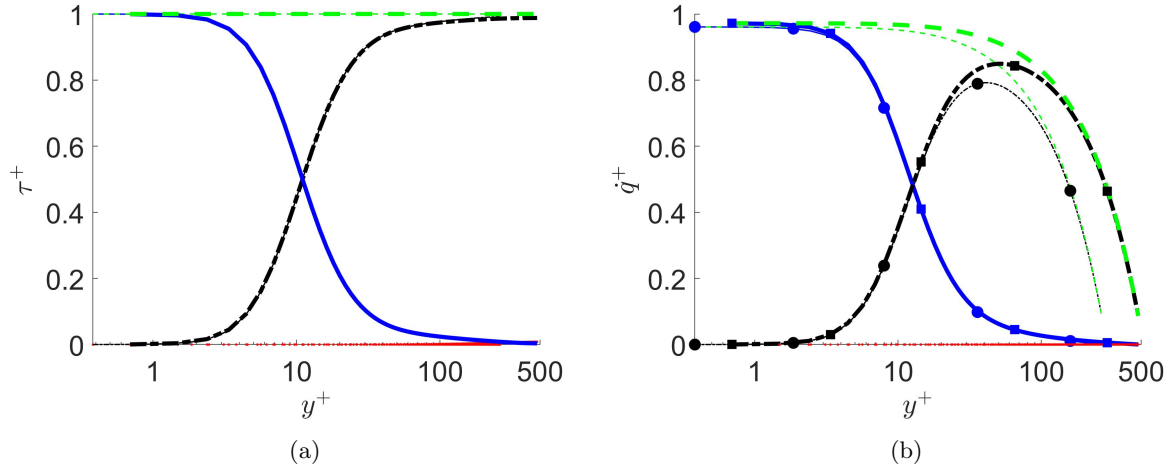
Figure 4.9: For $Re_\tau = 250$ (thin lines) and 500 (thick lines). (a) Shear stresses: $d\overline{U}^+/dy^+$ (blue, solid), $-\overline{uv}^+$ (black, dash-doted) (b) Heat fluxes: molecular (blue, solid), turbulent (black, dash-doted) and total (green, dashed). In both cases, the red pointed line represents the difference between LHS and RHS of either equations (4.4) or (4.2).

wall, up to $\Delta y^+ \simeq 2.3$ at the center-line. The wall-parallel resolution in physical space for x and z is $\Delta x^+ \simeq 8.4$ and $\Delta z^+ \simeq 4.3$. Simulations are submitted in a similar way to Poiseuille flows.

In order to further validate the database, the balance equations of the shear stresses and heat fluxes in a Couette flow have been computed and plotted. The balance of heat fluxes is calculated as in equation (4.2), while the balance equation of shear stresses is slightly different for Couette flows:

$$\tau^+ = \overbrace{\frac{d\overline{U}^+(y^+)}{dy^+}}^{\text{Molecular}} \overbrace{-\overline{u^+v^+}(y^+)}^{\text{Turbulent}} = \overbrace{1}^{\text{Total}}. \tag{4.4}$$

The results of this validation are shown in figure 4.9, for cases V and VI. It has been considered that enough statistics were obtained when this error was below 10^{-3}. In figure 4.9a, apart from the small error, a very good agreement is found between both simulations, as the curves collapse almost perfectly. Molecular and turbulent heat fluxes are compared with the total flux in figure 4.9b. Again a very small error is obtained, validating both simulations.

4.3 Configuration of the stratified flow simulations

The study of stratified flows has been done as an extension of the study of the Couette flows. The main idea is to investigate how the rolls that appear in Couette flows, described in section §2.3.1, are affected by a change of density in the wall-normal direction. Instantaneous density is denoted by ρ_t. Because a capital ρ is indistinguishable to P the subindex t is used, and, thus, $\rho_t = \overline{\rho} + \rho$.

The governing equations are written under the Boussinesq approximation, so the continuity equation is identical to equation (1.5) and the momentum equation in the wall-normal direction includes an extra term to consider buoyancy effects. Their nondimensional form is

$$\frac{\partial U_i^+(t, \boldsymbol{x})}{\partial t} + U_j^+(t, \boldsymbol{x})\frac{\partial U_i^+(t, \boldsymbol{x})}{\partial x_j^+} = -\frac{\partial P^+(t, \boldsymbol{x})}{\partial x_i^+} + \frac{1}{Re_\tau}\frac{\partial^2 U_i^+(t, \boldsymbol{x})}{\partial x_j^+ \partial x_j^+} - Ri_\tau \rho_t^+ \delta_{i2}, \tag{4.5}$$

59

Case	Re_b	Re_τ	Ri_τ	tu_τ/h	tU_b/L_x
P0	10200	500	0	48.11	34.19
C0	10500	480	0	41.96	33.03
C1	10700	476	0.50	54.74	44.26
C3	11300	483	1.65	34.98	29.43
C6	11480	476	2.90	31.51	27.33

Table 4.4: Parameters of the simulations. Two different Reynolds numbers are given depending on the bulk velocity, U_b, and u_τ. Ri_τ is given in the fourth column. The last two columns denote the computational time span while statistics were taken in wash-outs (U_b/L_x) and eddy turn-overs (u_τ/h).

and the equation for the scalar field is

$$\frac{\partial \rho_t^+(t, \boldsymbol{x})}{\partial t} + U_j^+(t, \boldsymbol{x})\frac{\partial \rho_t^+(t, \boldsymbol{x})}{\partial x_j^+} = \frac{1}{Re_\tau Sc}\frac{\partial^2 \rho_t^+(t, \boldsymbol{x})}{\partial x_j^+ \partial x_j^+}, \tag{4.6}$$

where the scalar, in this case, is the density ρ_t. Equation (4.6) is completely analogous to the energy equation (1.7) but for mass dissipation, where Sc is the Schmidt number, which is defined as the ratio of momentum diffusivity, ν, and mass diffusivity, D. Sc is analogous to Pr in the case of heat transfer. In equation (4.5), Ri_τ is the Richardson friction number, given by $Ri_\tau = \Delta\rho gh/\rho_0 u_\tau^2$. This $\Delta\rho$ is the difference in density between the two walls, being the flow denser at the bottom wall. Thus, Dirichlet boundary conditions are used to model ρ_t. This boundary condition is completely equivalent to a temperature difference between both walls in a heat transfer problem. g is the gravitational acceleration and ρ_0 is a reference density. Schmidt number of air is used in this study, $Sc = 0.71$. The way in which equations are solved is completely equivalent to that of Poiseuille and Couette flows, and it is explained in detail in Appendix §7.1.

Five new simulations have been made for this work, summarised in table 4.4. The first simulation is a Poiseuille flow with $Ri_\tau = 0$. The other four simulations are Couette flows at different small values of Ri_τ. In every case, the domain chosen is ($8\pi h \times 2h \times 3\pi h$), to completely contain a pair of rolls, described in subsection §2.3.1. The mesh has a size of ($1536 \times 251 \times 1152$) points which give a resolution of 8.2 and 4.1 wall units in x and z. The wall-normal grid spacing is adjusted to keep the resolution at $\Delta y = 1.5\eta$, as for all previous cases. In wall units, Δy^+ varies from 0.83 at the wall, up to $\Delta y^+ \simeq 2.3$ at the center line. This grid size is similar to the one typically used in channel flows, for both Poiseuille and Couette flows [73, 54, 52, 55].

The initialization of each case has been done following the same procedure as for Poiseuille and Couette flow simulations. The code was run until a transition phase was passed and the flow had adjusted to the new set of parameters. The transition is characterized through, among other variables, the value of the shear stress in the moving wall. Once this parameter reaches a plateau, statistics are collected. In order to further validate the database, the total density flux, which is equal to one, has been calculated as the sum of the turbulent and molecular density fluxes. The following equation comes from the integration of equation (4.6),

$$1 = \overline{v\rho}^+ - \frac{d\overline{\rho_t}^+}{dy^+}, \tag{4.7}$$

This equation is completely equivalent to the shear balance in a Couette flow (4.4). The different terms are shown in figure 4.10. All fluxes collapse perfectly, and in every case, their sum is one, with an error below 5×10^{-3}, validating, therefore, the simulation.
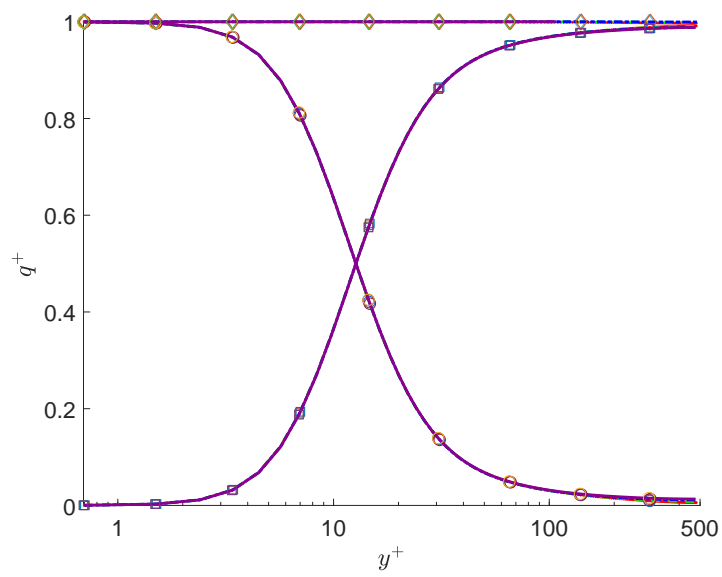
Figure 4.10: Turbulent (squares), molecular (circles), and total (diamonds) density fluxes for cases C0, C1, C3 and C6. The collapsing of the different curves is perfect.

Chapter 5

Results

In this chapter the results of the project will be presented. It is organized as follows:

1. The first section of the chapter §5.1 contains the major focus of the study, i.e. Poiseuille flows in a turbulent channel under the MBC. This section is separated in several subsections in order to differentiate the behaviour of different ranges of Reynolds and Prandtl numbers.

   - First subsection contains the results for the simulations at $Re_\tau = 500$, 1000 and 2000 for low to medium Prandtl numbers, i.e. Pr ranging from 0.007 up to the Prandtl number of air, $Pr = 0.71$.´

   - Second subsection contains the results for simulations with the same friction Reynolds numbers, $Re_\tau = 500$, 1000 and 2000, and medium to high Prandtl numbers ranging from $Pr = 1$ up to $Pr = 10$, 7 and 7 for each Re_τ, respectively.

   - Third subsection collect the results for the highest friction Reynolds number ever simulated in a turbulent channel flow with heat transfer, $Re_\tau = 5000$, with $Pr = 0.71$.

   - Fourth subsection presents the results of the Poiseuille isothermal flow, using the highest friction Reynolds number ever simulated in a turbulent channel: $Re_\tau = 5000$.

   - In fifth and last subsection, the Lie symmetries theory is used to obtain scaling laws of the velocity, temperature and high order moments of both.

2. The second section is dedicated to other type of flows:

   - First subsection presents the results of heat transfer in a Couette flow under the MBC for $Re_\tau = 180$, 250 and 500, with the Prandtl number of air, $Pr = 0.71$.

   - In second and final subsection, the results of a stratified flow are shown. The friction Reynolds number of $Re_\tau = 500$ is used with friction Richardson numbers up to 2.9 and the Prandtl number of air, $Pr = 0.71$. In this section, the thermal boundary condition is a temperature difference between both walls.

5.1 Poiseuille flows

In this section, the results obtained from the DNS of Poiseuille flows will be presented. This section concludes with the use of Lie symmetries to generate scaling laws of the velocity, temperature and high order moments of both, for the Poiseuille turbulent channel.

In order to distinguish among the different cases, line colours as in table 5.1 will be used to differentiate each friction Reynolds number in the plots of section §5.1 (unless otherwise specified).

Re_τ	500	1000	2000	5000
Line colour	▬	▬	▬	▬

Table 5.1: Line colours used to represent each simulation throughout pots of section §5.1.

Pr	0.007	0.01	0.02	0.05	0.1	0.3	0.5	0.71
Symbol	▽	◇	□	◯	◁	▷	★	△

Table 5.2: Symbols used to identify the Prandtl number through all the figures of this subsection.

5.1.1 Medium and low Reynolds and Prandtl numbers

This subsection presents the results for friction Reynolds numbers of values $Re_\tau = 500$, 1000 and 2000 with low to medium Prandtl numbers, ranging from $Pr = 0.007$ up to $Pr = 0.71$. Symbols in table 5.2 will be used to distinguish lines with different Prandtl numbers in the figures of this subsection (unless otherwise specified).

Mean temperature profiles

Mean temperature profiles, $\overline{\Theta}^+$, are shown in figure 5.1a. Keeping Pr constant, all $\overline{\Theta}^+$ collapse in the near-wall and logarithmic region. In the central zone, when Re_τ increases, temperature profiles go deeper and, for the same Pr, the slope of the line slightly decreases.

An important parameter that can be derived from the mean temperature profile is the thermal von Kármán constant, κ_t. For sufficiently high Pr numbers, the mean temperature profile can be described in the logarithmic region with the following relation

$$\overline{\Theta}^+ = \frac{1}{\kappa_t} \ln\left(y^+\right) + B, \tag{5.1}$$

which was already introduced in section §1.1.2, equation (1.44), and it is written here for the sake of readability. The classic limits for this logarithmic region for the streamwise velocity are $y^+ \approx 70$ and $y/h = 0.2$, according to Jiménez [77]. The same limits have been used for the thermal flow. Even if a logarithmic layer is not really present until a higher Reynolds is reached [63, 76, 78], an indicator of this region is the first minimum of the diagnostic function (see figure 5.1b). This first minimum, and thus an emerging logarithmic layer, appear for Prandtl numbers greater than approximately 0.3. It is worthy to stress that all the calculations shown below are a first approximation to the actual value of κ_t. A truly logarithmic layer is not expected until at least $Re_\tau \approx 5000$, which will be seen in section §5.1.3.

The values of κ_t and B are collected in table 5.3. Notice that the value of κ_t increases slightly with an increase of the Re_τ number. This is caused by a slight reduction of the slope of $\overline{\Theta}^+$ in the logarithmic region for the same Pr when Re_τ is increased. However, the variation of κ_t from $Re_\tau = 1000$ to 2000 is much smaller than that from $Re_\tau = 500$ to 1000, which may indicate that κ_t converges towards a constant value for high Reynolds numbers. The values of κ_t agree with the ones obtained by Abe et al. [45]. The constant B changes for each Prandtl number. For $Pr = 0.71$, a value of $B \approx 3$ is obtained, which also agrees with the one obtained by Abe et al [45]. When the Prandtl number is reduced to 0.5 and 0.3, the values of B are reduced to approximately 0.6 and -1.9, respectively.

To further explore this logarithmic region, the thermal diagnostic function, defined as

$$\Xi_T = y^+ \partial_{y^+} \overline{\Theta}^+, \tag{5.2}$$

is used. In figure 5.1b, Ξ_T is plotted for all cases. It can be seen how for the three greater Prandtl numbers, there exist two maximum values. The y^+ location of the first maximum does not depend on
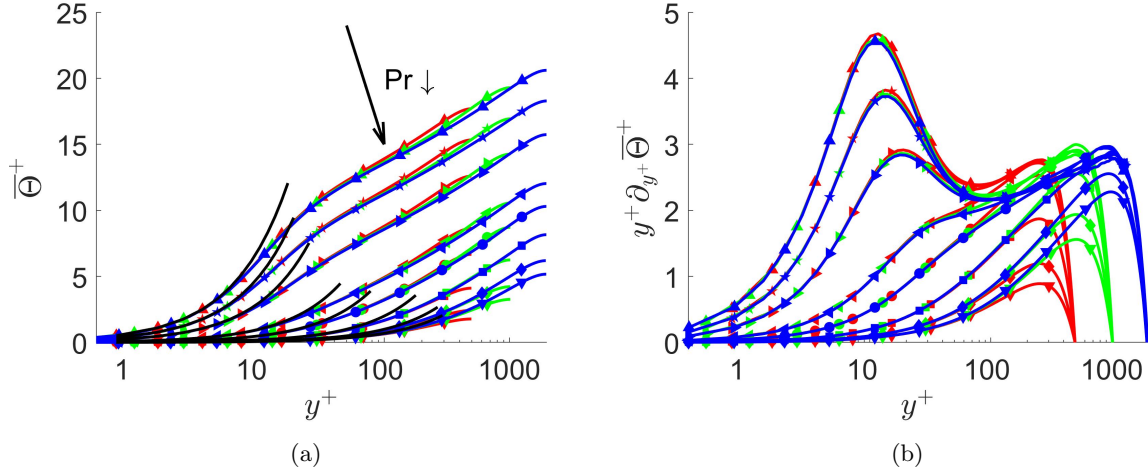
Figure 5.1: (a) Mean temperature profile. Black lines correspond to the thermal law of the wall. (b) Thermal diagnostic function. Colours as in table 5.1 and symbols as in table 5.2.

κ_t		Re_τ			B		Re_τ		
		500	1000	2000			500	1000	2000
	0.71	0.418	0.436	0.440		0.71	2.89	3.11	3.05
Pr	0.5	0.420	0.434	0.436	Pr	0.5	0.55	0.70	0.64
	0.3	0.427	0.438	0.437		0.3	-1.99	-1.87	-2.00

Table 5.3: Thermal von Kármán constant and B values from equation (5.1) for medium Prandtl numbers.

Re_τ. However, its value decreases slightly for an increase in the Reynolds number. When the Prandtl number is decreased below 0.3, this first maximum disappears and, therefore, the logarithmic region. On the other hand, the y^+ coordinate of the second maximum is independent of Pr. In outer coordinates (not shown), the position of the second maximum is independent of both Re_τ and Pr and it is located at $y/h = 0.5$. It has been observed that the value of Ξ_T at this second maximum is constant for $Pe_\tau > 30$. When this Péclet number is reduced below 30, the value of the second maximum is then reduced. Therefore, the behaviour of the second maximum cannot be characterized only by Pr.

Nusselt number

Coming back to figure 5.1a, black lines represent the thermal law of the wall, $\overline{\Theta}^+ = Pry^+$. In the conduction region of the flow, $\overline{\Theta}^+$ behaves approximately according to this law. It can be seen that a decrease in the Pr number entails a bigger conductive region. Therefore, an increase in the heat transfer by conduction is expected.

The Nusselt number is calculated according to the following definition [40]:

$$Nu = \frac{L\mathfrak{h}}{k} = \frac{2Re_\tau Pr}{\langle \overline{\Theta}^+ \rangle_{xyz}} = \frac{2Pe_\tau}{\langle \overline{\Theta}^+ \rangle_{xyz}}, \quad (5.3)$$

where L is a characteristic length, in this case the channel height, $2h$; $\mathfrak{h}$ is the convective heat transfer coefficient; and k is the thermal conductivity. According to this definition, the minimum Nusselt number that can be obtained for the present configuration is 4. In such a case, the temperature will behave following the thermal law of the wall in the entire channel. In Figure 5.2, obtained Nusselt numbers are
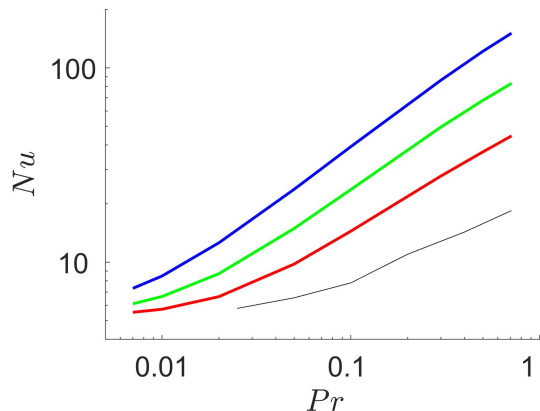
Figure 5.2: Nusselt number. Thin black line from Kawamura et al [40] for $Re_\tau = 180$. Colours as in table 5.1.

plotted as a function of the Prandtl number. Nu was calculated by Kawamura et al [40] for $Re_\tau = 180$ and Prandtl numbers from 0.025 to 5. They found that in the range of Prandtl between 0.2 and 1.5, Nu had a linear logarithmic increment. This agrees with the results obtained here for larger Re numbers. In addition, it is seen that the range of Prandtl numbers where Nu has a linear logarithmic increment is larger when Re is increased (at least the lowest limit is reduced). As it was expected, the Nusselt number decreases with Re_τ or Pr numbers. This entails a decrement of the heat transferred by convection.

Temperature and heat fluxes intensities

The root mean square of the temperature variance, θ'^+, and the heat fluxes in the streamwise, $\overline{u^+\theta^+}$, and wall-normal, $\overline{v^+\theta^+}$, directions are represented in figure 5.3. All $Re_\tau = 2000$ cases are plotted as a function of y/h in figures 5.3a and 5.3c. Meanwhile, in figures 5.3b and 5.3d, the same functions are plotted for three Reynolds numbers of values $Re_\tau = 500$, 1000 and 2000 and for three different Prandtl numbers: 0.71, 0.3 and 0.02. The tendency of the results of these turbulent intensities agrees perfectly with the results obtained by Abe et al. [45] and Kawamura et al. [40].

First of all, in figure 5.3a, for Prandtl numbers greater than approximately 0.3, θ'^+ tends to collapse in the outer region, approximately for $y/h > 0.3$. However, when Re_τ is reduced (figure 5.3b), the value of Pr at which θ'^+ collapses increases. It is observed again, that the use of the Péclet number gives a good approximation to determine which cases collapse in the central region of the channel. For $Pe_\tau > 325$, θ'^+ tends to collapse for $y/h > 0.3$. The maximum value of θ'^+ increases when Re_τ increases. The location of this maximum depends on the Prandtl number. On the one hand, when Pr is greater than approximately 0.3, the y^+ coordinate of the maximum is independent of the Re_τ number. In such cases, it is located in the buffer layer or logarithmic region. On the other hand, for Pr lower than 0.3 the morphology of θ'^+ changes. Now, its maximum location moves to the outer region. For these cases, the coordinate y^+ of the maximum depends on both Reynolds and Prandtl numbers.

In the same way as θ'^+, all the profiles for $\overline{v^+\theta^+}$ (figure 5.3a) collapse in the outer region, for $y/h > 0.1$ and Péclet numbers greater than approximately 225. The minima location of $\overline{v^+\theta^+}$ is always in the outer region. This location depends on both the Reynolds and Prandtl numbers.

Finally, $\overline{u^+\theta^+}$ is shown in figures 5.3b and 5.3d. The behaviour of this function is the same as the previous turbulent intensities. Values collapse from $y/h = 0.07$ up to the center of the channel when $Pe_\tau > 325$. Regarding the location of the function maxima, the analysis is the same as for θ'^+, and the
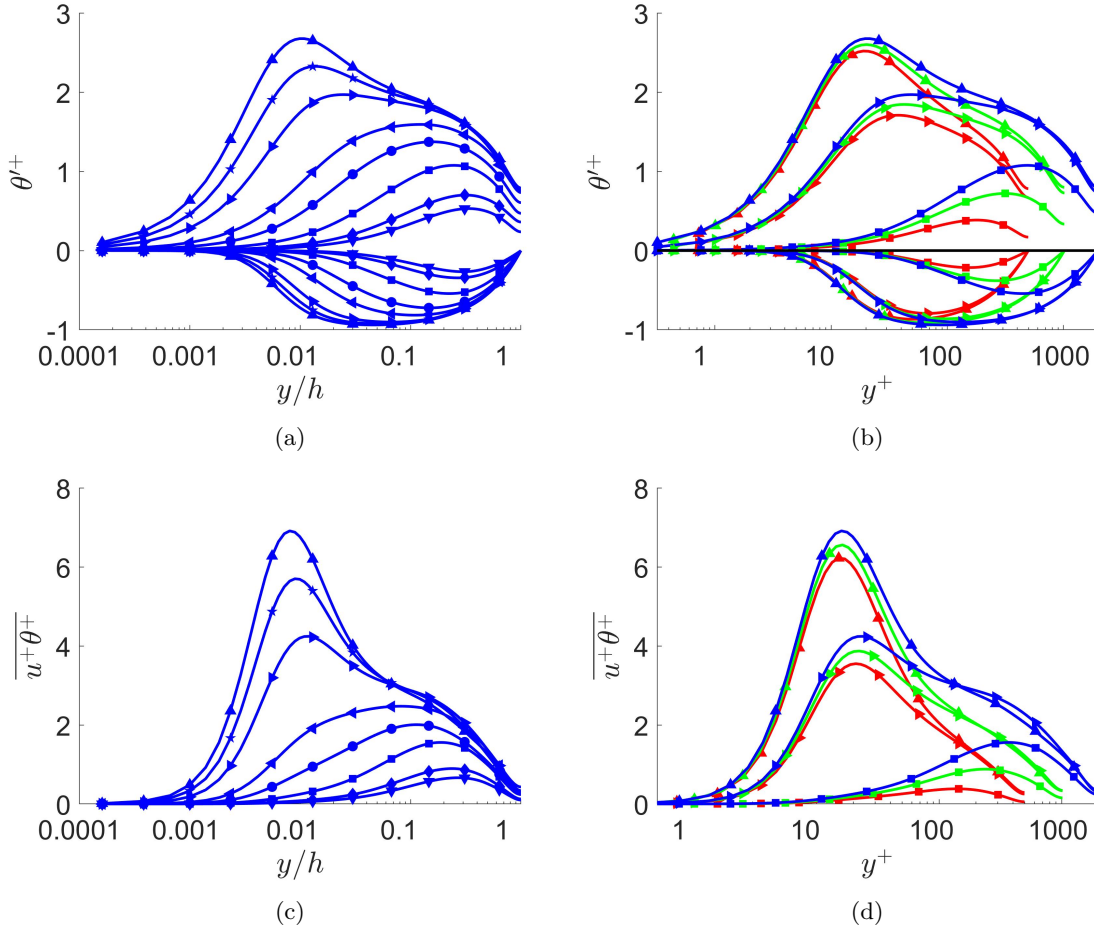
Figure 5.3: Root mean square of the temperature variance and wall-normal heat flux for (a) $Re_\tau = 2000$ as a function of y/h and (b) $Pr = 0.71$, 0.3 and 0.02 as a function of y^+. Streamwise heat flux for (c) $Re_\tau = 2000$ as a function of y/h and (d) $Pr = 0.71$, 0.3 and 0.02 as a function of y^+. Colours as in table 5.1 and symbols as in table 5.2.

threshold is again $Pr \approx 0.3$. For Prandtl numbers above this threshold, these maxima are located in the buffer layer or logarithmic region. Their positions are independent of the Re_τ number. For the lower Prandtl numbers, the y^+ coordinate of the maxima depends on both Re_τ and Pr. These similitudes between θ'^+ and $\overline{u^+\theta^+}$ come from the high correlation that exists between the streamwise velocity and thermal field. However, as the Prandtl number is reduced, this correlation is also reduced, and the differences between the different profiles are increased.

As a general rule, one can conclude that the location of the maxima does not depend on the Reynolds number when the maximum is located in the buffer layer or in the logarithmic region. However, for lower Prandtl numbers, the maxima location moves to the outer region. Here, it does depend on the Reynolds number.

In every case, the values of the root mean square of the temperature variance and both heat fluxes decrease when Pr decreases. This means that, for lower Prandtl numbers, turbulent intensities decrease, in other words, the thermal flow is less turbulent. This confirms the result obtained during the validation
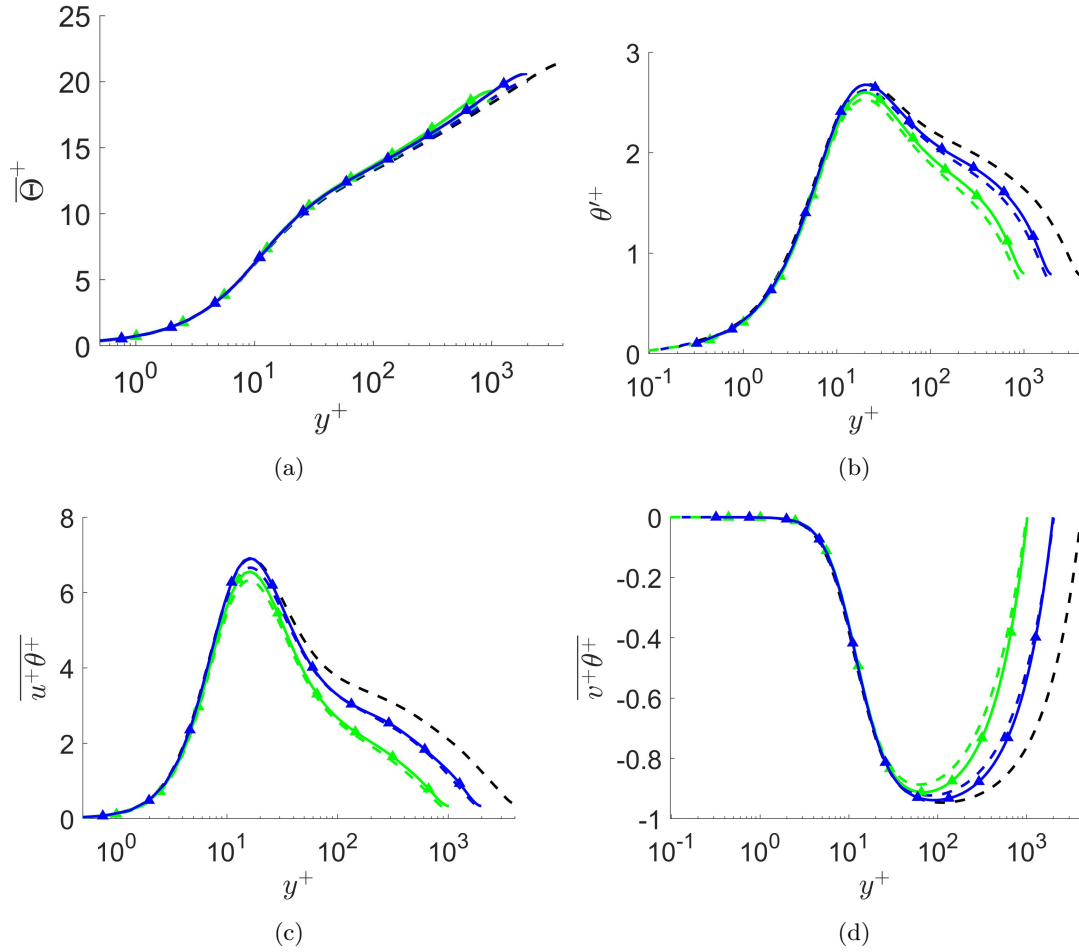
Figure 5.4: Temperature statistics of this work (solid lines) and the ones obtained by Pirozzoli et al. [50] (dashed lines; black dashed line is for $Re_\tau = 4000$). $Pr = 0.71$ in all cases. (a) $\overline{\Theta}^+$, (b) θ'^+, (c) $\overline{u^+\theta^+}$ and (d) $\overline{v^+\theta^+}$. Colours as in table 5.1 and symbols as in table 5.2.

of the simulations when molecular and turbulent heat fluxes were obtained.

Boundary conditions influence

The results obtained for the cases of $Pr = 0.71$ and $Re_\tau = 1000$ and 2000 are now compared with the ones calculated by Pirozzoli et al. [50], where a different boundary condition to the MBC is used. In Pirozzoli et al. [50], the uniform heat generation boundary condition was used. Therefore, one cannot expect to obtain the same results, but the tendencies of the temperature and its intensities would not differ abruptly.

In figure 5.4, the mean temperature, the root mean square of the temperature variance, and the streamwise and wall-normal heat fluxes are represented, in figures 5.4a, 5.4b, 5.4c and 5.4d, respectively. Indeed, all magnitudes increase when the MBC is used, specially in the central region of the channel. Values for $Pr = 0.71$ and $Re_\tau = 4000$ obtained in [50] are also represented with the dashed black line to visualize the tendency of the variables when increasing the Reynolds number.

Nu	Present work	Pirozzoli et al. [50]
$Re_\tau = 1000$	85.0416	86.0682
$Re_\tau = 2000$	153.378	159.854

Table 5.4: Comparison of the Nusselt number for $Pr = 0.71$ and $Re_\tau = 1000$ and 2000 with the ones obtained by Pirozzoli et al. [50].
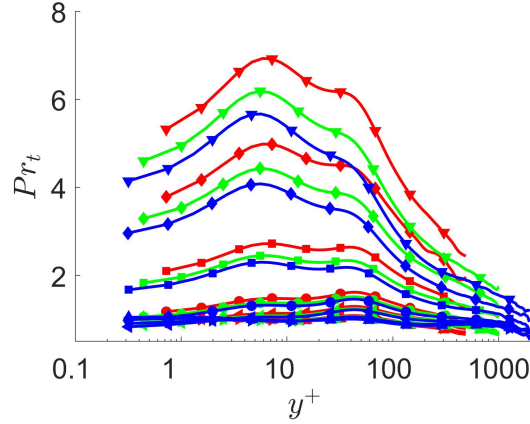
Figure 5.5: Turbulent Prandtl number. Colours as in table 5.1 and symbols as in table 5.2.

With respect to the Nusselt number, table 5.4 shows a comparison between the Nusselt numbers obtained for $Pr = 0.71$ and $Re_\tau = 1000$ and 2000 in this work and the ones obtained in [50]. A decrease in the value of Nu is obtained when the MBC is used. This was expected since the temperature profiles were slightly greater. Nevertheless, the results are reasonably similar.

Turbulent Prandtl number

Definition of the turbulent Prandtl number, Pr_t (already defined in section §2.3.1 equation (2.16)), which represents the ratio between the momentum eddy diffusivity and the heat transfer eddy diffusivity, is written here again for the sake of readability

$$Pr_t = \frac{\overline{u^+ v^+}}{\overline{v^+ \theta^+}} \frac{d\overline{\Theta}^+/dy^+}{d\overline{U}^+/dy^+}.$$ (5.4)

Pr_t is shown, as a function of y^+, in figure 5.5. These results reaffirm the well-known law that states that Pr_t is approximately constant and equal to 1 for medium molecular Prandtl numbers but it increases for low Prandtl numbers (Kawamura et al. [40]). It can be seen how for $Pr \leq 0.05$ the values of Pr_t are higher, not only in the wall vicinity but along the whole channel. In addition, an increase in the Reynolds number entails a slight decrease in the turbulent Prandtl number. Therefore, new scaling laws for low Prandtl numbers are needed.

Turbulent budgets

Budgets of the temperature variance, k_θ^+ (2.19)-(2.21d), the dissipation rate of the temperature variance, ε_θ^+ (2.22)-(2.24g), and the turbulent heat fluxes, $\overline{u_i^+ \theta^+}$ (2.25)-(2.28f), have been calculated. These equations are defined in subsection §2.3.1.
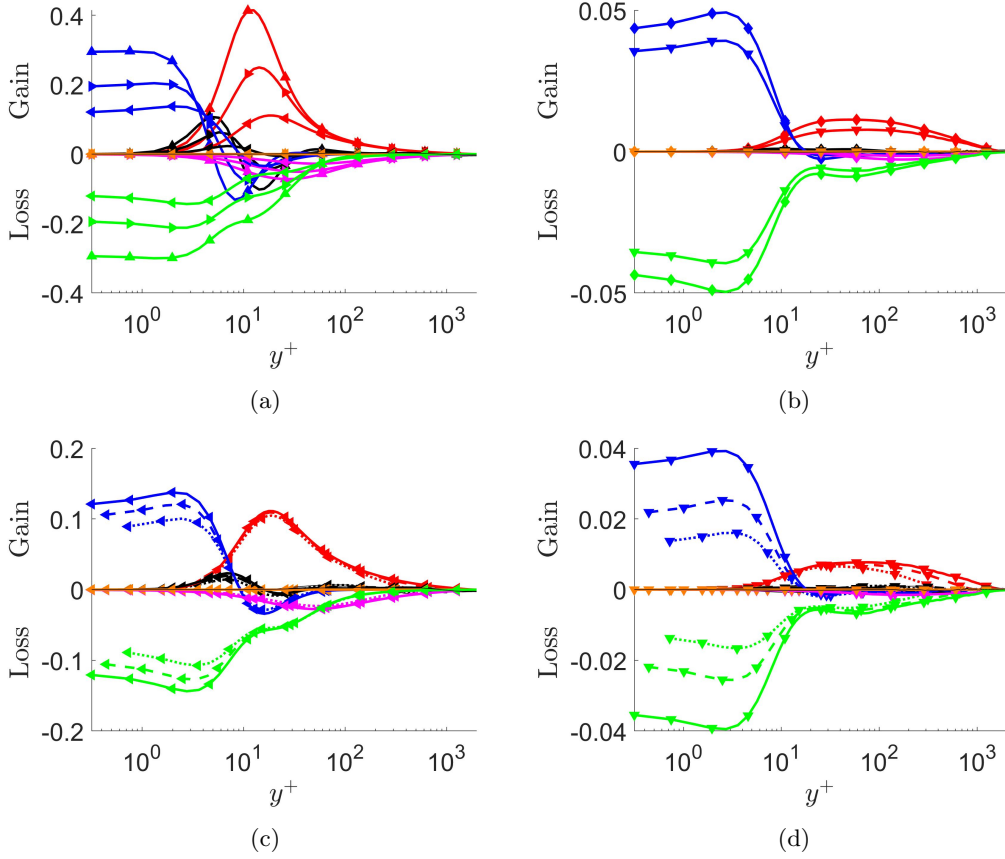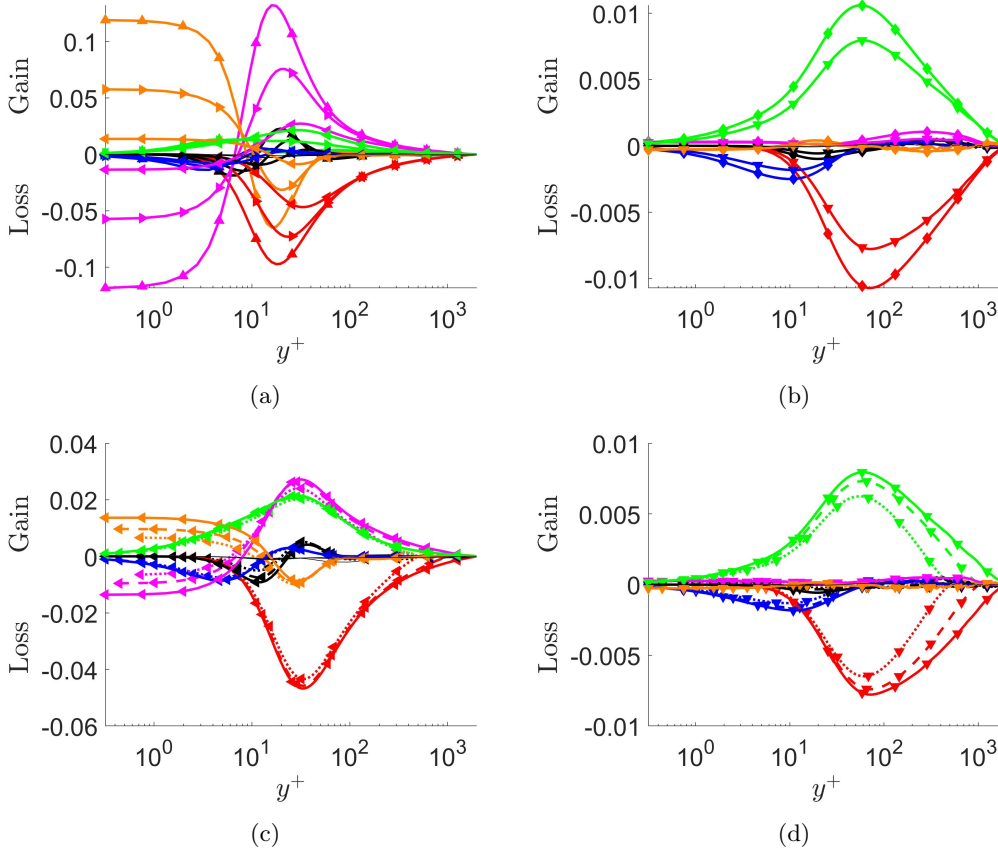
Figure 5.6: Budgets of the streamwise heat flux, $\overline{u^+\theta^+}$, for $Re_\tau = 2000$ and (a) medium Prandtl numbers: $Pr = 0.71$, 0.3 and 0.1; (b) low Prandtl numbers: $Pr = 0.01$ and 0.007. $Re_\tau = 2000$, 1000 and 500 for (c) $Pr = 0.1$ and (d) $Pr = 0.007$. Colours here denote budget terms: production (red), turbulent diffusion (black), viscous diffusion (blue), dissipation (green), pressure-temperature-gradient correlation (magenta) and pressure diffusion (orange). Line style determines the Re_τ number: $Re_\tau = 2000$ (solid line), $Re_\tau = 1000$ (dashed line) and $Re_\tau = 500$ (pointed line). Symbols as in table 5.2.

The idea of this subsection is to check if the budget terms scale for low values of the Prandtl number. As an anticipated result, for low Prandtl numbers, scaling failures are amplified.

Budgets for $\overline{u^+\theta^+}$ are shown in figure 5.6. Cases for $Re_\tau = 2000$ and medium Prandtl numbers (0.71, 0.3 and 0.1) are plotted in figure 5.6a. For the same Reynolds, the lowest Prandtl numbers (0.01 and 0.007) are selected for figure 5.6b. On the other two subfigures, the analysis is done for a variation of Re_τ. Budget terms for one of the medium Prandtl numbers, 0.1, are plotted for all three Reynolds numbers in figure 5.6c. Meanwhile, the lowest Prandtl, 0.007, is used, again for all three Reynolds numbers, in figure 5.6d. For both, medium and low Prandtl numbers, dissipation is compensated by viscous diffusion near the wall. From the end of the buffer layer up to the center of the channel, the production term increases and becomes more important than the viscous diffusion. In this part of the channel, for medium Prandtl numbers (figures 5.6a and 5.6c), dissipation and pressure-temperature gradient correlation terms are compensated by production. However, for low values of Pr (figures 5.6b and 5.6d), production compensates dissipation, and the rest of terms are negligible. Regarding the scaling

70

Figure 5.7: Budgets of the wall-normal heat flux, $\overline{v^+\theta^+}$, for $Re_\tau = 2000$ and (a) medium Prandtl numbers: $Pr = 0.71$, 0.3 and 0.1; (b) low Prandtl numbers: $Pr = 0.01$ and 0.007. $Re_\tau = 2000$, 1000 and 500 for (c) $Pr = 0.1$ and (d) $Pr = 0.007$. Colours here denote budget terms: production (red), turbulent diffusion (black), viscous diffusion (blue), dissipation (green), pressure-temperature-gradient correlation (magenta) and pressure diffusion (orange). Line style determines the Re_τ number: $Re_\tau = 2000$ (solid line), $Re_\tau = 1000$ (dashed line) and $Re_\tau = 500$ (pointed line). Symbols as in table 5.2.

of the budget terms, it can be seen that it presents several errors when Pr varies (figures 5.6a and 5.6b). Not only the magnitudes of all the budget terms change along the entire channel, but also the location of the maximum changes depending on the Prandtl number. When Pr is kept constant and with a medium value (figure 5.6c) all terms seem to scale well in the logarithmic layer and in the center of the channel (difference are due to the difference in Re_τ). However, in the wall vicinity, viscous diffusion and dissipation present noticeable differences from one case to another. When Pr is reduced (figure 5.6d), these differences are even larger.

Budgets for $\overline{v^+\theta^+}$ are shown in figure 5.7. The arrangement of the subfigures is the same as for the streamwise heat flux. It can be seen how for medium Prandtl numbers (figures 5.7a and 5.7c) the more important budget terms are pressure-temperature gradient correlation, pressure diffusion, dissipation and production. However, when Pr is reduced (figures 5.7b and 5.7d), dissipation becomes more important than both pressure terms. For the lowest Prandtl numbers, these pressure terms become negligible and production is compensated only by the dissipation term. Dissipation becomes more important for lower
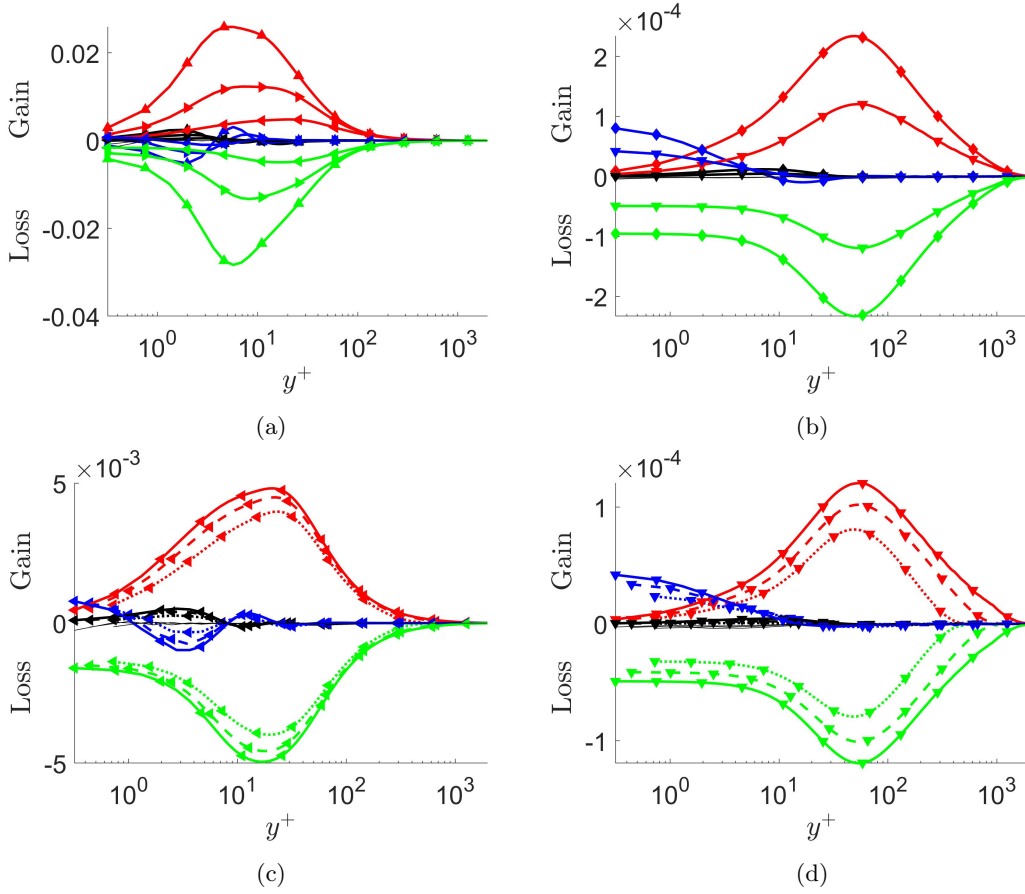
71
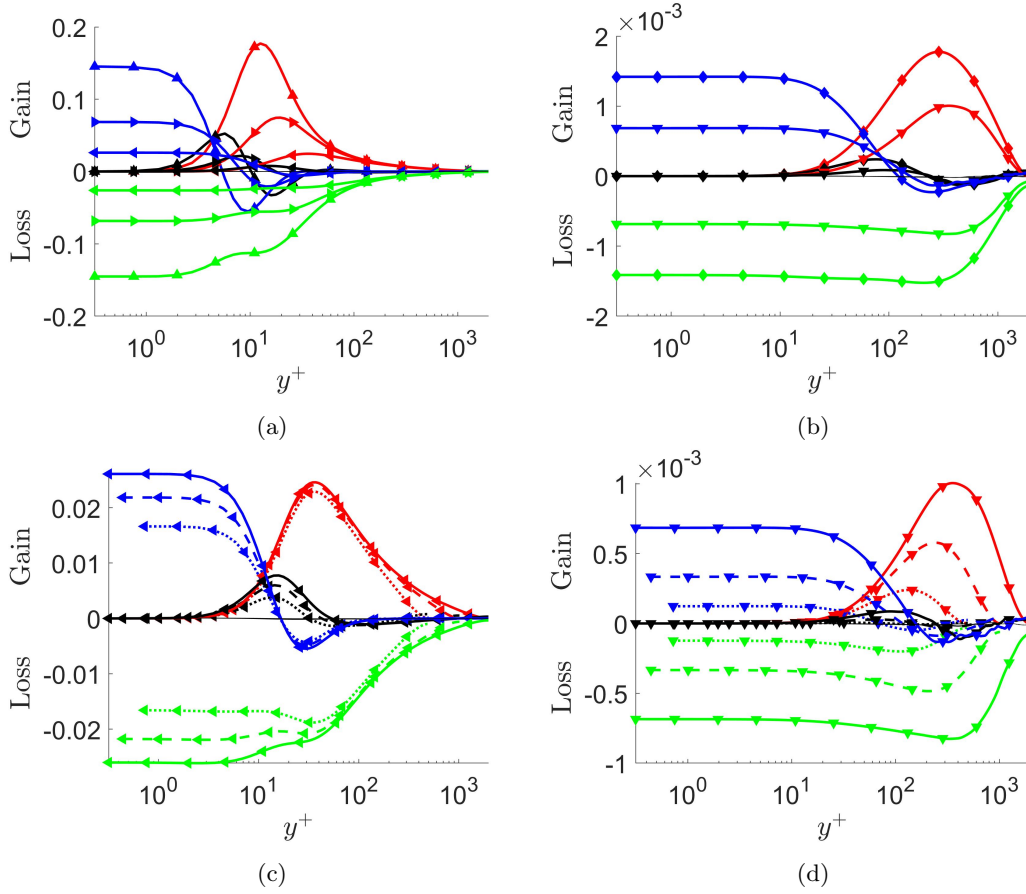
Figure 5.8: Budgets of the temperature variance, k_θ^+, for $Re_\tau = 2000$ and (a) medium Prandtl numbers: $Pr = 0.71$, 0.3 and 0.1; (b) low Prandtl numbers: $Pr = 0.01$ and 0.007. $Re_\tau = 2000$, 1000 and 500 for (c) $Pr = 0.1$ and (d) $Pr = 0.007$. Colours here denote budget terms: production (red), turbulent diffusion (black), viscous diffusion (blue) and dissipation (green). Line style determines the Re_τ number: $Re_\tau = 2000$ (solid line), $Re_\tau = 1000$ (dashed line) and $Re_\tau = 500$ (pointed line). Symbols as in table 5.2.

Prandtl numbers since it occurs in eddies of a larger scale, as it was seen in the visualization of the velocity and temperature structures in section §4 in figure 4.2. Regarding the scaling of the budget terms, the same problems as for $\overline{u^+\theta^+}$ appear. For a constant Re_τ (figures 5.7a and 5.7b), the magnitude of the budget terms and the location of their maxima do not scale properly. When Pr is kept constant with value 0.1 (figure 5.7c) all terms seems to scale well except for the pressure terms in the near wall region. For the lowest Prandtl number (figure 5.7d) scaling failures are seen in the center of the channel for the production and dissipation terms.

Budget terms for k_θ^+ are shown in figure 5.8. Again, the sub-figures information is presented in the same order as in the previous ones. For all cases, dissipation compensates molecular diffusion in the wall vicinity and production in the center of the channel. The y^+ coordinate where the production term becomes more important than molecular diffusion increases with a decrease of the Prandtl number. Turbulent diffusion appears to be more noticeable at the end of the buffer layer for medium Prandtl numbers. The scaling law used for these budget terms presents the same problems as before when a variation in the Prandtl number is introduced (figures 5.8a and 5.8b). In addition, the problem for the

Figure 5.9: Budgets of the dissipation rate of the temperature variance, ε_θ^+, for $Re_\tau = 2000$ and (a) medium Prandtl numbers: $Pr = 0.71$, 0.3 and 0.1; (b) low Prandtl numbers: $Pr = 0.01$ and 0.007. $Re_\tau = 2000$, 1000 and 500 for (c) $Pr = 0.1$ and (d) $Pr = 0.007$. Colours here denote budget terms: summation of the four production terms (red), turbulent diffusion (black), viscous diffusion (blue) and dissipation (green). Line style determines the Re_τ number: $Re_\tau = 2000$ (solid line), $Re_\tau = 1000$ (dashed line) and $Re_\tau = 500$ (pointed line). Symbols as in table 5.2.

dissipation term is even more complex. In the buffer layer, not only the magnitude of this term changes, but also its morphology. For a variation of Reynolds and $Pr = 0.1$ (figure 5.8c), the same scaling problem for dissipation arises again. Molecular and turbulent diffusion also present scaling problems in the buffer layer. For the lowest Prandtl number (figure 5.8d) a better scaling is needed.

Finally budget terms for ε_θ^+ are shown in figure 5.9. The cases shown in each sub-figure are the same as in the previous analysis. Production is mostly compensated by dissipation, except in the wall vicinity, where viscous diffusion overcomes the production term. For lower Prandtl numbers, the effect of viscous diffusion close to the wall is more remarkable. The scaling used for ε_θ^+ presents the same problems for variations of Prandtl numbers (figures 5.9a and 5.9b). When the Reynolds number is changed and $Pr = 0.1$ (figure 5.9c) scaling errors appear in the logarithmic region for production and dissipation terms. Also, in the buffer layer, the viscous diffusion term does not scales properly. For $Pr = 0.007$ (figure 5.9d), the differences in the production and dissipation terms are larger.

In general, it is seen that scaling of the budget terms fail for lower Prandtl numbers, especially in

the near wall region. The most conflicting terms are dissipation and viscous diffusion. Also, remark the scaling errors in the pressure terms for $\overline{v^+\theta^+}$ and the production term for ε_θ^+. It has been seen through all this section that the behaviour of the thermal field changes for low Prandtl numbers. Therefore, one could have expected these scaling differences. This suggest that the modeling of some of the budget terms depends on both Re_τ and Pr, which makes their modeling a very complex problem.

Conclusions

A new set of Direct Numerical Simulations of turbulent heat transfer in a channel flow are presented. Uniform heating from both walls is used as the boundary condition. The effects in the thermal flow of Re_τ and medium to low molecular Prandtl numbers is studied for a range of values of: $Re_\tau = 500$, 1000 and 2000; and $Pr = 0.007 - 0.71$.

A balance of the heat fluxes is calculated to validate the simulations. It is seen that when Pr is reduced, molecular heat flux becomes more important than turbulent heat flux. Indeed, for the lowest Prandtl number, turbulent heat flux is almost negligible except in the central region of the channel.

Mean temperature profiles, the diagnostic function and turbulent intensities (θ'^+, $\overline{u^+\theta^+}$ and $\overline{v^+\theta^+}$) are shown. The logarithmic region appears only for Prandtl numbers greater than approximately 0.3. The von Kármán constant has been calculated, obtaining an approximately constant value of $\kappa_t = 0.43$ for $Re_\tau >= 1000$. The values of the diagnostic function in the central region of the channel collapse for $Pe_\tau > 30$. On the other hand, the morphology of the turbulent intensities change when $Pr > 0.3$. Also, in the outer region, their values collapse when the Péclet number is greater than 325 for θ'^+ and $\overline{u^+\theta^+}$; and 225 for $\overline{v^+\theta^+}$. In addition, the location of the maxima of the functions does not depend on the Reynolds number when the maximum is located in the buffer layer or in the logarithmic region. However, for lower Prandtl numbers, the maxima location moves to the outer region and it does depend on the Reynolds number. The absolute values of all three intensities decrease when Pr is reduced, which means that, in fact, the thermal flow is less turbulent.

The Nusselt number is derived from the mean temperature profile. It is seen that it can be represented with a linear logarithmic expression for medium-low to medium Prandtl numbers. This range seems to increase, at least the lower limit of Pr, when Re_τ is increased. However, the upper limit of the linear behaviour is not captured in this section, since it is greater than 0.71, but it will be studied in next subsection. Another dimensionless number calculated is the turbulent Prandtl number. As it was known, for $Pr > 0.05$, its value is more or less constant and approximately 1 in all the channel. For $Pr \leq 0.05$, the turbulent Prandtl number increases as the molecular Prandtl or Re_τ decrease.

A comparison with the results from [50] for the simulations of higher Reynolds and a value of Prandtl of $Pr = 0.71$ have been done. For that work a boundary condition different to the MBC and similar to the one used in [30] was used. Results are not exactly the same but similar. Also, tendencies of the thermal variables are the same. Thermal values tend to increase when the MBC is used, especially in the central region of the channel.

Finally, turbulent budgets for heat fluxes, temperature variances and its dissipation rate are presented. For $\overline{v^+\theta^+}$, the pressure terms become negligible when Pr is reduced, and dissipation compensates the production term. As it was expected, turbulent diffusion is negligible for all low Prandtl number cases. Also, scalings of the budget terms are analyzed. It is seen that for low Prandtl numbers, any of them work properly and a deeper study is needed. The most conflicting terms, especially in the near wall region, are dissipation and viscous diffusion, pressure terms for $\overline{v^+\theta^+}$ and production for ε_θ^+.

Finally, to help other researchers to test their theories, the statistics of all simulations can be downloaded from the following website:

http://personales.upv.es/serhocal/.

Pr	0.007	0.05	0.3	0.71	1	2	4	7	10
Symbol	$\triangledown$	$\triangleright$	$\triangle$	$\bigcirc$	$\triangledown$	$\square$	$\bigcirc$	$\triangle$	$*$

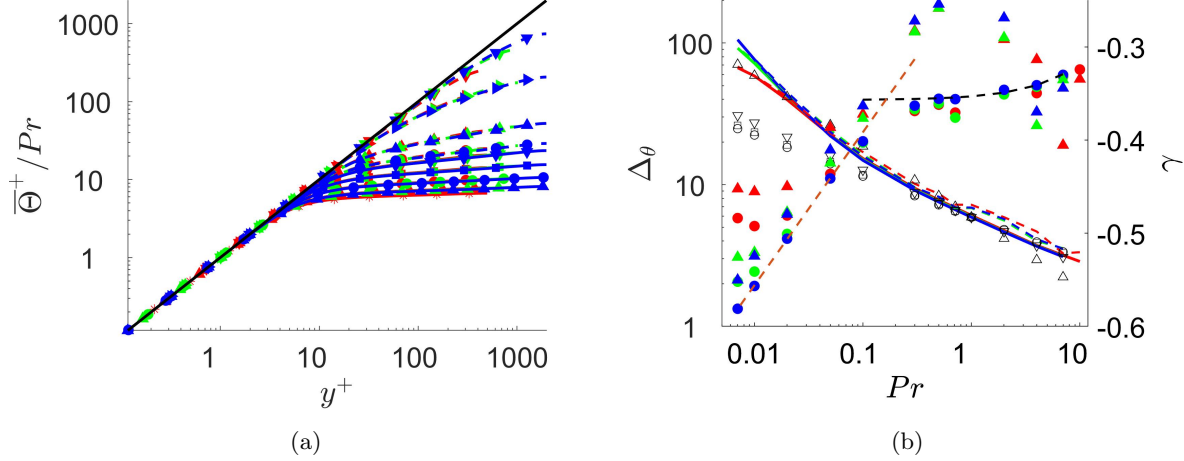Table 5.5: Symbols used to identify the Prandtl numbers through all the figures of this subsection.

(a)　　　　　　　　　　　　　　　　　(b)

Figure 5.10: (a) $\overline{\Theta}^+/Pr$. Black line represents the law of the wall, $\overline{\Theta}^+ = Pry^+$. (b) Left axis: solid and dashed lines represent Δ_θ as a function of Pr using and not using a linear interpolation of $\overline{\Theta}^+/Pr$ in between two mesh points, respectively. Black empty symbols represent Δ_θ according to Shaw and Hanratty 1977 [79] (squares): $\Delta_\theta \sim Pr^{-0.3}$; Kader 1981 [31] (triangle down): $\Delta_\theta \sim Pr^{-1/3}$; Na et al. 1999 [43] (triangle up): $\Delta_\theta \sim Pr^{-0.5}$; and Schwertfirm and Manhart 2007 [46] (circle): $\Delta_\theta \sim Pr^{-0.29}$. Right axis: circles and triangles represent values of γ with and without the linear interpolation of $\overline{\Theta}^+/Pr$, respectively. Black and orange dashed lines represent the scaling of γ for medium–high and low Prandtl numbers, respectively, using the linear interpolation of $\overline{\Theta}^+/Pr$. Colours as in table 5.1 and symbols as in table 5.5.

5.1.2　Medium and low Reynolds numbers and high Prandtl numbers

In this subsection, the results of simulations with $Pr \geq 1$ will be presented, with $Re_\tau = 500$, 1000 and 2000, reaching a Prandtl number of 10, 7 and 7, respectively. Symbols used to distinguish among the different Prandtl number in figures of this subsection (unless otherwise specified) are collected in table 5.5. Prandtl number lower than 1 will also be used to compare the different behaviours of the thermal field. These cases where $Pr < 1$ will be distinguished with dashed lines.

Temperature statistics

The mean temperature, $\overline{\Theta}^+$, is presented in figure 5.10a as $\overline{\Theta}^+/Pr$. The law of the wall, $\overline{\Theta}^+ = Pry^+$, is fulfilled for every case close to the wall. The size of this region of the flow, Δ_θ, i.e. the conductive sublayer, is determined here by the value of the y^+ coordinate where $\overline{\Theta}^+$ differs by a 5% with the law of the wall.

As its name indicates, in this region the heat transferred by conduction is dominant over the turbulent heat flux. It can be seen how this layer gets thinner as the Prandtl number increases. In figure 5.10b it is represented Δ_θ for every case. Due to the discretization of the problem, there is noise in the value of Δ_θ,
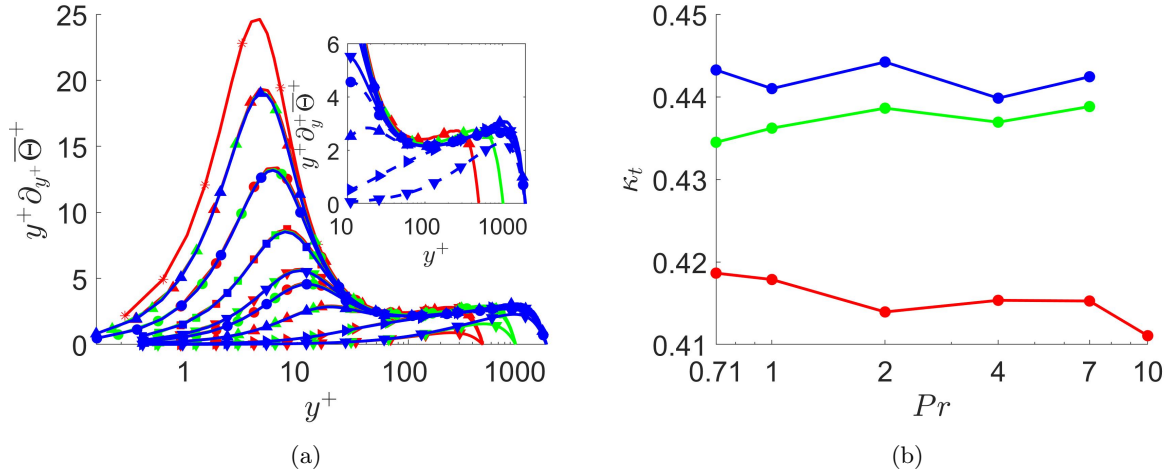
Figure 5.11: (a) Diagnostic function of $\overline{\Theta}^+$. Zoom of the logarithmic layer. (b) Von Kármán constant as a function of Prandtl number. Colours as in table 5.1 and symbols as in table 5.5.

specially when its value is low, see dashed lines of figure 5.10b. A linear interpolation of $\overline{\Theta}^+/Pr$ between the two closest mesh points where $\overline{\Theta}^+$ differs by a 5% with the law of the wall gives a more realistic result of where Δ_θ is actually located (solid lines of figure 5.10b). The depth of the conductive sublayer ranges from values of 100 for very low Prandtl numbers down to barely 3 wall units for $Pr = 7$ and 10. This is a great indicator that for low Prandtl numbers, the thermal field is dominated by conductive heat transfer, and as the Prandtl increases, the turbulent heat transfer overcomes the conductive one.

The classical scaling proposed for Δ_θ is a power function, such as $\Delta_\theta \sim Pr^{-0.5}$, $\Delta_\theta \sim Pr^{-1/3}$, $\Delta_\theta \sim Pr^{-0.3}$ or $\Delta_\theta \sim Pr^{-0.29}$, depending on the range of Prandtl numbers, [43, 31, 79, 46], respectively. A more precise way to define the scaling of Δ_θ is using a power function with a dependence on the Prandtl number in the exponent, $\Delta_\theta \sim Pr^\gamma$, where $\gamma = \gamma(Pr)$. Thus, the following relation can be used $\Delta_\theta = aPr^\gamma$, where a must be the value of Δ_θ for $Pr = 1$. Then, the value of γ for every other Prandtl numbers is calculated as $\gamma = \ln(\Delta\theta/a)/\ln(Pr)$ to fit the data. Note that, for the value of γ at $Pr = 1$ an indeterminate form of the type $0/0$ is obtained. Therefore, limits must be used to obtain this specific value. As can be seen in figure 5.10b, the value of γ is a linear function of Pr for $Pr \geq 0.5$ (x-axis is in logarithmic scale). Noise on the results arises near $Pr = 1$, where very small errors entail big discrepancies in the value of γ, as it is the case for $Pr = 0.71$. As can be seen, if the interpolation of $\overline{\Theta}^+/Pr$ is not done, even higher errors are obtained for γ at Pr near 1 (see triangles of figure 5.10b). This is due to the sensitivity of the fitting of a power function near values with base 1. The relation for Δ_θ obtained is $\Delta_\theta = 5.9Pr^{-0.36+0.004Pr}$. The value of γ is reasonable comparable to other values given in previous works, which ranged from -0.3 to -0.5, depending on the Prandtl number. As seen in figure 5.10b, for high Prandtl numbers, the scaling proposed by Shaw and Hanratty 1977 [79] (squares): $\Delta_\theta \sim Pr^{-0.3}$; Kader 1981 [31] (triangle down): $\Delta_\theta \sim Pr^{-1/3}$; and Schwertfirm and Manhart 2007 [46] (circle): $\Delta_\theta \sim Pr^{-0.29}$, are very precise for the range of Prandtl between 0.3 to 7. Furthermore, the impact on Δ_θ due to the Prandtl number dependence on the exponent appears to be small in the these range of Prandtl numbers. On the other hand, the scaling of Na et al. 1999 [43] (triangle up): $\Delta_\theta \sim Pr^{-0.5}$ provides a more precise result for lower Prandtl numbers. Also, remark the small dependence of Pr in the value of γ. Therefore, considering γ constant in a small range of values of Prandtl would not entail big errors. For low Prandtl numbers and sufficiently high Re_τ, the value of γ is a logarithmic function of Pr. The relation in this case is $\Delta_\theta = 5.9Pr^{-0.23+0.071\log(Pr)}$.
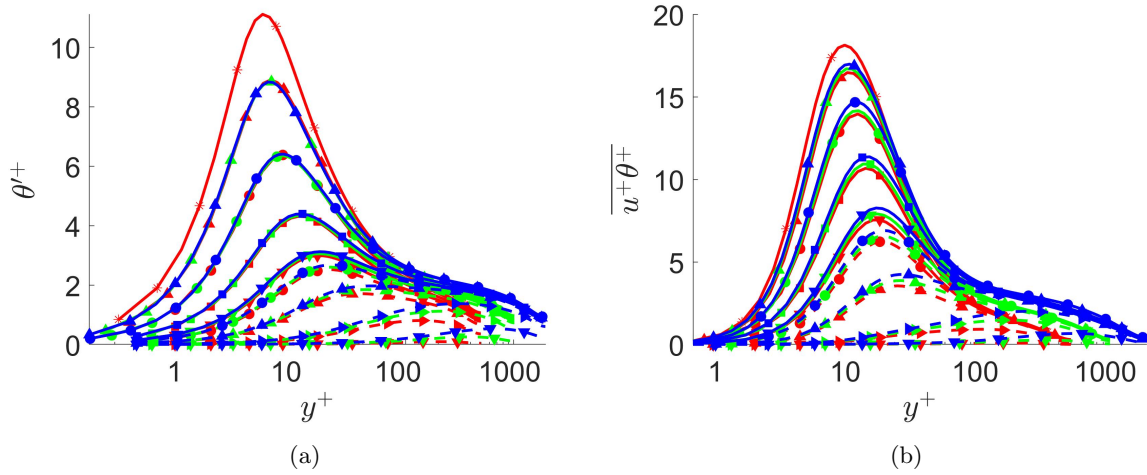
Figure 5.12: (a) Temperature fluctuation, θ'^+, and (b) streamwise heat flux, $\overline{u^+\theta^+}$. Colours as in table 5.1 and symbols as in table 5.5.

As a remark, the definition of Δ_θ could be changed and the limiting value of 5% difference between the wall law and $\overline{\Theta}^+/Pr$ could have been increased or reduced. Then, the value of Δ_θ would had obviously changed. However, in the scaling of Δ_θ with the Prandtl number, the value of γ will remain the same. Therefore, as long as the limiting value of the conductive sublayer is reasonable, the value of γ will always be comparable between different criteria to obtain Δ_θ.

The diagnostic function of the mean temperature, Ξ_T, is represented in figure 5.11a. If the flow presents a logarithmic layer, then Ξ_T must be constant in the region approximately between $y^+ = 70$ and $y/h = 0.2$ [77]. In the work done by Jiménez and Moser 2007 [51] it was stated that the diagnostic function of the velocity field presents a linear dependence with y^+. This dependence tends to 0 as Re_τ goes to infinity. The same occurs for the diagnostic function of $\overline{\Theta}^+$. This linear dependence with y^+, although small, still exists for $Re_\tau = 2000$. One can see in the zoom of figure 5.11a that in the logarithmic region, where the diagnostic function must be a plateau, there is still a small increment. For cases with the lowest Prandtl numbers, Ξ_T does not even collapse in the outer region. As the Prandtl number increases, Ξ_T starts to collapse in the outer region, then in the logarithmic region, and, for the highest Prandtl numbers, also in the buffer layer. Therefore, for medium–high Prandtl numbers, whether a logarithmic region appears or not for the mean temperature profile will only depend on the Reynolds number.

The previous statement can be confirmed calculating the von Kármán constant, κ_t. As in previous section, the logarithmic equation (5.1) is fitted to the value of $\overline{\Theta}^+$. Again, the limits of the logarithmic layer where the fitting is done are set to be $y^+ = 70$ for the lower limit and $y/h = 0.2Re_\tau$ for the upper limit, as in [77]. In figure 5.11b, κ_t is represented for the three Reynolds numbers and $Pr \geq 0.71$. It can be seen how κ_t is approximately constant for a constant Re_τ. The small variation (smaller than 2%) can be due to numerical discrepancies. When the Reynolds number is increased, κ_t slightly increases. Also, differences of κ_t were expected, since for these values of Reynolds number, the logarithmic layer is not perfectly developed. Nevertheless, the value of κ_t seems to converge with the Reynolds number towards a value of roughly 0.45 or slightly above. This result is very close to to the one provided in the work of Pirozzoli et al. [50], where a value of $\kappa_t = 0.46$ is obtained for $Re_\tau = 4000$ and a thermal boundary condition that consisted in a thermal heat generation. Regarding the work of Abe and Antonia [80], where the MBC was also used, a value of $\kappa_t = 0.43$ was obtained for $Re_\tau = 1000$, which agrees with the one presented here.
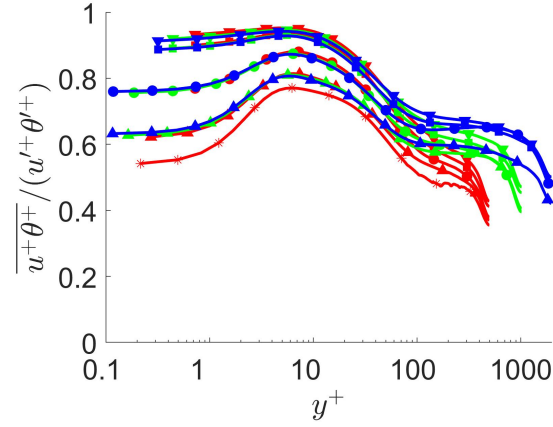
Figure 5.13: Correlation coefficient, $\overline{u^+\theta^+}/(u'^+\theta'^+)$. Colours as in table 5.1 and symbols as in table 5.5.

Information of the turbulent intensities such as the transformed temperature fluctuation, θ'^+, the streamwise heat flux, $\overline{u^+\theta^+}$, the correlation coefficient, $\overline{u^+\theta^+}/(u'^+\theta'^+)$, the wall-normal heat flux, $\overline{v^+\theta^+}$, and a quadrant analysis of $\overline{v^+\theta^+}$, have been calculated. They are represented in figures 5.12, 5.13 and 5.14. One of the main differences between θ'^+ and $\overline{u^+\theta^+}$, is that, at the highest Prandtl numbers, or more precisely, highest friction Péclet numbers, the maximum of θ'^+ does not grow with the Reynolds number (see figure 5.12a). Analogously, this feature is observed in Couette flows for the velocity fluctuation, u'^+, when the Reynolds number is high enough [62]. However, this is the first time that this feature is reported for a thermal Poiseuille flow. This scaling of the maximum of θ'^+ have more benefits in the scaling of some turbulent budgets, as will be seen later.

As reported in section §2.3.1, near the wall, the streamwise velocity and the temperature fields are highly correlated, specially for Prandtl numbers close to 1. But as as the Prandtl number moves away from 1 this correlation is weaker. In figure 5.13, the correlation coefficient is shown for all cases with $Pr \geq 1$. The same tendencies were obtained by Abe et al. [81] for cases with lower Reynolds numbers and Prandtl close to 1. Note that some noise appears at the center due to small values of $\overline{u^+\theta^+}$, u'^+ and θ'^+. Nevertheless, the important result is obtained at $y^+ \approx 10$, where, effectively, the correlation coefficient decreases from 0.95 for $Pr = 1$, down to 0.8 for $Pr = 7$.

The wall-normal heat flux, $\overline{v^+\theta^+}$, is represented in figure 5.14a. For higher Pe_τ, $\overline{v^+\theta^+}$ approaches to its bound value of -1 in a wider region of y. This is in accordance with Townsend's hypothesis [11], applied to the temperature field. Additionally, a quadrant analysis like in [82] has been performed to study the generation mechanism of $\overline{v^+\theta^+}$ compared with the one of $\overline{u^+v^+}$ (figures 5.14b, 5.14c and 5.14d). On one hand, events on the first quadrant, Q1 (θ, $u > 0$ and $v > 0$), and third quadrant, Q3 (θ, $u < 0$ and $v < 0$), are referred to as outward and inward interactions, respectively. On the other hand, the second quadrant, Q2 (θ, $u < 0$ and $v > 0$), and fourth quadrant, (θ, $u > 0$ and $v < 0$), represent ejection and sweep events, respectively. A good scaling in the Reynolds number is observed from figures 5.14c and 5.14d, with indeed similar tendencies for both $\overline{v^+\theta^+}$ and $\overline{u^+v^+}$. Dominant contributions from the sweep events (Q4) appear very close to the wall. At a certain y^+ coordinate, the ejection events (Q2) become the most important. Obviously, this y^+ coordinate is constant for different Reynolds numbers, since the generation mechanism scales with Re_τ. However, the y^+ coordinate where the alternation of the dominant event occurs moves closer to the wall as the Prandtl number increases, going from $y^+ = 16$ for $Pr = 1$ (similar to the $y^+ = 17$ for $Pr = 0.71$ obtained in [82]) to $y^+ = 8$ for $Pr = 7$ (see figure 5.14b). Related with the constant maximum of θ'^+ for different Reynolds numbers, one can see how the maximums of Q1, Q2 and Q3 events also scale for $\overline{v^+\theta^+}$, in contrast to $\overline{u^+v^+}$, where all maximums increase with the
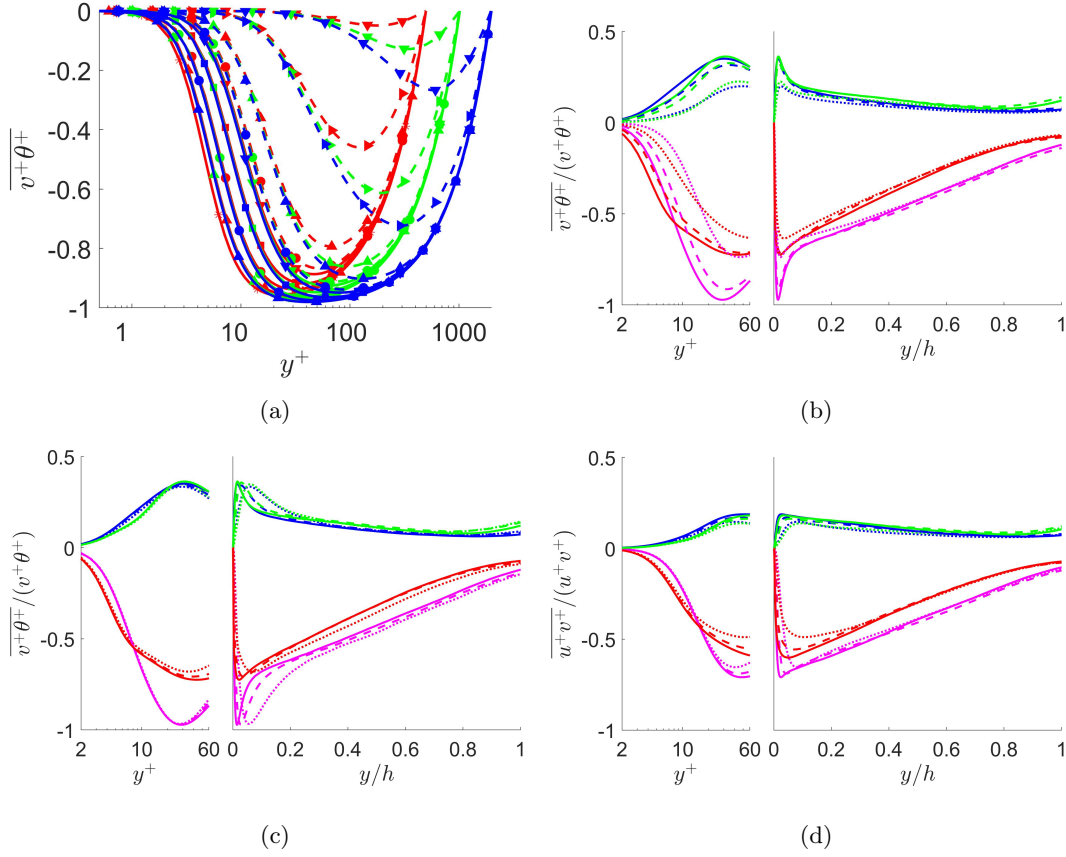
Figure 5.14: (a) $\overline{v^+\theta^+}$. Colours as in table 5.1 and symbols as in table 5.5. Quadrant analysis of $\overline{v^+\theta^+}$ for (b) $Re_\tau = 2000$ and $Pr = 1$ (dotted lines), $Pr = 4$ (dashed lines) and $Pr = 7$ (solid lines) and (c) $Pr = 7$ and $Re_\tau = 500$ (dotted lines), $Re_\tau = 1000$ (dashed lines) and $Re_\tau = 2000$ (solid lines). (d) Quadrant analysis of $\overline{u^+v^+}$ for $Pr = 7$ and $Re_\tau = 500$ (dotted lines), $Re_\tau = 1000$ (dashed lines) and $Re_\tau = 2000$ (solid lines). In (b), (c) and (d) colour blue is for events of Q1, magenta for Q2, green for Q3 and red for Q4.

Reynolds number, as in $\overline{u^+\theta^+}$. Regarding the scaling in the outer region, a good similarity is observed for the cases at $Re_\tau = 2000$ and $Pr = 4$ and 7 in figure 5.14b. However, if the Reynolds or Prandtl number are decreased, some discrepancies appear, specially in the region below $y/h < 0.3$ (see figure 5.14c). The same result was obtained by [82] for a low Prandtl number of 0.025 and Reynolds numbers ranging from 180 up to 1020.

The dimensionless numbers Nu and Pr_t, defined in equations (5.3) and (5.4), respectively, have been calculated. In figure 5.15, Nu is presented as a function of Pr. As shown in previous section, Nu is a power function of Pr for $Pe_\tau \leq 20$. Also, in [40], it was noted that, for $Re_\tau = 180$, the increment of Nu begins to reduce for Prandtl numbers greater than 1. This feature is also observed here for medium–high Prandtl numbers at Re_τ up to 2000. However, it is not Pr that determines when Nu is no longer a power function of Pr, but Pe_τ. As a conclusion, Nu is a power function of Pr in the specific range of the friction Péclet number, $20 \leq Pe_\tau \leq 1500$. Fitting a power function to the data, it is obtained:
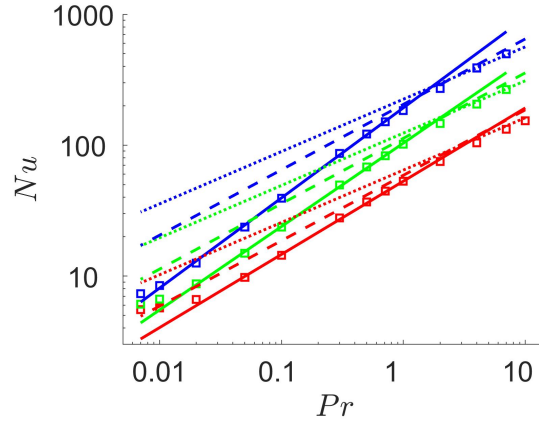
Figure 5.15: Nu as a function of Pr. Squares are the values from the DNS. Solid lines represent correlations from this work (5.5a)-(5.5c). Dotted lines represent Dittus and Boelter correlation (5.6), and, dashed lines represent Kays et al. correlation (5.7). Colours as in table 5.1.

$$Nu = 53.1Pr^{0.560}, \quad \text{for} \quad Re_\tau = 500 \tag{5.5a}$$

$$Nu = 103.7Pr^{0.638}, \quad \text{for} \quad Re_\tau = 1000 \tag{5.5b}$$

$$Nu = 192.9Pr^{0.689}, \quad \text{for} \quad Re_\tau = 2000 \tag{5.5c}$$

for $20 \leq Pe_\tau \leq 1500$. Two more correlations are also included in figure 5.15. On one hand, the correlation obtained by Dittus and Boelter 1930 [83] for turbulent pipe flows

$$Nu = 0.023Re_D^{0.8}Pr^n, \tag{5.6}$$

where Re_D is the Reynolds number based on the diameter of the pipe and $n = 0.4$ since the flow is being heated. On the other hand, the correlation obtained by Kays et al. 1980 [48] for constant temperature walls, which reads

$$Nu = 0.021Re^{0.8}Pr^{0.5}. \tag{5.7}$$

The correlations proposed here (5.5a)-(5.5c) are very precise in the range of $20 \leq Pe_\tau \leq 1500$. However, as mention before, for Prandtl numbers above 1 the scaling of Nu with Pr changes and, in the small range obtained here, Dittus and Boelter correlation (5.6) fits well with an exponent of 0.4 in the Prandtl, while the exponent of 0.5 from the Kays et al. correlation (5.7) seems to be overestimating the value of Nu. Nevertheless, if the scaling of Nu for higher Prandtl numbers is still a power function of Pr with exponent approximately 0.4 cannot be determined with the data from this work only. Even higher Prandtl numbers must be simulated. This, however, is beyond the scope of the study of this work.

With respect to Pr_t an important change in its value near the wall occurs (see figure 5.16a). For medium molecular Prandtl numbers, Pr_t value is approximately 1.1 at the wall, as reported by many other authors [34, 37, 40, 44, 82]. However, for medium–high Prandtl numbers, Pr_t in the wall increases. The reason of this increase can be explained using the decomposition of the fluctuating variables near the wall proposed by Antonia and Kim [34] and Kawamura et al. [40], which was introduced in section §2.3.1, equations (2.17a)-(2.17i). Using the definition of Pr_t, (5.4), where $(d\overline{\Theta}^+/dy^+)/(d\overline{U}^+/dy^+) = Pr$ at the wall, and the approximations of $\overline{v^+\theta^+}$ and $\overline{u^+v^+}$ near the wall, (2.17i) and (2.17g), respectively, one gets $Pr_t|_{y=0} \approx d_{12}/d_{2\theta}$.
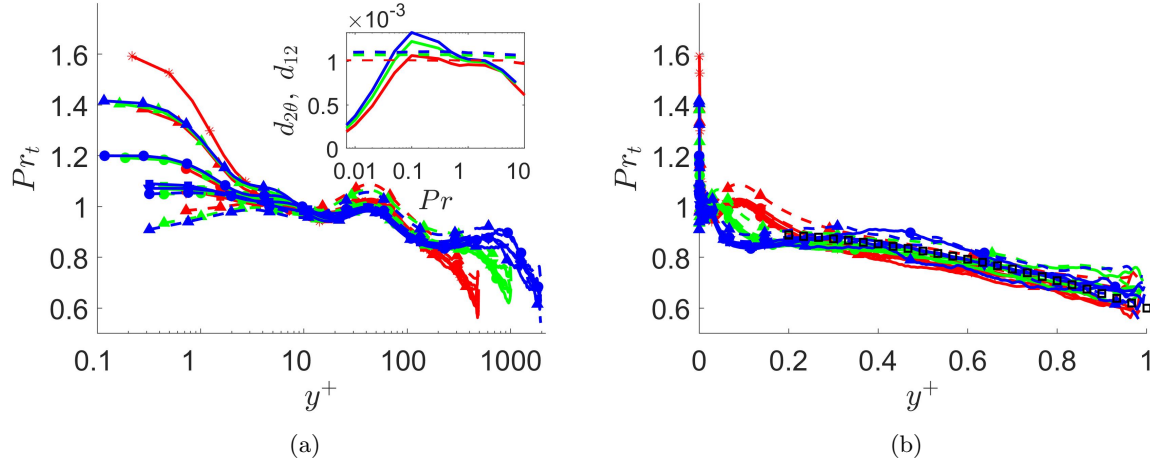
Figure 5.16: (a) Pr_t focused in the near-wall region. Box: Values of $d_{2\theta}$ (solid) and d_{12} (dashed). (b) Pr_t in the core region. Black squares represent the distribution proposed by Abe and Antonia 2009 [81]. Colours as in table 5.1 and symbols as in table 5.5.

The value of these coefficients can be observed in the box inside figure 5.16a. The coefficient $d_{2\theta}$ has a constant value approximately equal to d_{12} in the range of Prandtl numbers near one. However, for $Pr \geq 4$, $d_{2\theta}$ decreases due to the reduction of the normal-wall heat fluxes over the Prandtl number, i.e. $\overline{v^+\theta^+}/Pr$ reduces when the Prandtl is increased above $Pr \approx 4$. This makes Pr_t greater than 1 in the wall. This variation has serious consequences in the modelling of fluids with medium–high Prandtl number, like water, since Pr_t is one of the the main parameters for modelling.

In the core region of the channel, Abe and Antonia 2009 [81] proposed a quadratic distribution for Pr_t:

$$Pr_t = 0.9 - 0.3(y/h)^2. \tag{5.8}$$

In figure 5.16b, it is observed how this approximation captures the mean behaviour of Pr_t, even for Reynolds and Prandtl numbers up to 2000 and 7, respectively.

Turbulent budgets

Turbulent budgets of the temperature variance, k_θ^+ (2.19)-(2.21d), the dissipation rate of the temperature variance, ε_θ^+ (2.22)-(2.24g), and the streamwise, $\overline{u^+\theta^+}$ (2.25)-(2.27f), and wall-normal heat flux, $\overline{v^+\theta^+}$ (2.28a)-(2.28f), are analyzed in this subsection. Reader is referred to subsection §2.3.1 for the equations of the turbulent budgets.

Although it was stated in chapter §4 that the size of the computational box, $L_x = 2\pi h$, $L_y = 2h$ and $L_z = \pi h$, was enough to accurately compute first order statistics, it is also big enough to accurately calculate the turbulent budgets. Figure 5.17 presents the budget terms of k_θ^+ obtained by the code used in this work, for $Pr = 0.71$ and $Re_\tau = 500$ (dashed lines) and 1000 (solid lines). These results have been compared with those obtained by Abe et al. [45] for $Pr = 0.71$ and $Re_\tau = 640$ (dotted lines). The size of the computational box used by Abe et al. [45] is $L_x = 4\pi h$, $L_y = 2h$ and $L_z = 2\pi h$. A perfect collapsing or following of the trends is observed for the budgets of k_θ^+. The same results have been obtained for the budget terms of the heat fluxes, but they are not shown here for brevity. This validates the size of the computational box used in this work to calculate turbulent budgets.

Figures 5.18a, 5.18b, 5.18c and 5.18d present the results obtained for every budget term. Only simulations for the three Reynolds numbers, $Re_\tau = 500$, 1000 and 2000, with $Pr = 2$ and 7 are plotted
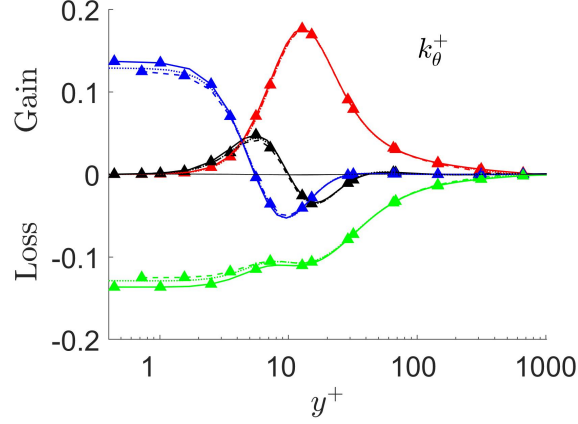
Figure 5.17: Budgets of the temperature variance, k_θ^+ for $Pr = 0.71$. Here, colours denote budget terms: production, turbulent diffusion (black), viscous diffusion (blue) and dissipation (green). Here, line style denotes the Reynolds number: $Re_\tau = 1000$ in solid lines and $Re_\tau = 500$ in dashed lines. $Re_\tau = 640$ in dotted lines is from Abe et al. [45].

for better visibility. The main result obtained is the better scaling near the wall of the viscous diffusion, V_θ^+, and the dissipation, ε_θ^+, in the budget of k_θ^+. For $Pr = 7$, V^+ varies less than 5% in the wall between cases at $Re_\tau = 500$ and 2000. This is a significant reduction compared with the 16% difference obtained for $Pr = 0.71$ in previous section §5.1.1.

The value of V_θ^+ and ε_θ^+ at the wall can be calculated as

$$V_\theta^+\big|_{y^+=0} = \frac{1}{2Pr}\partial_{yy}\overline{\theta'^{+2}}\bigg|_{y^+=0} = -\varepsilon_\theta^+\big|_{y^+=0}. \tag{5.9}$$

Using the approximation of θ'^+ near the wall from equation (2.17f), one gets

$$V_\theta^+\big|_{y^+=0} = -\varepsilon_\theta^+\big|_{y^+=0} \approx Pr b_\theta^2. \tag{5.10}$$

If the first maximum of θ'^+ is constant and it is placed at the same distance to the wall, b_θ will be the same for two cases with the same Prandtl number. It was shown before (figure 5.12a), that this is fulfilled for medium–high Prandtl numbers. Therefore, since b_θ is approximately constant, a good scaling is obtained in the wall. Note that the scaling of $V_\theta^+\big|_{y^+=0}$ and $\varepsilon_\theta^+\big|_{y^+=0}$ with b_θ is quadratic, so small differences in b_θ will make scaling errors larger. In figure 5.19a the values of b_θ for all simulations are represented (solid lines and left axis). Effectively, when the Prandtl number is increased, the values of b_θ converge among the three different Reynolds numbers. Specifically, b_θ seems to converge to a value between 0.3 and 0.4.

In the ideal case where b_θ does not depend neither on Re_τ nor Pr, V_θ^+/Pr and ε_θ^+/Pr will perfectly scale in the wall for all Re_τ and Pr. If, in addition, the wall-normal direction is scaled with $Pr^{1/3}$, as in [40], the peaks of the other terms will also scale. The results for the cases of $Pr = 2$ and 7 are shown in figure 5.19b. The scaling is almost perfect in the entire channel except in the wall, where the small differences in b_θ are amplified due to this quadratic behaviour. In this context, Abe and Antonia [80] found that the peak value of the product term reaches a constant maximum of value $Pr/4$ when the MBC is used, for Re_τ larger than 400. This seems to be convincing with the result obtained here for Re_τ up to 2000.

82
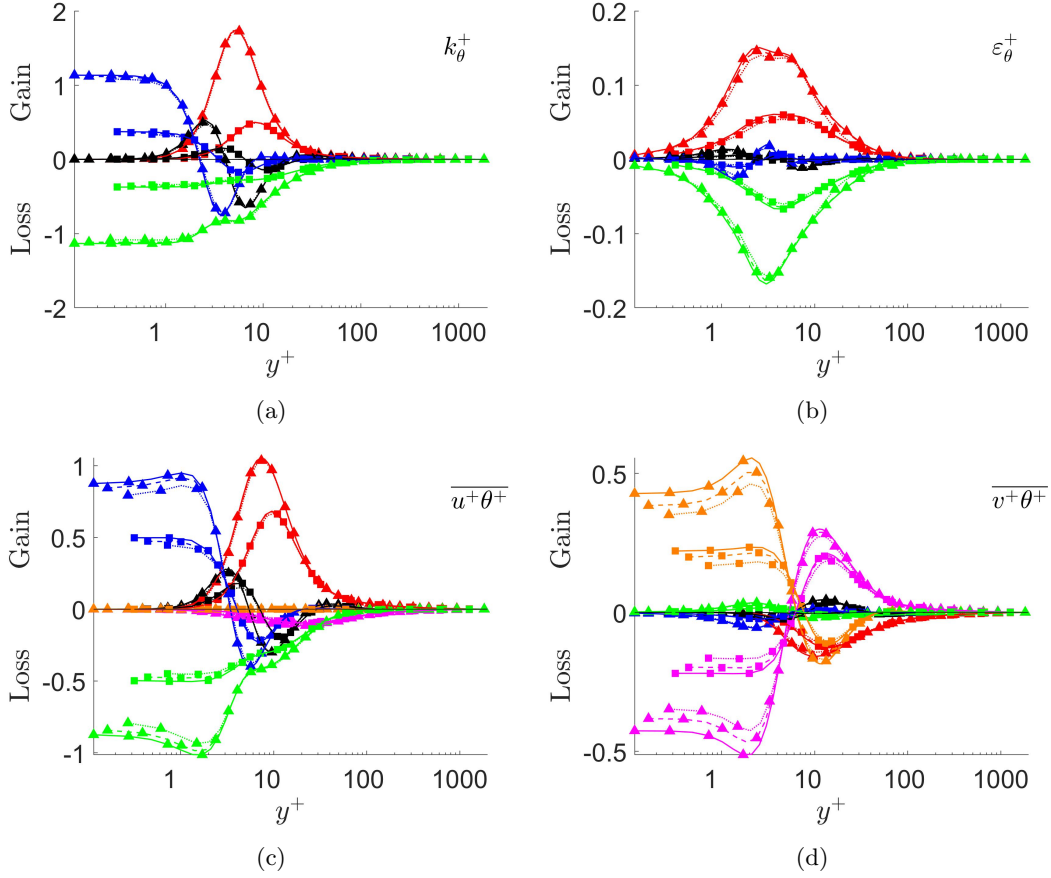
Figure 5.18: Budgets of (a) k_θ^+ (b) ε_θ^+ (c) $\overline{u^+\theta^+}$ and (d) $\overline{v^+\theta^+}$. Here, colours denote budget terms: production or sum of productions in (b) (red), turbulent diffusion (black), viscous diffusion (blue), dissipation (green), pressure strain (magenta) and pressure diffusion (orange). Line style denotes the Reynolds number: $Re_\tau = 2000$ in solid lines, $Re_\tau = 1000$ in dashed lines and $Re_\tau = 500$ in dotted lines. Black line with value 0 is the summation of all terms. Symbols as in table 5.5.

Following this procedure, the same analysis can be done for the viscous diffusion, $V_{u\theta}^+$, and dissipation, $\varepsilon_{u\theta}^+$, in the budget of $\overline{u^+\theta^+}$. Their values at the wall are obtained using the approximation of $\overline{u^+\theta^+}$ near the wall (2.17h), obtaining:

$$V_{u\theta}^+\big|_{y^+=0} = -\,\varepsilon_{u\theta}^+\big|_{y^+=0} \approx \frac{Pr+1}{Pr}\partial_{yy}\overline{u^+\theta^+}\bigg|_{y^+=0} = (Pr+1)c_{1\theta}. \qquad (5.11)$$

Therefore, if the $c_{1\theta}$ values are different, $V_{u\theta}^+$ and $\varepsilon_{u\theta}^+$ will not scale in the wall. In figure 5.19a, the values of $c_{1\theta}$ are represented with dashed lines (right axis). Effectively, $c_{1\theta}$ is not the same for different Reynolds numbers and it oscillates for different Prandtl numbers.

Finally, regarding the budgets of ε_θ^+, Abe et al. [81] did an analysis focusing of the Reynolds dependence of the production terms of the transport equation of the mean square scalar gradient, whose terms are analogous to the ones of ε_θ^+, defined in equations (2.22)-(2.24g). They found that for $Pr = 0.71$, with the increase of the friction Reynolds number, from $Re_\tau = 180$ up to 640, the mixed production, mean gradient production and turbulent production also increased. Meanwhile, the gradient production term

83
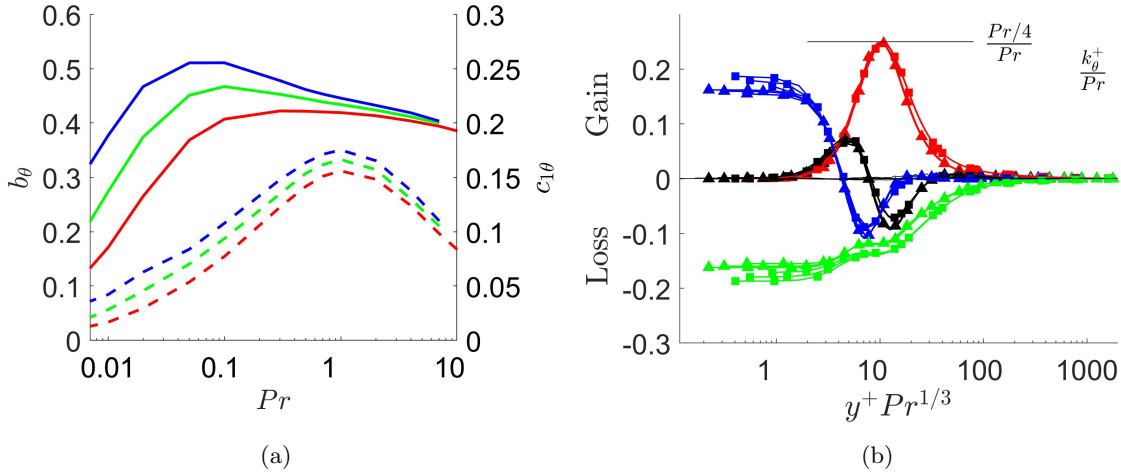
Figure 5.19: (a) Values of b_θ (solid and left axis) and $c_{1\theta}$ (dashed and right axis). Colours as in table 5.1. (b) Budgets of k_θ^+/Pr as a function of $y^+ Pr^{1/3}$. Cases for $Pr = 2$ and 7 are represented. Here, colours denote budget terms: production (red), turbulent diffusion (black), viscous diffusion (blue) and dissipation (green). Line style denotes the Reynolds number: $Re_\tau = 2000$ in solid lines, $Re_\tau = 1000$ in dashed lines and $Re_\tau = 500$ in dotted lines. Black line with value 0 is the summation of all terms. Symbols as in table 5.5.

was independent of the Reynolds number. The same tendency can be observed in figure 5.20a, where the product terms of ε_θ^+ are shown for $Pr = 1$ and $Re_\tau = 500$, 1000 and 2000. However, an interesting result is obtained when the Prandtl number is increased to $Pr = 7$ (figure 5.20b). At this higher Prandtl number, the mixed and mean gradient production seem to be independent of the Reynolds number when this is high enough, i.e. $Re_\tau \geq 1000$. Therefore, the only Reynolds dependent term is the turbulent production. Although not shown here for the sake of brevity, for $Pr = 4$ a clearer difference was notice between the mixed and mean gradient production terms at $Re_\tau = 500$ and 1000. This suggests that a thermal equilibrium is achieved depending on a combination of Re_τ and Pr, i.e. the friction Péclet number, Pe_τ. This thermal equilibrium may be linked with the inner collapsing obtained for the thermal fluctuations with high Péclet numbers (figure 5.12a).

Conclusions

A new set of DNS in a thermal channel flow at medium and medium–high Prandtl numbers have been conducted. The MBC has been used as the thermal boundary condition. The mean temperature field has been studied and a new scaling for the thickness of the conductive sublayer has been proposed for medium to medium–high Prandtl numbers, $\Delta_\theta \sim Pr^{-0.36+0.004Pr}$.

The presence of a logarithmic region in the temperature field is still not perfectly observed at the ranges of Re_τ and Pr simulated, although the Reynolds number dependencies are small. Also, it is demonstrated that, for medium and medium–high Prandtl numbers, whether or not the logarithmic layer perfectly appears, depends only on the Reynolds number. Therefore, the values of κ_t are constant for different Prandtl numbers, but converges towards a constant value when the Reynolds number tends to infinity.

Turbulent intensities have been calculated. The main result is that, it is observed for the first time in Poiseuille thermal channel flows, that the maximum value of θ'^+ does not increase when Re_τ is increased for medium–high Prandtl numbers. As a consequence, in the budgets of the temperature variance, the
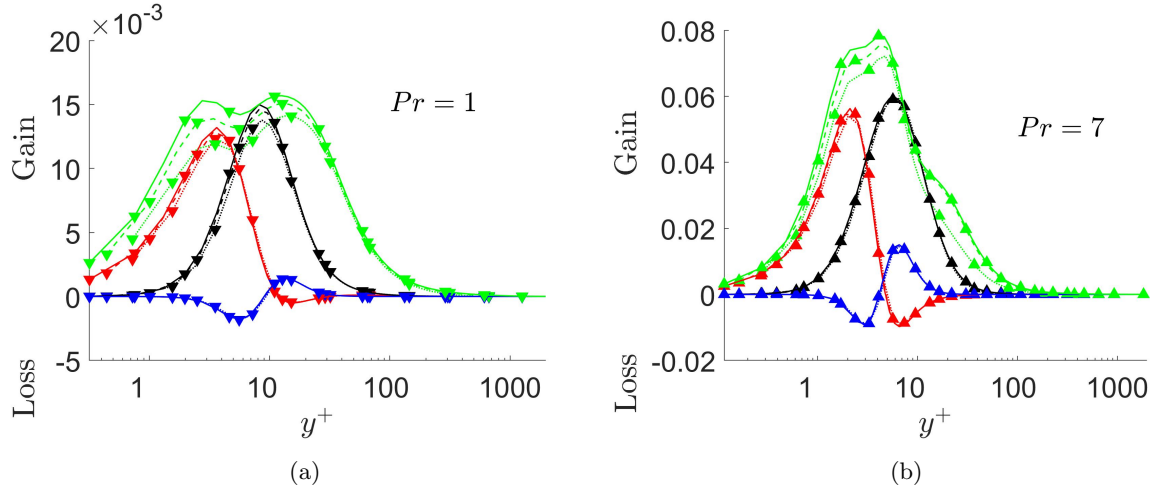
Figure 5.20: Production terms of ε_θ^+. (a) $Pr = 1$ and (b) $Pr = 7$. Here, colours denote production term: mixed production (red), mean gradient production (black), gradient production (blue) and turbulent production (green). Line style denotes the Reynolds number: $Re_\tau = 2000$ in solid lines, $Re_\tau = 1000$ in dashed lines and $Re_\tau = 500$ in dotted lines. Symbols as in table 5.5.

scaling of the viscous diffusion and dissipation terms is more accurate near the wall. This may also be the consequence of a Reynolds number independence of the mixed and mean gradient production terms in the transport equation of ε_θ^+. As a conclusion, a thermal equilibrium seems to be achieved in the near-wall region when the Pe_τ number is high enough, so that the aforementioned thermal quantities become constant with the Reynolds number.

Finally, the Nusselt and the turbulent Prandtl numbers have been calculated. It is observed how the Nu can be written as a power function of Pr in a range of Pe_τ between 20 and 1500. On the other hand, Pr_t is no longer equal to 1 near the wall for medium–high Prandtl numbers. Pr_t increases due to the decrease of the wall-normal heat flux near the wall, which entails a lower thermal eddy diffusivity.

Remark, that the Prandtl numbers simulated in this work reach up to the Prandtl number of water ($Pr \approx 7$), and with the Reynolds numbers reached, up to $Re_\tau = 2000$, these new features of the thermal field have been obtained. The tendency has been to observe statistics that become Reynolds independent when the Reynolds was increased (θ'^+, the viscous diffusion and dissipation budgets of k_θ^+ near the wall, and the mixed and mean gradient production budget terms of ε_θ^+). Although an extrapolation should always be made carefully, the Reynolds numbers in practical applications are even well above $Re_\tau = 2000$, which suggest that a perfect scaling with Re_τ is achieved for this variables, making thermal models for water much easier and accurate.

The raw data that support the findings of this study are available in the following website:

http://personales.upv.es/serhocal/.

5.1.3 High Reynolds number for $Pr = 0.71$

This subsection contains the results of the first simulation of a thermal channel flow for a friction Reynolds number of value $Re_\tau = 5000$ and the Prandtl number of air, $Pr = 0.71$. Results will be compared with simulation presented in section §5.1.1 for lower Reynolds numbers and the Prandtl number of air, i.e. $Re_\tau = 500$, 1000 and 2000, and $Pr = 0.71$. Also, results from the simulation of Pirozzoli et al. 2016 [50] will be used for comparisons. This simulation used the highest friction Reynolds number in a thermal channel flow until now, $Re_\tau = 4000$, and the thermal boundary condition consisted in an internal and
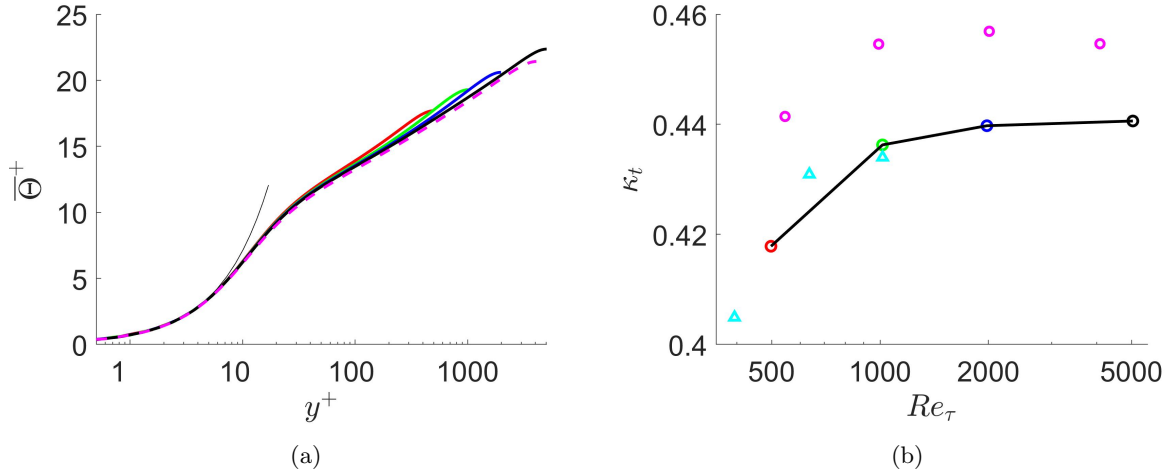
Figure 5.21: (a) Mean temperature. Magenta dashed line is from Pirozzoli et al. [50]. Black thin line shows the law of the wall. (b) κ_t as a function of Re_τ. Magenta circles represents the data from [50]. Cyan triangles is the data from [45], where the MBC is used. Colours as in table 5.1.

uniform heat generation (UHG) removed from both isothermal walls. Therefore, small differences should be expected. In all plots of this subsection, magenta dashed line will be used to represent data from Pirozzoli et al. [50] (unless otherwise specified).

Temperature statistics

The value of the mean temperature, $\overline{\Theta}^+$, has been obtained and it is represented in figure 5.21a. As it was expected, in the viscous layer, all values of $\overline{\Theta}^+$ collapse with the law of the wall: $\overline{\Theta}^+ = Pry^+$. Even the values from [50], where a different boundary condition for the thermal field is used, coincide with the ones obtained in the present work. This shows the universality of turbulence near the wall. However, in the logarithmic layer and in the central region of the channel, the slope of $\overline{\Theta}^+$ tends to decrease with an increasing Reynolds number. For the UHG boundary condition used in [50], the slope is smaller than the one obtained using the MBC.

The von Kármán constant, κ_t, has been derived from the mean temperature profile fitting the logarithmic equation (5.1) to the value of $\overline{\Theta}^+$ in the range of $y^+ = 70$ up to $y/h = 0.2Re_\tau$, as suggested in [77]. Therefore, in this range, κ_t represents the inverse of the slope of $\overline{\Theta}^+$. The values of κ_t are represented in figure 5.21b. Results at lower Reynolds numbers from the work of [50] have also been added (magenta circles). In addition, the values of κ_t obtained in [45], where the MBC was also used, are represented with cyan triangles. Results are coherent among all different works.

Here, it is seen that κ_t slightly increases with Re_τ, but, asymptotically, tends to a value slightly above 0.44. One may think that κ_t depends on the Reynolds number. However, the reason of the variations in the value of κ_t is that the logarithmic region is not properly developed and it is influenced by the buffer layer and the outer region. A value of $\kappa_t = 0.441$ is obtained for $Re_\tau = 5000$. This value is slightly above the von Kármán constant of the velocity field, which ranges between 0.38 and 0.4 [75, 76]. With respect to the UHG, the value of κ_t increases to 0.455, since the slope of $\overline{\Theta}^+$ is lower, as it was mentioned before. Regarding the constant B from equation (5.1), their values are collected in table 5.6. Notice that this more or less constant value of $B \approx 3$ obtained in all simulations is totally different when the Prandtl number changes, as it was shown in the previous sections.

Re_τ	κ_t	B	κ_∞	α_1	κ	α_2
500	0.418	2.89	–	–	–	–
1000	0.436	3.11	0.4625	150	0.433	1.304
2000	0.440	3.05	0.4635	150	0.448	1.436
5000	0.441	2.96	0.4466	150	0.441	0.756
4000	0.455	3.09	0.4651	150	0.457	0.961

Table 5.6: Values of the parameters of equations (5.1) and (5.12).
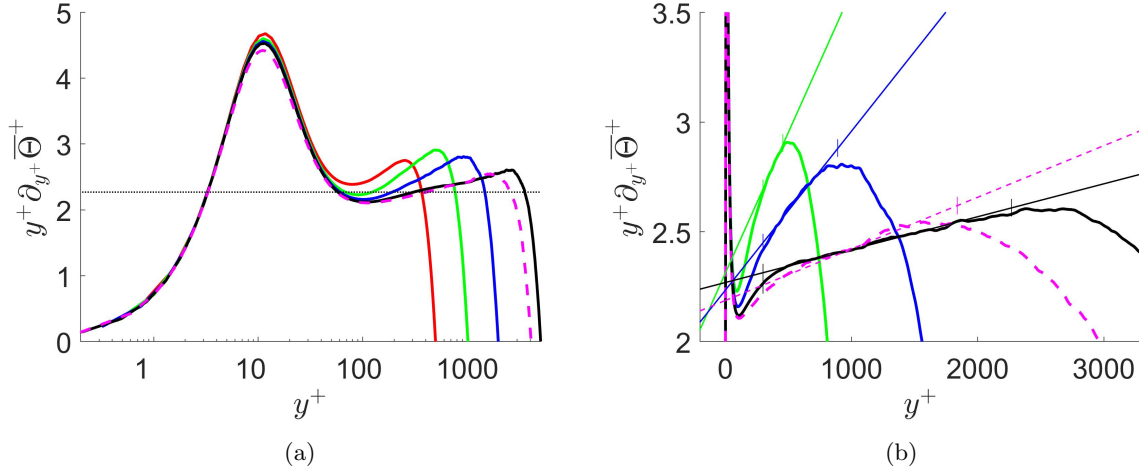
Figure 5.22: (a) Diagnostic function (5.2). Dotted black line represents where the plateau should be for $\kappa_t = 0.44$. (b) Diagnostic functions, solid, and approximations of equation (5.12), dashed. Colours as in table 5.1 and magenta dashed line is from Pirozzoli et al. [50].

A visual way of checking how well developed is the logarithmic layer is using the diagnostic function, Ξ_T, defined in equation (5.2). If equation (5.1) holds, then the diagnostic function will have a value of $1/\kappa_t$ in the logarithmic layer. In figure 5.22a, the diagnostic function of the mean temperature is represented. This logarithmic layer appears between the two peaks of the diagnostic function that are obtained in the buffer layer and the outer region. Regarding the peak in the buffer layer, its position is constant at $y^+ \approx 12$ and its magnitude continues decreasing with the increase of the Reynolds number. This peak is even lower for the UHG boundary condition. Regarding the peak in the outer region, it is positioned at a constant value in outer coordinates, $y/h \approx 0.5$. In the ideal case where a logarithmic region appears perfectly developed, the plateau of value $1/\kappa_t$ should be observed approximately between $y^+ > 70$ and $y/h < 0.2$. This is not observed in any of the cases, since Ξ_T increases along the logarithmic layer. However, it is true that the slope of Ξ_T tends to 0 as the Reynolds number increases. This indicates that higher Reynolds numbers must be simulated in order to be able to find a plateau in the logarithmic layer.

This problem was addressed by Jiménez and Moser [51]. They studied this influence of the Reynolds number in the slope of the diagnostic function of the velocity, Ξ, on the logarithmic region for the mean velocity profile, U^+. They used a higher-order truncation in which the diagnostic function had the form

$$\Xi = y^+ \partial_{y^+} \overline{U}^+ = \overbrace{\left(\frac{1}{\kappa_\infty} + \frac{\alpha_1}{Re_\tau} \right)}^{1/\kappa} + \alpha_2 \frac{y^+}{Re_\tau}, \qquad (5.12)$$
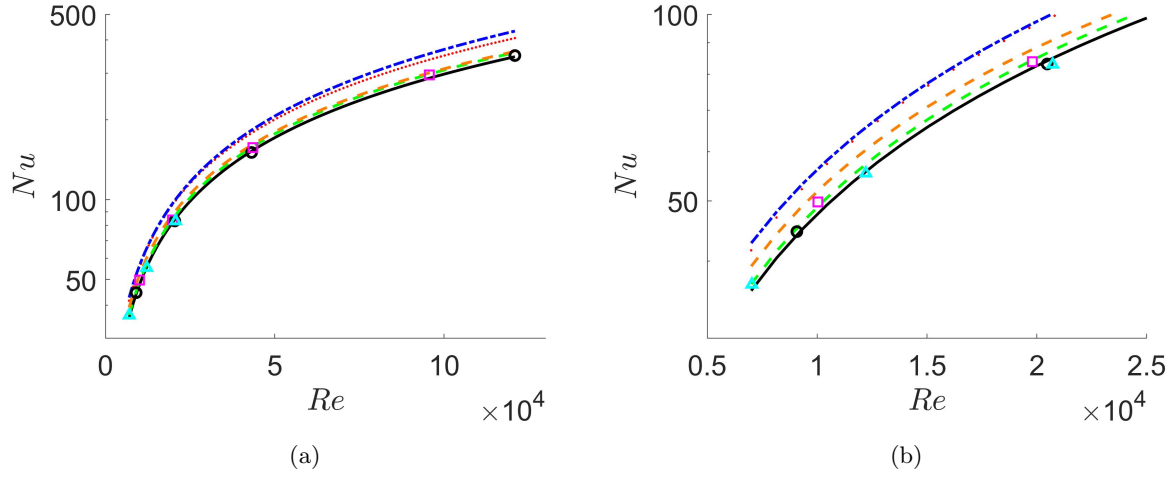
Figure 5.23: (a) Nusselt number as a function of Re. (b) Zoom for the lower Reynolds numbers. Black circles represents the data from this work, magenta squares are the data from [50] and cyan triangles are the data from [45]. Lines represent correlations: Black solid (5.13), red dotted [83] (5.14), orange dashed [84] (5.15), green dashed [48] (5.16) and blue dotted-dashed [85] (5.17).

where the Reynolds number dependence is introduced in the term κ and a linear dependence with y/h is introduced in the term y^+/Re_τ. This approximation was valid in the range $y^+ > 300$ and $y/h < 0.45$. The same analysis has been performed here for $\overline{\Theta}^+$. Note that the case $Re_\tau = 500$ does not appear in this analysis since the range where the approximation is valid does not exist. In figure 5.22b, a zoom of the diagnostic function together with the approximations of equation (5.12) are represented.

Values of the parameters of the approximation are presented in table 5.6. The value of α_1 has been set to 150 as in [51]. While κ and κ_t seem to be more or less converged, α_2 is still larger than the expected limit value of 0 for very high Reynolds number.

Another parameter that can be derived from the mean thermal field is the Nusselt number, Nu, defined in equation (5.3). In figure 5.23, the obtained Nusselt numbers, as a function of Re, are presented. In the range of Reynolds numbers studied, the Nusselt number can be approximated as a power function of Re

$$Nu = 0.031Re^{0.796} \quad \text{for} \quad Pr = 0.71, \tag{5.13}$$

where the coefficient of determination is $R^2 = 0.99976$, for $R^2 = 1$ representing a perfect fit. The data has been compared with results from [50] at lower Reynolds numbers and from [45]. Also four correlations have been used to compare them with correlation (5.13). Two of them are correlations for turbulent flows in pipes: Dittus and Boelter [83]

$$Nu = 0.023Re_D^{0.8}Pr^n, \tag{5.14}$$

and Gnielinski [84]

$$Nu = \frac{(f/8)(Re_D - 1000)Pr}{1 + 12.7(f/8)^{1/2}\left(Pr^{2/3} - 1\right)}, \tag{5.15}$$

where Re_D is the diameter of the pipe, n is a coefficient of value 0.4 since the fluid is being heated and f is proportional to the skin friction coefficient, $f = (0.79\ln(Re_D) - 1.64)^{-2}$. On the other hand, two correlations for constant temperature walls are used. The Kays et al. [48] correlation reads

$$Nu = 0.021Re^{0.8}Pr^{0.5}, \tag{5.16}$$

88

and the Sleicher and Rouse [85] correlation

$$Nu = 4.8 + 0.0156Re^{0.85}Pr^{0.93} \quad \text{for} Pr < 0.1. \tag{5.17}$$

On one hand, figure 5.23a presents a global image, with all the Reynolds numbers that are being analyzed in this work, including the ones from [50] and [45] for comparison. Figure 5.23b presents a zoom in the low Reynolds numbers for a better view of the discrepancies between different boundary conditions and correlations in this range of Re.

One can see that the Nusselt number obtained in [45] follows the same trend than the ones obtained in this work, since the MBC is employed in both cases. However, Nu in [50] is slightly higher, since the magnitude of the mean temperature is lower when the UHG thermal condition is used. In other words, the convective heat transfer is lower when the MBC is used.

Regarding the correlations, the ones from Dittus and Boelter [83] (5.14) and Sleicher and Rouse [85] (5.17) overestimate the value of Nu, either because it is for turbulent pipes or because the correlation is valid for lower Prandtl numbers. Correlations from Gnielinski [84] (5.15) and Kays et al. [48] (5.16) adjust much better to the results obtained. They perfectly adjust to the result from [50]. Anyway, note that the exponent of Re from correlations (5.14), (5.16) and (5.17) is (or it is close to) 0.80, which is also the case for the correlation proposed in this work (5.13).

Turbulent intensities are represented in figure 5.24. The root mean square of the temperature variance, θ'^{+}, and the wall-normal heat flux, $\overline{v^{+}\theta^{+}}$, are represented in figures 5.24a and 5.24b as a function of outer and inner coordinates, respectively. Also, streamwise heat flux, $\overline{u^{+}\theta^{+}}$, is represented in figures 5.24c and 5.24d as a function of outer and inner coordinates, respectively.

The main result is that a perfect collapse of the statistics is observed in the inner layer, when the plot is represented in inner coordinates, figures 5.24b and 5.24d. On the other hand, when the statistics are represented as a function of the outer coordinates, the collapse is observed in the outer region of the channel.

The maximum values of the turbulent intensities θ'^{+} and $\overline{u^{+}\theta^{+}}$ occur in the buffer layer. Their values can be observed in figures 5.25a and 5.25b. The peaks increase with Reynolds number, which indicates a more turbulent flow, as it was expected. θ'^{+} and $\overline{u^{+}\theta^{+}}$ present a linear increase with respect to $\log(Re_{\tau})$. Values of the peaks can be obtained with the following correlations

$$\theta'^{+}_{max} = 0.112 \log(Re_{\tau}) + 1.82, \tag{5.18}$$

$$\overline{u^{+}\theta^{+}}_{max} = 0.508 \log(Re_{\tau}) + 3.06. \tag{5.19}$$

On the other hand, $\overline{v^{+}\theta^{+}}$ does not present this linear increase of its absolute value. The peak occurs in the outer region and its absolute value increases slowly as the Reynolds number increases. Actually, $\overline{v^{+}\theta^{+}}$ is bounded by -1 as can be observed from heat fluxes balance equation (1.41). The maximum value of $\dot{q}^{+}$ is 1. The turbulent heat flux, has its maximum in the core region of the channel. The higher the Reynolds number is, the closer to 1 the value of $\dot{q}^{+}$ will be in this core region. Since in this region $\dot{q}^{+} \approx -\overline{v^{+}\theta^{+}}$, for very high Reynolds numbers $-\overline{v^{+}\theta^{+}}$ will be close to 1.

Regarding the UHG case, the peaks of the three intensities have a lower absolute value, which indicates a less turbulent thermal field than the one obtained using the MBC. Lower Reynolds number cases have been also represented to see how this feature happens for all simulations, obtaining the same tendency. Also, data from Abe et al. [45] has been added. This has been done to verify the results, since [45] also used the MBC. Effectively, the results are very similar, and the small differences (lower than 1%) can be due to numerical discrepancies or different mesh resolution.

In a similar way that the mean velocity and temperature are studied through the diagnostic function in the log layer, velocity intensities can be analyzed through the Townsend's attached eddy hypothesis [11]. This hypothesis is valid for high Reynolds number flows, in a certain region of y, where the velocity
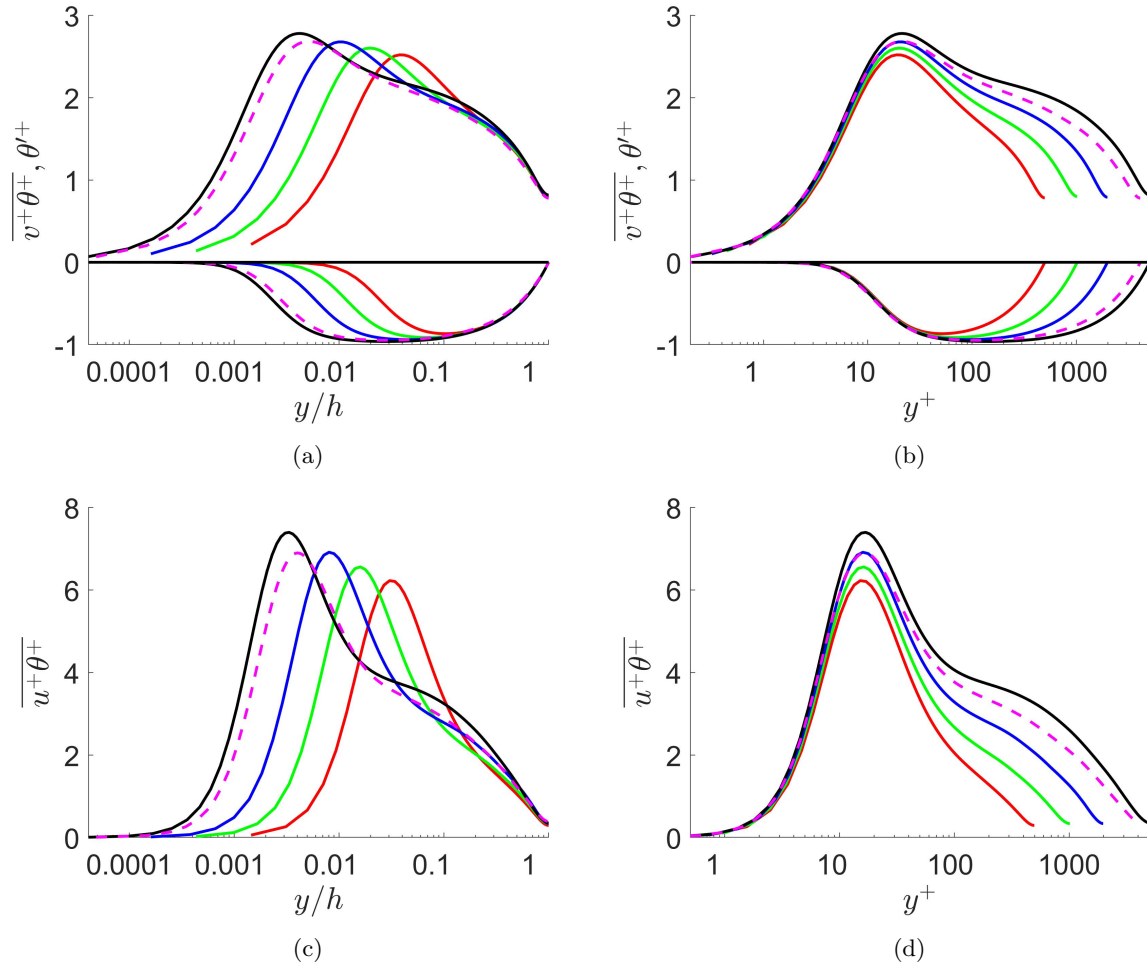
89

Figure 5.24: θ'^+ and $\overline{v^+\theta^+}$ in (a) outer coordinates and (b) inner coordinates. $\overline{u^+\theta^+}$ in (c) outer coordinates and (d) inner coordinates. Colours as in table 5.1 and magenta dashed lines are from Pirozzoli et al. [50].
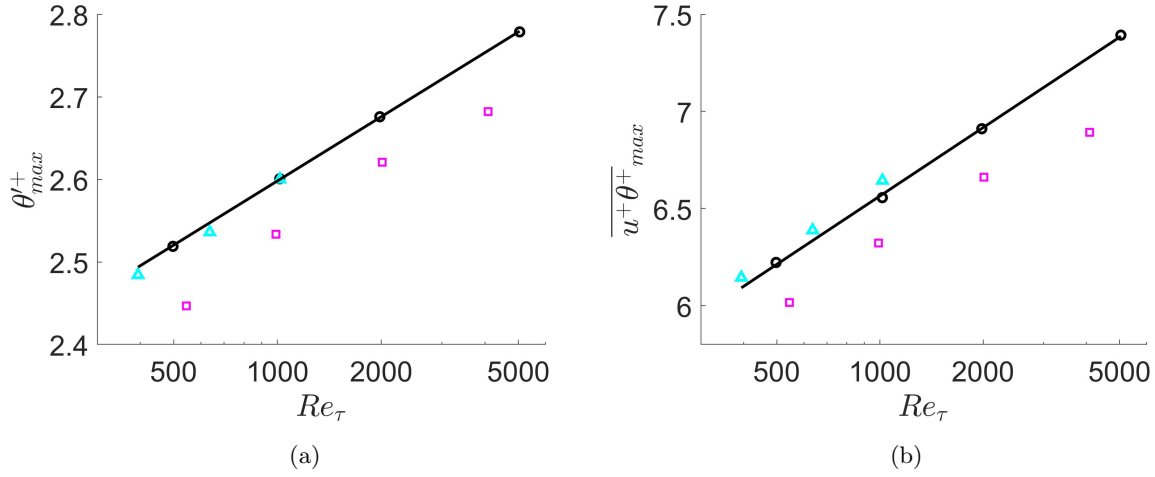
(a)

(b)

Figure 5.25: Maximum value of (a) θ'^+ and (b) $\overline{u^+\theta^+}$, both as a function of Re_τ. Black line represents correlation (5.18) in (a) and correlation (5.19) in (b). Black circles: data from this work; magenta squares are from Pirozzoli et al. [50]; and cyan triangles are from Abe et al. [45].

intensities satisfy

$$
\begin{align}
{u'^+}^2 &= A_1 - B_1 \log(y/h), \tag{5.20a} \\
{v'^+}^2 &= A_2, \tag{5.20b} \\
{w'^+}^2 &= A_3 - B_3 \log(y/h), \tag{5.20c} \\
\overline{u^+ v^+} &= -1. \tag{5.20d}
\end{align}
$$

Analogously, due to the high correlation between u'^+ and θ'^+, one may think that the Townsend's hypothesis is valid for the thermal field when u'^+ is replaced by θ'^+. Doing this, the following relations are obtained

$$
\begin{align}
{\theta'^+}^2 &= A_4 - B_4 \log(y/h), \tag{5.21a} \\
\overline{u^+ \theta^+} &= A_5 - B_6 \log(y/h), \tag{5.21b} \\
\overline{v^+ \theta^+} &= -1. \tag{5.21c}
\end{align}
$$

It has already been shown that the minimum value of $\overline{v^+\theta^+}$ tends to -1 in a wider range of y/h when the Reynolds number is increased (figures 5.24a and 5.24b). This is in accordance with equation (5.21c). Regarding ${\theta'^+}^2$ and $\overline{u^+\theta^+}$, their diagnostic functions can be observed in figures 5.26a and 5.26b, respectively. If Townsend's criteria can be applied to the thermal field, there should be a plateau in $y^+ \partial_{y^+} {\theta'^+}^2$ and $y^+ \partial_{y^+} \overline{u^+\theta^+}$ profiles. For this values of Re_τ there are no evidences of this plateau, although the trends may indicate that for higher Reynolds numbers it may appear in the logarithmic layer.

The turbulent Prandtl number, Pr_t, has been calculated. It is defined in equation (5.4). In figure 5.27, Pr_t is shown as a function of y^+. In the viscous layer, it can be seen how Pr_t is close to 1 and constant for all values of Reynolds numbers. This confirms the well-know law that states $Pr_t \approx 1$ in the wall for medium molecular Prandtl numbers [40]. Some differences are observed with respect to the Pr_t obtained by Pirozzoli et al. [50]. However, in the buffer layer and logarithmic region, all values of Pr_t seem to collapse, including the ones obtained in [50]. In the outer layer, values of Pr_t decrease. As
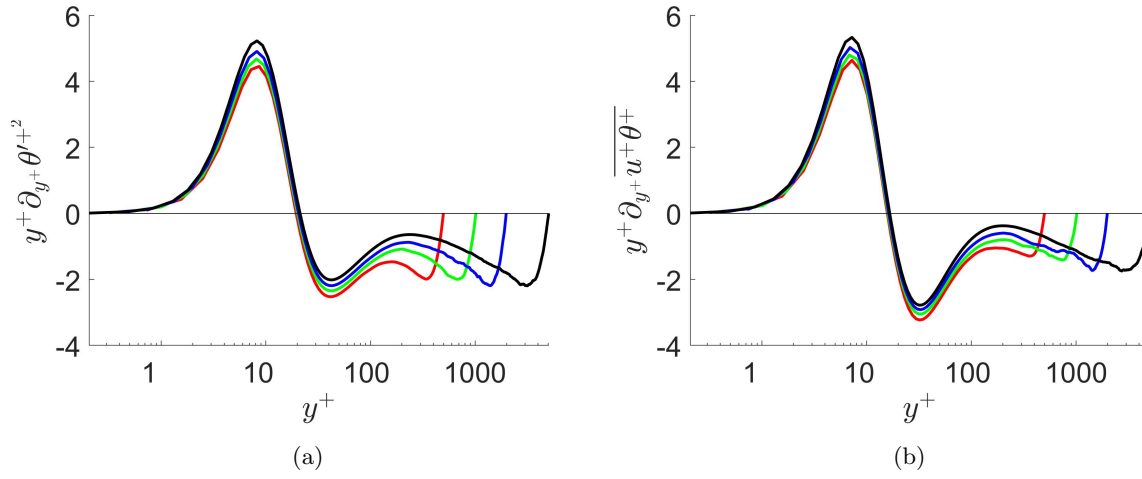
Figure 5.26: Diagnostic function for (a) θ'^{+2} and (b) $\overline{u^+\theta^+}$. Colours as in table 5.1.
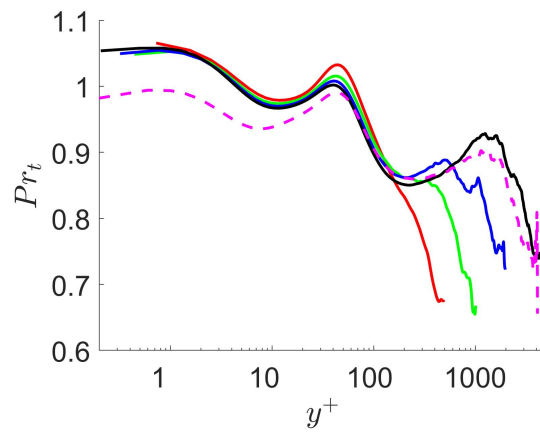

Figure 5.27: Turbulent Prandtl number. Colours as in table 5.1 and magenta dashed lines are from Pirozzoli et al. [50].

92

Re_τ	b_θ	$V_\theta^+\big|_{y^+=0}$	$Pr \cdot b_\theta^2$
500	0.4202	0.1246	0.1254
1000	0.4385	0.1360	0.1365
2000	0.4529	0.1449	0.1456
5000	0.4692	0.1565	0.1563

Table 5.7: First column shows the Re_τ of each case. Values of b_θ are in second column. Third and fourth columns show the value of $V_\theta^+\big|_{y^+=0}$ obtained from the DNS and calculated with equation (5.10), respectively.

a conclusion, there has not been observed new behaviours of the turbulent Prandtl number for the new friction Reynolds number $Re_\tau = 5000$.

Turbulent budgets

In this section, budgets of the temperature variance, k_θ^+ (2.19)-(2.21d), the dissipation rate of the temperature variance, ε_θ^+ (2.22)-(2.24g), and the turbulent heat fluxes, $\overline{u^+\theta^+}$ and $\overline{v^+\theta^+}$ (2.25)-(2.28f), are presented (see equations in subsection §2.3.1).

Figure 5.28 shows the different budget terms for all cases that use the MBC with $Re_\tau = 500$, 1000, 2000 and 5000. Figure 5.28a represents the budget terms of k_θ^+. In figure 5.28b, the budgets of ε_θ^+ are represented, where the four production terms of ε_θ^+ have been added as in the previous subsections. Finally, figures 5.28c and 5.28d show the budget terms of $\overline{u^+\theta^+}$ and $\overline{v^+\theta^+}$, respectively.

For k_θ^+, figure 5.28a, all terms collapse for $y^+ > 10$. In the buffer layer, the turbulent diffusion terms present small discrepancies between all cases. Furthermore, in the viscous layer there are big differences between each viscous diffusion and the dissipation terms. The absolute values of these terms increase with the Reynolds number.

The reason of the discrepancies in the wall for the viscous diffusion and the dissipation terms can be understood by using the Taylor series approximation of the turbulent intensities proposed by Antonia and Kim [34] and Kawamura et al. [40], which were introduced in section §2.3.1, equations (2.17a)-(2.17i). Near the wall, $\theta'^+ \approx Pr b_\theta y^+$. In figure 5.29a it is shown how this is true for approximately $y^+ < 3$. The values of b_θ are collected in table 5.7.

On the other hand, one can approximate the value of the viscous diffusion term, V_θ^+, with equation (5.10). The result of the approximation is almost the actual value obtained in the DNS (table 5.7). In all cases the error is lower than 1%. Therefore, the reason why this term of the turbulent budget does not scale in the wall comes from the differences in the b_θ terms. This term represents the slope of θ'^+/Pr near the wall. Looking at the zoom in figure 5.29a, one can see that, effectively, the lines of θ'^+/Pr are parallel, but they do not collapse. The differences in V_θ^+ for cases with the same Prandtl is due to the increase in the slope of θ'^+ with the Reynolds number. One may think that this value of b_θ converges for very large Reynolds numbers, as it may look from the trend in table 5.7. However, it was seen in figure 5.24b that the maximum value of θ'^+ always increases with Re_τ, at least for $Re_\tau \leq 5000$. Because the position of the peak was constant in y^+, the slope of θ'^+ has to be higher for larger Re_τ. In other words, as long as the peak of θ'^+ increases with Re_τ, b_θ will also increase and V_θ^+ cannot scale at the wall. It was observed in previous section §5.1.2, that for high Prandtl numbers, the peak value of θ'^+ was approximately constant, which yielded an approximately constant value of b_θ and, therefore, a much better scaling of the viscous diffusion term near the wall. Whether this thermal equilibrium depends only on the Prandtl number or on both, Prandtl and Reynolds number, i.e. the Péclet number cannot be answered with the data calculated in this work, since a friction Reynolds number of $Re_\tau = 14000$ should be calculated with a Prandtl number of $Pr = 1$ in order to obtain the same friction Péclet number $Pe_\tau = 14000$ from the simulation with $Re_\tau = 5000$ and $Pr = 7$ from previous subsection. However, this
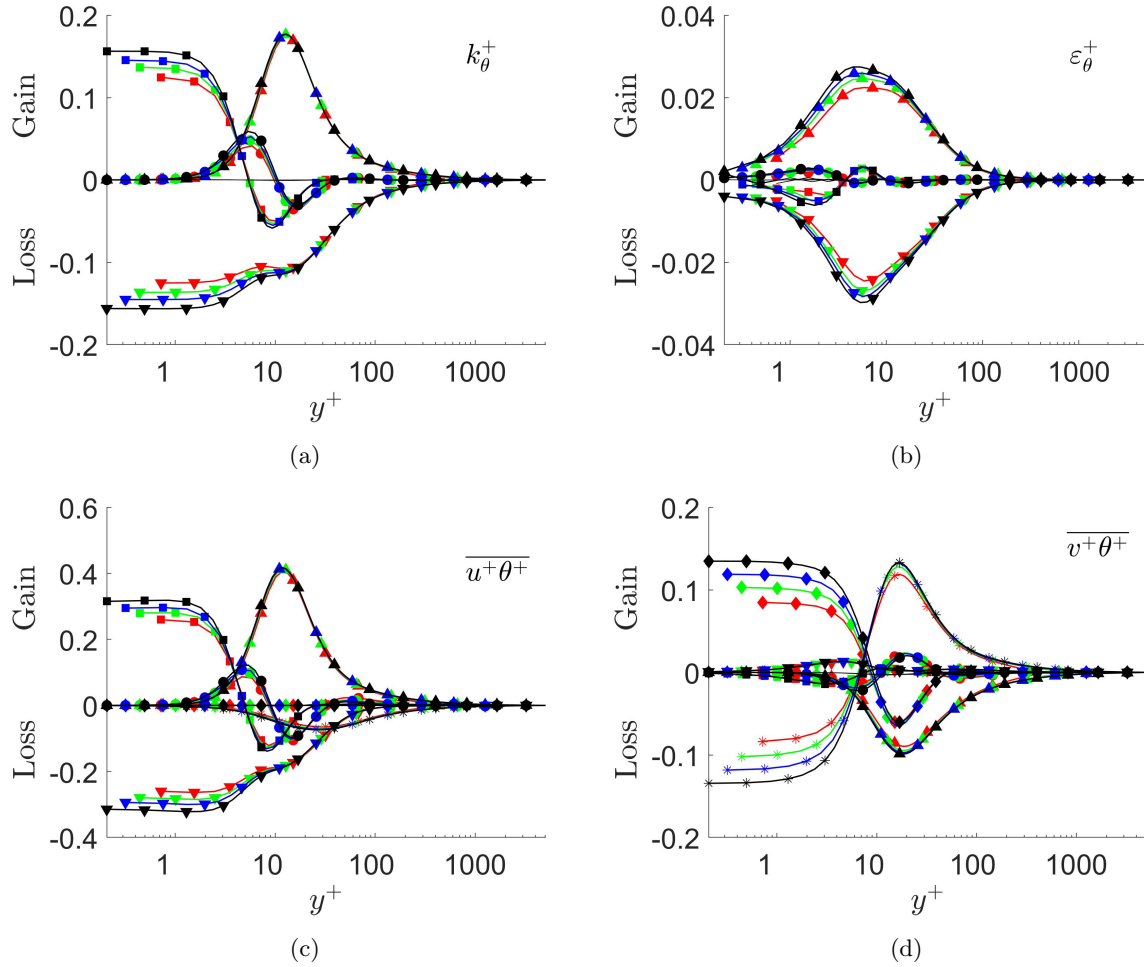
Figure 5.28: Budgets of (a) k_θ^+, (b) ε_θ^+, (c) $\overline{u^+\theta^+}$ and (d) $\overline{v^+\theta^+}$. Symbols denote budget terms: production or sum of productions in (b), (triangle up), turbulent diffusion (circle), viscous diffusion (square), dissipation (triangle down), pressure strain (star) and pressure diffusion (diamond). Black line with value 0 is the summation of all terms. Colours as in table 5.1.
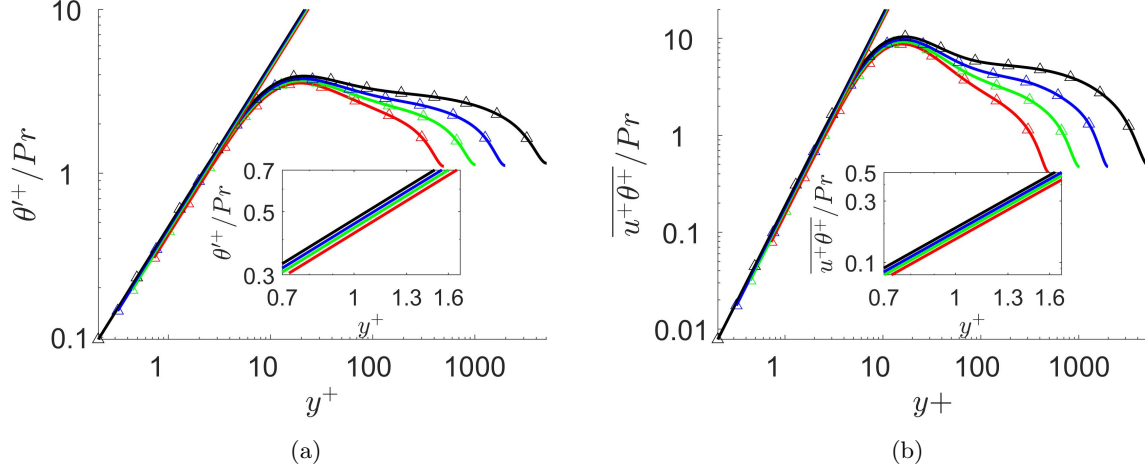
(a) (b)

Figure 5.29: (a) θ'^+/Pr and (b) $\overline{u^+\theta^+}/Pr$ in wall coordinates. Zooms of the viscous layer. Colours as in table 5.1.

Re_τ	$b_{1\theta}$	$V_{u\theta}^+\big|_{y^+=0}$	$(Pr+1)b_{1\theta}$
500	0.1512	0.2562	0.2586
1000	0.1619	0.2717	0.2768
2000	0.1713	0.2853	0.2930
5000	0.1836	0.3138	0.3139

Table 5.8: First column shows the case. Values of $b_{1\theta}$ are in second column. Third and fourth columns show the value of $V_{u\theta}^+\big|_{y^+=0}$ obtained from the statistics and calculated with equation (5.11), respectively.

simulation is far beyond the computational possibilities of nowadays supercomputers. The same analysis can be done for the dissipation term, since, at the wall, $V_\theta^+ = -\varepsilon_\theta^+$.

In the case of the dissipation rate of the temperature variance, ε_θ^+, plotted in figure 5.28b, the scaling failures appear in the buffer layer for the sum of production terms and the dissipation. This increase of the production terms was already reported in other works such as [81].

For the budgets of $\overline{u^+\theta^+}$ (figure 5.28c), the viscous diffusion, $V_{u\theta}^+$, and dissipation, $\varepsilon_{u\theta}^+$, terms do not scale near the wall, in the same way that for k_θ^+. Actually, the phenomenon is very similar and it can be studied in the same way. $V_{u\theta}^+$, can be calculated at the wall with equation (5.11). The value of $c_{1\theta}$ is obtained from the Taylor series approximation of $\overline{u^+\theta^+}$, equation (2.17h), which near the wall reads $\overline{u^+\theta^+} \approx Pr c_{1\theta} y^{+2}$. This approximation is shown for in figure 5.29b and the values of $c_{1\theta}$ are collected in table 5.8. The approximation is very accurate up to $y^+ < 4$. The values of $V_{u\theta}^+$ at the wall using equation (5.11) differ less than a 3% for all cases (table 5.8), proving a good accuracy of the approximation. Similarly to V_θ^+, while the coefficient $c_{1\theta}$ increases with the Reynolds number, the value of $V_{u\theta}^+$ will also increase at the wall. This will occur as long as the peak of $\overline{u^+\theta^+}$ keeps increasing (figure 5.24d).

As a conclusion, the scaling failure near the wall of V_θ^+ and $V_{u\theta}^+$ are due to the increase of the peak of θ'^+ and $\overline{u^+\theta^+}$, respectively.

Regarding the turbulent budgets of $\overline{v^+\theta^+}$ (figure 5.28d), small scaling failures appear in the buffer layer for the production and pressure strain terms. Near the wall, bigger discrepancies appear for the
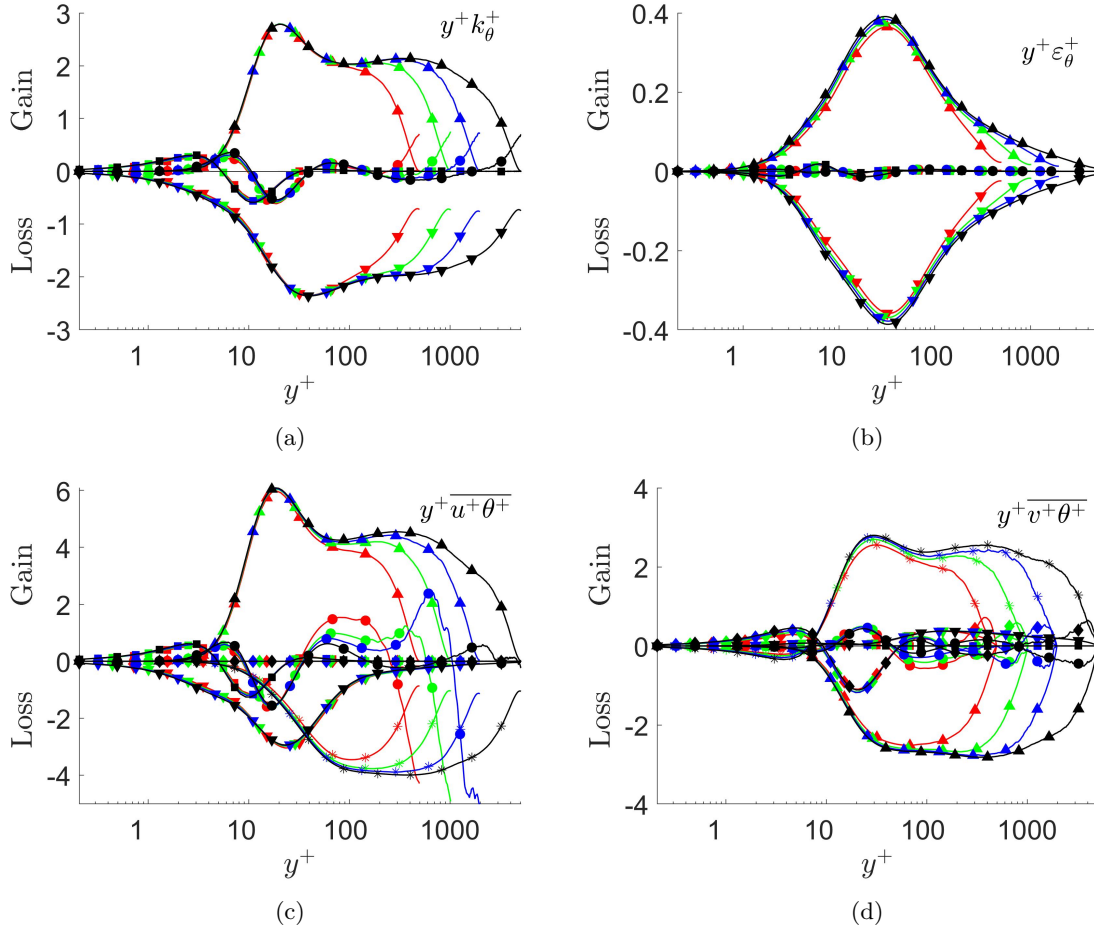
Figure 5.30: Budgets of (a) $y^+ k_\theta^+$, (b) $y^+ \varepsilon_\theta^+$, (c) $y^+ \overline{u^+\theta^+}$ and (d) $y^+ \overline{v^+\theta^+}$. Symbols denote budget terms: production or sum of productions in (b), (triangle up), turbulent diffusion (circle), viscous diffusion (square), dissipation (triangle down), pressure strain (star) and pressure diffusion (diamond). Black line with value 0 is the summation of all terms. Colours as in table 5.1.

pressure strain and pressure diffusion terms. The pressure strain term can be written as

$$\Pi_{v\theta}^{s^+} = \overline{p^+ \partial_{y^+} \theta^+} \tag{5.22}$$

The reason why $\Pi_{v\theta}^{s^+}$ does not scale in the wall is again because the term $\overline{p^+ \partial_{y^+} \theta^+}$ has a peak at a constant y^+ and it continuously increases with the Reynolds number. Not shown here for brevity.

As a general comment, the budgets of k_θ^+ and $\overline{u^+\theta^+}$ are very similar due to the high correlation between u'^+ and θ'^+. Near the wall, the energy enters to the thermal flow through viscous diffusion and it is extracted by dissipation. Also, the peak of the production term is constant for different Reynolds numbers. For k_θ^+, the value of P_θ^+ is $Pr/4$, as noted by [80]. On the other hand, there is not a clear scaling with Pr for the peak of $P_{u\theta}^+$. In the case of the budgets of $\overline{v^+\theta^+}$, a similar picture to that of $\overline{u^+v^+}$ is obtained (not shown here for brevity), again, due to the high correlation between u'^+ and θ'^+. In this case, the energy is introduced by the pressure strain and it is extracted by the pressure diffusion.

A different picture is obtained above the buffer layer, up to approximately $y/h = 0.4$. Figure 5.30

shows the same turbulent budgets as before, pre-multiplied by y^+. In a perfectly developed logarithmic layer, the kinetic energy production scales with $1/y^+$ [38]. Note that this is approximately true for the dominant budgets of k_θ^+, $\overline{u^+\theta^+}$ and $\overline{v^+\theta^+}$. Therefore, a much better comparison between the dominant budget terms above the buffer layer can be done. As in the near-wall region, production is the dominant budget term of k_θ^+, which is compensated by the dissipation term. However, in the case of $\overline{u^+\theta^+}$, and also for $\overline{v^+\theta^+}$, it is the pressure strain what compensates the production term.

In the center of the channel (above $y/h = 0.4$) the velocity and temperature flatten and all production terms tend to 0, since the velocity and thermal boundary conditions imposed imply a zero gradient in the velocity and temperature in the center of the channel. Turbulent diffusion becomes the dominant budget of k_θ^+ and it is compensated by the dissipation.

As a final comment, there are no noticeable changes in the behaviour of the turbulent budgets with respect to lower Reynolds number cases.

Conclusions

A Direct Numerical Simulation of a thermal channel flow at $Re_\tau = 5000$ has been conducted for the first time. The Mixed Boundary Condition has been used. The Prandtl number of air, 0.71, was used. The results obtained are compared with other simulations using the same Prandtl number and lower Reynolds numbers: $Re_\tau = 500$, 1000 and 2000. Also, the simulation with closest Reynolds number, $Re_\tau = 4000$, is used to compare results. In that simulation the Uniform Heat Generation boundary condition was used. A comparison among both boundary conditions is provided.

The mean temperature is calculated and its diagnostic function still does not show a plateau in the logarithmic layer. Higher Reynolds number are needed in order to properly study the behaviour of the thermal field in this logarithmic region. The von Kármán constant presents an asymptotic behaviour with an increasing Reynolds number and it trends to converge at a value of approximately 0.44. The reason why κ_t is not constant is attributed to the influence of the inner and outer regions on the logarithmic region, since for these Reynolds numbers this logarithmic region is small. This effect of the Reynolds number on the logarithmic layer is also studied through a slightly different diagnostic function. For this case, a new term that contemplates the dependence of the Reynolds number is introduced. Effectively, the value of this term trend towards zero when the Reynolds number is increased.

A new correlation for the Nusselt number is provided. This correlation is valid for turbulent thermal channel flows, $Pr = 0.71$, and $500 \leq Re_\tau \leq 5000$. It has been compared with classical Nusselt number correlations. Regarding the turbulent Prandtl number, there are no relevant results at $Re_\tau = 5000$ and the trends of Pr_t are the same as for lower Reynolds numbers.

Thermal intensities increase with the Reynolds number and the values of the inner peaks increase logarithmically with Re_τ for θ'^+ and $\overline{u^+\theta^+}$. $\overline{v^+\theta^+}$ tends to have a minimum value close to -1 in a wider range of y^+ for high Reynolds numbers. This agrees with the application of Townsend's hypotheses to the thermal intensities. However, θ'^{+2} and $\overline{u^+\theta^+}$ do not present a logarithmic dependence at any region of y as it indicates Townsend's hypotheses. A remarkable difference between the MBC and UHF thermal conditions is observed in the temperature intensities. Magnitudes of this intensities are higher when the MBC is used, meaning that a more turbulent thermal field is obtained.

Turbulent budgets are presented and scaling failures are analyzed. The most relevant scaling failures are the ones that occur near the wall for the dissipation and viscous diffusion terms of k_θ^+ and $\overline{u^+\theta^+}$. These scaling failures are a direct result of the increase of the inner peak of θ'^+ and $\overline{u^+\theta^+}$, respectively. In the cases of the budgets of $\overline{v^+\theta^+}$, the scaling failures occur in the pressure strain and pressure diffusion terms. In the same way, this occurs due to the increase of the inner peak of the variable $\overline{p^+\partial_{y^+}\theta^+}$.

The raw data that support the findings of this study are on the following link:

http://personales.upv.es/serhocal/

Case	HJ02 [73]	LJ04 [75]	LM05 [76]	HAKO10
Re_τ	2000	4200	5200	10000
Line	· · · · · ·	- - - -	▬·	▬▬▬

Table 5.9: Friction Reynolds number and line code to distinguish each simulation during the plots of this subsection.

5.1.4 Poiseuille isothermal flows

This subsection contains the results of the simulation of a Poiseuille turbulent channel flow. For the first time, a friction Reynolds number of value $Re_\tau = 10000$ have been simulated in a DNS. The data has been compared with other simulations at different Reynolds numbers [73, 75, 76]. Table 5.9 shows the line colours and styles used to distinguish between each simulation in the different plots of this subsection (unless otherwise specified).

One point statistics

The mean velocity profile is shown in figure 5.31 in terms of the diagnostic function, $\Xi = y^+ \partial_{y^+} \bar{U}^+$. This function should show a plateau if the classical scaling for the logarithmic layer $\bar{U}^+ = \kappa^{-1} \log(y^+) + B$ holds, where κ is the von Kármán constant. For every case, the first local minimum of Ξ is reached around $y^+ \approx 70$, which more or less coincide with the classic starting point of the logarithmic layer [12]. However, the diagnostic function is not really flat until $y^+ \approx 400$. The logarithmic layer extends to around $y^+ \approx 2500$ or $y/h = 0.3$, above the usual value of $y/h = 0.2$. To obtain the values of κ and B, the fitting of the logarithmic function has been restricted to the region where the diagnostic function is flatter, $y^+ = 400$ to $y/h = 0.27$, obtaining $\kappa = 0.394$ and $B = 4.61$. This value for κ is only 0.010 and 0.007 units larger than the one given by [76] and [86], respectively.

The intensity of the streamwise velocity, u'^+, is shown in figure 5.32a. The well known scaling failure in the buffer layer is still present [73]. Lee & Moser [76] found that this limit is growing in several DNS studies of canonical flows, in the range $Re_\tau = 1000 - 5200$. This first maximum is still growing, and its value $u'^+ = 3.07$ is in agreement with [76] and the experimental results of [87]. Notice that several experimental researchers, [88], have found that this limit is not growing. However, as it is shown later, this is related to the scaling failure of the dissipation [38].

About the open question of a possible second maximum of u'^+ the situation is shown in figure 5.32b. Notice that the existence of this second maximum could lead to the presence of new phenomena at the beginning of the logarithmic layer [89]. If it exists, this maximum would be located around $y^+ \approx 120$. However, the derivative of u'^+ is still not zero. Moreover, if it is plotted the maximum value of $d_{y^+} u'^+$ close to $y^+ \approx 120$ with respect to the Reynolds number, figure 5.32b box, it is not clear that this second maximum would ever exist. A fitting of these data with a first order polynomial gives a value of only $Re_\tau \approx 13000$ for the existence of this maximum. This would oppose the results obtained in [87], where for $Re_\tau = 20000$ a second maximum was not present. However, a fitting with a second order polynomial leads to a never existing second maximum, leaving the question open.

The other three components of the Reynolds stress tensor can be seen in figure 5.32c. As expected, the scaling of $\overline{u^+ v^+}$ and v'^+ is almost perfect near the wall. In the case of w'^+, the maximum keeps growing, causing a minor scaling failure in the viscous sub-layer. Pressure, figure 5.32d, is computed as in [90], growing at the wall logarithmically [51, 91]. The peak is at $y^+ \approx 30$ for all simulations. It could be thought that the problem of the scaling is mainly a translation problem, which would seem natural, as the pressure is defined as an additive constant. However, in the box of figure 5.32d, where the peaks of cases HJ02, LJ04 and LM05 have been shifted so they coincide in their maximum with the peak of the present work, it is appreciated that the scaling is not perfect either.
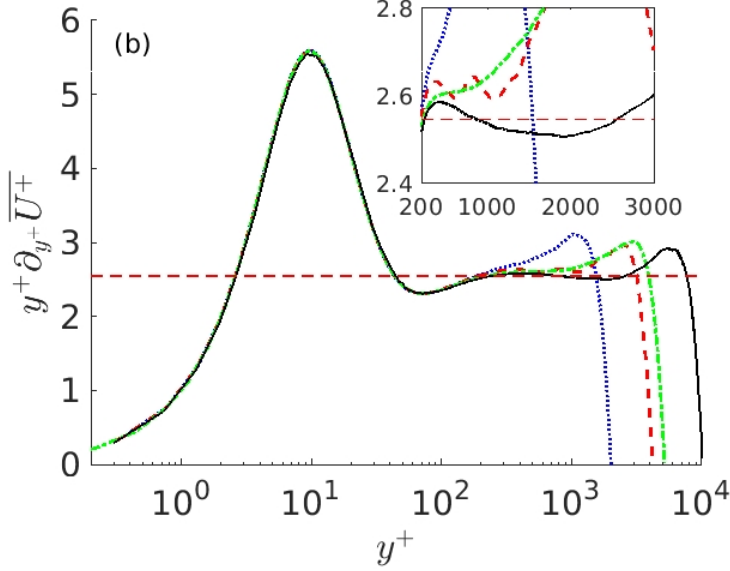
Figure 5.31: Diagnostic function, showing a log layer in the range $y^+ = 400 - 2500$. Lines as in table 5.9. Horizontal red dashed line represents where the plateau of the logarithmic layer would be for a value of $\kappa = 0.394$.

The spectral energy densities for U^+ and V^+, $\phi = k_x k_z E(k_x, k_z)$, at $y^+ \approx 15$ are given in figure 5.33a. Here $\lambda = 2\pi/k$ is the wavelength and k is the wavenumber. This further confirms that the large and wide structures at the right corner are inactive in the sense of Townsend [11, 73, 92]. They are present in U^+ spectra but neither in V^+ or U^+V^+ co-spectra. This situation differs in the logarithmic region. As can be see in figure 5.33b, a large spectral ridge, containing half of the most energetic eddies of the flow goes roughly across the extension of the logarithmic layer for V^+. This confirms what was hinted in [73], where only a few points in the logarithmic layer were present. Notice also that the isolines for larger values of y/h are approximately parallel, suggesting a similar cascade process for both U^+ and V^+. The dashed lines of figure 5.33b show the approximate position of the maximum of the 1D $z-$spectra. These peaks grow linearly as $y_{max} \approx \lambda_z/6$ for U^+, and $y_{max} \approx \lambda_z/2.5$ for V^+. Similar plots can be obtained for the $x-$spectra with $y_{max} \approx \lambda_z/2.5$ for V^+ too. It can also be noticed, in both plots, that more than 95% of the energy has been captured in the box, further assuring the validity of the statistics.

Turbulent budgets

The budget equation for the component $\overline{u_i^+ u_j^+}$ of the Reynolds-stress tensor is written as in [38, 93]

$$B_{ij}^+ \equiv D\overline{u_i^+ u_j^+}/Dt = P_{ij}^+ + \varepsilon_{ij}^+ + T_{ij}^+ + \Pi_{ij}^{s^+} + \Pi_{ij}^{d^+} + V_{ij}^+. \tag{5.23}$$

This equation has been nondimensionalized as $B_{ij}^+ = B_{ij}\nu/u_\tau^3$. The terms in the right hand side of equation (5.23) are referred to as production, dissipation, turbulent diffusion, viscous diffusion, pressure-

(a)

(b)

(c)

(d)
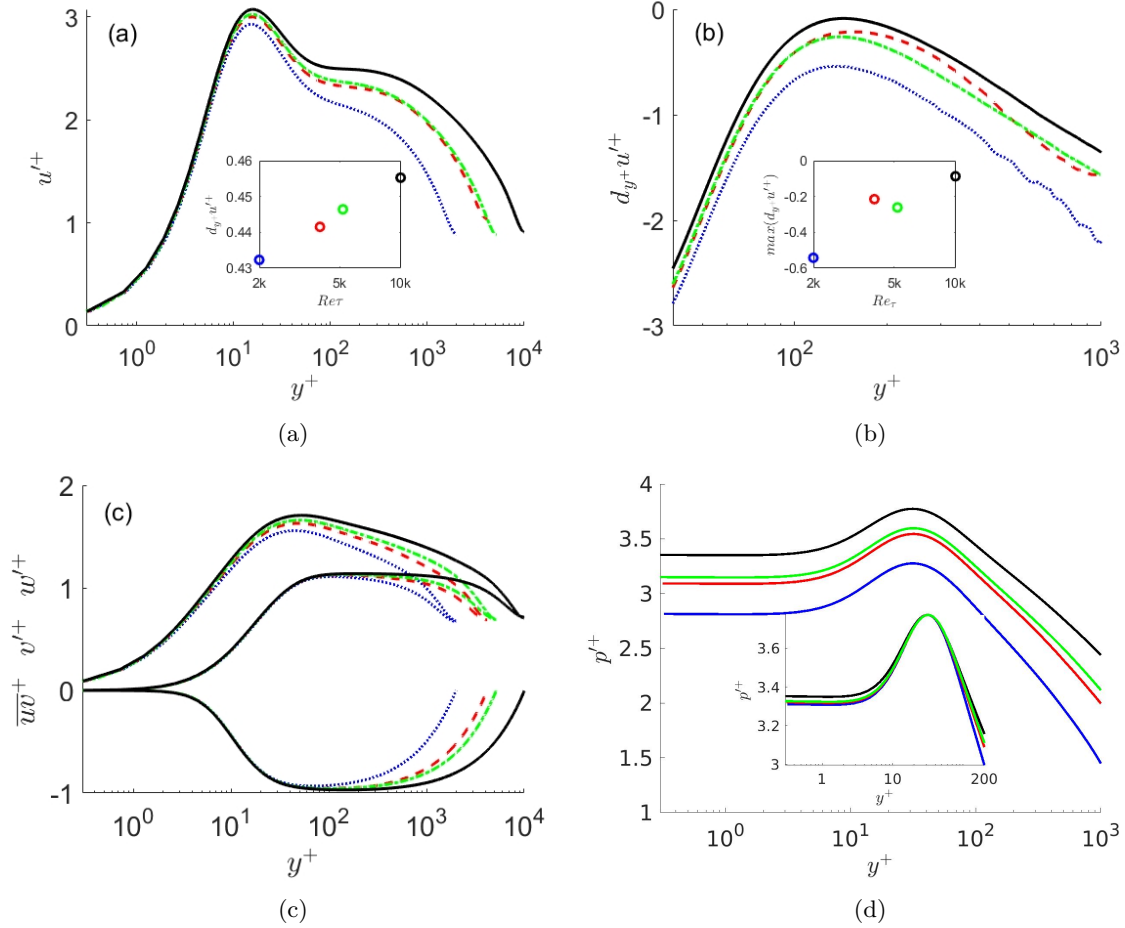
Figure 5.32: (a) u'^+. Box: $d_{y^+}u'^+$ evaluated at the wall. (b) $d_{y^+}u'^+$, close to the possible second maximum. Box: maximum value of $d_{y^+}u'^+$ (c) v'^+, w'^+ and $\overline{u^+v^+}$. (d) Intensity of total pressure. Box: shifting of all pressures to the peak of the case of this work. Lines as in table 5.9.
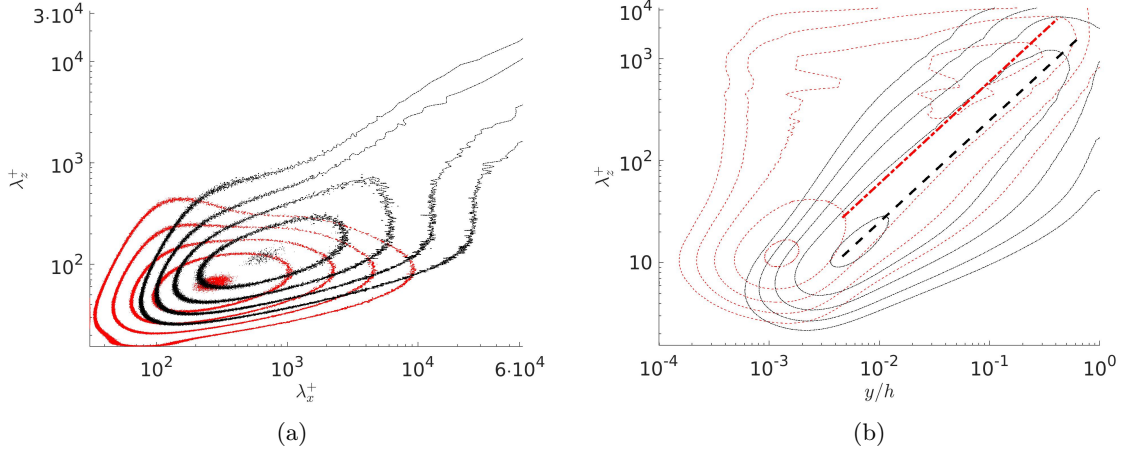
Figure 5.33: (a) 2D power spectra at $y \approx 15$. (b) 1D z-spectra. In both cases, U^+ (black) and V^+ (red). The inner isolines represents 90% of the energy. From there, each isoline is half of the energy of the previous one.

strain, and pressure-diffusion. They are defined by

$$P_{ij}^+ = -\overline{u_i^+ u_k^+} \partial_k \overline{U_j}^+ - \overline{u_j^+ u_k^+} \partial_k \overline{U_i}^+ \tag{5.24a}$$

$$\varepsilon_{ij}^+ = -2\overline{\partial_k u_i^+ \partial_k u_j^+}, \tag{5.24b}$$

$$T_{ij}^+ = \partial_k \overline{u_i^+ u_j^+ u_k^+}, \tag{5.24c}$$

$$V_{ij}^+ = \partial_{kk} \overline{u_i^+ u_j^+}, \tag{5.24d}$$

$$\Pi_{ij}^{s+} = \overline{p^+ (\partial_j u_i^+ + \partial_j u_i^+)}, \tag{5.24e}$$

$$\Pi_{ij}^{d+} = \partial_k \left(\overline{p^+ u_i^+} \delta_{jk} + \overline{p^+ u_j^+} \delta_{ik} \right). \tag{5.24f}$$

Finally, in channels $B_{ij}^+ \equiv 0$. In the viscous and buffer layers, budgets should scale in wall units. The budgets are shown in figure 5.34, using this scale. Except those terms that are identically zero, all are active. The well-known scaling failure [38] of the dissipation at the wall for B_{11}^+ is still present, figure 5.34a. As expected all terms collapse for $y^+ > 10$. However, below this more or less arbitrary limit, the absolute values of ε_{11}^+ and V_{11}^+ increase with the Reynolds number. This scaling failure can be linked to the growing of the first maximum of u'^+, as the scaling failure of V_θ^+ was linked to the growing of the first maximum of θ'^+. At the wall,

$$V_{11}^+ \big|_{y^+=0} = \partial_{y^+ y^+} \overline{u^{+2}} \big|_{y^+=0} = 2\overline{(\partial_y u^+)^2} \big|_{y^+=0} = -\varepsilon_{11}, \tag{5.25}$$

as all other terms vanish. Using the Taylor series decomposition (2.17c) proposed in [34] and [40], near the wall, $u'^+ \approx b_1 y^+$, and $V_{11}^+ \approx b_1^2$. Thus, the reason why this term of the turbulent budget does not scale with the Reynolds number in the wall comes from the differences in the b_1 terms. This term represents the slope of u'^+ near the wall. Looking at the box in figure 5.32a, one can see that, effectively, the value of du'^+/dy^+ at the wall does not collapse, but slightly increases. Apart from the data of this work, there are also experimental evidences that the peak at $y^+ \approx 15$ keeps growing with respect to Re_τ [87]. Because the position of the peak is constant in y^+, the slope of u'^+ has to be higher for larger Re_τ. In other words, as long as the peak of u'^+ increases with Re_τ, b_1 will also increase and V_{11}^+ cannot scale
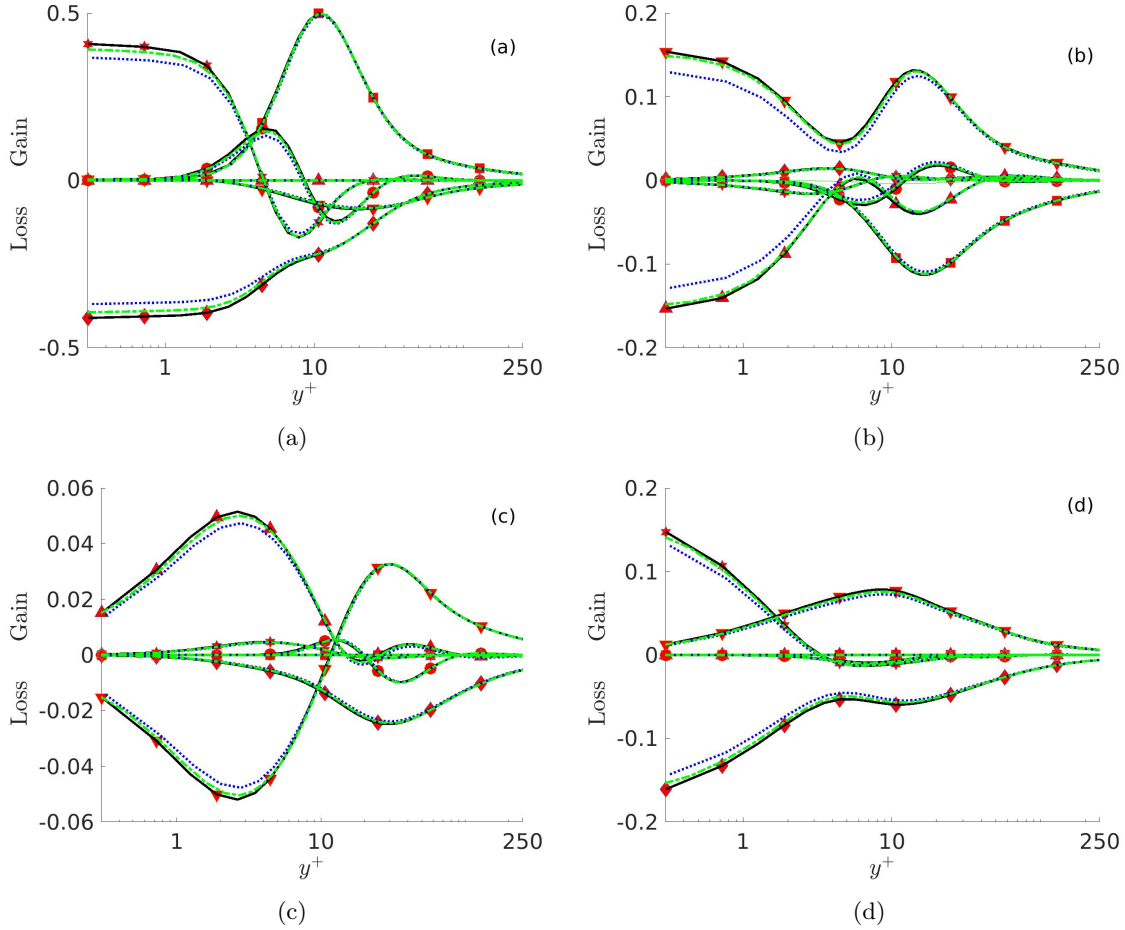
Figure 5.34: Budgets for Reynolds stresses in wall units. (a) B_{11}^+, (b) B_{12}^+, (c) B_{22}^+, (d) B_{33}^+. Production ■, dissipation ♦, viscous diffusion *, pressure-strain ▼, pressure diffusion ▲, turbulent diffusion ●. Lines as in table 5.9.

at the wall. This behaviour is identical to that of $V_{u\theta}^+$ observed in sections §5.1.2 and §5.1.3 and V_θ^+ observed in section §5.1.3.

The scaling failures of the pressure terms, figures 5.34b and 5.34c, are harder to explain because there are no good models for them [38]. However, it seems that this scaling failure is decreasing with the Reynolds number, even if the pressure keeps growing at the wall, as it is shown in 5.32d.

The situation in the center of the channel is better explained using a different nondimensionalization, $B_{ij}^* = yB_{ij}/u_\tau^3$, see figure 5.35. This scaling counteracts the expected decay of these terms far from the wall, which is roughly as y^{-1}. To avoid numerical noise, the turbulent diffusion has been computed here using the fact that $B_{ij} \equiv 0$. Above $y/h \approx 0.2$ the scaling is almost perfect. In agreement with previous results [38, 93], all the budgets above the buffer layer, $y/h > 10^{-3}$ in this case, are dominated by a few terms. The streamwise velocity fluctuations introduce the turbulent energy in the flow. This energy is dissipated by the dissipation and the pressure-strain terms (see figure 5.35a). Notice that $P_{11} \approx 2\varepsilon_{11}$ and that, in the channel center, the turbulent diffusion becomes dominant in the production of energy, as U^+ flattens.
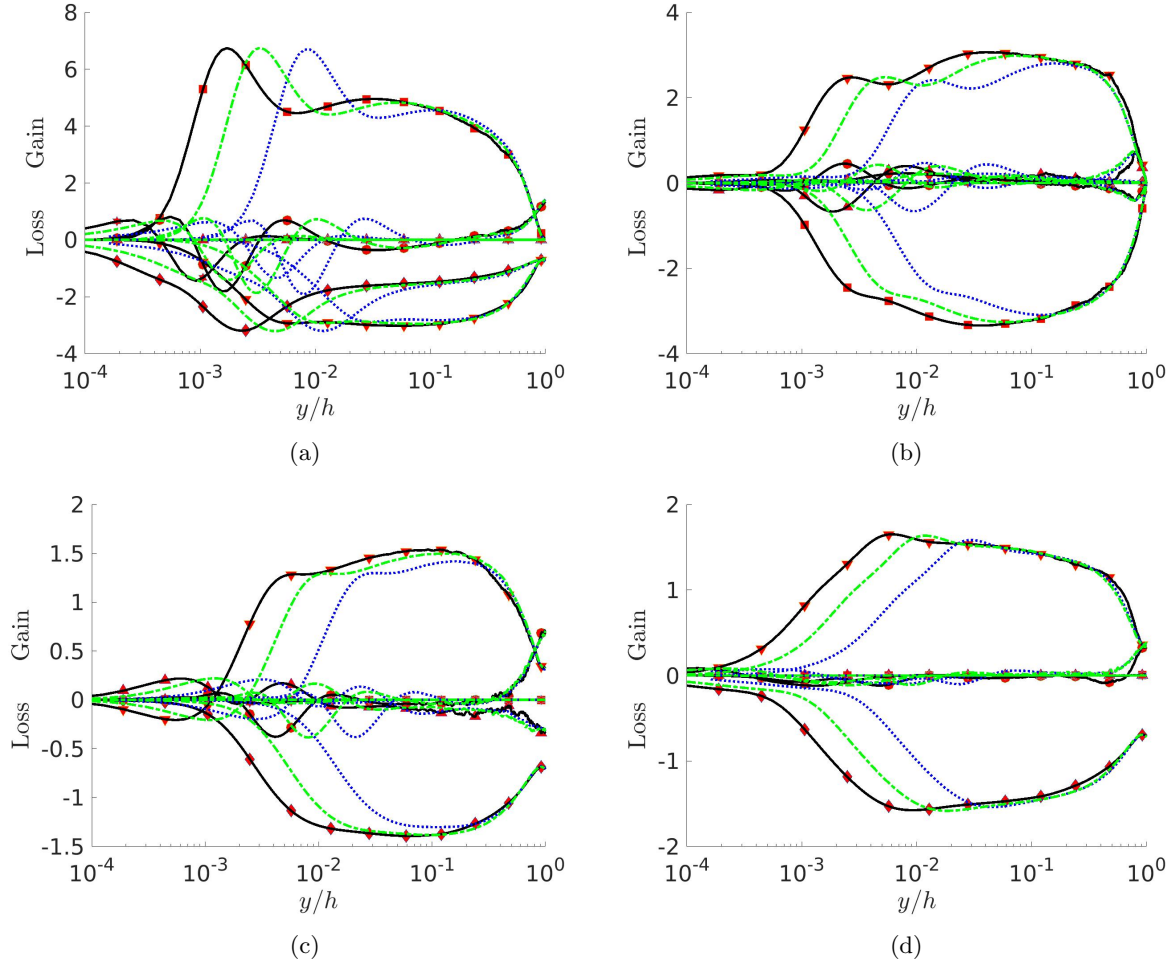
Figure 5.35: Premultiplied budgets for Reynolds stresses, $B_{ij}^* = yB_{ij}/u_\tau^3$. (a) B_{11}^*, (b) B_{12}^*, (c) B_{22}^*, (d) B_{33}^*. Production ■, dissipation ♦, viscous diffusion ∗, pressure-strain ▼, pressure diffusion ▲, turbulent diffusion ●. Lines as in table 5.9.

This energy is redistributed by pressure to V^+ and W^+, where it is dissipated by, certainly, the dissipation (see figures 5.35c and 5.35d). Notice, however, that pressure diffusion plays an important role in the channel center. Finally, for the Reynolds stress $\overline{u^+v^+}$, figure 5.35b, production and pressure strain are the dominant terms, but above $y/h \approx 0.5$ pressure diffusion and turbulent diffusion are also present.

Conclusions

To conclude, a Poiseuille turbulent channel flow at a friction Reynolds number of $Re_\tau = 10000$ has been simulated. This simulation was made in a small box of size $(2\pi h, 2h, \pi h)$, large enough to accurately compute the statistics of the flow. The profile of $\overline{U}^+$ shows a long log layer, extending from $y^+ \approx 400$ to $y^+ \approx 2500$. The value of the von Kármán constant is $\kappa = 0.394$. The first maximum of the streamwise profile u'^+ continues growing, which is the cause of the scaling failure of the dissipation at the wall. The second maximum of u'^+ has not appeared yet, and it is not clear if it eventually will. On the other hand, The turbulent budgets show a perfect scaling in the outer region with $B^*_{ij} = yB_{ij}/u^3_\tau$. Finally, the 1D spectra grow linearly in the logarithmic layer. Near the wall, the spectral analysis reinforces Townsend's hypothesis of inactive motions.

The data presented here can be download from the following link:

https://www.fdy.tu-darmstadt.de/fdyresearch/dns/direkte_numerische_simulation.en.jsp

5.1.5 Scaling laws of velocity, temperature and high order moments with Lie symmetries

Lie symmetries of the governing equations

In this section, the Lie symmetries of the governing equations (1.5), (1.6) and (1.7) are presented. For high Reynolds numbers flows, i.e. for $Re_\tau \to \infty$, one can neglect the viscous term for length scales beyond the Kolmogorov length scales, and the Navier-Stokes equations reduce to the Euler equations (see [94]). For the case of the Euler equations a 10-parameter symmetry group of transformation is obtained. For a complete set of the 10-parameter symmetry group, the reader is referred to [17]. Here, only the scaling groups needed further below to derive the scaling laws are presented

$$T_{Sx} \quad : \quad t^* = t, \quad \boldsymbol{x}^* = \mathrm{e}^{a_{Sx}}\boldsymbol{x}, \quad \boldsymbol{U}^* = \mathrm{e}^{a_{Sx}}\boldsymbol{U}, \quad P^* = \mathrm{e}^{2a_{Sx}}P, \tag{5.26}$$

$$T_{St} \quad : \quad t^* = \mathrm{e}^{a_{St}}t, \quad \boldsymbol{x}^* = \boldsymbol{x}, \quad \boldsymbol{U}^* = \mathrm{e}^{-a_{St}}\boldsymbol{U}, \quad P^* = \mathrm{e}^{-2a_{St}}P,. \tag{5.27}$$

The coefficients a_{Sx} and a_{St} are the group parameters of scaling in space and time, respectively.

If the Navier-Stokes equations are considered, i.e. the viscous term is not neglected, the two scaling symmetries, T_{Sx} and T_{St}, linearly combine into a simple scaling symmetry. This phenomenon, in which a multi-parameter symmetry group of transformations is reduced after a certain condition is applied is known as symmetry breaking.

An analogous simplification, as the transition from the Navier-Stokes to the Euler equation, applied to the energy equation (1.7) can be done by neglecting the diffusive term, i.e. $Pe_\tau \to \infty$. Considering this, the energy equation admits the following infinite dimensional symmetry

$$T_\Theta : \quad t^* = t, \quad \boldsymbol{x}^* = \boldsymbol{x}, \quad \boldsymbol{U}^* = \boldsymbol{U}, \quad P^* = P, \quad \Theta^* = f(\Theta). \tag{5.28}$$

For scaling purposes, and in analogy with the scaling symmetries of the Euler equations, it is consider the simplification $f(\Theta) = \mathrm{e}^{a_\Theta}\Theta$, so that T_Θ represents a scaling of temperature.

As noted in [71], the symmetries obtained for the Navier-Stokes and energy equations transfer to the MPC equations (3.15). So, in the limit of zero viscosity and diffusion, the MPC equations (3.15) admit

the following scaling symmetries:

$$
\overline{T}_{Sx} \quad : \quad t^* = t, \quad \boldsymbol{x}^* = \mathrm{e}^{a_{Sx}}\boldsymbol{x}, \quad H^*_{i_{\{n\}}\Theta_{\{m\}}} = \mathrm{e}^{na_{Sx}}H_{i_{\{n\}}\Theta_{\{m\}}},
$$

$$
I^*_{i_{\{n-1\}}\Theta_{\{m\}}[a]_P} = \mathrm{e}^{(n+1)a_{Sx}}I_{i_{\{n-1\}}\Theta_{\{m\}}[a]_P}, \tag{5.29}
$$

$$
\overline{T}_{St} \quad : \quad t^* = \mathrm{e}^{a_{St}}t, \quad \boldsymbol{x}^* = \boldsymbol{x}, \quad H^*_{i_{\{n\}}\Theta_{\{m\}}} = \mathrm{e}^{-na_{St}}H_{i_{\{n\}}\Theta_{\{m\}}},
$$

$$
I^*_{i_{\{n-1\}}\Theta_{\{m\}}[a]_P} = \mathrm{e}^{-(n+1)a_{St}}I_{i_{\{n-1\}}\Theta_{\{m\}}[a]_P}, \tag{5.30}
$$

$$
\overline{T}_{S\Theta} \quad : \quad t^* = t, \quad \boldsymbol{x}^* = \boldsymbol{x}, \quad H^*_{i_{\{n\}}\Theta_{\{m\}}} = \mathrm{e}^{ma_\Theta}H_{i_{\{n\}}\Theta_{\{m\}}},
$$

$$
I^*_{i_{\{n-1\}}\Theta_{\{m\}}[a]_P} = \mathrm{e}^{ma_\Theta}I_{i_{\{n-1\}}\Theta_{\{m\}}[a]_P}, \tag{5.31}
$$

which are immediate consequences of (5.26), (5.27) and the scaling version of (5.28).

In addition to the symmetries induced from the Navier-Stokes/Euler and energy equations, the MPC equations (3.15) admit an extended set of symmetry transformations. These symmetries are called statistical symmetries and they are the key in the process of deriving scaling laws [17] for high order moments of the velocity and temperature. These symmetries were discovered in [71] and detailed information on the physical meaning of the statistical symmetries can be found in [95]. First, because of the linearity of the MPC equations (3.15) a scaling symmetry of the dependent variables is admitted

$$
\overline{T}_{Ss} \quad : \quad t^* = t, \quad \boldsymbol{x}^* = \boldsymbol{x}, \quad H^*_{i_{\{n\}}\Theta_{\{m\}}} = \mathrm{e}^{a_{Ss}}H_{i_{\{n\}}\Theta_{\{m\}}},
$$

$$
I^*_{i_{\{n-1\}}\Theta_{\{m\}}[a]_P} = \mathrm{e}^{a_{Ss}}I_{i_{\{n-1\}}\Theta_{\{m\}}[a]_P}. \tag{5.32}
$$

This symmetry, as proven in [95], represents a measure of intermittency. Moreover, as all dependent variables in (3.15) appear inside derivatives, a translation symmetry of the moments is also admitted

$$
\overline{T}_{tra,H} \quad : \quad t^* = t, \quad \boldsymbol{x}^* = \boldsymbol{x}, \quad H^*_{i_{\{n\}}\Theta_{\{m\}}} = H_{i_{\{n\}}\Theta_{\{m\}}} + \boldsymbol{a}^H_{i_{\{n\}}\Theta_{\{m\}}},
$$

$$
I^*_{i_{\{n-1\}}\Theta_{\{m\}}[a]_P} = I_{i_{\{n-1\}}\Theta_{\{m\}}[a]_P} + \boldsymbol{a}^I_{i_{\{n-1\}}\Theta_{\{m\}}}. \tag{5.33}
$$

Apart from the symmetries presented, it will also be included the classical translation in space symmetry

$$
\overline{T}_{tra,x} \quad : \quad t^* = t, \quad \boldsymbol{x}^* = \boldsymbol{x} + \boldsymbol{a}_x, \quad H^*_{i_{\{n\}}\Theta_{\{m\}}} = H_{i_{\{n\}}\Theta_{\{m\}}},
$$

$$
I^*_{i_{\{n-1\}}\Theta_{\{m\}}[a]_P} = I_{i_{\{n-1\}}\Theta_{\{m\}}[a]_P}. \tag{5.34}
$$

Note that, in contrast to (5.32), where a_{Ss} is a single group parameter, symmetries (5.33) and (5.34) are a condensed way of showing several symmetries. Each component of the vector and tensors $\boldsymbol{a}^H_{\{n\}\{m\}}$, $\boldsymbol{a}^I_{\{n-1\}\{m\}}$ and $\boldsymbol{a}_x$ represent the group parameter of different and independent symmetries. Therefore, infinite symmetries are contained in (5.33), while (5.34) contains three symmetries, one for each spatial direction.

In summary, six symmetries have been identified, that will be used to derive the scaling laws of high order moments of the velocity and temperature. One property of the Lie symmetries is that one can combine different one-parameter Lie symmetries into a multi-parameter Lie symmetry. Following this, one can obtain the following multi-parameter Lie symmetry group from the symmetries (5.29)-(5.34)

$$
T \quad : \quad t^* = \mathrm{e}^{a_{St}}t, \quad \boldsymbol{x}^* = \mathrm{e}^{a_{Sx}}\boldsymbol{x} + \boldsymbol{a}_x,
$$

$$
H^*_{i_{\{n\}}\Theta_{\{m\}}} = \mathrm{e}^{n(a_{Sx}-a_{St})+ma_\Theta+a_{Ss}}H_{i_{\{n\}}\Theta_{\{m\}}} + \boldsymbol{a}^H_{i_{\{n\}}\Theta_{\{m\}}}, \tag{5.35}
$$

$$
I^*_{i_{\{n-1\}}\Theta_{\{m\}}[a]_P} = \mathrm{e}^{(n+1)(a_{Sx}-a_{St})+ma_\Theta+a_{Ss}}I_{i_{\{n-1\}}\Theta_{\{m\}}[a]_P} + \boldsymbol{a}^I_{i_{\{n-1\}}\Theta_{\{m\}}}.
$$

105

A different way of writing the symmetry group (5.35) is using the infinitesimal notation (3.25), from which one obtains

$$
\begin{aligned}
\xi_t &= a_{St}t, \quad \boldsymbol{\xi}_x = a_{Sx}\boldsymbol{x} + \boldsymbol{a}_x, \\
\eta_{H_{i_{\{n\}}\Theta_{\{m\}}}} &= [n(a_{Sx} - a_{St}) + ma_\Theta + a_{Ss}]\,H_{i_{\{n\}}\Theta_{\{m\}}} + \boldsymbol{a}^H_{i_{\{n\}}\Theta_{\{m\}}}, \\
\eta_{I_{i_{\{n-1\}}\Theta_{\{m\}}[a]_P}} &= [(n+1)(a_{Sx} - a_{St}) + ma_\Theta + a_{Ss}]\,I_{i_{\{n-1\}}\Theta_{\{m\}}[a]_P} + \boldsymbol{a}^I_{i_{\{n-1\}}\Theta_{\{m\}}}.
\end{aligned}
\tag{5.36}
$$

New high order moment scaling laws

Using the symmetries (5.35), or rather its infinitesimal form (5.36), it is possible to compute the invariant solutions of the equations (3.15), which in turbulence are called the turbulent scaling laws. For this purpose the infinitesimals (5.36) are inserted into the invariant surface condition (3.86) and it is obtained

$$
\begin{aligned}
\frac{dx_2}{a_{Sx}x_2 + a_{x_2}} &= \frac{dH_{1_{\{1\}}}}{[a_{Sx} - a_{St} + a_{Ss}]\,H_{1_{\{1\}}} + \boldsymbol{a}^H_{1_{\{1\}}}} \\
&= \frac{dH_{\Theta_{\{1\}}}}{[a_\Theta + a_{Ss}]\,H_{\Theta_{\{1\}}} + \boldsymbol{a}^H_{\Theta_{\{1\}}}} \\
&= \frac{dH_{1_{\{1\}}\Theta_{\{1\}}}}{[a_{Sx} - a_{St} + a_\Theta + a_{Ss}]\,H_{1_{\{1\}}\Theta_{\{1\}}} + \boldsymbol{a}^H_{1_{\{1\}}\Theta_{\{1\}}}} \\
&= \dots \\
&= \frac{dH_{1_{\{n\}}\Theta_{\{m\}}}}{[n(a_{Sx} - a_{St}) + ma_\Theta + a_{Ss}]\,H_{1_{\{n\}}\Theta_{\{m\}}} + \boldsymbol{a}^H_{1_{\{n\}}\Theta_{\{m\}}}}
\end{aligned}
\tag{5.37}
$$

Since a shear flow is considered, which is fully parallel in the statistical mean, all moments in the one-point limit depend only on x_2. Furthermore, the dependencies of the other points for the higher order tensors would have to be formally considered as well, because this would result in further similarity variables. However, from now on, the study will be focus on the one-point statistics, so that every point of application of the variables in (3.15) will be $\boldsymbol{x}_{(1)} = \boldsymbol{x}_{(2)} = \dots = \boldsymbol{x}_{(n+m)}$.

For the integration of the characteristic system (5.37), there are two cases to be distinguished and their solutions correspond to the logarithmic layer and centre region of the channel. The first case describes the logarithmic law, which was only perfectly observed for the mean velocity in the case of $Re_\tau = 10000$ in subsection §5.1.4. Therefore, the application of Lie symmetries to obtain scaling laws in the logarithmic layer will only be applied to that case. The key parameter here is the wall shear stress velocity, $u_\tau = \sqrt{\tau_w/\rho}$. u_τ uniquely determines the only velocity scale in the problem. For a given flow, this refers to a specific value, which implies that a scaling of the velocities according to infinitesimal transformation (5.36), with arbitrary parameter a_{Sx}, a_{St} and a_{Ss}, is no longer feasible. Hence, in terms of symmetry theory, u_τ is symmetry breaking for the velocity and for the group parameters in (5.36). This implies that $a_{Sx} - a_{St} + a_{Ss} = 0$. Using this during the integration of the characteristic system (5.37), it is obtained

$$
\overline{U}_1 = \frac{a_1}{a_{Sx}}\ln\left(x_2 + \frac{a_{x_2}}{a_{Sx}}\right) + \tilde{C}_1,
\tag{5.38a}
$$

$$
H_{1_{\{n\}}} = \tilde{C}_n\left(x_2 + \frac{a_{x_2}}{a_{Sx}}\right)^{\omega(n-1)} - \frac{a^H_{1_{\{n\}}}}{(n-1)(a_{Sx} - a_{St})},
\tag{5.38b}
$$

$$
\text{with} \quad \tilde{C}_n = e^{\tilde{c}_n(n-1)(a_{Sx} - a_{St})},
\tag{5.38c}
$$

where $\tilde{C}_1$ and $\tilde{c}_n$ represent integration constants and $\omega = 1 - a_{St}/a_{Sx}$. The three central results here are that in the logarithmic region for the mean velocity (i) the moment $n = 1$ follows a logarithmic law, (ii) the

moments $n > 1$ behave like a power-law, (iii) the exponents for all n^{th} moments are determined by a single parameter which is the exponent ω for the second moment. For the classical near-wall logarithmic region for the mean velocity in equation (5.38a), these laws are now to be transformed into wall-coordinates using ν and u_τ to nondimensionalize, obtaining

$$\overline{U}_1^+ = \frac{1}{\kappa}\ln\left(x_2^+\right) + B_1, \tag{5.39a}$$

$$H_{1_{\{n\}}}^+ = C_n\left(x_2^+\right)^{\omega(n-1)} - B_n, \quad \text{for} \quad n \geq 2, \tag{5.39b}$$

$$C_n = \alpha e^{\beta n}, \quad B_n = \tilde{\alpha} e^{\tilde{\beta} n}, \quad \text{for} \quad n \geq 2. \tag{5.39c}$$

where in κ, B_1, B_n, C_n, α, β, $\tilde{\alpha}$ and $\tilde{\beta}$ it is subsumed the various constants appearing in equations (5.38a) and (5.38b). κ refers to the usual von Kármán constant and equation (5.39a) is identical to the already introduced equation (1.28) in chapter §1. The shift in x_2 by a_{x_2} in equations (5.38a) and (5.38b) has been set to zero, although there are works, [96], that suggest a non-zero shift. However, the numerical value is small and thus is negligible for large x_2^+. A value of $\kappa = 0.394$ was obtained, as reported in section §5.1.4, similar to previous simulations at lower Reynolds numbers [73]. Interestingly, the data below shows that the α and β are essentially independent of n, so C_n results in a simple exponential function in n. Actually, this also results for $\tilde{\alpha}$ and $\tilde{\beta}$ in B_n, although the reason for this is unknown.

For the case of integration of the characteristic system (5.37) in the center of the channel, both, velocity and temperature fields, will be consider to validate the scaling laws. In this case, no a priori symmetry breaking scale is introduced into the characteristic system, i.e. the factors $(a_{Sx} - a_{St} + a_\Theta + a_{Ss}), \ldots, n(a_{Sx} - a_{St}) + m a_\Theta + a_{Ss}$, are all assumed to be non-zero. This results in power-laws for all moments $n + m$, including the first moment $n = 1$, $m = 0$ and $n = 0$, $m = 1$. After the integration, it is observed that the parameters a_{Sx}, a_{St}, a_Θ and a_{Ss} only occur as ratios and hence only three free parameters exist. If the exponents for the first two moments, σ_1, σ_2 and σ_Θ, are given, it is obtained that

$$H_{1_{\{n\}}\Theta_{\{m\}}} = \tilde{C}'_{1_{\{n\}}\Theta_{\{m\}}} \left(x_2 + \frac{a_{x_2}}{a_{Sx}}\right)^{n(\sigma_2-\sigma_1)+m\sigma_\Theta+2\sigma_1-\sigma_2}$$
$$- \frac{a_{1_{\{n\}}\Theta_{\{m\}}}^H}{n(a_{Sx}-a_{St})+m a_\Theta+a_{Ss}}, \tag{5.40}$$

where $\tilde{C}'_{1_{\{n\}}\Theta_{\{m\}}}$ denote the constants of integration, $\sigma_1 = 1 - a_{St}/a_{Sx} + a_{Ss}/a_{Sx}$, $\sigma_2 = 2(1 - a_{St}/a_{Sx}) + a_{Ss}/a_{Sx}$ and $\sigma_\Theta = a_\Theta/a_{Sx}$. The choice of parameters in the exponent of (5.40) has been designed so that the high order moments depend on those of the first and second order. This can be easily seen by using $n = 1$ and $n = 2$ for $m = 0$ and $m = 1$ for $n = 0$. Therefore, σ_1 and σ_2, which come from symmetries of the Navier-Stokes equations (1.5) and (1.6), are determined from velocity moments, while σ_Θ is determined from the first temperature moment, which is influenced by the velocity. In such a way, the condition of passive scalar is also extended to the parameters of the scaling law. It is important to recall that the invariant solution (5.40) has been derived in the limit of vanishing viscosity and heat conduction. Therefore, this solution, will be only valid in the region where these conditions apply, i.e. the center of the channel. The invariant solution (5.40) shows that the moments of velocity, temperature and higher order moments scale as power-laws, whose exponents are determined by the parameters σ_1, σ_2 and σ_Θ.

Analogously to [14], where the scaling law of the mean velocity of a turbulent shear flow was presented as a deficit law, equation (5.40) can be rewritten to form the final scaling law of the velocity, temperature and higher order moments of both as

$$\frac{H_{1_{\{n\}}\Theta_{\{m\}}cl} - H_{1_{\{n\}}\Theta_{\{m\}}}}{u_\tau^n \theta_\tau^m} = C'_{1_{\{n\}}\Theta_{\{m\}}} \left(\frac{x_2}{h}\right)^{n(\sigma_2-\sigma_1)+m\sigma_\Theta+2\sigma_1-\sigma_2}, \tag{5.41a}$$

$$\text{with} \quad C'_{1_{\{n\}}\Theta_{\{m\}}} = \alpha' e^{n\beta'_1 + m\beta'_\Theta}, \tag{5.41b}$$

107

where the subscript cl refers to the value of the moment in the center line, which comes from the last term on the right hand side of equation (5.40), and similar to equation (5.39c) above, α', β_1' and β_Θ' subsume various constants and are presumed to be universal. Also note that, in equation (5.41a), the shift in x_2 coordinate has be neglected, since the value of a_{x_2}/a_{Sx} can be set to 0 or at least, it is negligible, as suggested in [96]. Equation (5.41a) is the final scaling law in the center of the channel of velocity, temperature and high order moments of both.

Validation of the scaling laws with DNS data

The new scaling laws (5.39a), (5.39b) and (5.41a) will be validated by using DNS data presented in the previous subsections. The moments calculated in the simulations go up to order seven for pure moments of velocity and temperature and up to order six for mixed moments of velocity and temperature. The procedure to fit the scaling laws to the DNS data has been done by minimizing the infinite norm of the relative error between the fit and the value of the DNS data, i.e.

$$\min \left(\left\| \frac{data(x_2) - fit(x_2)}{data(x_2)} \right\|_\infty \right). \tag{5.42}$$

Using the infinite norm, more accurate results were obtained. With this, the exponent for any high order moment is know and only the constants of integration must be calculated.

Starting first with the validation of the scaling laws in the logarithmic region, (5.39a) and (5.39b), for the velocity field, as mentioned in subsection §5.1.4, the logarithmic law is linked to a flat region of the diagnostic function, Ξ,

$$\Xi = x_2^+ \partial_{x_2^+} \overline{U}_1^+, \tag{5.43}$$

which was indeed nicely observed in figure 5.31 of previous subsection employing the new DNS data in the region $x_2^+ = 400 - 2500$.

Figure 5.36 shows the first central result of the application of Lie symmetries to turbulent flows, which is the comparison between DNS data for the moments $n \geq 2$ and equation (5.39b). A double logarithmic plotting has been adopted to make the power-laws visible more clearly. The universal numerical value ω in equation (5.39b) has been chosen to $\omega = 0.10$ to match the DNS data and gives the best fit for all higher moments up to $n = 6$.

The two key results in figure 5.36a are (i) a nearly perfect representation of the power law for all moments solely based on the single parameter ω and (ii) the validity of all moments in the logarithmic region with range of $x_2^+ \simeq 400 \ldots 2500$.

Looking closely at figure 5.36a one might get the impression that the power-law scaling of equation (5.39b) continues beyond the domain $x_2^+ \simeq 400 \ldots 2500$, however, it does not, as can be shown with the definition of a power-law diagnostic function. To extract the exponent in (5.39b) it is defined

$$\Xi_n = \frac{x_2^+}{H_{1_{\{n\}}}^+ + B_n} \frac{dH_{1_{\{n\}}}^+}{dx_2^+} = \omega(n-1). \tag{5.44}$$

DNS data are now inserted into (5.44) and compared with the exact value $\omega(n-1)$ in figure 5.36b. It can be seen that especially for higher moments the constant range of validity stands out very clearly. The horizontal lines in figure 5.36b denote the theoretical values $\omega(n-1)$ and even for the highest moment with $n = 6$ the deviation is less than 2.1%.

Further, in addition to the validity of wall-distance based scaling properties, it is important to verify the exponential scaling of C_n and B_n with n, equation (5.39c). Indeed, it is found an almost optimal agreement of this scaling given in equation (5.39c) with the DNS data shown in figure 5.37 where also the scaling of $C'_{1_{\{n\}}\Theta_{\{m\}}}$ from equation (5.41b) has been included for the case of the velocity with $Re_\tau = 10000$. It should be reminded that this is due to the fact that the constants of integration $\tilde{c}_n$ emerging from the
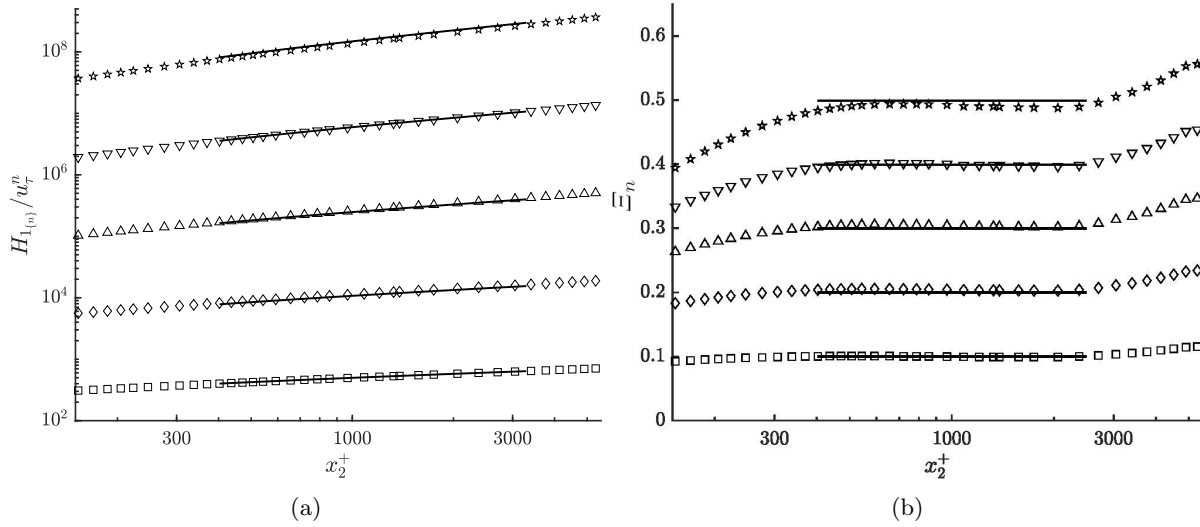
Figure 5.36: Symbols $n = 2$: $\square$, $n = 3$: $\diamond$, $n = 4$: $\triangle$, $n = 5$: $\triangledown$, and $n = 6$: $\star$ DNS data; (a): moments $H_{1_{\{n\}}}$; ▬▬: equation (5.39b) with coefficients fitted to DNS data. (b): Ξ_n according to equation (5.44); ▬▬: $\Xi_n = \omega(n-1)$ with $\omega = 0.10$.

integration of the characteristic system (5.37) are essentially independent of n and are all of order one. The deeper background for this is not fully evident so far.

Regarding the scaling law in the center of the channel, given in equation (5.41a), the results of the fits of the velocity moments for $Re_\tau = 500$ and $Pr = 4$ can be seen in figure 5.38a, together with the fits of the velocity moments for $Re_\tau = 2000$ and $Pr = 7$, in figure 5.38b. Also for $Re_\tau = 2000$ and $Pr = 7$, the fits of the temperature and heat fluxes moments are presented in figures 5.38c and 5.38d, respectively. Solid lines represent the values from the DNS, while squares are the values obtained from the scaling law (5.41a). In these figures, the wall and center of the channel are swapped, so the center line is at $x_2/h = 0$, while the wall is at $x_2/h = 1$. Also, it is important to mention that the range of the center of the channel where the scaling law has been applied is up to $x_2/h = 0.75$. The most important result is the high accuracy of the scaling law to fit the data of the DNS for all moments, with highest relative errors of only 0.2%. Even for the lowest Reynolds numbers of value 500, the accuracy of the fit is almost as good as for $Re_\tau = 2000$, as can be seen in figures 5.38a and 5.38b. In the same way, the scaling law is validated for the temperature and all high order moments with figures 5.38c and 5.38d, respectively.

On the other hand, a comparison of the scaling between a high Prandtl number of 4 and a very low one of 0.01 is done in figure 5.39. In the case of the scaling of temperature and its high order moments, figures 5.39a and 5.39b, for cases of $Pr = 4$ and 0.01, respectively, there is a noticeable difference. While for $Pr = 4$ the scaling presents a high accuracy with errors lower than 0.01%, for the case of $Pr = 0.01$, the errors are high and clearly visible in figure 5.39b. The reason of this error comes from the assumption of zero heat conduction, which, obviously, for $Pr = 0.01$ is not true. The high diffusivity for very low Prandtl numbers affects the temperature field in a deeper region away from the wall, and the temperature moments are no longer parallel for x_2/h approximately grater than 0.2. In the same manner, the scaling of mixed moments is no longer correct for very low Prandtl numbers. While in figure 5.39c, the scaling is again very accurate for $Pr = 4$, in figure 5.39d, similar failures appear in the scaling for $Pr = 0.01$. Note that in figure 5.39d, only moments for $n + m = 2$, 4 and 6 are plotted for clarity of the figure.

It is important to analyse the values of the different parameters of the scaling law and see the influence of each symmetry on the final scaling. As it was shown in equation (5.41a), the exponent of the power-law is formed by a constant term, $2\sigma_1 - \sigma_2$, that comes from the scaling symmetry of the moments, $\overline{T}_{Ss}$ (5.32);
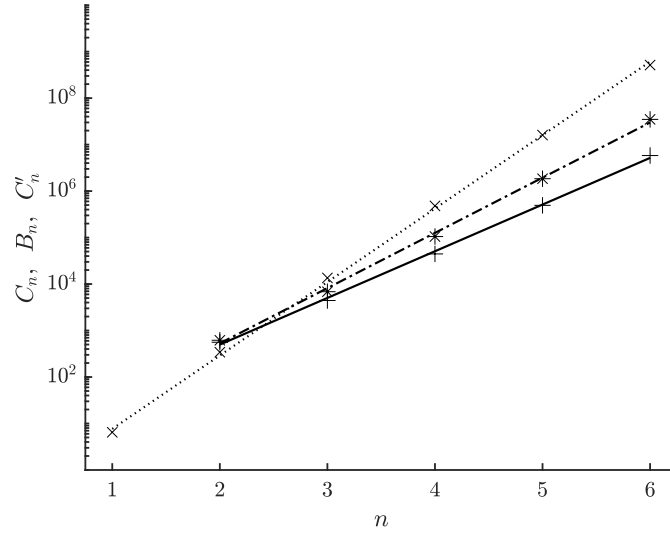
Figure 5.37: Lines refer to coefficients C_n (——) and B_n (—·—·) defined in equation (5.39c) with $\alpha = 4.88$, $\beta = 2.31$, $\tilde{\alpha} = 2.23$, $\tilde{\beta} = 2.74$, and coefficient $C'_{1_{\{n\}}\Theta_{\{m\}}}$ (▬ ▬) defined in equation (5.41b) with $\alpha' = 0.21$, $\beta' = 3.64$; data points ($+$), ($*$) and ($\times$) are fitted directly to DNS data at $Re_\tau = 10000$.

a second term that depends on n, $n(\sigma_2 - \sigma_1)$, which comes from the scaling symmetries in space and time, $\overline{T}_{Sx}$ (5.29) and $\overline{T}_{St}$ (5.30), respectively; and a third term that depends on m, $m\sigma_\Theta$, which has its roots in the scaling symmetry of the temperature, $\overline{T}_{S\Theta}$ (5.31). However, as can be clearly seen in figure 5.38, all moments have a more or less constant slope in the log-log plot, which translates into a non-existent or very small dependence on n and m. In other words, the values of σ_1 and σ_2 should be very similar, and σ_Θ should be small compared with the value of $2\sigma_1 - \sigma_2$. Regarding the scaling symmetries, this means that scaling in space and time have almost no influence in the center of the channel. On the other hand, the scaling of moments has to be dominant in the center of the channel, which makes sense, since, as it was said before, it is a measure of intermittency.

Figure 5.40a presents the values of σ_1 and σ_2 for all the DNS simulations, while the values of σ_Θ are shown in figure 5.40b. The values of σ_1 are almost the same than σ_2, which confirms that the symmetries of scaling in space and time have almost no influence in the center of the channel. Similarly, the scaling symmetry of temperature has barely no influence, since $\sigma_\Theta \ll 2\sigma_1 - \sigma_2$. This latest term, $2\sigma_1 - \sigma_2$, is indeed the only dominant term in the exponent of the scaling law (5.41a), with a value slightly below 2, confirming that the symmetry of scaling of moments, $\overline{T}_{Ss}$ (5.32), is dominant in the center of the channel. One last point to be analysed is whether the values of the parameters obtained are constant for every Re_τ and Pr or not, which, according to the scaling law (5.41a), should be. For all the parameters, σ_1, σ_2 and σ_Θ, an almost constant value is obtained in all ranges of the parameters Re_τ and Pr used. Small differences can be due to small numerical errors or small noise in the fitting.

The other part of the scaling law (5.41a) is the constant of integration $C'_{1_{\{n\}}\Theta_{\{m\}}}$. Figure 5.41a shows the values of $C'_{1_{\{n\}}\Theta_{\{m\}}}$ for $Re_\tau = 500$ and $Pr = 4$. An almost perfect plane is observed in a z-log plot, which suggest that $C'_{1_{\{n\}}\Theta_{\{m\}}}$ is an exponential function in n and m, obtaining equation (5.41b).

Note that relation (5.41b) is not obtained from first principles, but just from inspection. In figures 5.41b, 5.41c and 5.41d, the values of α', β'_1 and β'_Θ for every simulation are presented, respectively. In order to calculate them, only the constants of integration of the moments up to order 2 have been used, i.e. $C'_{1_{\{1\}}}$, $C'_{1_{\{2\}}}$, $C'_{\Theta_{\{1\}}}$, $C'_{\Theta_{\{2\}}}$ and $C'_{1_{\{1\}}\Theta_{\{1\}}}$. With these five values, a fit of the parameters have been done minimizing again as in equation (5.42).
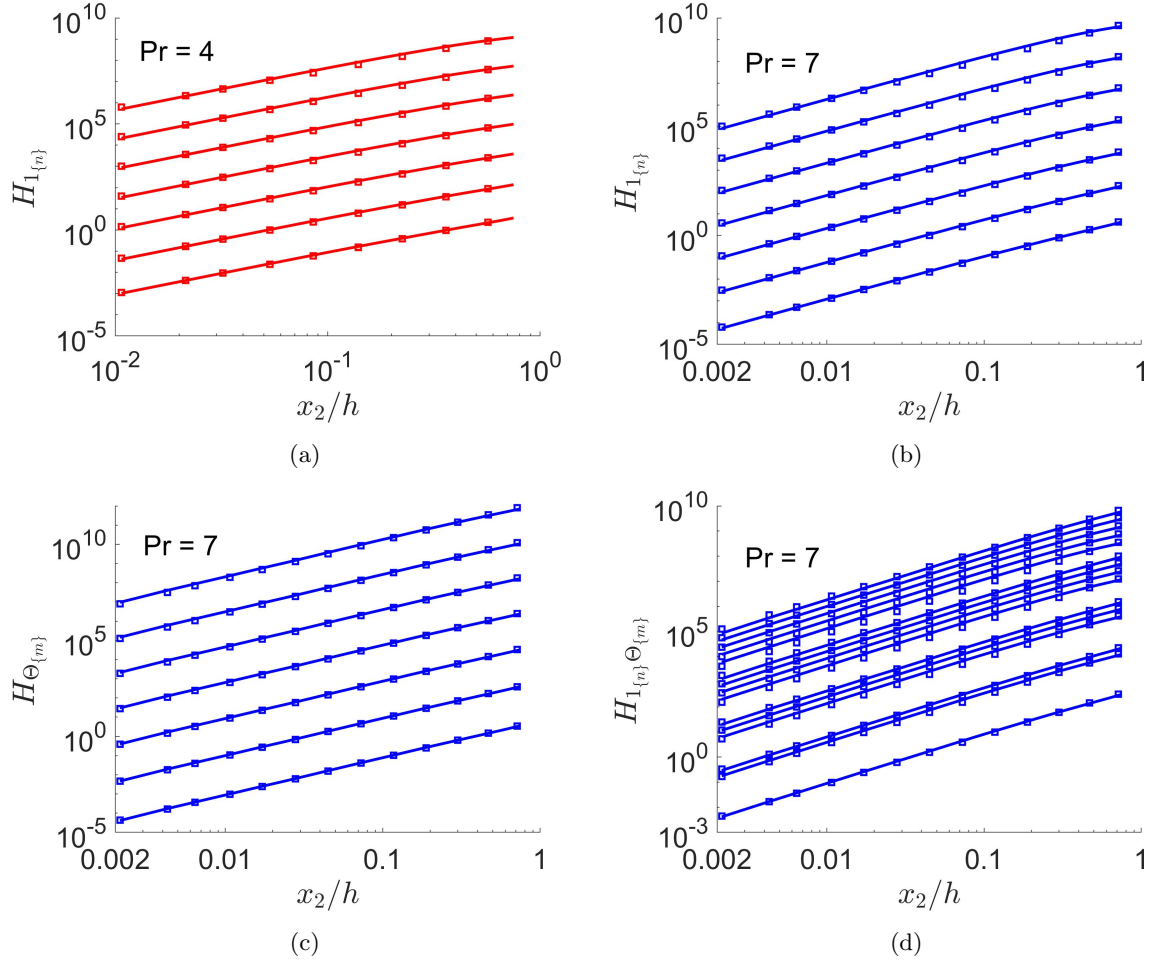
110

Figure 5.38: Moments of velocity, $H_{1_{\{n\}}}$, for (a) $Re_\tau = 500$ and $Pr = 4$ and (b) $Re_\tau = 2000$ and $Pr = 7$. (c) Moments of temperature, $H_{\Theta_{\{m\}}}$, and (d) mixed moments, $H_{1_{\{n\}}\Theta_{\{m\}}}$, for $Re_\tau = 2000$ and $Pr = 7$. In (a), (b) and (c), velocity and temperature moments are obtained for n and $m = 1, 2,..., 7$, appearing in that order from bottom to top of the plot. For (d), mixed moments are shown for $n + m = 2, 3,...,$ 6, appearing in that order from bottom to top of the plot. For mixed moments of the same order, the lower lines are for $m = 0$, while the upper lines are for $n = 0$. Solid lines are the values from the DNS, while squares represent the values from the scaling law (5.41a). The wall and center of the channel are swapped, so the center line is at $x_2/h = 0$, while the wall is at $x_2/h = 1$. Colours as in table 5.1.

111
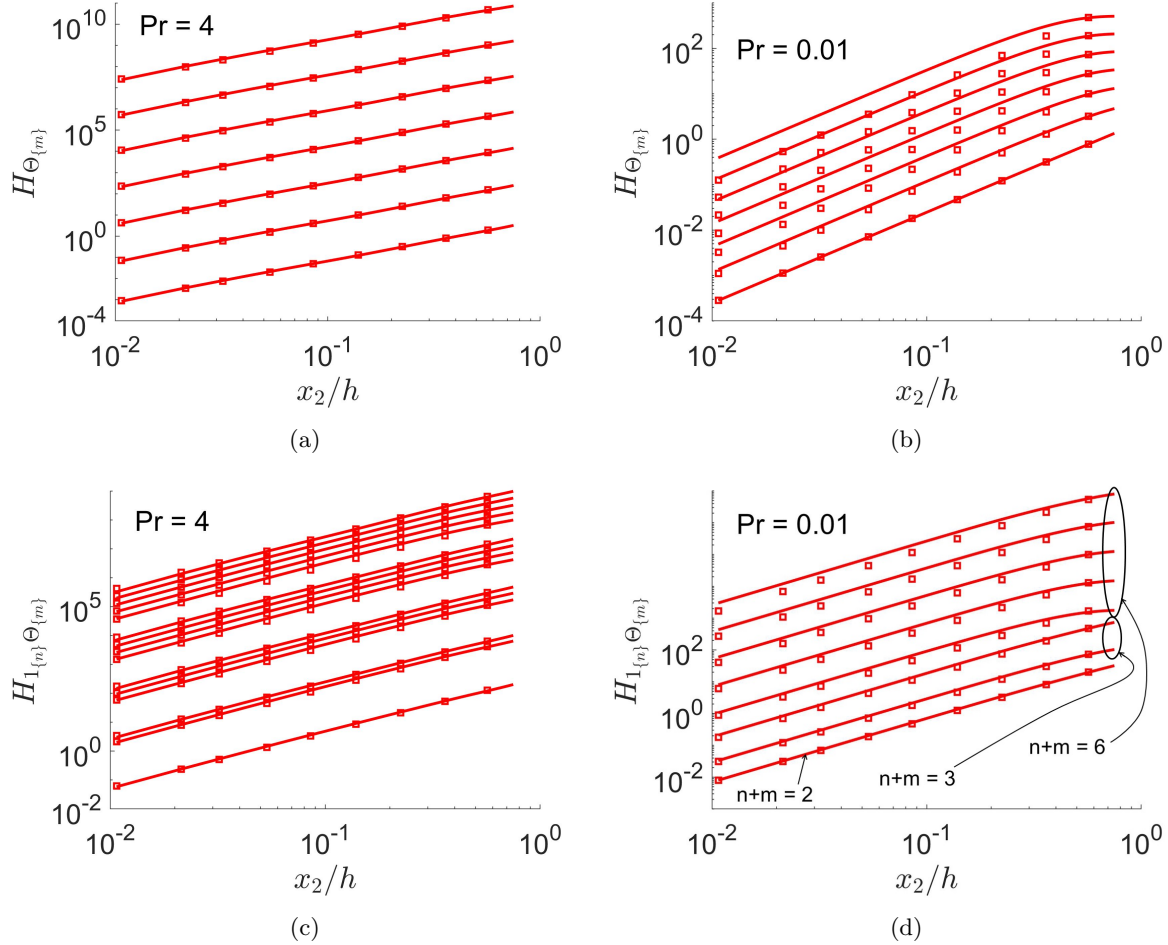
Figure 5.39: Moments of temperature, $H_{\Theta_{\{m\}}}$, for (a) $Re_\tau = 500$ and $Pr = 4$ and (b) $Re_\tau = 500$ and $Pr = 0.01$. Mixed moments, $H_{1_{\{n\}}\Theta_{\{m\}}}$, for (c) $Re_\tau = 500$ and $Pr = 4$ and (d) $Re_\tau = 500$ and $Pr = 0.01$. In (a) and (b), temperature moments are obtained for $m = 1, 2,..., 7$, appearing in that order from bottom to top of the plot. In (c), mixed moments are shown for $n + m = 2, 3,..., 6$, appearing in that order from bottom to top of the plot. For mixed moments of the same order, the lower lines are for $m = 0$, while the upper lines are for $n = 0$. In (d), mixed moments are shown for $n + m = 2, 3$ and 6, appearing in that order from bottom to top of the plot. For mixed moments of the same order, the lower lines are for $n = 0$, while the upper lines are for $m = 0$. Solid lines are the values from the DNS, while squares represent the values from the scaling law (5.41a). The wall and center of the channel are swapped, so the center line is at $x_2/h = 0$, while the wall is at $x_2/h = 1$. Colours as in table 5.1.
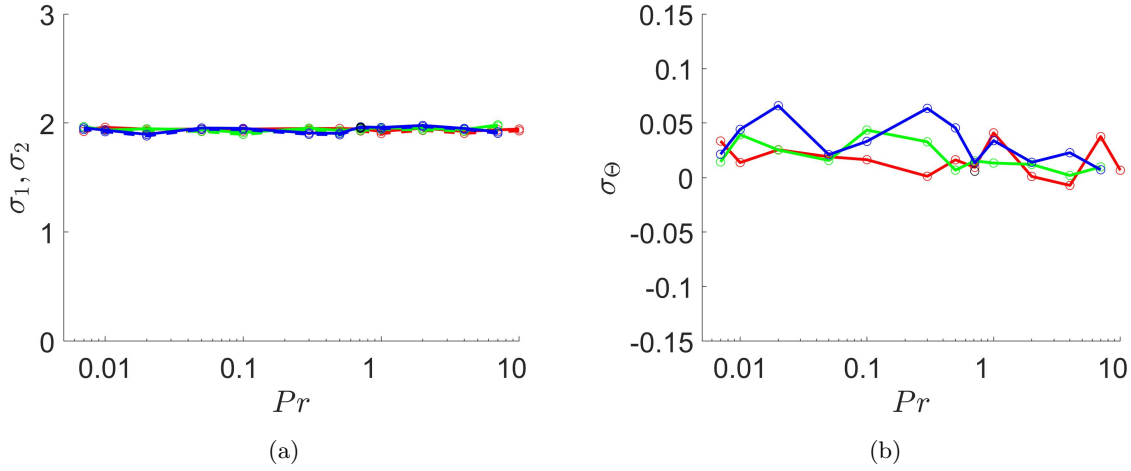
Figure 5.40: Values of (a) σ_1, solid lines, and σ_2, dashed lines, and (b) σ_Θ. Colours as in table 5.1. Note that black points at $Pr = 0.71$ represent the value for the single simulation at $Re_\tau = 5000$.

A first problem arises at this point. The coefficients are not constant for different values of Re_τ and Pr. From the symmetries derived in subsection §5.1.5, there is not dependence of this constant with respect to Re_τ or Pr. However, this dependence goes beyond the scope of the study of this work. Here the study is limited to confirm that the scaling law (5.41a) can represent the behaviour of the arbitrary moments obtained from the DNS data, which indeed happens, as it has been proved, and to give the actual values of $C'_{1_{\{n\}}\Theta_{\{m\}}}$.

Conclusions

A new set of scaling laws for arbitrary moments of the velocity, temperature and high order moments of both in a turbulent channel flow have been obtained using the Lie symmetries theory. These scaling laws are for incompressible flows moved by a pressure difference and with a passive scalar. In addition, the scaling laws are valid for zero viscosity and zero diffusion, i.e. Re_τ and $Pr \to \infty$, and two cases are distinguished: the logarithmic layer and the center of the channel.

In the logarithmic layer, the mean velocity behaves as the well-known logarithmic function, first derived by von Kármán and derived here from first principles. The high order moments are power functions that depend on the order of the moment n. No derivation of a scaling law for the temperature field has been derived in the logarithmic region, since no perfectly plateau was observed in the diagnostic function of the mean temperature in previous subsections.

On the other hand, in the center of the channel, scaling laws of the arbitrary moments are presented in deficit form in the wall-normal direction. These scaling laws are represented as power functions, where the exponent is determined by the order of the moments and three different parameters that come from different symmetries (σ_1, σ_2 and σ_Θ). In order to derive the scaling laws, symmetries of the classical Navier-Stokes and energy equations have been obtained. However, these symmetries are not enough to generate a scaling law that to properly represents the arbitrary moments. The use of the MPC equations is the key to obtain a constant term in the exponent of the power function that can accurately represent the real data. The usual fluctuation approach to obtain the MPC equations is not used because it yields a non-linear system of equations. Using the instantaneous approach results in a linear system of equations with two trivial symmetries, scaling and translation of moments. The scaling of moments represents a measure of intermittency. Thus, it makes sense that the term in the scaling law, $2\sigma_1 - \sigma_2$, which arises
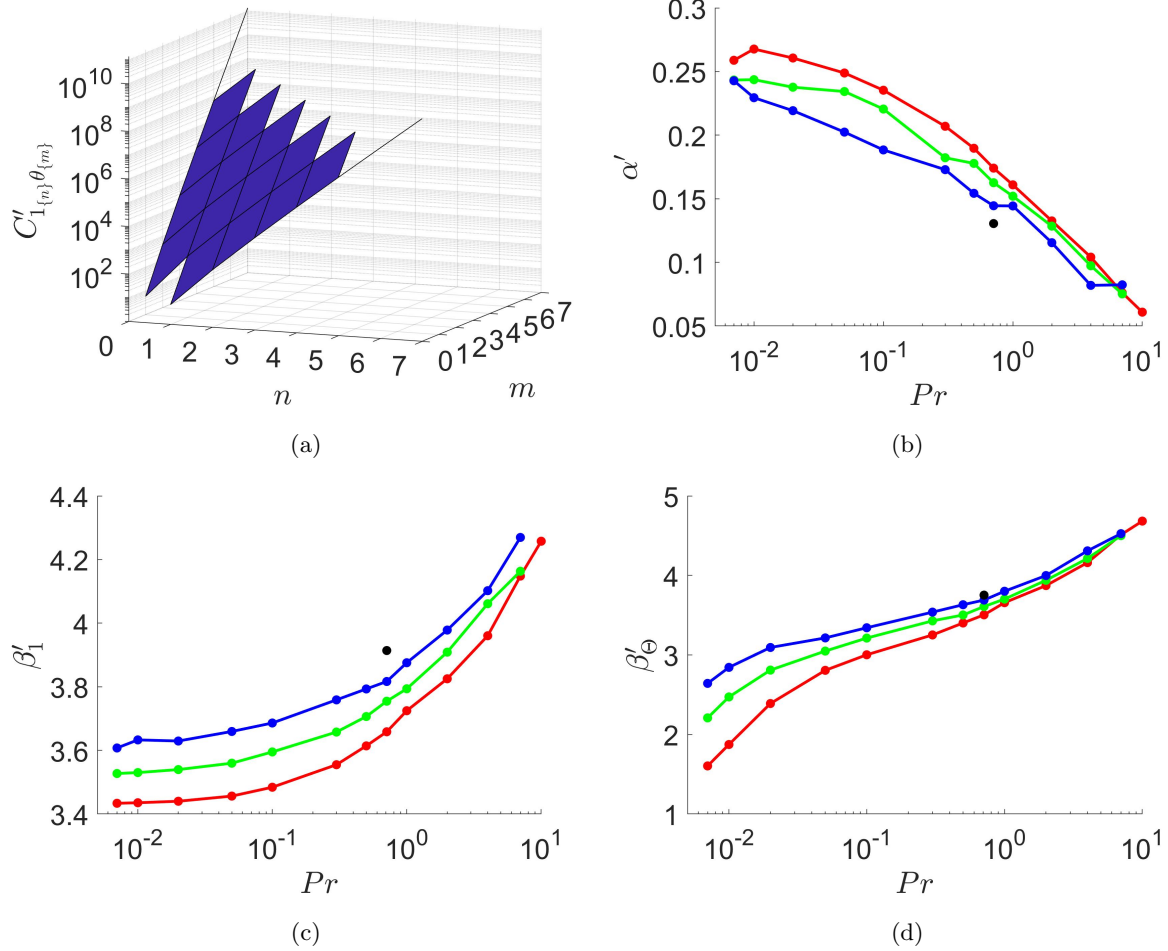
Figure 5.41: (a) Values of $C'_{1_{\{n\}}\Theta_{\{m\}}}$ for $Re_\tau = 500$ and $Pr = 4$. Parameters from equation (5.41b): (b) α', (c) β'_1 and (d) β'_Θ. Colours as in table 5.1. Note that black points at $Pr = 0.71$ in (b), (c) and (d) represent the values for the single simulation at $Re_\tau = 5000$.

Cases	I	II	III	IV	V	VI
Re_τ	166	177	176	178	262	476
Box spawn	$4\pi h$	$2\pi h$	$4\pi h$	$16\pi h$	$16\pi h$	$16\pi h$
Box span	$0.5\pi h$	πh	$2\pi h$	$6\pi h$	$6\pi h$	$6\pi h$
Line	········	▪▪▪▪▪	——	---	········	——

Table 5.10: Lines used through plots of this subsection to identify the different cases.

from this scaling of moments, is the dominant term of the exponent.

The scaling laws have been validated with data obtained from different DNS at different Reynolds and Prandtl numbers. The accuracy of the the scaling law to represent the data is remarkable, specially for high Reynolds and Péclet numbers. For cases with low Péclet numbers, no logarithmic region exist and the center of the channel gets influenced by the viscosity and heat conduction, and the assumption of Re and $Pr \to \infty$ is no longer correct, what entails a wrong scaling of the moments.

An analysis of the parameters of the scaling law at the center of the channel has been done, showing consistency for the cases where Re and $Pr \to \infty$ can be applied. The conclusion regarding the parameters is clear, and it is that, in the center region of the channel, the symmetry of scaling of moments is dominant over the symmetry of scaling in time, space and temperature.

Finally, regarding the constant of integration, note that, according to the analysis done in this work, no relation is obtained between $C'_{1_{\{n\}}\Theta_{\{m\}}}$ and the order of the moments n and m. The exponential function of the constant of integration (5.41b) has been obtained by observation of the values of $C'_{1_{\{n\}}\Theta_{\{m\}}}$. However, this does not mean that the Lie symmetries theory is limited, but additional symmetries may be missing. In the same way that extra symmetries have been obtained from the MPC equations, the Probability Density Function (PDF) contains deeper information about the turbulent behaviour of the flow. Therefore, it is an idea that the exponential behaviour of $C'_{1_{\{n\}}\Theta_{\{m\}}}$ may be found from symmetries contained in the PDF equations. However, this is only a suggestion and the study of these symmetries of the PDF equations is beyond the scope of this work, and it is considered as a future work.

5.2 Other flows

5.2.1 Couette flows

In this subsection, the results obtained from the DNS of a thermal Couette flow are presented. Table 5.10 collect the line colours and styles used in this subsection to distinguish among the different cases (unless otherwise specified).

Temperature statistics

Couette and Poiseuille flows affect in different ways the thermal flow under MBC for these low Reynolds numbers. A first result is that mean and one-point statistics are no longer symmetric. In figure 5.42a, it can be seen that temperature profiles are slightly different in both halves of the channel for Couette flows. On the other hand, the Poiseuille flow thermal profile is perfectly symmetric [52]. A first insight of the collapse of the statistics depending on the computational box size can be obtained from figure 5.42b. Here, temperature profiles of the bottom part of the channel of cases I-IV are shown. All profiles of $\overline{\Theta}^+$ collapse fairly well, except for case I. This case uses a computational box similar to the one in [64]. The collapse error is probably due to the narrowness of the box. Another remarkable difference between Couette and Poiseuille flows is the presence or absence of a thermal logarithmic layer between the viscous and the outer layers. For Poiseuille flows, this logarithmic layer appears for $Pr \approx 0.3$ and above [97]. However, for Couette flows, it is not present for $Pr = 0.71$. It is uncertain if this logarithmic layer in
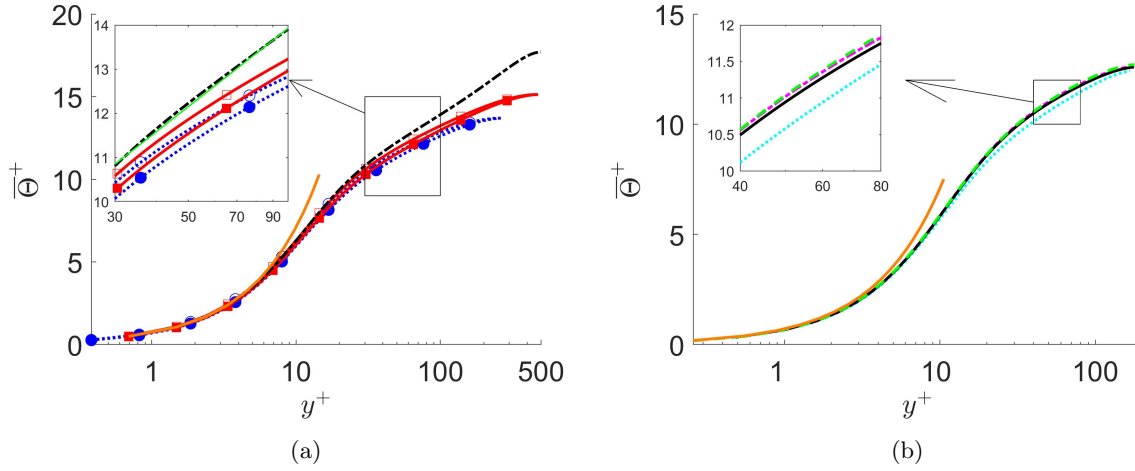
115

Figure 5.42: (a) $\overline{\Theta}^+$ for cases V (blue dotted) and VI (red solid). Closed symbols, bottom half. Empty symbols, top half. Black dash-pointed line represents a Poiseuille flow at $Re_\tau = 497$. (b) $\overline{\Theta}^+$ for cases I-IV at the stationary wall. In both cases, orange solid line: thermal law of the wall, $\overline{\Theta}^+ = Pry^+$. Colours and line style as in table 5.10.

the temperature field will appear for higher Prandtl numbers in a Couette flow. However, as it is said before, Couette flows are far more computationally expensive than Poiseuille ones. To see if a thermal logarithmic layer does exist in Couette flows will still be a challenge for the next decade.

In figure 5.43 turbulent intensities for the three different Reynolds numbers are shown. As a general result, it is seen that the maximum of all turbulent intensities increases and moves towards the wall with an increase of the Reynolds number. A difference between Couette and Poiseuille flows appears in u'^+ (see figure 5.43a). A second maximum can be observed for the higher friction Reynolds number, 500. This was already noted in previous simulations [54], and from this work it is confirmed that for $Re_\tau = 500$, u'^+ shows a second maximum in the central region of the channel. Also, as it was shown before for $\overline{\Theta}^+$, intensities related with temperature are not totally symmetric or antisymmetric. This can be seen in figures 5.43b, 5.43c and 5.43d. Another important point is the antisymmetry obtained for the turbulent intensity $\overline{u^+\theta^+}$ (see figure 5.43c). This opposes to the behaviour of $\overline{u^+\theta^+}$ in a Poiseuille flow when the MBC is employed, where a symetric profile is obtained. This is discussed below.

A distinctive feature of Couette flows is the existence of velocity large instantaneous structures in the flow [56, 57], described in section §2.3.1. Corresponding long and wide structures of the thermal fluctuation field are also present. These instantaneous structures, figure 5.44, appear in a strip-like pattern in $x-z$ planes. Isocontours of θ^+ (see figure 5.44 middle) show long and wide, coherent three dimensional thermal structures, that mainly extend along the streamwise direction. Couette Thermal Flow Superstructures (CTFS) are a consequence of this particular distribution of the values of $\boldsymbol{u}^+$ and θ^+, as they reflect the effect of these instantaneous structures in the time-averaged flow and thermal field. CTFS are defined as a characteristic of the time-averaged perturbations, which does not need to be zero. A first proof of the existence of the CTFS appears in the $x-$averaged fields. The values of $\langle u^+ \rangle_x$, $\langle v^+ \rangle_x$, $\langle w^+ \rangle_x$, and $\langle \theta^+ \rangle_x$ are shown in figure 5.45b. In this figure, white and green lines represent contours of positive and negative $\langle u^+ \rangle_x$, respectively. $(\langle v^+ \rangle_x, \langle w^+ \rangle_x)$ vector field is represented by arrows. Colours show contours of $\langle \theta^+ \rangle_x$. While the $u-$velocity structures expand across the whole height of the channel, a pair of hot-cold thermal structures appear for every velocity structure. These thermal structures are as long as the box itself, $L_x = 16\pi h$ (figure 5.45c), in the same way as the velocity structures [55].
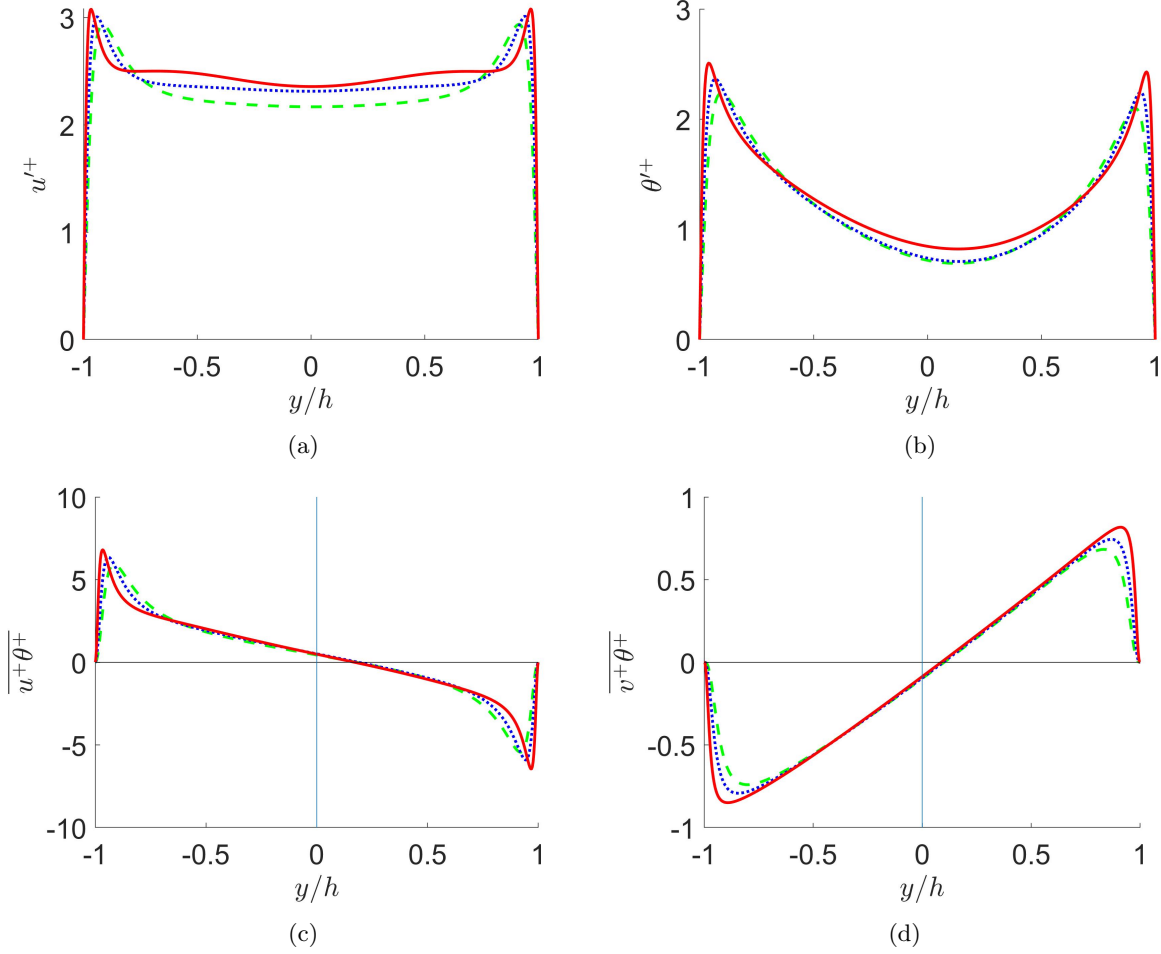
116

Figure 5.43: (a) u'^+, (b) θ'^+, (c) $\overline{u^+\theta^+}$ and (d) $\overline{v^+\theta^+}$ for cases IV-VI. Colours and line style as in table 5.10.

The black box of figure 5.45b shows the footprint of a CTFS. These structures are made of two velocity rolls (positive-negative velocity fluctuations) and four thermal ones. They are organized in such a way that the thermal flux, $\overline{u^+\theta^+}$, is positive in the lowest part of the channel and negative in the top one. A large vortex in $\langle v^+ \rangle$ and $\langle w^+ \rangle$ appears at the center of the CTFS.

In Poiseuille flows, these structures do not exist. In fact, the time averaged of any perturbation field is simply noise. This is due to the inclination of large-scale structures in the Poiseuille flow. In this context, Abe et al. [98] recently examined the effects of the streamwise domain size in the Poiseuille flow for a flow field for $Re_\tau = 395$ and 1020. They found out that when the streamwise domain is reduced to $L_x^+ \approx 400$ for $Re_\tau = 1020$, the two-dimensional behavior is indeed established in the Poiseuille flow. Thus, only trivial symmetries are present. CTFS, on the other hand, exhibit two non-trivial symmetries never described before. First, there is a translation symmetry of period $2L_R$. This length is the distance between the centers of two consecutive rolls. In this case is $L_R/h = 6\pi/8 \approx 2.3$. Second, there exists a symmetry, for $\langle \theta^+ \rangle_x$, with respect to the origin of every (v^+, w^+) vortex (see black box of figure 5.45b).

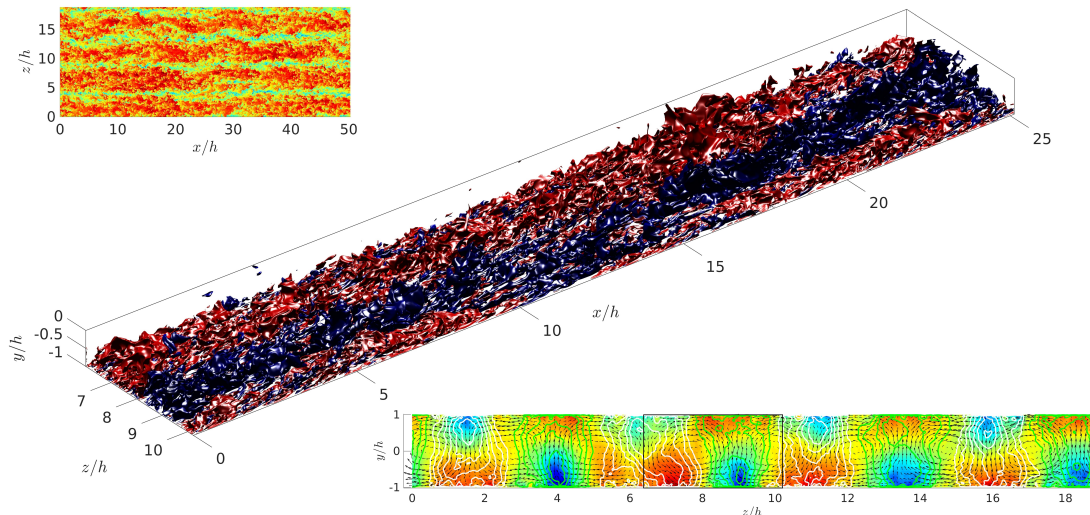Quantities related to the mean flow seem not to be seriously affected by the CTFS. As an example,

117

Figure 5.44: Instantaneous value of θ^+ at $Re_\tau = 500$. Top: $x - z$-plane at $y = 0.3\,h$. Middle: isocontours of θ^+. Red, hotter than mean; blue, colder than mean. Bottom: mean in the streamwise direction of u^+ (isolines), v^+ and w^+ (arrows) and θ^+ (contours). The black box indicates the region plotted in the middle figure.

the Nusselt number has been computed using equation (5.3). Table 5.11 summarizes the difference in Nusselt number for Couette flows, Nu_C, and Poiseuille flows, Nu_P. Value of Nu_P at $Re_\tau = 180$ has been obtained from [40]. In order to obtain Nu_P at $Re_\tau = 250$ a new simulation had to be run.

One can consider the hypothesis of a linear behaviour of the Nusselt number in the range from $Re_\tau = 180$ to 500, as shown in section §5.1. Therefore, precise values of Nu_P have been extrapolated to the Reynolds number of the corresponding Couette flow. All simulations I-IV give approximately the same value (less than a 0.6% deviation) of Nu_C, regardless of the box size. Thus, short and narrow boxes do not introduce a big error when calculating the Nusselt number. An interesting property to be investigated is the difference in Nu between Couette flows and Poiseuille flows. As can be seen in table 5.11, this difference gets reduced with an increase of Re_τ.

Re_τ	Nu_C	Nu_P	Δ (%)
178	21.60	18.33	17.9
262	29.39	25.35	16.0
476	47.96	42.86	11.9

Table 5.11: Nu for each Reynolds number in a Couette flow, second column, and a Poiseuille flow, third column. The fourth column shows the relative difference.

However, local Nusselt number can be different to the average one due to the effect of the CTFS. In figure 5.45a, local Nusselt number for case VI is shown in red and the averaged one, in black. Despite it looks like hot rolls compensate the cold ones when averaging in the y direction (figure 5.45b), local Nusselt number shows that the lower thermal rolls are stronger, especially the cold ones. For this reason,
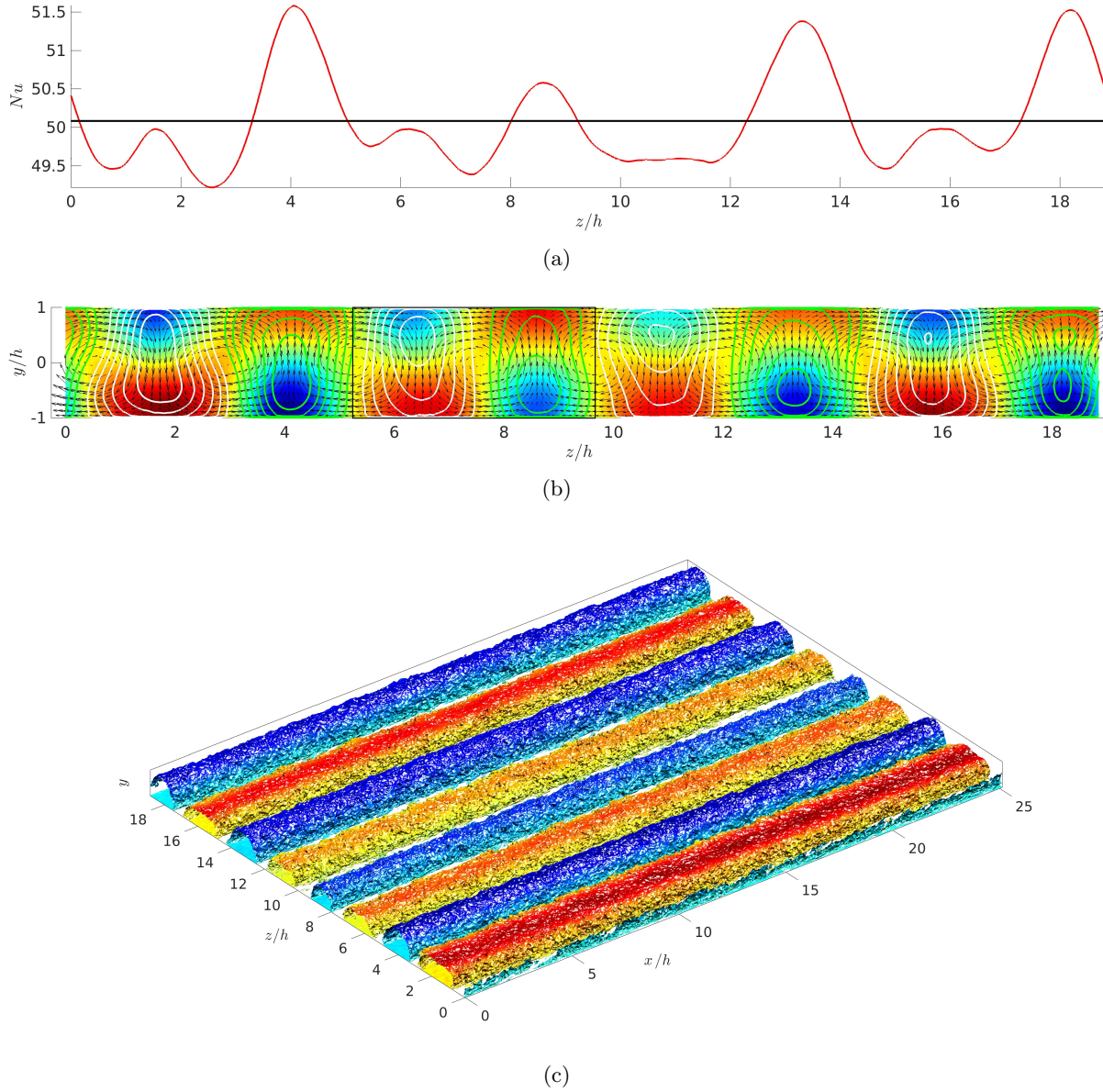
(a)

(b)

(c)

Figure 5.45: Case VI. (a) Local Nusselt number averaged in x direction (red) and averaged Nusselt number (black). (b) Contours of $\langle\theta^+\rangle_x$. White and green lines represent contours of positive and negative $\langle u^+\rangle_x$, respectively. $(\langle v^+\rangle_x, \langle w^+\rangle_x)$ vector field is represented by arrows. (c) Isocontours of cold (blue) and hot (red) $\langle\theta^+\rangle$. The values of the isocontours are $0.4\langle\theta^+\rangle_{min}$ and $0.4\langle\theta^+\rangle_{max}$ for the cold and hot $\langle\theta^+\rangle$, respectively.

119
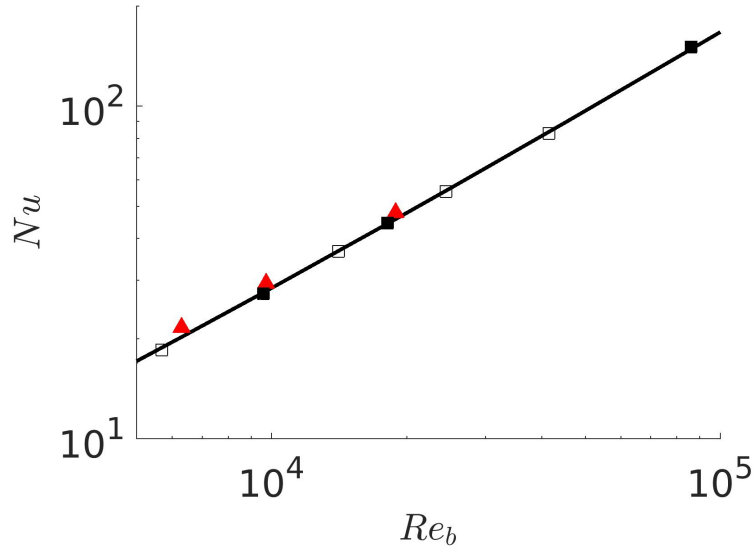
Figure 5.46: Nusselt number as a function of Re_b for Prandtl number of 0.71. Black line represents correlation of Abe and Antonia [80]. ▲ represent Nu for Couette flows, □ are the Nu values for Poiseuille flows from [80] and ■ are the Nu values for Poiseuille flows from [97].

$\langle Nu \rangle_x$ have greater peaks above the average Nu in the z coordinates where a cold roll is present in the lower part of the channel. Here, local Nu number differs up to a 3% from the averaged one. Remark that local Nusselt number shows two frequencies: one that corresponds to the wavelength of the CTFS. The other, whose amplitude is half of the CTFS one, and whose intensity is lower, corresponds to smaller structures that cannot be seen in isocontours plots of mean u'^+ and θ'^+, but that will be observed in the spectral analysis.

To conclude the analysis of the Nusselt number, a comparison of the results obtained in this work with the correlation obtained by Abe and Antonia in [80] for Poiseuille flows has been performed. This correlation expresses the Nusselt number as a function of Reynolds bulk number, Re_b, where the entire height of the channel is considered for its calculation,

$$Nu = h_t Re_b Pr, \tag{5.45}$$

where h_t is the heat transfer coefficient, computed as

$$h_t = \frac{\sqrt{\frac{C_f}{2}}}{2.18 \ln \left(Re_b \frac{\sqrt{C_f}}{2\sqrt{2}} \right) + 2.4}, \tag{5.46}$$

where C_f is the skin friction coefficient, which is obtained form the next expression,

$$\frac{1}{C_f} = 1.8 \ln \left(Re_b \sqrt{C_f} \right) - 0.163. \tag{5.47}$$

Figure 5.46 represents the values of the Nusselt numbers obtained for the Couette flows, ▲, and the ones obtained for Poiseuille flows in [80], □, and from subsection §5.1.1, ■ for $Re_\tau = 500$. As it was
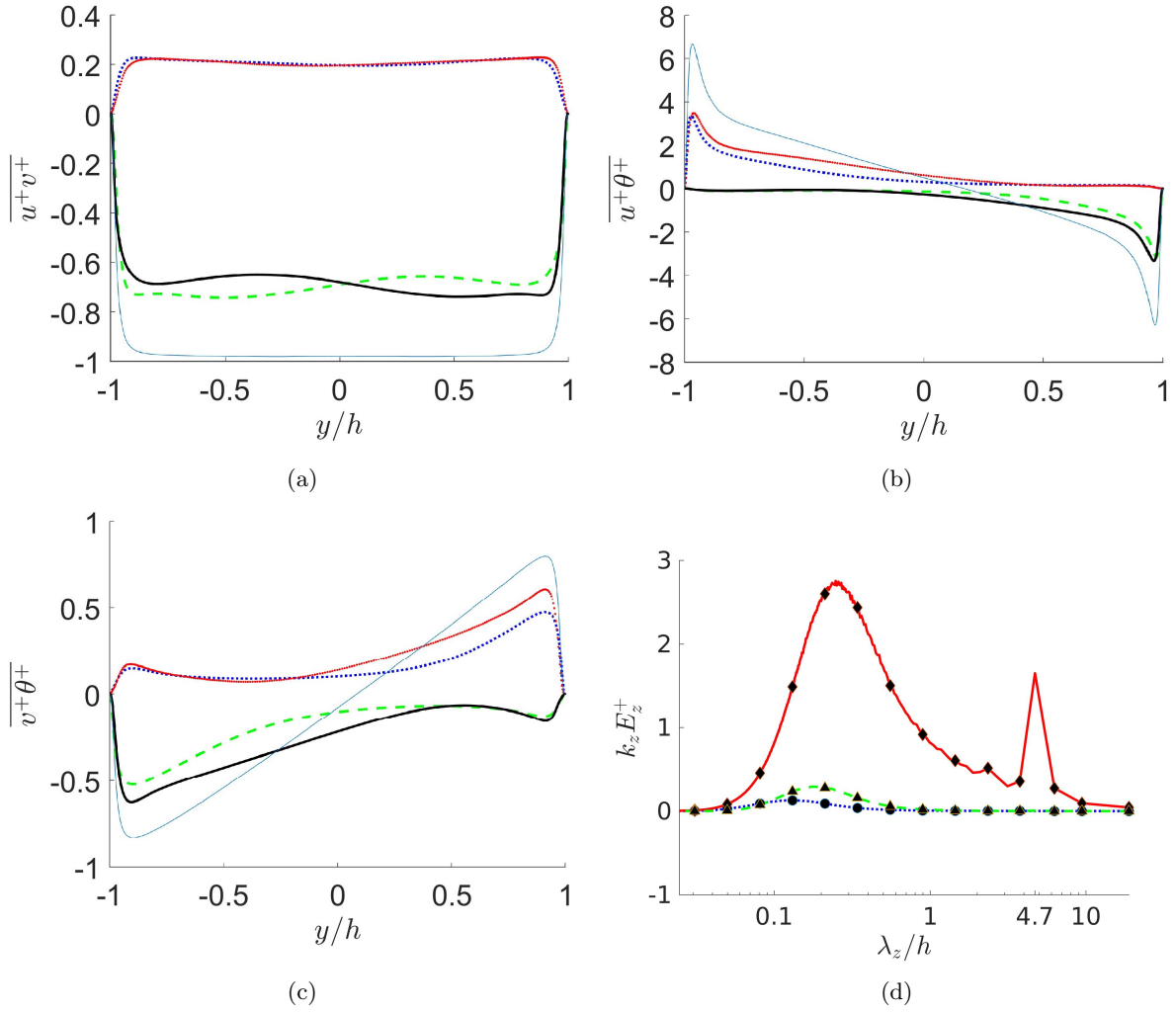
Figure 5.47: Quadrant analysis of case VI for a) $\overline{u^+v^+}$, b) $\overline{u^+\theta^+}$ and c) $\overline{v^+\theta^+}$. Dotted blue line: quadrant 1; dashed green line: quadrant 2; solid red line: quadrant 3; solid black line: quadrant 4. Solid thin blue line is the sum of the four quadrants. d) 1D coespectral density of u^+, θ^+ and $\overline{u^+\theta^+}$ (red solid), for $Re_\tau = 500$.
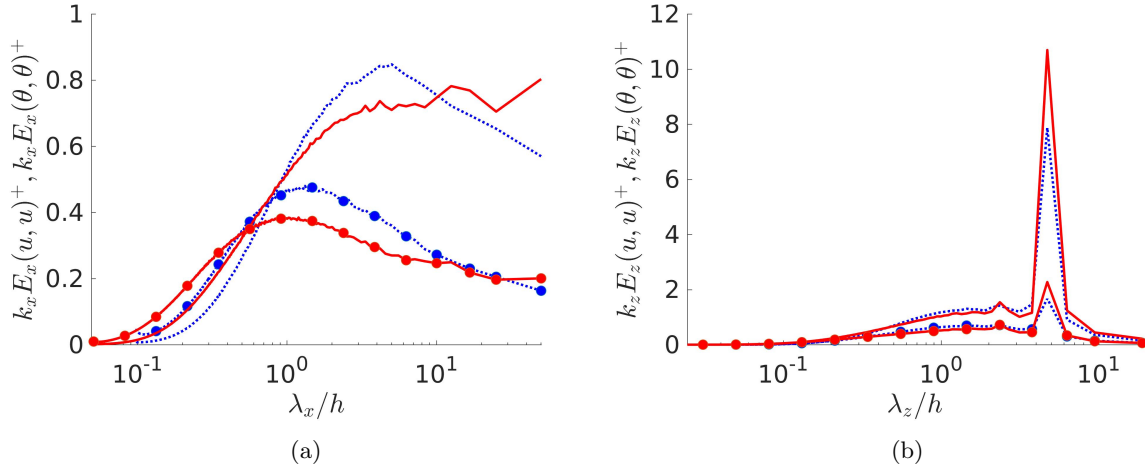
Figure 5.48: 1D spectral density of u^+ (without marks) and θ^+ (●) at $Re_\tau = 250$ and 500 for (a) x and (b) z. $y^+ = 160$. Colours and line style as in table 5.10.

expected, Nu for Couette flows are slightly above the line of the correlation for Poiseuille flows and when Re_b is increased, this difference gets reduced.

A quadrant analysis for case VI, like in subsection §5.1.2 for a Poiseuille flow, has been performed to see if the large-scale temperature structures are active in generating wall-normal turbulent heat flux. Also, the generation mechanism of $\overline{v^+\theta^+}$ is compared with the one of $\overline{u^+v^+}$ and $\overline{u^+\theta^+}$. As a reminder, for this analysis, the flux is divided in four quadrants. In the case of the wall-normal heat flux, quadrant 1 ($v^+ > 0$ and $\theta^+ > 0$) and quadrant 3 ($v^+ < 0$ and $\theta^+ < 0$), are referred to as the outward and inward interactions. While quadrant 2 ($v^+ > 0$ and $\theta^+ < 0$) and quadrant 4 ($v^+ < 0$ and $\theta^+ > 0$) are referred to as the ejection and sweep events. In figure 5.47 all three fluxes are plotted together with the decomposition in the four quadrants. In contrast with the results obtained in Poiseuille flows, the generation mechanism of $\overline{u^+v^+}$ and $\overline{v^+\theta^+}$ are quite different for Couette flow. On the other hand, $\overline{u^+\theta^+}$ and $\overline{v^+\theta^+}$ generation mechanisms are very similar, although interactions and events occur in the opposite walls: for $\overline{u^+\theta^+}$, outward and inward interactions occur in the stationary wall, while for $\overline{v^+\theta^+}$, ejection and sweep events happen in this wall. The opposite happens in the moving wall. This is perfectly correlated with the result obtained in the black box of figure 5.45b, i.e. the CTFS. In the black box, it can be seen how, in the lower part of the channel, hot θ^+ are related with positive u^+ (quadrant 1) and negative v^+ (quadrant 4) or cold θ^+ are related with negative u^+ (quadrant 3) and positive v^+ (quadrant 2). The contrary occurs in the upper part of the channel.

A spectral analysis has been performed for u^+ and θ^+. In figure 5.48, 1D spectral density of the two intensities is shown for $Re_\tau = 250$ and 500, for coordinates x and z and a wall distance of $y^+ = 160$. The most important result is the peak that appears in figure 5.48b at $\lambda_z^+ \approx 4.7$, which agrees with the one obtained in [99]. The wavelength of the peak corresponds to the width of the CTFS or, in other words, to half of the width of the velocity and thermal fluctuation structures shown previously in figure 5.45b, i.e. $2L_R \approx 4.7$. In addition, it can be appreciated that the peak increases as the Reynolds number increases, which means that the structures become more intense for higher Reynolds numbers.

Contour plots are shown in figure 5.49 to visualize the y dependencies of the spectrum. First, mention that at $y^+ = 10$ there is a concentration of energy corresponding to the small scales of the velocity and temperature, intrinsic to every turbulent flow. The new feature appears at the previously mentioned wavelength, $\lambda_z^+ \approx 4.7$, which corresponds to the CTFS. Here it can be seen how the velocity rolls are perfectly symmetric, while the temperature ones are more intense in the lower half of the channel. In
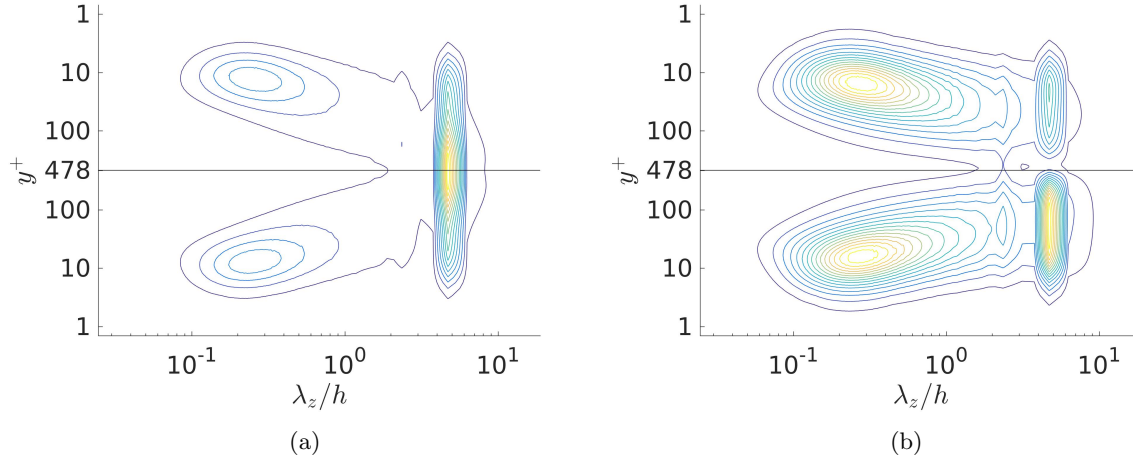
Figure 5.49: Contours of a) u^+ and b) θ^+ spectral density for $Re_\tau = 500$ in the $Y - Z$ plane. Central horizontal line is the center of the channel. Vertical axis is the wall distance to the closest wall.

addition, one can see a small increase of the energy intensity at $\lambda_z^+ \approx 2.3$, which is the half of the previously mentioned wavelength. This second harmonic is the one appreciated in the local Nusselt number (see figure 5.45a).

As it was said before in figure 5.43c, one of the major differences between Poiseuille and Couette flows, when the same thermal boundary condition is used, is the different behaviour of the streamwise thermal flux, $\overline{u^+\theta^+}$, shown in figure 5.50c. When the MBC is used, this flux is symmetric in the case of Poiseuille flows and (almost) antisymmetric for Couette flows. This antisymmetry is totally related to the second symmetry of the rolls explained above. In the lower half of the channel, hot temperature fluctuations are related to positive velocity fluctuations and vice-versa, causing a positive value of $\overline{u^+\theta^+}$. This situation is inverted in the upper part, where hot temperature fluctuations appear with negative velocity fluctuations, causing a negative value of $\overline{u^+\theta^+}$. Other point of view to explain the antisymmetry of $\overline{u^+\theta^+}$ is the difference in the flow and thermal boundary conditions. In a Couette flow, the flow boundary conditions is that one wall is moving, while other wall is stationary. This is analogous to a temperature difference for the thermal boundary condition. However, in this simulations, the MBC is used for the thermal field. Therefore, both walls are kept at the same temperature, which is analogous to a Poiseuille boundary condition for the velocity field.

Box size analysis

All intensities related with temperature (figures 5.50b, 5.50c, and 5.50d) are almost symmetric or anti-symmetric, in contrast with Poiseuille flows, where perfect symmetry or antisymmetry is always present in both halves of the channel. Values of θ'^+ have been compared with other trusted simulations for Poiseuille flows [40] and pipe flows [100] and tendencies agree fairly well.

As it was shown before, the effect of the box size in the mean flow, both in the mean temperature or the Nusselt number is small. This is not the case for the statistics of the perturbations. As it can be seen in figure 5.50, the one-point statistics of the flow for $Re_\tau = 180$ in different boxes do not collapse. The problem is evident in figures 5.50a, 5.50b, and 5.50c, mainly for case I, but not only. However, in the case of Poiseuille flows, a $(2\pi h, \pi h)$ box in x and z, respectively, is enough to accurately compute every first-order statistics [52, 75]. The collapsing problem here is also not an effect of the mesh size, as the cell lengths used for cases I-IV are smaller than in many other available DNS.
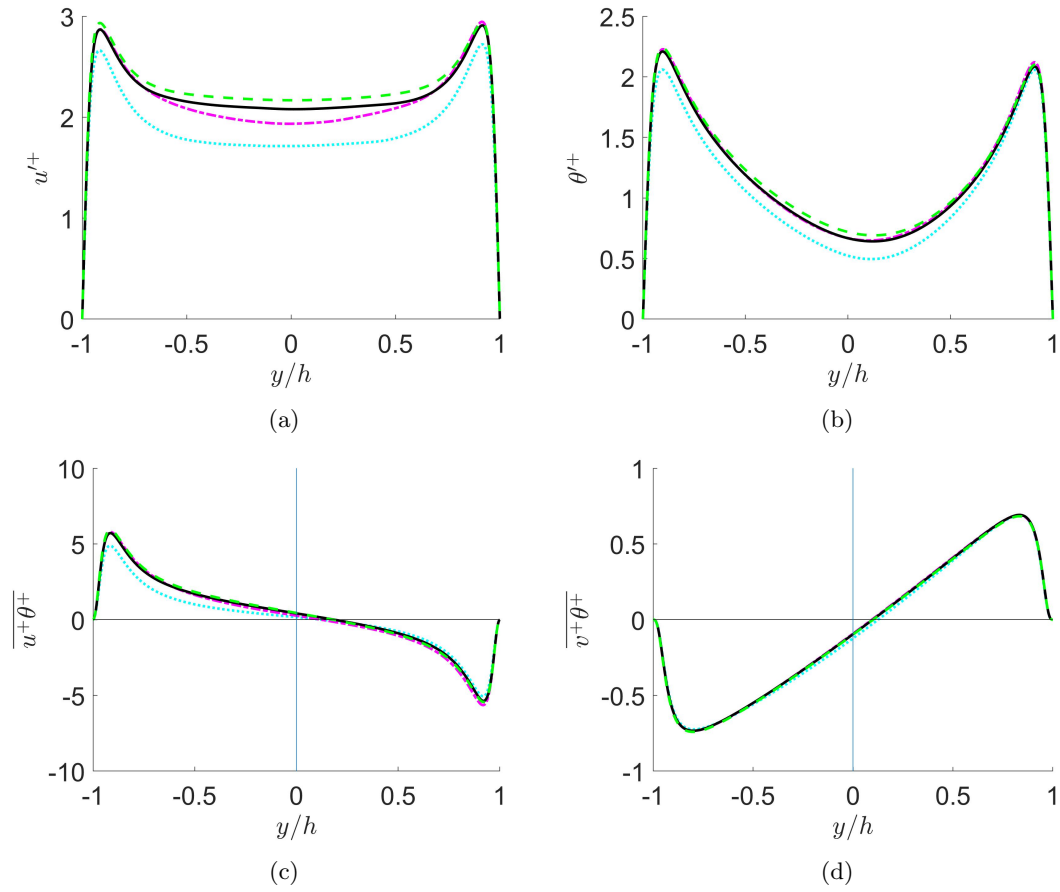
Figure 5.50: (a) u'^+, (b) θ'^+, (c) $\overline{u^+\theta^+}$ and (d) $\overline{v^+\theta^+}$ for cases I-IV. Colours and line styles as in table 5.10.
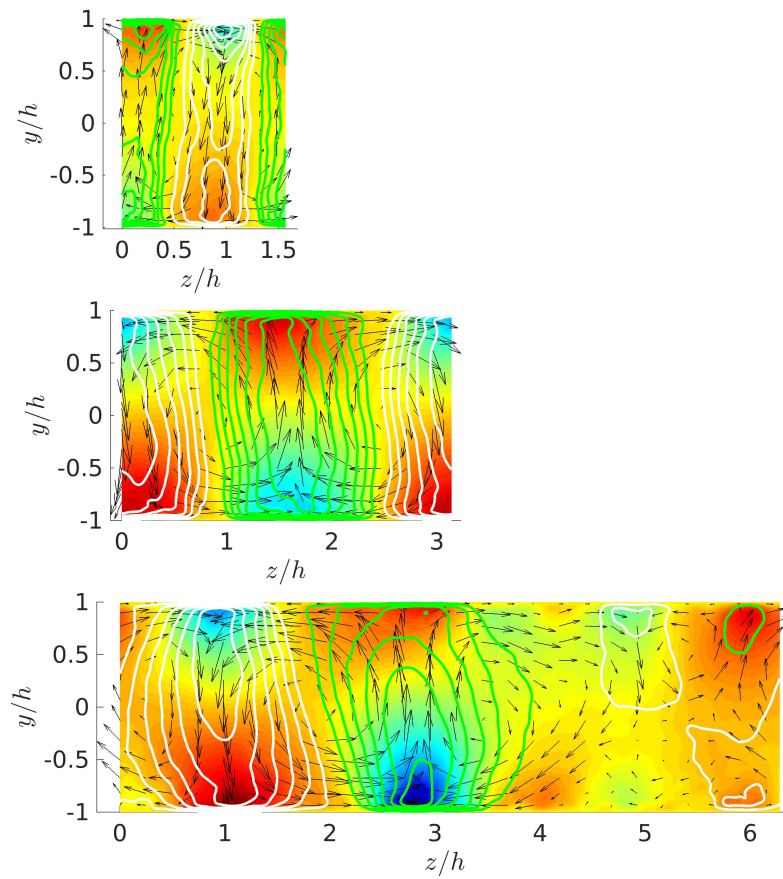
Figure 5.51: Top: case I. Middle: case II. Bottom: case III. Contours of $\langle \theta^+ \rangle_x$. White and green lines represent contours of positive and negative $\langle u^+ \rangle_x$, respectively. $(\langle v^+ \rangle_x, \langle w^+ \rangle_x)$ vector field is represented by arrows.

Thus, the collapse problem has to be related to the CTFS. An analysis of θ^+ in cases I-IV shows that the CTFS are always present (see figure 5.51), even if the box is too small (case I) to obtain accurate statistics. The width of the CTFS grows with the box until a transition phase, where a new CTFS fits in the box. For the two smaller computational boxes in the z direction ($\pi/2$ and π), only one CTFS appears (see figure 5.51 top and middle). Therefore, $L_R/h = 0.78$ and 1.57 for cases I and II, respectively. However, when extending the computational box to 2π in the spanwise direction, a transition phase occurs (see figure 5.51 bottom). Two velocity vortices and four thermal ones are perfectly visible in the left part of the channel. In the right side, the same CTFS is starting to be created, but it is still in process. A slightly wider computational box is needed in order to properly capture 2 CTFS perfectly structured. This explains the differences in the statistics and the discrepancy about the width of the velocity CTFS with other works [54, 61, 62]. Accurate statistics, both for the flow and the thermal field, need wide boxes, with at least four CTFS well represented.

Conclusions

In summary, two simulations of thermal flows at larger numbers of Reynolds and larger boxes than those previously simulated have been described. The perturbations of the flow field present a well organized structure in form of positive and negative velocity rolls. These structures leave a trace in the time-averaged flow field. The superstructure made of two velocity rolls and four thermal ones in the time-averaged field has been defined as a Couette Thermal Flow Superstructure. This implies that unlike for the Poiseuille flow, there seems to be less spanwise meandering of large-scale structures in the Couette flow. In this context, Abe et al. [82] also reported in the Poiseuille flow that when the streamwise domain is reduced down to $L_x \approx 400$ at $Re_\tau = 1020$, the two-dimensional behavior is established so that there is a tight coupling between the near-wall and outer-layer structures. This tight coupling may also be observed in the present CTFS and will be studied in future works. The CTFS presents two symmetries and their size and number has been found to depend on the computational box size. Thermal quantities appear to be not totally symmetric or antisymmetric, in contrast to Poiseuille flows. Using a second set of simulations at $Re_\tau = 180$, it has been seen that the CTFS do not strongly affect neither the mean velocity nor the mean thermal flow. Moreover, mean-related quantities such as the Nusselt number are also not affected. On the other hand, the width and numbers of rolls, i.e. the size of the computational box, affect the value of the first order statistics of the flow. This explains the small differences found in the bibliography about the width of these rolls. Moreover, this makes the width of the box an essential parameter to obtain accurate statistics. The statistics of all simulations can be downloaded from the following link:

http://personales.upv.es/serhocal/

5.2.2 Stratified flows

In this last subsection, the results of simulations for stratified flows are presented. Line colours and styles to distinguish the different cases in the plots of this subsection (unless otherwise specified) are shown in table 5.12.

Stratification on velocity fields

Isosurfaces of $\langle u/U_b \rangle_t$ are plotted at the channel centre for cases C0 and C6 in figure 5.52. The streamwise streaks in case C0 are trackers of the large-scale rolls [55, 56]. While these rolls are strong and clearly defined for C0, their strength and definition is reduced in C6 due to stratification. This can be seen in figure 5.53, where $\langle u(y/h = 1)/U_b \rangle_{tx}$ is shown for the four cases. While C0 and C1 present four extrema, corresponding to the yellow (fast) and blue (slow) streaks of figure 5.52 top, C3 and C6 present six weaker peaks. The disruption of the self-sustaining mechanism by a stable stratification in channel Couette flows was predicted by Eaves and Caulfield [68] by observing the laminar to turbulent transition of neutral

Case	Re_τ	Ri_τ	Line
P0	500	0	——————
C0	480	0	· · · · · ·
C1	476	0.50	– – – –
C3	483	1.65	—·—
C6	476	2.90	——————

Table 5.12: Line colour and style to distinguish the different simulation throughout the figures of this subsection.
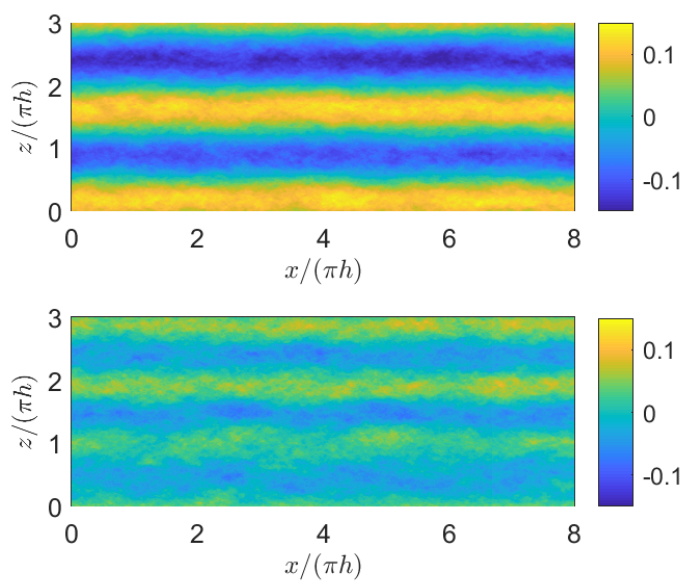

Figure 5.52: $X - Z$ plane at the center of the channel of $\langle u/U_b \rangle_t$ for the cases C0 (top) and C6 (bottom).
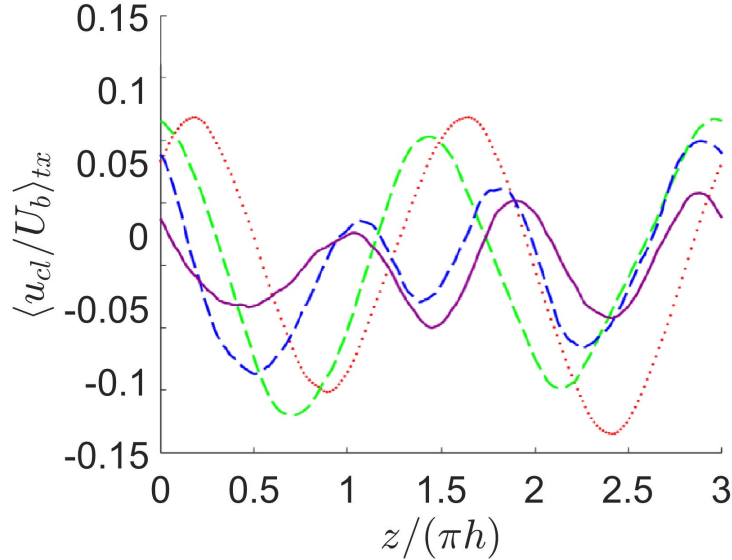
Figure 5.53: $\langle u/U_b \rangle_{xt}$ at the center of the channel represented along the spanwise direction. Colours and line style as in table 5.12.

and stratified cases. Stable stratification damps turbulent wall-normal motions by imposing a potential energy toll [101]. This feature disrupts the well-established self-sustaining mechanism by modifying the energy input into rolls and consequently reducing the kinetic energy density of the streaks. The level of disruption increases with the bulk Richardson number, Ri_b. It is observed that the disruption is significant at a Richardson bulk number $Ri_b \geq 3 \times 10^{-3}$. In this study, the case C6 has $Ri_b = 1.2 \times 10^{-2}$.

More information about the 3D shape of the rolls can be obtained from the spectral density, $\Phi = k_x k_z E(k_x, k_z)$, where k_x and k_z are wave numbers in their sub-index direction and $E(k_x, k_z)$ is the energy spectrum of u. They are presented in figure 5.54. The four figures have been plotted using the same scale to highlight the range in the energy from the largest scales to shorter ones. The black lines correspond to case P0. The two rolls in C0 and C1 are identified by the energy spectrum peak at $\lambda_z/h = 3\pi/2 = 4.7$ in the channel center. This is the same wavelength that was identified in [56] for unstratified Couette at $Re_\tau = 125$, which confirms that the width of the rolls is independent of the Re_τ. For a box with spanwise dimension of $3\pi h$, rolls have a width of $3\pi h/4 \approx 2.4h$. Even if figure 5.53 can give the impression that the rolls in C6 are present but only in more quantity and less energetic, it can be seen in figure 5.54 that in C6, they have disappeared for $y^+ < 100$. Additionally, their width has reduced. Near-wall structures are also identified in figure 5.54 at $y^+ = 10$ at both walls. This region is mainly dominated by coherent streaks of streamwise velocity with an average spanwise separation of the order $\lambda_z^+ \approx 100$ [25].

Thus, increasing Ri_τ causes the break-up of the rms-averaged rolls by weakening the streaks in the channel center as observed in figure 5.52. However, other quantities such as the turbulent density flux $\overline{v^+ \rho^+}$ and the Reynolds stress $\overline{u^+ v^+}$ (not shown here) do not change for the range of stratification achieved in this work. The reason that both quantities are unaffected can be linked to the close relationship between the streamwise velocity and the scalar fields. Deusebio et al. [67] indicates that the Reynolds stress and the turbulent scalar flux decrease proportionally with stratification, so their ratio remains close to constant. Moreover, Garcia-Villalba [101] shows that a deviation of the Reynolds stress in a stratified turbulent channel at $Re_\tau = 550$ is only appreciable from $Ri_\tau \geq 60$. Thus, changes in these averaged quantities shall not be expected at $Ri_\tau < 3$.

Conclusions

Using a database of several Couette flows with active thermal flow, it is observed that the stratification at $Ri_\tau \approx 3$ is enough to weaken the outer streamwise streaks, consequently vanishing the large-scale counter-rotating rolls, characteristic in neutral turbulent Couette channels. The weakening of the outer streaks is presumably caused by the well-known restriction on vertical motions imposed by the stratification, which at low stratification levels is only notorious above the buffer layer. Based on these facts, large-scale rolls will hardly appear in real-life Couette flows of air with a stable wall-normal gradient of temperature, as soon as Ri_τ passes a relatively low threshold.
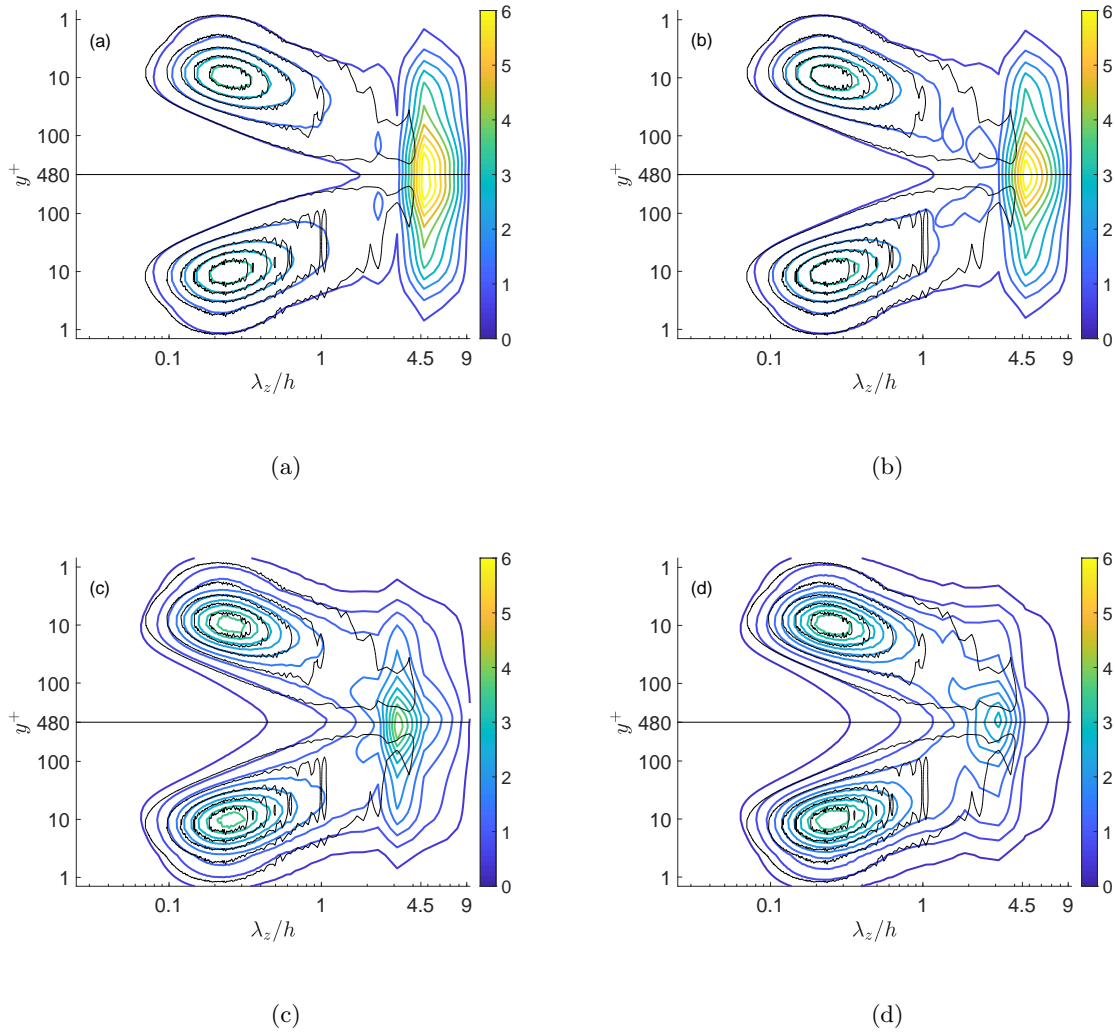
Figure 5.54: Contours of u^+ spectral density for cases C0, C1, C3 and C6 ((a) to (d), respectively) in the $Y - Z$ plane. Central horizontal line is the center of the channel. Vertical axis is the wall distance to the closest wall.

Chapter 6

Conclusions

In this thesis a study of wall turbulence has been performed. The principal focus has been set on thermal flows driven by a pressure gradient and heated uniformly from both walls. Also Couette and stratified flows have been analysed. The main tool to carry out the study has been the Direct Numerical Simulations. A vast database has been generated for very high Reynolds numbers and a wide range of Prandtl numbers never simulated before. New behaviours of these turbulent flows have been addressed and deeply analyzed. The second pillar of this work has been the derivation of scaling laws to describe universal behaviours of turbulence flows. For this purpose, Lie symmetries has been employed.

A extensive review of the previous state of the art bibliography has been presented in section §2.3.1, summarizing the most important works in the sense of high friction Reynolds numbers and extreme Prandtl numbers. As mentioned before, in this work, the state of the art have been extended in all senses: higher friction Reynolds numbers have been simulated, together with a wider range of Prandtl numbers. Specifically, in figure 6.1, a schematic representation of the previous stated of the art (red) and the contributions from this work (blue) for thermal Poiseuille flows is shown.

Also, in Couette flows, the maximum friction Reynolds number simulated has been increased from $Re_\tau = 395$ in [42] up to $Re_\tau = 500$. As a conclusion, a extensive contribution to the new state of the art is provided. All the data collected has been upload to the database of the research team. This database is open to all the scientific community with the aim of validating new codes and data from future research works. The link to the database is:

http://personales.upv.es/serhocal/

The most relevant results for the mean temperature are that the logarithmic layer only appears for $Pr > 0.3$ and for sufficiently high Prandtl numbers, the formation of this logarithmic layer only depends on the Reynolds number. Therefore, the value of κ_t tends towards a constant value and it is independent of Pr for higher Re_τ, obtaining a value of $\kappa_t = 0.44$ for the highest friction Reynolds number simulated at this work, $Re_\tau = 5000$. Also, the scaling of the conductive sublayer is found to be a power function of Pr with a dependence of Pr in the exponent for high Prandtl numbers.

Regarding turbulent intensities, the values of θ'^+ and $\overline{u^+\theta^+}$ tend to collapse in the outer region depending on the friction Péclet number. For low and medium Pr, the peaks of these intensities increase logarithmically with Re_τ, but for high Pr, one of the most important results of this thesis is obtained: the inner peak of θ'^+ is constant for different Re_τ. This has a direct impact in the scaling the the dissipation and viscous diffusion terms of the temperature variance budget: the scaling near the wall of these terms is more accurate. On the other hand, for low Prandtl numbers, the result is the opposite, requiring better scaling for the dissipation and viscous diffusion terms of the temperature variance and the streamwise heat flux and the pressure strain and pressure diffusion terms of the wall-normal heat flux budgets.

Dimensionless numbers Nu and Pr_t have been analysed, with no relevant results for the latter in the new range of Re_τ and Pr simulated. For the former, Nu, new correlations have been proposed in a range
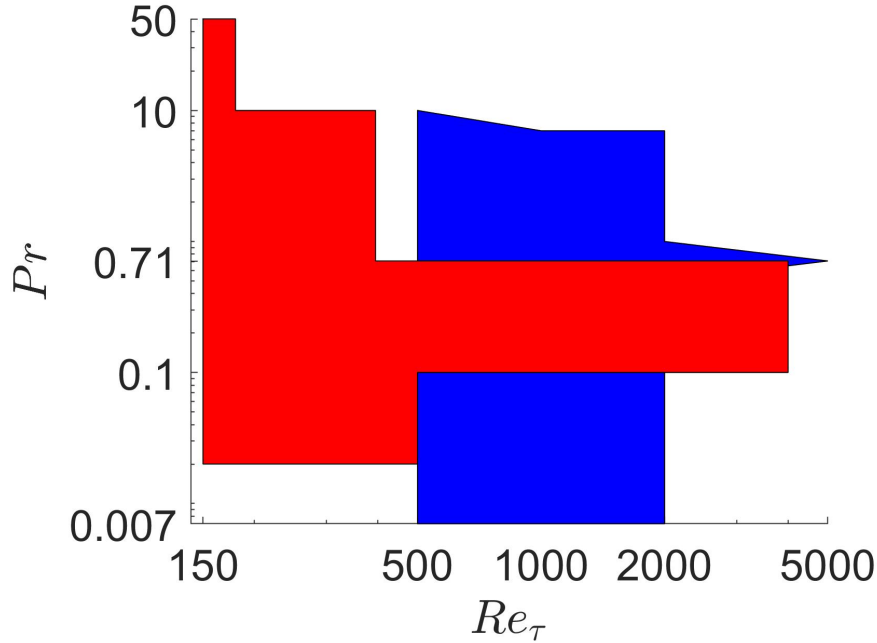
Figure 6.1: Previous stated of the art (red) and the contributions from this work (blue) for thermal Poiseuille flows.

of Pr_τ where Nu behaves as a power function of Pr.

Last comment about Poiseuille flows is that for the case of isothermal flows, it has been obtained for the first time a perfectly developed logarithmic layer at a friction Reynolds number of $Re_\tau = 10000$, with a value of the von Kármán constant of $\kappa = 0.394$.

All the data from Poiseuille flows has been used to validate new scaling laws for turbulent channel flows. These scaling laws have been derived using the Lie symmetries theory. They describe the velocity, temperature and high order moments of both in a defect law of power functions of the wall distance. The strength of these scaling laws is that they are obtained from first principles and that only the first two moments of the velocity and temperature are needed to obtain the exponent of the scaling law for all higher moments. Therefore, one can write in an analytical form, a scaling law for arbitrary moments of order n or m. Also a scaling law for the logarithmic layer of the mean velocity and higher order terms has been derived. The classical logarithmic function for the mean velocity has obtained and validated for the case of $Re_\tau = 10000$. High order moments are obtained as power functions of the wall distance, and the exponent of each moment can be determined from the parameter that determines the second moment. To conclude, the scaling laws derived have proven to describe the turbulence behaviour with an extreme accuracy.

Finally, the behaviour of Couette flows without and with stratification has been studied. A deep analysis of the superstructures that appear in Couette flows (CTFS) has been presented. It has been proved that the dimensions of the computational box directly influence the value of several flow statistics, as turbulent intensities. Therefore, box dimensions are crucial in Couette flow simulations to obtain results that accurately represent the actual flow. The effect of the CTFS, which is not influenced by transversal flows, seem to be dissipated or at least clearly weakened when stratification is presented.

Several future works emerge after this thesis. The use of different canonical domains should be studied to have a broader view of turbulence. The research team is already working on boundary layers. For this

purpose, the code has been adapted to be able to simulate this type of problem and simulations will be run in a near future. The main problem that arise in a DNS of a boundary layer is that, a priori, the flow is no longer periodic in the streamwise direction. In order to solve this problem, a laminar flow is introduced. This laminar flow receives a perturbation which makes it turbulent and it starts to develop into a growing boundary layer. Data is collected in this stage. Then, the flow is made laminar at the end of the computational domain. In such a way, periodicity in the x-direction is achieved and efficient Fourier methods can be used in this direction.

Also, a different way of analysing turbulence can be applied. The one used in this work is based on the Reynolds decomposition, and it focus on the stochastic nature of the flow. The second one, which focus on the turbulent structures that appear on the flow, should also be considered as an alternative to understand turbulence. This point of view was deeply studied by del Álamo et al. in [102, 103] and it has been already addressed by the research team of the author of this thesis in [104].

Regarding Lie symmetries, the results obtained in this thesis have central implications for turbulence model development. More precisely, the statistical symmetries developed in this work should be incorporated into turbulence models to make them reproduce the derived scaling laws. This was recently published by the research team in [105]. It was shown how the statistical symmetries can be considered and a first base-model was developed. Furthermore, it implies that model equations need only to be used up to the second moment to reproduce the scaling exponent for all higher moments as well. In addition, further research and finding of new statistical symmetries seem to be essential for the further development of this theory. Symmetries of the PDF equations and for the wall-normal and spanwise velocity fluctuations are still to be derived.

Chapter 7

Appendix

7.1 Appendix A: a DNS code

In this appendix, the code used to run the simulations will be explained in detail. Simultaneously, different point about a DNS will be addressed. The original code, named LISO, has been previously used in several DNS described in section §2.3.1. Several types of flows can be simulated by the LISO code: Poiseuille, Couette or a mix of both for isothermal flows and, a new version of the code allows to run thermal flows with passive or active scalar. Nevertheless, in order to explain the code in this appendix, the case of a Poiseuille channel flow with a passive scalar will be used, since it is the main flow described in this thesis.

The properties of the computational box, i.e. the domain of the problem, are given in section §4, where the length of the box, the spatial coordinates, the velocity components and temperature are defined. In addition, it should be introduced two important terms: the vorticity, $\boldsymbol{\Omega} = \boldsymbol{\nabla} \times \boldsymbol{U}$; and the helicity, $\boldsymbol{H} = \boldsymbol{U} \times \boldsymbol{\Omega}$. Developing these terms, their definition based on the velocities and their derivatives are for the vorticity

$$\boldsymbol{\Omega} = \begin{Bmatrix} \Omega_x \\ \Omega_y \\ \Omega_z \end{Bmatrix} = \begin{Bmatrix} \frac{\partial W}{\partial y} - \frac{\partial V}{\partial z} \\ \frac{\partial U}{\partial z} - \frac{\partial W}{\partial x} \\ \frac{\partial V}{\partial x} - \frac{\partial U}{\partial y} \end{Bmatrix}. \tag{7.1}$$

And for the helicity

$$\boldsymbol{H} = \begin{Bmatrix} H_1 \\ H_2 \\ H_3 \end{Bmatrix} = \begin{Bmatrix} V\Omega_z - W\Omega_y \\ W\Omega_x - U\Omega_z \\ U\Omega_y - V\Omega_x \end{Bmatrix} = \begin{Bmatrix} V\left(\frac{\partial V}{\partial x} - \frac{\partial U}{\partial y}\right) - W\left(\frac{\partial U}{\partial z} - \frac{\partial W}{\partial x}\right) \\ W\left(\frac{\partial W}{\partial y} - \frac{\partial V}{\partial z}\right) - U\left(\frac{\partial V}{\partial x} - \frac{\partial U}{\partial y}\right) \\ U\left(\frac{\partial U}{\partial z} - \frac{\partial W}{\partial x}\right) - V\left(\frac{\partial W}{\partial y} - \frac{\partial V}{\partial z}\right) \end{Bmatrix}. \tag{7.2}$$

At this point, the equations solved by the code are going to be derived. These, for the velocity field, are the second component of the evolution equations derived from the Navier-Stokes equations (1.5) and (1.6), together with the energy equation (1.7). This method of resolution was first introduced by [25] in what is the seminal DNS work. It is important to note that, from now on, regular vector notation will be used instead of index notation to facilitate the comprehension. In addition, the dimensionless variables in inner coordinates will be presented, but the superscript will be omitted for readability reasons. If the curl ($\boldsymbol{\nabla} \times$) of the momentum equation (1.6) is taken, it is directly obtained that the vorticity appears inside the derivatives of the linear terms and the pressure term dissapears. Regarding the nonlinear term,

$(\boldsymbol{U} \cdot \boldsymbol{\nabla}) \cdot \boldsymbol{U}$, the following operation must be calculated

$$\boldsymbol{H} = \boldsymbol{\nabla} \times ((\boldsymbol{u} \cdot \boldsymbol{\nabla}) \cdot \boldsymbol{u}). \tag{7.3}$$

Developing this term, the second component of the resulting vector is

$$
\begin{aligned}
H_2 = & \frac{\partial U}{\partial z} \frac{\partial U}{\partial x} + U \frac{\partial^2 U}{\partial x \partial z} + \frac{\partial V}{\partial z} \frac{\partial U}{\partial y} + V \frac{\partial^2 U}{\partial y \partial z} + \frac{\partial W}{\partial z} \frac{\partial U}{\partial z} + W \frac{\partial^2 U}{\partial z^2} \\
& - \frac{\partial U}{\partial x} \frac{\partial W}{\partial x} - U \frac{\partial^2 W}{\partial x^2} - \frac{\partial V}{\partial x} \frac{\partial W}{\partial y} - V \frac{\partial^2 W}{\partial x \partial y} - \frac{\partial W}{\partial x} \frac{\partial W}{\partial z} - W \frac{\partial^2 W}{\partial x \partial z}.
\end{aligned}
\tag{7.4}
$$

If the terms $\pm(\partial V / \partial x)(\partial V / \partial z)$ and $\pm V \partial^2 V / (\partial x \partial z)$ are introduced, one can identify the derivatives of the first and third component of the helicity (7.2), with respect to z and x, respectively. Therefore, the final result of the second component of the curl of the nonlinear term is

$$\frac{\partial H_3}{\partial x} - \frac{\partial H_1}{\partial z}. \tag{7.5}$$

A second evolution equation must be taken, which is obtaining after calculating the second curl of the momentum equation. In the linear terms, the laplacian of the velocity, $\nabla^2 \boldsymbol{U}$, is directly obtained, while the pressure term does not need to be calculated after being 0 with the first curl. For the nonlinear term, it must be calculated

$$\boldsymbol{\nabla} \times \overbrace{(\boldsymbol{\nabla} \times ((\boldsymbol{u} \cdot \boldsymbol{\nabla}) \cdot \boldsymbol{u}))}^{a}. \tag{7.6}$$

The terms in the parenthesis (a) are known from the previous calculation,

$$\boldsymbol{\nabla} \times ((\boldsymbol{u} \cdot \boldsymbol{\nabla}) \cdot \boldsymbol{u}) = \left\{ \begin{array}{c} \frac{\partial H_2}{\partial z} - \frac{\partial H_3}{\partial y} \\ \frac{\partial H_3}{\partial x} - \frac{\partial H_1}{\partial z} \\ \frac{\partial H_1}{\partial y} - \frac{\partial H_2}{\partial x} \end{array} \right\}, \tag{7.7}$$

where the first and third component have been obtained in an equivalent way to that of the second component. Therefore, the second component of the second curl of the momentum equation is

$$-\frac{\partial}{\partial y} \left(\frac{\partial H_1}{\partial x} + \frac{\partial H_3}{\partial z} \right) + \left(\frac{\partial^2}{\partial x^2} + \frac{\partial^2}{\partial z^2} \right) H_2. \tag{7.8}$$

With this, the evolution equations that are solved in the DNS code are the second component of the derived equations

$$
\begin{aligned}
\frac{\partial \nabla^2 V}{\partial t} &= h_v + \frac{1}{Re_\tau} \nabla^4 V, & \text{(7.9a)} \\
\frac{\partial \Omega_y}{\partial t} &= h_g + \frac{1}{Re_\tau} \nabla^2 \Omega_y, & \text{(7.9b)}
\end{aligned}
$$

where h_v and h_g resume the nonlinear part of the equations, and are given by

$$
\begin{aligned}
h_v &= \frac{\partial}{\partial y} \left(\frac{\partial H_1}{\partial x} + \frac{\partial H_3}{\partial z} \right) - \left(\frac{\partial^2}{\partial x^2} + \frac{\partial^2}{\partial z^2} \right) H_2, & \text{(7.10a)} \\
h_g &= \frac{\partial H_1}{\partial z} - \frac{\partial H_3}{\partial x}. & \text{(7.10b)}
\end{aligned}
$$

In these equations, $\nabla^2 V = \phi$. An obvious advantage arises for this system, which is that the pressure term is not present, considerably simplifying the problem. Finally, the energy equation can be equivalently written as

$$\frac{\partial \Theta}{\partial t} = h_t + \frac{1}{Re_\tau Pr} \nabla^2 \Theta, \tag{7.11}$$

where h_t is the nonlinear term of the energy equation, and it is defined as

$$h_t = -(\boldsymbol{U} \cdot \boldsymbol{\nabla}) \cdot \Theta. \tag{7.12}$$

While only the second component of the velocity and vorticity are calculated in these evolution equations, (7.9a)-(7.9b), one can easily recover the rest of velocities and vorticities from the definition of the continuity equation and the vorticity,

$$\frac{\partial U}{\partial x} + \frac{\partial W}{\partial z} = -\frac{\partial V}{\partial y}, \tag{7.13a}$$

$$\frac{\partial U}{\partial z} - \frac{\partial W}{\partial x} = \Omega_y. \tag{7.13b}$$

Deriving with respect to x and z, it is obtained

$$\frac{\partial(7.13a)}{\partial x} + \frac{\partial(7.13b)}{\partial z} \rightarrow \left(\frac{\partial^2}{\partial x^2} + \frac{\partial^2}{\partial z^2} \right) U = -\frac{\partial^2 V}{\partial x \partial y} + \frac{\partial \Omega_y}{\partial z}, \tag{7.14a}$$

$$\frac{\partial(7.13a)}{\partial z} - \frac{\partial(7.13b)}{\partial x} \rightarrow \left(\frac{\partial^2}{\partial x^2} + \frac{\partial^2}{\partial z^2} \right) W = -\frac{\partial^2 V}{\partial y \partial z} - \frac{\partial \Omega_y}{\partial x}. \tag{7.14b}$$

As the flow is periodic in both x and z, it is natural to use Fourier methods in these directions. The Fourier transform of any field $\phi(x, y, z)$ is

$$\phi(x, y, z) = \sum_{k_x} \sum_{k_z} \hat{\phi}(y) e^{i(k_x x + k_z z)}, \tag{7.15}$$

where $(\hat{\bullet})$ represents the variable in Fourier space in x and z, and k_x and k_z are the wavenumbers in x and z, respectively. Therefore, equations (7.14a) and (7.14b) can be trivially solved as the become

$$\hat{U} = \frac{-ik_x \frac{\partial \hat{V}}{\partial y} + ik_z \hat{\Omega}_y}{-(k_x^2 + k_z^2)}, \tag{7.16a}$$

$$\hat{W} = \frac{-ik_z \frac{\partial \hat{V}}{\partial y} - ik_z \hat{\Omega}_y}{-(k_x^2 + k_z^2)}. \tag{7.16b}$$

Notice that this technique cannot be used for the $(0, 0)$-modes of U and W. For that case, using the Navier-Stokes equations, one can write

$$\frac{\partial \hat{U}_{00}}{\partial t} = -\frac{\partial \hat{P}}{\partial x} + \hat{H}_{1,00} + \frac{1}{Re_\tau} \frac{\partial^2 \hat{U}_{00}}{\partial y^2}, \tag{7.17a}$$

$$\frac{\partial \hat{W}_{00}}{\partial t} = -\frac{\partial \hat{P}}{\partial z} + \hat{H}_{3,00} + \frac{1}{Re_\tau} \frac{\partial^2 \hat{W}_{00}}{\partial y^2}. \tag{7.17b}$$

The pressure gradient in the spanwise direction is negligible. However, the pressure gradient in the streamwise direction can be used to keep the flow mass constant. Using Fourier transforms, equations

(7.9a), (7.9b) and (7.11) are transformed into Fourier space in x and z, obtaining three decoupled problems

$$\frac{\partial \hat{\phi}}{\partial t} = \hat{h}_v + \frac{1}{Re_\tau}\nabla^2\hat{\phi}, \tag{7.18a}$$

$$\frac{\partial \hat{\omega}_y}{\partial t} = \hat{h}_g + \frac{1}{Re_\tau}\nabla^2\hat{\omega}_y, \tag{7.18b}$$

$$\frac{\partial \hat{\Theta}}{\partial t} = \hat{h}_t + \frac{1}{Re_\tau Pr}\nabla^2\hat{\Theta}. \tag{7.18c}$$

The boundary conditions are

$$\hat{V}(y=\pm 1) = 0, \quad \left.\frac{\partial \hat{v}}{\partial y}\right|_{y=\pm 1} = 0, \tag{7.19a}$$

$$\hat{\omega}_y(y=\pm 1) = 0, \tag{7.19b}$$

$$\hat{\Theta}(y=\pm 1) = 0. \tag{7.19c}$$

Problem (7.18a), (7.19a) is usually solved splitting $\hat{V}$ in three parts,

$$\hat{V} = \hat{V}_p + a\hat{V}_a + b\hat{V}_b, \tag{7.20}$$

where a and b are chosen in order to fulfill the homogeneous Neumann condition.

$$\begin{cases} \frac{\partial \hat{\phi}_p}{\partial t} = \hat{h}_v - \frac{1}{Re_\tau}\left(k_x^2 + k_z^2 - \frac{\partial^2}{\partial y^2}\right)\hat{\phi}_p, \\ \hat{\phi}_p(y=\pm 1) = 0, \\ -\left(k_x^2 + k_z^2 - \frac{\partial^2}{\partial y^2}\right)\hat{V}_p = \hat{\phi}_p, \\ \hat{V}_p(y=\pm 1) = 0, \end{cases} \tag{7.21a}$$

$$\begin{cases} \frac{\partial \hat{\phi}_a}{\partial t} = -\frac{1}{Re_\tau}\left(k_x^2 + k_z^2 - \frac{\partial^2}{\partial y^2}\right)\hat{\phi}_a, \\ \hat{\phi}_a(y=\pm 1) = 0, \\ -\left(k_x^2 + k_z^2 - \frac{\partial^2}{\partial y^2}\right)\hat{V}_a = \hat{\phi}_a, \\ \hat{V}_a(y=1) = 1, \quad \hat{V}_a(y=-1) = 0, \end{cases} \tag{7.21b}$$

$$\begin{cases} \frac{\partial \hat{\phi}_b}{\partial t} = -\frac{1}{Re_\tau}\left(k_x^2 + k_z^2 - \frac{\partial^2}{\partial y^2}\right)\hat{\phi}_b, \\ \hat{\phi}_b(y=\pm 1) = 0, \\ -\left(k_x^2 + k_z^2 - \frac{\partial^2}{\partial y^2}\right)\hat{V}_b = \hat{\phi}_b, \\ \hat{V}_b(y=1) = 0, \quad \hat{V}_b(y=-1) = 1, \end{cases} \tag{7.21c}$$

$$\begin{cases} \frac{\partial \hat{\omega}_y}{\partial t} = \hat{h}_g - \frac{1}{Re_\tau}\left(k_x^2 + k_z^2 - \frac{\partial^2}{\partial y^2}\right)\hat{\omega}_y, \\ \hat{\omega}_y(y=\pm 1) = 0, \end{cases} \tag{7.21d}$$

$$\begin{cases} \frac{\partial \hat{\Theta}}{\partial t} = \hat{h}_t - \frac{1}{Re_\tau Pr}\left(k_x^2 + k_z^2 - \frac{\partial^2}{\partial y^2}\right)\hat{\Theta}, \\ \hat{\Theta}(y=\pm 1) = 0, \end{cases} \tag{7.21e}$$

138

although, due to the symmetry of the problem, $\hat{V}_a(y) = \hat{V}_b(-y)$, so that only systems (7.21a), (7.21b), (7.21d) and (7.21e) have to be solved.

As it is said in section §4, it is natural and efficient the use of Fast Fourier Transforms (FFT) techniques in x and z. This, in fact, decouples the problems (7.21a), (7.21b), (7.21d) and (7.21e), and then, instead of a large Partial Differential Equation (PDE), a large number of individual Ordinary Differential Equations (ODEs) have to be solved. The numerical technique used for y is thus critical to obtain an accurate and fast algorithm. These kind of problems had been addressed mostly by spectral methods [25, 106]. A typical technique used in channels is Chebyshev polynomials, [107]. This has also been applied to thermoconvective problems [108, 109, 110]. However, in this case it is more efficient the use of Compact Finite Differences, (CFD). Note that CFD should no be confused with CFD from Computational Fluid Dynamics. Nevertheless, both terms will be clearly distinguished by the context. The CFD method was introduced in a groundbreaking article by Lele in 1992 [111]. Lele's idea was to use Finite Difference (FD) to solve problems presenting a range of spatial scales, generalizing some Padé schemes that had been used early [112, 113]. Lele's CFD main advantage is that maintaining the freedom in choosing the mesh points of typical finite difference methods offers a very high precission, comparable to that of spectral methods. This is critical in turbulent problems, as one tipically needs many more points close to the wall than in the outer regions of the flow.

Through this part of this work the following notation is going to be used. Let $u(x)$ be a real evaluated function. Supposing that $u(x)$ is differentiable enough, the first and second derivative of $u(x)$ at the point x_i will be denoted by $u_i'(x) = u'(x_i)$ and $u_i''(x) = u''(x_i)$, respectively. In the case of a derivative of grade n, it is expressed as $u_i^{(n)}(x) = \frac{d^n}{dx^n}u(x_i)$. Here, x_i is a point belonging to a certain discretization of the interval $[a, b]$, where a and b are finite and $x_0 = a$, $x_n = b$. Without loss of generality, the schemes will be derived for the second derivative. FD schemes aims to compute an approximation of $u_i''(x)$ trough a linear combination of the values of the function close to x_i. CFD, instead, relates a linear combination of the second derivatives with the values of the function. In order to explain a practical use of CFD schemes, one specific example will be presented, the scheme used in [114]. In that work, the authors used a stencil of seven points in the function and five in the second derivative. Let's assume that the following relation holds (the x dependence is not shown from now on for the sake of readability)

$$\alpha_{-2}u_{i-2}'' + \alpha_{-1}u_{i-1}'' + \alpha_0 u_i'' + \alpha_1 u_{i+1}'' + \alpha_2 u_{i+2}'' =$$
$$a_{-3}u_{i-3} + a_{-2}u_{i-2} + a_{-1}u_{i-1} + a_0 u_i + a_1 u_{i+1} + a_2 u_{i+2} + a_3 u_{i+3}, \tag{7.22}$$

for some unknowns coefficients, α_j and a_j. Without loss of generality, it is possible to assume that one of these coefficients is one, so from now on, $\alpha_0 = 1$. Defining $h_j = (x_i - x_{i+j})$, Taylor's Theorem states that

$$u_{i-2}'' = u_i'' + \frac{h_{-2}}{1!}u_i^{(3)} + \frac{h_{-2}^2}{2!}u_i^{(4)} + ... + \frac{h_{-2}^n}{n!}u_i^{(n+2)} + O\left(h_{-2}^{n+1}\right), \tag{7.23a}$$

$$u_{i-1}'' = u_i'' + \frac{h_{-1}}{1!}u_i^{(3)} + \frac{h_{-1}^2}{2!}u_i^{(4)} + ... + \frac{h_{-1}^n}{n!}u_i^{(n+2)} + O\left(h_{-1}^{n+1}\right), \tag{7.23b}$$

$$u_i'' = u_i'', \tag{7.23c}$$

$$u_{i+1}'' = u_i'' + \frac{h_1}{1!}u_i^{(3)} + \frac{h_1^2}{2!}u_i^{(4)} + ... + \frac{h_1^n}{n!}u_i^{(n+2)} + O\left(h_1^{n+1}\right), \tag{7.23d}$$

$$u_{i+2}'' = u_i'' + \frac{h_2}{1!}u_i^{(3)} + \frac{h_2^2}{2!}u_i^{(4)} + ... + \frac{h_2^n}{n!}u_i^{(n+2)} + O\left(h_2^{n+1}\right). \tag{7.23e}$$

139

and

$$u_{i-3} \;=\; u_i + \frac{h_{-3}}{1!}u_i' + \frac{h_{-3}^2}{2!}u_i'' + ... + \frac{h_{-3}^n}{n!}u_i^{(n)} + O\left(h_{-3}^{n+1}\right), \tag{7.24a}$$

$$u_{i-2} \;=\; u_i + \frac{h_{-2}}{1!}u_i' + \frac{h_{-2}^2}{2!}u_i'' + ... + \frac{h_{-2}^n}{n!}u_i^{(n)} + O\left(h_{-2}^{n+1}\right), \tag{7.24b}$$

$$u_{i-1} \;=\; u_i + \frac{h_{-1}}{1!}u_i' + \frac{h_{-1}^2}{2!}u_i'' + ... + \frac{h_{-1}^n}{n!}u_i^{(n)} + O\left(h_{-1}^{n+1}\right), \tag{7.24c}$$

$$u_i \;=\; u_i, \tag{7.24d}$$

$$u_{i+1} \;=\; u_i + \frac{h_1}{1!}u_i' + \frac{h_1^2}{2!}u_i'' + ... + \frac{h_1^n}{n!}u_i^{(n)} + O\left(h_1^{n+1}\right), \tag{7.24e}$$

$$u_{i+2} \;=\; u_i + \frac{h_2}{1!}u_i' + \frac{h_2^2}{2!}u_i'' + ... + \frac{h_2^n}{n!}u_i^{(n)} + O\left(h_2^{n+1}\right), \tag{7.24f}$$

$$u_{i+3} \;=\; u_i + \frac{h_3}{1!}u_i' + \frac{h_3^2}{2!}u_i'' + ... + \frac{h_3^n}{n!}u_i^{(n)} + O\left(h_3^{n+1}\right), \tag{7.24g}$$

The relations between the coefficients α_i and a_i are derived by matching the Taylor series coefficients. In this case the formal truncation error of the approximation is tenth order. Translating this information into an algebraic equation leads to the system

$$
\begin{pmatrix}
0 & 0 & 0 & 0 & 1 & 1 & 1 & 1 & 1 & 1 & 1 \\
0 & 0 & 0 & 0 & h_{-3} & h_{-2} & h_{-1} & 0 & h_1 & h_2 & h_3 \\
-1 & -1 & -1 & -1 & \frac{h_{-3}^2}{2!} & \frac{h_{-2}^2}{2!} & \frac{h_{-1}^2}{2!} & 0 & \frac{h_1^2}{2!} & \frac{h_2^2}{2!} & \frac{h_3^2}{2!} \\
-h_{-2} & -h_{-1} & -h_1 & -h_2 & \frac{h_{-3}^3}{3!} & \frac{h_{-2}^3}{3!} & \frac{h_{-1}^3}{3!} & 0 & \frac{h_1^3}{3!} & \frac{h_2^3}{3!} & \frac{h_3^3}{3!} \\
-h_{-2}^2 & -h_{-1}^2 & -h_1^2 & -h_2^2 & \frac{h_{-3}^4}{4\cdot3} & \frac{h_{-2}^4}{4\cdot3} & \frac{h_{-1}^4}{4\cdot3} & 0 & \frac{h_1^4}{4\cdot3} & \frac{h_2^4}{4\cdot3} & \frac{h_3^4}{4\cdot3} \\
-h_{-2}^3 & -h_{-1}^3 & -h_1^3 & -h_2^3 & \frac{h_{-3}^5}{5\cdot4} & \frac{h_{-2}^5}{5\cdot4} & \frac{h_{-1}^5}{5\cdot4} & 0 & \frac{h_1^5}{5\cdot4} & \frac{h_2^5}{5\cdot4} & \frac{h_3^5}{5\cdot4} \\
-h_{-2}^4 & -h_{-1}^4 & -h_1^4 & -h_2^4 & \frac{h_{-3}^6}{6\cdot5} & \frac{h_{-2}^6}{6\cdot5} & \frac{h_{-1}^6}{6\cdot5} & 0 & \frac{h_1^6}{6\cdot5} & \frac{h_2^6}{6\cdot5} & \frac{h_3^6}{6\cdot5} \\
-h_{-2}^5 & -h_{-1}^5 & -h_1^5 & -h_2^5 & \frac{h_{-3}^7}{7\cdot6} & \frac{h_{-2}^7}{7\cdot6} & \frac{h_{-1}^7}{7\cdot6} & 0 & \frac{h_1^7}{7\cdot6} & \frac{h_2^7}{7\cdot6} & \frac{h_3^7}{7\cdot6} \\
-h_{-2}^6 & -h_{-1}^6 & -h_1^6 & -h_2^6 & \frac{h_{-3}^8}{8\cdot7} & \frac{h_{-2}^8}{8\cdot7} & \frac{h_{-1}^8}{8\cdot7} & 0 & \frac{h_1^8}{8\cdot7} & \frac{h_2^8}{8\cdot7} & \frac{h_3^8}{8\cdot7} \\
-h_{-2}^7 & -h_{-1}^7 & -h_1^7 & -h_2^7 & \frac{h_{-3}^9}{9\cdot8} & \frac{h_{-2}^9}{9\cdot8} & \frac{h_{-1}^9}{9\cdot8} & 0 & \frac{h_1^9}{9\cdot8} & \frac{h_2^9}{9\cdot8} & \frac{h_3^9}{9\cdot8} \\
-h_{-2}^8 & -h_{-1}^8 & -h_1^8 & -h_2^8 & \frac{h_{-3}^{10}}{10\cdot9} & \frac{h_{-2}^{10}}{10\cdot9} & \frac{h_{-1}^{10}}{10\cdot9} & 0 & \frac{h_1^{10}}{10\cdot9} & \frac{h_2^{10}}{10\cdot9} & \frac{h_3^{10}}{10\cdot9}
\end{pmatrix}
\begin{pmatrix}
\alpha_{-2} \\ \alpha_{-1} \\ \alpha_1 \\ \alpha_2 \\ a_{-3} \\ a_{-2} \\ a_{-1} \\ a_0 \\ a_1 \\ a_2 \\ a_3
\end{pmatrix}
=
\begin{pmatrix}
0 \\ 0 \\ 1 \\ 0 \\ 0 \\ 0 \\ 0 \\ 0 \\ 0 \\ 0 \\ 0
\end{pmatrix}. \tag{7.25}
$$

Note that this is the direct matrix coming from matching Taylor's expansions. Usually this matrix is bad conditioned, so results can be very inaccurate. A typical procedure to overcome this problem consists in normalizing each row by its absolute value maximum.

As the mesh can be non-uniform, it is necessary to solve this system for each point in the mesh. When approaching to the boundaries, no ghost points are used but the stencils are adapted, removing the points which lay outside the interval. This reduces the formal truncation error of the system. Once the coefficients for every point have been computed, we obtain two sparse matrices, one containing the a_i coefficients, A_{yy}, and another one made by the α_i coefficients, B_{yy}, such that

$$B_{yy}(u_0'', ..., u_n'')^t = A_{yy}(u_0, ..., u_n)^t, \tag{7.26}$$

where the superscript $()^t$ denotes the transpose. Note that (7.26) can be used in both ways, to derive a function or to integrate it.

Regarding the time discretization, in order to get a good accuracy in reasonable computational times, a third order Runge-Kutta method has been chosen, derived in [115]. For

$$\frac{\partial \varphi}{\partial t} = L(\varphi) + N(\varphi), \tag{7.27}$$

where L is a linear operator and N is nonlinear, the equation is discretized as follows

$$
\begin{aligned}
(I - \beta_1 \Delta t L)\varphi_1 &= (I + \Delta t \alpha_1 L)\varphi_0 + \Delta t \gamma_1 N_0, & \text{(7.28a)} \\
(I - \beta_2 \Delta t L)\varphi_2 &= (I + \Delta t \alpha_2 L)\varphi_1 + \Delta t (\gamma_2 N_1 + \zeta_1 N_0), & \text{(7.28b)} \\
(I - \beta_3 \Delta t L)\varphi_3 &= (I + \Delta t \alpha_3 L)\varphi_2 + \Delta t (\gamma_3 N_1 + \zeta_2 N_1), & \text{(7.28c)}
\end{aligned}
$$

with $\varphi_i = \varphi(t^i)$, for $t^n = t^0$, t^1, t^2, $t^3 = t^{n+1}$. This stepper presents two problems. The first one is a problem of memory, due to the necessity of saving two nonlinear terms in steps two and three. The second problem is a possible loss of accuracy near the wall, due to the explicit computation of the linear operator in the right hand,

$$L_i^t \varphi_0 = (I + \Delta t \alpha_i L)\varphi_0. \tag{7.29}$$

Both problems are solved in the algorithm, using a little bit of algebra. Suppose that (7.28a) is solved, and φ_2 is to be computed. Let

$$Rh_1 = (I + \Delta t \alpha_1 L)\varphi_0 + \Delta t \gamma_1 N_0, \tag{7.30}$$

then

$$L\varphi_1 = \frac{\varphi_1 - Rh_1}{\beta_1 \Delta t}, \tag{7.31}$$

and it can be computed and stored in a single buffer the right hand side of (7.28b) but the nonlinear term N_1. This tactic can be also applied in the computation of φ_1, but only in the cases where Δt does not change. If the time step changes, the derivative of φ_0 has to be computed explicitly. To avoid this loss of accuracy it is a good idea to recompute the maximum Δt every few steps, using the Courant-Friedichs-Lewy (CFL) condition

$$\max\left(\frac{U\Delta t}{\Delta x}, \frac{V\Delta t}{\Delta y}, \frac{W\Delta t}{\Delta z}\right) \leq CFL. \tag{7.32}$$

All simulations made with this code ran with a CFL of 0.7, showing remarkable stability.

Equations (7.28a)-(7.28c) are solved for ϕ, Ω_y and Θ using CFD. The lineal operator is given by $L = Re_\tau^{-1}\nabla^2$ for ϕ and Ω_y, and $L = (Re_\tau Pr)^{-1}\nabla^2$ for Θ. As a practical example, the energy equation system (7.21e) will be used. Using Fourier transforms, its lineal operator is

$$\hat{L} = -\frac{1}{Re_\tau Pr}\left(k_x^2 + k_z^2 - \frac{\partial^2}{\partial y^2}\right). \tag{7.33}$$

Thus, for each one of the three substeps, the problem becomes

$$(I - \beta_i \Delta t L)\varphi_i = RHS, \tag{7.34}$$

where RHS summarise the right hand side of the equation. This transforms into

$$
\begin{aligned}
\left(I + \beta_i \Delta t \frac{k_x^2 + k_z^2 - \frac{\partial^2}{\partial y^2}}{Re_\tau Pr}\right)\varphi_i &= RHS, \\
\underbrace{\left(I + \beta_i \Delta t \frac{k_x^2 + k_z^2}{Re_\tau Pr}\right)}_{\eta}\varphi_i - \frac{\beta_i \Delta t}{Re_\tau Pr}\frac{\partial^2 \varphi_i}{\partial y^2} &= RHS.
\end{aligned}
\tag{7.35}
$$

Now using matrix equation (7.26), and calling η to the first constant of the previous equation, it is obtained that

$$\eta\varphi_i - \frac{\beta_i \Delta t}{Re_\tau Pr}\frac{\partial^2 \varphi_i}{\partial y^2} = RHS,$$

$$\eta B_{yy}\varphi_i - \frac{\beta_i \Delta t}{Re_\tau Pr}B_{yy}\frac{\partial^2 \varphi_i}{\partial y^2} = B_{yy}RHS,$$

$$\eta B_{yy}\varphi_i - \frac{\beta_i \Delta t}{Re_\tau Pr}A_{yy}\varphi_i = B_{yy}RHS, \qquad (7.36)$$

$$M\varphi_i = B_{yy}RHS,$$

where

$$M = \eta B_{yy} - \frac{\beta_i \Delta t}{Re_\tau Pr}A_{yy}. \qquad (7.37)$$

M is the final matrix to solve. Notice that this matrix is banded, which allows low-storage schemes and the use of very efficient LAPACK routines.

It is also important to mention that as the three problems are decoupled and heat transfer is modelled as a passive scalar, several Prandtl numbers can be solved at the same moment. It is only necessary to use two buffers of memory, φ_i and φ_{i+1} per Prandtl number. Note that this is true in this case that $Pr < 1$, because if not, the mesh size depends on temperature instead of the flow and this would impose the use of finer meshes for the flow and the other Prandtl numbers.

The most expensive part of the algorithm is the computation of the nonlinear terms h_v, h_g and h_t, approximatelly the 80% of the time of the simulation. This is because it is necessary to compute these terms in physical space, due to the aliasing problem [116]. Notice that there are two global operations

1. Direct and inverse Fourier transforms in x and z, as the nonlinear term has to be computed in physical space.

2. Integration-derivation in y.

As the data is distributed throughout the supercomputer, it is necessary to perform several all-to-all communications, which are critical and extremely demanding. The code demands a total of $3(9 + 3hp)$ global communications per step, where hp is the total number of heat transfer problems studied.

The number of points of the problem, and thus memory, depend on the Reynolds number studied. Another constrain is the efficiency of the FFT transforms, so tipically numbers of points made up of powers of 2 and 3 are chosen to increase the velocity of the FFT. Assuming a mesh with $mx \times my \times mz$ points, typically mx is the largest one. It is then natural to start each sub-step of the Runge-Kutta time-stepper scheme with the data set distributed in $y - z$ planes. To avoid load imbalances, the number of nodes must be a divisor of the number of complex planes, which is $mx/2$ after dealiasing. This number is also the maximum number of nodes that can be used. The maximum number of OpenMP processes at each node is $mx/2/nprocs$, where $nprocs$ is the number of processors of the node.

The code to implement the algorithm described above is as follows (schematized in figure 7.1:

1. Calculation of velocity and vorticity in Fourier-Physical-Fourier (F-P-F) space (OpenMP). Transformation of z from Fourier space into physical space (OpenMP). This step requires 15% of the time step.

2. Move the data set from $y - z$ planes into $x-$lines using MPI routines. This step requires 30% of the time step.
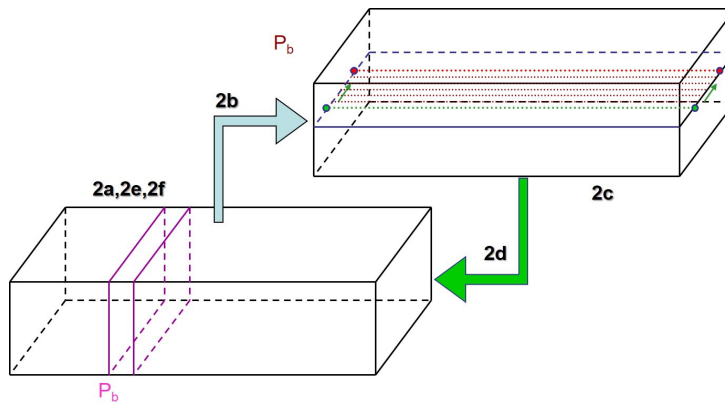
Figure 7.1: Plane-line parallelization scheme of the code.

3. Transformation of the data to physical space in x and computation of nonlinear terms (OpenMP). Then nonlinear terms are transformed back into $x-$Fourier space. This step requires 15% of the time step.

4. Nonlinear terms are moved back into $y - z$ planes, using MPI routines. This step requires 20% of the time step.

5. Transformation of the nonlinear terms in F-P-F space and solution of the viscous problem, using OpenMP. This step requires 20% of the time step.

6. Move to step 1.

Bibliography

[1] Osborne Reynolds. An experimental investigation of the circumstances which determine whether the motion of water shall be direct or sinuous, and of the law of resistance in parallel channels. *Proc. R. Soc. Lond.*, 174:935–982, 1883.

[2] Osborne Reynolds. On the dynamical theory of incompressible viscous fluids and the determination of the criterion. *Philosophical Transactions of the Royal Society of London.*, (A.) 186:123–164, 1895.

[3] G. I. Taylor. Difussion by continuous movements. *Proc. London Math. Soc.*, 20:196–212, 1921.

[4] L Prandtl. Bericht über die Entstehung der Turbulenz. *Z. Angew. Math. Mech.*, 5:136–139, 1925.

[5] von Kármán, T. Mechanische Ähnlichkeit und Turbulenz. *En Proceedings Third Int. Congr. Applied Mechanics, Stockholm,*, pages 85–105, 1930.

[6] J. Boussinesq. A review of the bases of predicting heat transfer to gas turbine rotor blades. *Mem. de L'Académie des Sciences*, 23(2):209–224, 1877.

[7] L. F. Richardson. The supply of energy from and to atmospheric eddies. *Proc. R. Soc. Lond.*, A 97:354–373, 1920.

[8] A. N. Kolmogorov. Local structure of turbulence in an incompressible fluid at very high reynolds numbers. *Dokl. Akad. Nauk.*, SSSR (30):9–13, 1941.

[9] A. N. Kolmogorov. Dissipation of energy in isotropic turbulence. *Dokl. Akad. Nauk.*, SSSR (32):19–21, 1941.

[10] H. Tennekes and J. L. Lumley. *A first course on turbulence.* MIT Press, 1972.

[11] A.A. Townsend. *The Structure of Turbulent Shear Flows, 2nd ed.* Cambridge University Press, New York,, 1976.

[12] S. B. Pope. *Turbulent flows.* Cambridge University Press, 2000.

[13] J. Slotnick, A. Khodadoust, J. Alonso, D. Darmofal, W. Gropp, E. Lurie, and D. Mavriplis. "cfd vision 2030 study: A path to revolutionary computational aerosciences". *NASA TECHNICAL REPORT*, page 218178, 2014.

[14] M. Oberlack. A unified approach for symmetries in plane parallel turbulent shear flows. *Journal of Fluid Mechanics*, 427:299–328, 2001.

[15] V. Avsarkisov, M. Oberlack, and S. Hoyas. New scaling laws for turbulent Poiseuille flow with wall transpiration. *Journal of Fluid Mechanics*, 746:99–122, 2014.

[16] Andreas M Rosteck. *Scaling laws in turbulence – a theoretical approach using Lie-point symmetries.* PhD thesis, Darmstadt, Technische Universität, 2014.

[17] Martin Oberlack, Marta Wacławczyk, Andreas Rosteck, and Victor Avsarkisov. Symmetries and their importance for statistical turbulence theory. *Mechanical Engineering Reviews*, 2(2):15–00157, 2015.

[18] H. Sadeghi, M. Oberlack, and M. Gauding. On new scaling laws in a temporally evolving turbulent plane jet using lie symmetry analysis and direct numerical simulation. *Journal of Fluid Mechanics*, 854:233–260, 2018.

[19] H. Sadeghi and M. Oberlack. New scaling laws of passive scalar with a constant mean gradient in decaying isotropic turbulence. *Journal of Fluid Mechanics*, 775:A10, 2020.

[20] H. Sadeghi, M. Oberlack, and M. Gauding. On new scaling laws in a temporally evolving turbulent plane jet using lie symmetry analysis and direct numerical simulation-corrigendum. *Journal of Fluid Mechanics*, 885:E1, 2020.

[21] A. Leonard. Energy cascade in large-eddy simulations of turbulent fluid flows. In F.N. Frenkiel and R.E. Munn, editors, *Turbulent Diffusion in Environmental Pollution*, volume 18 of *Advances in Geophysics*, pages 237–248. Elsevier, 1975.

[22] James W. Deardorff. A numerical study of three-dimensional turbulent channel flow at large reynolds numbers. *Journal of Fluid Mechanics*, 41(2):453–480, 1970.

[23] J. Smagorinsky. General circulation experiments with the primitive equations. *Monthly Weather Review*, 91(3):99–164, 1963.

[24] Mark P. Simens, Javier Jimenez, Sergio Hoyas, and Yoshinori Mizuno. A high-resolution code for turbulent boundary layers. *Journal of Computational Physics*, 228(11):4218–4231, JUN 20 2009.

[25] J. Kim, P. Moin, and R. Moser. Turbulence statistics in fully developed channels flows at low Reynolds numbers. *Journal of Fluid Mechanics*, 177:133–166, 1987.

[26] H. Eckelmann. The structure of the viscous sublayer and the adjacent wall region in a turbulent channel flow. *Journal of Fluid Mechanics*, 65(3):439–459, 1974.

[27] R. Brodkey, J. Wallace, and H. Eckelmann. Some properties of truncated turbulence signals in bounded shear flows. *Journal of Fluid Mechanics*, 63, 1974.

[28] H. P. Kreplin and H. Eckelmann. Behavior of the three fluctuating velocity components in the wall region of a turbulent channel flow. *The Physics of Fluids*, 22:1233–1239, 1979.

[29] R. Barlow and J. Johnston. Structure of a turbulent boundary layer on a concave surface. *Journal of Fluid Mechanics*, 191:137–176, 1988.

[30] John Kim and Parviz Moin. Transport of passive scalars in a turbulent channel flow. *NASA*, 1(TM-89463):1–14, 1987.

[31] B.A. Kader. Temperature and concentration profiles in fully turbulent boundary layers. *International Journal of Heat and Mass Transfer*, 24(9):1541–15441, 1981.

[32] C.S. Subramanian and R.A. Antonia. Effect of reynolds number on a slightly heated turbulent boundary layer. *International Journal of Heat and Mass Transfer*, 24(11):1833–1846, 1981.

[33] Y. Iritani, N. Kasagi, and M. Hirata. Heat transfer mechanism and associated turbulence structure in the near-wall region of a turbulent boundary layer. *4th Symposium on Turbulent Shear Flows*, pages 17.31–17.36, jan 1983.

[34] R. A. Antonia and Kim J. Turbulent Prandtl number in the near-wall region of a turbulent channel flow. *International Journal of Heat and Mass Transfer*, 34(7):1905–1908, 1991.

[35] S.L. Lyons, T.J. Hanratty, and J.B. McLaughlin. Turbulence-producing eddies in the viscous wall region. *AlChE Journal*, 35(12):1962–1974, 1991.

[36] S.L. Lyons, T.J. Hanratty, and J.B. McLaughlin. Direct numerical simulation of passive heat transfer in a turbulent channel flow. *International Journal of Heat and Mass Transfer*, 34(4-5):1149–1161, 1991.

[37] N. Kasagi, Y. Tomita, and A. Kuroda. Direct numerical simulation of passive scalar field in a turbulent channel flow. *Journal of Heat Transfer*, 114(3):598–606, August 1992.

[38] S. Hoyas and J. Jiménez. Reynolds number effects on the Reynolds-stress budgets in turbulent channels. *Physics of Fluids*, 20(10):101511, 2008.

[39] N. Kasagi and Y. Ohtsubo. Direct numerical simulation of low Prandtl number thermal field in a turbulent channel flow. *Turbulent Shear Flows Springer, Berlin*, 8:97–119, 1993.

[40] Hiroshi Kawamura, Kouichi Ohsaka, Hiroyuki Abe, and Kiyoshi Yamamoto. DNS of turbulent heat transfer in channel flow with low to medium-high Prandtl number fluid. *International Journal of Heat and Fluid Flow*, 19(5):482–491, 1998.

[41] Hiroshi Kawamura, Hiroyuki Abe, and Yuichi Matsuo. DNS of turbulent heat transfer in channel flow with respect to Reynolds and Prandtl number effects. *International Journal of Heat and Fluid Flow*, 20:196–207, 1999.

[42] H. Kawamura, H. Abe, and K. Shingai. DNS of turbulence and heat transport in a channel flow with different Reynolds and Prandtl numbers and boundary conditions. *Turbulence, Heat and Mass Transfer 3 (Proc. of the 3rd International Symposium on Turbulence, Heat and Mass Transfer)*,, 2000.

[43] Y Na, D.V. Papavassiliou, and T.J. Hanratty. Use of direct numerical simulation to study the effect of prandtl number on temperature fields. *International Journal of Heat and Fluid Flow*, 20(3):187–195, 1999.

[44] Y Na and T.J. Hanratty. Limiting behavior of turbulent scalar transport close to a wall. *International Journal of Heat and Mass Transfer*, 43(10):1749 – 1758, 2000.

[45] Hiroyuki Abe, Hiroshi Kawamura, and Yuichi Matsuo. Surface heat-flux fluctuations in a turbulent channel flow up to $Re_\tau = 1020$ with $Pr = 0.025$ and 0.71. *International Journal of Heat and Fluid Flow*, 25(3):404–419, 2004.

[46] F. Schwertfirm and M. Manhart. DNS of passive scalar transport in turbulent channel flow at high Schmidt numbers. *International Journal of Heat and Fluid Flow*, 28(6):1204–1214, 2007.

[47] Makoto Kozuka, Yohji Seki, and Hiroshi Kawamura. DNS of turbulent heat transfer in a channel flow with a high spatial resolution. *International Journal of Heat and Fluid Flow*, 30(3):514–524, 2009.

[48] W. M. Kays, M.E. Crawford, and B. Weigand. Convective heat and mass transfer. *McGraw-Hill*, 1980.

[49] K. Abe, T. Kondoh, and Y. Nagano. A new turbulence model for predicting fluid flow and heat transfer in separating and reattaching flow – ii. thermal field calculations. *International Journal of Heat and Mass Transfer*, 38:1467–1481, 1995.

[50] S. Pirozzoli, M. Bernardini, and P. Orlandi. Passive scalars in turbulent channel flow at high Reynolds number. *Journal of Fluid Mechanics*, 788:614–639, 2016.

[51] J. Jiménez and R. D. Moser. What are we learning from simulating wall turbulence? *Phil. Trans. R. Soc. Lond. A*, 365:715–732, 2007.

[52] F. Lluesma-Rodríguez, S. Hoyas, and MJ Peréz-Quiles. Influence of the computational domain on DNS of turbulent heat transfer up to $Re_\tau = 2000$ for $Pr = 0.71$. *International Journal of Heat and Mass Transfer*, 122:983–992, 2018.

[53] T. Tsukahara, H. Kawamura, and K. Shingai. Dns of turbulent couette flow with emphasis on the large-scale structure in the core region. *Journal of Turbulence*, 7:1–16, 2006.

[54] V. Avsarkisov, S. Hoyas, M. Oberlack, and J.P. García-Galache. Turbulent plane Couette flow at moderately high reynolds number. *Journal of Fluid Mechanics*, 751:R1, 2014.

[55] M. Lee and R. Moser. Extreme-scale motions in turbulent plane couette flows. *Journal of Fluid Mechanics*, 842:128–145, 2018.

[56] Sergio Gandía-Barberá, Sergio Hoyas, Martin Oberlack, and Stefanie Kraheberger. The link between the Reynolds shear stress and the large structures of turbulent Couette-Poiseuille flow. *Physics of Fluids*, 30(4):041702, 2018.

[57] J. Komminaho, A. Lundbladh, and A. Johansson. Very large structures in plane turbulent couette flow. *Journal of Fluid Mechanics*, 320:259–285, 1996.

[58] N. Tillmark and P.H. Aldredsson. Large scale structures in turbulent plane couette flow. *Advances in Turbulence VII*, pages 59–62, 1998.

[59] O. Kitoh, K. Nakabyashi, and F. Nishimura. Experimental study on mean velocity and turbulence characteristics of plane Couette flow: Low-Reynolds-number effects and large longitudinal vortical structure. *Journal of Fluid Mechanics*, 539:199–227, 2005.

[60] O. Kitoh and M. Umeki. Experimental study on large-scale streak structure in the core region of turbulent plane Couette flow. *Physics of Fluids*, 20(2):025107, 2008.

[61] N. Tillmark. *Experiments on transition and turbulence in plane Couette flow.* PhD thesis, KTH, Royal Institute of Technology, 1995.

[62] S. Pirozzoli, M. Bernardini, and P. Orlandi. Turbulence statistics in Couette flow at high Reynolds number. *Journal of Fluid Mechanics*, 758:323–343, 2014.

[63] S. Kraheberger, S. Hoyas, and M. Oberlack. Dns of a turbulent couette flow at constant wall transpiration up to $Re_\tau = 1000$. *Journal of Fluid Mechanics*, 835:421–443, 2018.

[64] B. Debusschere and C.J. Rutland. Turbulent scalar transport mechanisms in plane channel and couette flows. *International Journal of Heat and Mass Transfer*, 47(8-9):1771–1781, 2004.

[65] T. Tsukahara, H. Kawamura, and K. Shingai. Dns of turbulent heat transfer in plane couette flow with emphasis on the large-scale structure. *Thermal Science & Engineering*, 13(4):10–11, 2005.

[66] R. Vinuesa, C. Prus, P. Schlatter, and H.M. Nagib. Convergence of numerical simulations of turbulent wall-bounded flows and mean cross-flow structure of rectangular ducts. *Meccanica*, 51(12):3025–3042, 2016.

[67] E. Deusebio, C. P. Caulfield, and J. R. Taylor. The intermittency boundary in stratified plane couette flow. *Journal of Fluid Mechanics*, 781:298–329, 2015.

[68] T. S. Eaves and C. P. Caulfield. Disruption of SSP/VWI states by a stable stratification. *Journal of Fluid Mechanics*, 784:548–564, 2015.

[69] R. K. Smith, G. Roff, and N. Crook. The morning glory: An extraordinary atmospheric undular bore. *Quarterly Journal of the Royal Meteorological Society*, 108:937–956, 1982.

[70] V. Avsarkisov, B. Strelnikov, and E. Becker. Analysis of the vertical spectra of density fluctuation variance in the strongly stratified turbulence. *Proceedings of the 11th International Symposium on Turbulence and Shear Flow Phenomena*, pages 1–5, 2019.

[71] Martin Oberlack and Andreas Rosteck. New statistical symmetries of the multi-point equations and its importance for turbulent scaling laws. *Discrete Continuous Dyn. Syst*, 3:451–471, 2010.

[72] G. Bluman and S. Anco. *Symmetry and integration methods for differential equations.* vol. 154 of Applied mathematical sciences, 2002.

[73] Sergio Hoyas and Javier Jiménez. Scaling of the velocity fluctuations in turbulent channels up to $Re_\tau = 2003$. *Physics of Fluids*, 18(1):011702, 2006.

[74] F. Alcántara-Ávila, Gandía Barberá, and S. Hoyas. Evidences of persisting thermal structures in couette flows. *International Journal of Heat and Fluid Flow*, 76:287–295, 2019.

[75] A. Lozano-Durán and J. Jiménez. Effect of the computational domain on direct simulations of turbulent channels up to $Re_\tau = 4200$. *Physics of Fluids*, 26(1):011702, 2014.

[76] M. Lee and R. Moser. Direct numerical simulation of turbulent channel flow up to $Re_\tau \approx 5200$. *Journal of Fluid Mechanics*, 774:395–415, 2015.

[77] J. Jiménez. Near-wall turbulence. *Physics of Fluids*, 25(10):101302, 2013.

[78] M. Bernardini, S. Pirozzoli, and P. Orlandi. Velocity statistics in turbulent channel flow up to $Re_\tau = 4000$. *Journal of Fluid Mechanics*, 758:327–343, 2014.

[79] D.A. Shaw and T.J. Hanratty. Turbulent mass transfer rates to a wall for large schmidt numbers. *AIChE Journal*, 23(1):28–37, 1977.

[80] Hiroyuki Abe and Robert Anthony Antonia. Relationship between the heat transfer law and the scalar dissipation function in a turbulent channel flow. *Journal of Fluid Mechanics*, 830:300–325, 2017.

[81] Hiroyuki Abe, Robert Anthony Antonia, and Hiroshi Kawamura. Correlation between small-scale velocity and scalar fluctuations in a turbulent channel flow. *Journal of Fluid Mechanics*, 627:1–32, 2009.

[82] Hiroyuki Abe and Robert Anthony Antonia. Mean temperature calculations in a turbulent channel flow for air andmercury. *International Journal of Heat and Mass Transfer*, 132:1152–1165, 2019.

[83] F. W. Dittus and L. M. K. Boelter. Heat transfer in automobile radiators of the tubular type. *Publications on Engineering 2*, 13:443–461, 1930.

[84] V Gnielinski. New equations for heat and mass transfer in turbulent pipe and channel flow. *International Chemical Engineering*, 16:359–367, 1976.

[85] C. A. Sleicher and M. W. Rouse. A convenient correlation for heat transfer to constant and variable property fluids in turbulent pipe flow. *International Journal of Heat and Mass Transfer*, 18:677–683, 1975.

[86] Yoshinobu Yamamoto and Yoshiyuki Tsuji. Numerical evidence of logarithmic regions in channel flow at $Re_\tau = 8000$. *Physical Review Fluids*, 3:012602(R), 2018.

[87] M. Samie, I. Marusic, N. Hutchins, M.K. Fu, Y. Fan, M. Hultmark, and A.J. Smits. Fully resolved measurements of turbulent boundary layer flows up to $Re_\tau = 20000$. *Journal of Fluid Mechanics*, 851:391–415, 2018.

[88] M. Hultmark, M. Vallikivi, S. C. C. Bailey, and A. J. Smits. Turbulent pipe flow at extreme reynolds numbers. *Phys. Rev. Lett.*, 108:094501, Feb 2012.

[89] I. Marusic, B. J. Mckeon, P. A. Monkewitz, H. M. Nagib, A. J. Smits, and K.R. Sreenivasan. Wall-bounded turbulent flows at high Reynolds numbers: recent advances and key issues. *Physics of Fluids*, 20(6):065103, 2010.

[90] J. Kim. On the structure of pressure fluctuations in simulated turbulent channel flow. *Journal of Fluid Mechanics*, 205:421–451, 1989.

[91] Javier Jiménez and Sergio Hoyas. Turbulent fluctuations above the buffer layer of wall-bounded flows. *Journal of Fluid Mechanics*, 611:215–236, 2008.

[92] Adrián Lozano-Durán and Hyunji Jane Bae. Characteristic scales of Townsend's wall-attached eddies. *Journal of Fluid Mechanics*, 868:698–725, 2019.

[93] N. N. Mansour, J. Kim, and P. Moin. Reynolds-stress and dissipation-rate budgets in a turbulent channel flow. *Journal of Fluid Mechanics*, 194:15, 1988.

[94] V. V. Pukhnachev. Invariant solutions of the navier-stokes equations describingmotions with a free boundary. *Sov. Phys., Dokl*, 17:24–27, 1972.

[95] Marta Wacławczyk, Nicola Staffolani, Martin Oberlack, Andreas Rosteck, Michael Wilczek, and Rudolf Friedrich. Statistical symmetries of the lundgren-monin-novikov hierarchy. *Physical Review E*, 90(1):013022, 2014.

[96] B. Lindgren, J. M. Österlund, and A. V. Johansson. Evaluation of scaling laws derived from lie group symmetry methods in zero pressure-gradient turbulent boundary layers. *Journal of Fluid Mechanics*, 502:127–152, 2004.

[97] F. Alcántara-Ávila, S. Hoyas, and M.J. Pérez-Quiles. DNS of thermal channel flow up to $Re_\tau = 2000$ for medium to low Prandtl numbers. *International Journal of Heat and Mass Transfer*, 127:349–361, 2018.

[98] Hiroyuki Abe, Robert Anthony Antonia, and Toh Sadayoshi. Large-scale structures in a turbulent channel fow with a minimal streamwise fow unit. *Journal of Fluid Mechanics*, 850:733–768, 2018.

[99] S. Hane, T. Tsukahara, and H. Kawamura. DNS of turbulent heat trander in plane Couette flow. *Proc of 13th International Heat Transfer Conference*, August 2006.

[100] Steffen Straub, Daniel Beck, Bettina Frohnapfel, Philipp Schlatter, and Ricardo Vinuesa. The effect of the selected thermal boundary conditions on a fully developed turbulent pipe flow. *16th European Turbulence Conference*, August 2017.

[101] M García-Villalba and Juan C Del Álamo. Turbulence modification by stable stratification in channel flow. *Physics of Fluids*, 23:045104, 2011.

[102] J. C. del Álamo and J. Jiménez. Spectra of the very large anisotropic scales in turbulent channels. *Physics of Fluids*, 15(6):L41–L44, 2003.

[103] J.C. Del Alamo, J. Jiménez, P. Zandonade, and R.D. Moser. Scaling of the energy spectra of turbulent channels. *Journal of Fluid Mechanics*, 500:135–144, 2004.

[104] J.J. Aguilar-Fuertes, F. Noguero-Rodríguez, J.C. Jaen-Ruiz, L.M. García-Raffi, and S. Hoyas. Tracking turbulent coherent structures by means of neural networks. *Energies*, 14(4):984, 2021.

[105] D. Klingenberg, D. Plümacher, and M. Oberlack. Symmetries and turbulence modeling. *Phys. Fluids*, 32:025108, 2020.

[106] Claudio Canuto, M Yousuff Hussaini, Alfio Maria Quarteroni, A Thomas Jr, et al. *Spectral methods in fluid dynamics*. Springer Science & Business Media, 2012.

[107] R.D. Moser, J. Kim, and N.N. Mansour. Direct numerical simulation of turbulent channel flow up to $Re_\tau = 590$. *Physics of Fluids*, 11(4):943–945, 1999.

[108] S. Hoyas, H. Herrero, and A.M. Mancho. Bifurcation diversity of dynamic thermocapillary liquid layers. *Physical Review E - Statistical Physics, Plasmas, Fluids, and Related Interdisciplinary Topics*, 66(5):4, 2002.

[109] S. Hoyas, A. Gil, P. Fajardo, and M.J. Pérez-Quiles. Codimension-three bifurcations in a bénard-marangoni problem. *Physical Review E - Statistical, Nonlinear, and Soft Matter Physics*, 88(1), 2013.

[110] S. Hoyas, P. Fajardo, and M.J. Pérez-Quiles. Influence of geometrical parameters on the linear stability of a bénard-marangoni problem. *Physical Review E*, 93(4), 2016.

[111] S. K. Lele. Compact finite difference schemes with spectral-like resolution. *Journal of Computational Physics*, 103(1):16–42, 1992.

[112] S A Orszag and M Israeli. Numerical simulation of viscous incompressible flows. *Annual Review of Fluid Mechanics*, 6(1):281–318, 1974.

[113] S.G Rubin and P.K Khosla. Polynomial interpolation methods for viscous flow calculations. *Journal of Computational Physics*, 24(3):217–244, 1977.

[114] Alcántara-Ávila, F. and Hoyas, S. Direct Numerical Simulation of thermal channel flow for medium–high Prandtl numbers up to $Re_\tau = 2000$. *Submited to International Journal of Heat and Mass Transfer*, 176:121412, 2021.

[115] Philippe R Spalart, Robert D Moser, and Michael M Rogers. Spectral methods for the Navier-Stokes equations with one infinite and two periodic directions. *Journal of Computational Physics*, 96(2):297–324, 1991.

[116] Claudio Canuto and Alfio Quarteroni. *Spectral Methods*, pages 1–16. American Cancer Society, 2017.